Experimental Investigations of the Vortex Flow Behind a Circular Cone at High Angles of Attack

by

Asad Asghar

A Thesis Presented to the

FACULTY OF THE COLLEGE OF GRADUATE STUDIES

KING FAHD UNIVERSITY OF PETROLEUM & MINERALS

DHAHRAN, SAUDI ARABIA

In Partial Fulfillment of the
Requirements for the Degree of

MASTER OF SCIENCE

In

MECHNICAL ENGINEERING

June, 1992

Order Number 1355310

Experimental investigations of the vortex flow behind a circular cone at high angles of attack

Asghar, Asad, M.S.

King Fahd University of Petroleum and Minerals (Saudi Arabia), 1992

U·M·I
300 N. Zeeb Rd.
Ann Arbor, MI 48106

EXPERIMENTAL INVESTIGATIONS OF THE VORTEX FLOW BEHIND A CIRCULAR CONE AT HIGH ANGLES OF ATTACK

BY

ASAD ASGHAR

A Thesis Presented to the

FACULTY OF THE COLLEGE OF GRADUATE STUDIES

KING FAHD UNIVERSITY OF PETROLEUM & MINERALS

DHAHRAN, SAUDI ARABIA

In Partial Fulfillment of the
Requirements for the Degree of

MASTER OF SCIENCE

In

MECHANICAL ENGINEERING

JUNE, 1992

KING FAHD UNIVERSITY OF PETROLEUM & MINERALS

DHAHRAN, SAUDI ARABIA

This thesis, written by

ASAD ASGHAR

under the direction of his thesis committee, and approved by all the members, has been presented to and accepted by the Dean, College of Graduate Studies, in partial fulfillment of the requirements for the degree of

MASTER OF SCIENCE IN MECHANICAL ENGINEERING

Thesis Committee

W. Stahl 28/6/92

Chairman (Dr. W. H. Stahl)

M. A. Z. Hasan

Member (Dr. M. A. Z. Hasan)

Maged El-Shaarawi June 30, 1992

Member (Dr. Maged A. I. El-Shaarawi)

Dr. M. U. Budair
Department Chairman

Dr. Ala H. Rabeh
Dean College of Graduate Studies

Date : 1/7/92

كلية الدراسات العليا
COLLEGE OF GRADUATE STUDIES

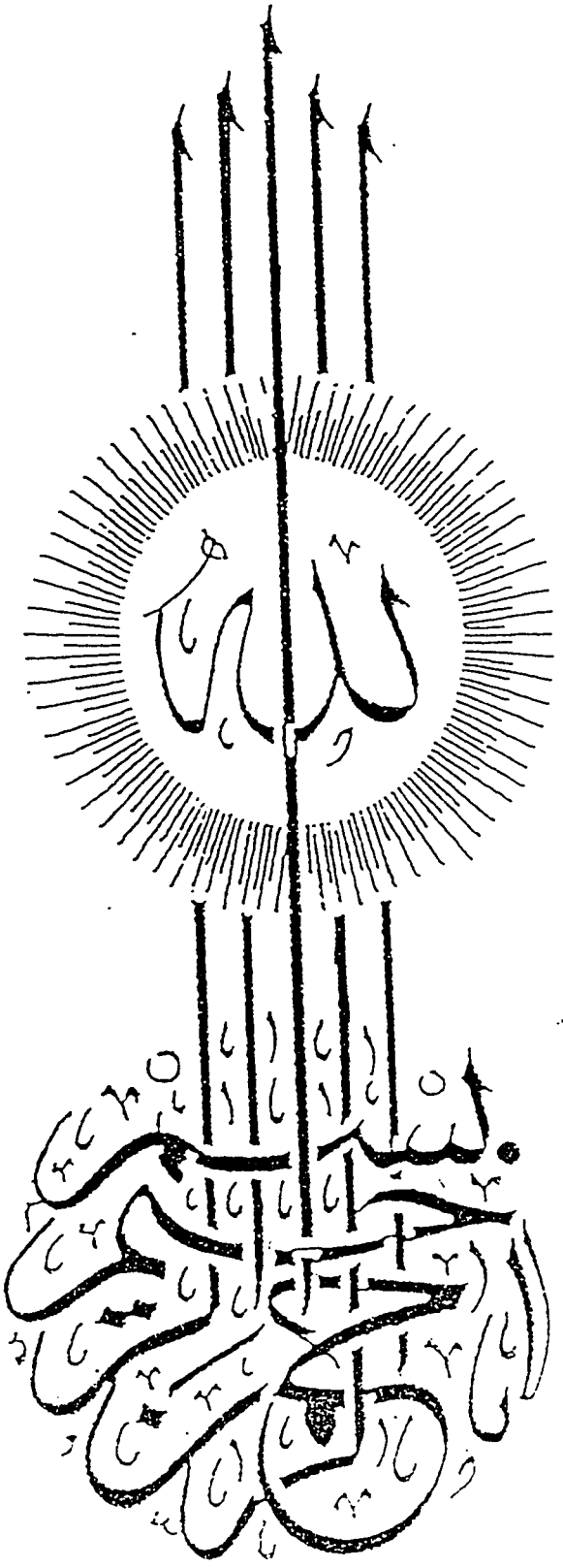

Dedicated

To

My beloved parents, brothers, sisters,

and

Rehana

ACKNOWLEDGEMENTS

Praise and gratitude be to Allah, the Almighty, with Whose gracious help, it was possible to accomplish this work.

Acknowledgement is due to the King Fahd University of Petroleum and Minerals for providing support to this work.

I wish to express my deep gratitude to my major thesis advisor Dr. W. H. Stahl for his constant cooperation in the development of the present work, and for the many hours of attention he devoted to the development of this student. He was always kind and sympathetic to me. Working with him was indeed a wonderful experience which I thoroughly enjoyed.

I am also grateful to other members of my thesis committee Dr. M. A. Z. Hasan and Dr. Maged A. I. El-Shaarawi for their interest, help, and advice.

I also want to thank all the staff of ME workshop for their cooperation, particularly, Mr Bakr Nooreldin, whose advice and experience were utilized in manufacturing of the models. I am also greatly indebted to other faculty and staff of Mechanical Engineering Department.

I wish to extend thanks to Mr. B.J. Aleem, Mr. M. Mahmmod, Mr. Shakeel, G. Dastagir and G. Peralta for their help, and my friends and fellow graduate students for their moral support.

Finally, I would like to express my deep appreciation to Dr. M. U. Budair, Chairman and Dr. H. I. Abualhamayel, previous Chairman of Mechanical Engineering Department for their help and providing necessary facilities for carrying out this research.

TABLE OF CONTENTS

Chapter *Page*

3. EXPERIMENTAL SETUP AND TECHNIQUES

4. RESULTS AND DISCUSSION

LIST OF TABLES

LIST OF FIGURES

NOMENCLATURE

A	:	flow-attachment line/point
A_1	:	windward flow-attachment line/point ($\varphi = 180\ deg$)
A_2	:	leeward flow-attachment line/point ($\varphi = 0\ deg$)
A_3	:	tertiary flow-attachment line/point
C_n	:	sectional normal-force coefficient, $C_n = \dfrac{N}{\frac{1}{2}\rho U_\infty^2 D_{sec}}$
C_p	:	Coefficient of pressure, $C_p = \dfrac{p - p_\infty}{\frac{1}{2}\rho U_\infty^2}$
C_y	:	sectional side-force coefficient, $C_y = \dfrac{Y}{\frac{1}{2}\rho U_\infty^2 D_{sec}}$
$C_{y,fin}$	:	sectional side-force on the fin
D	:	base diameter of the cone
D_{sec}	:	sectional diameter of the cone
H	:	height of fin above the cone surface
H_p	:	centre of pressure on the fin
L	:	length of the cone
l_{eff}	:	effective length or characteristic length (defined in sec. 4.8)
N	:	sectional normal-force
p	:	surface-pressure on the model
p_∞	:	freestream pressure
$R_{sectional}$	:	sectional radius of the cone
Re_D	:	Reynolds number based on base diameter, $Re_D = \dfrac{U_\infty D}{\nu}$
$Re_{l,eff}$	:	Reynolds number based on effective length, $Re_{l,eff} = \dfrac{U_\infty l_{eff}}{\nu}$

S	:	flow-separation line/point
S_1	:	primary flow-separation line/point
S_2	:	secondary flow-separation line/point
U_∞	:	freestream velocity
V_1	:	primary vortex
V_2	:	secondary vortex
X,Y,Z	:	cartesian coordinates, see Fig. 4.1
Y	:	sectional side-force

Greek Symbols

α	:	angle of attack
α_{onset}	:	angle of attack for onset of vortex asymmetry
β	:	yaw angle
δ_N	:	semi-apex angle of cone
ν	:	viscosity of air
ρ	:	density of air
σ	:	surface-flow inclination, see Fig. 4.73
φ	:	circumferential angle of cone from leeward generator, see Fig. 4.1
φ'	:	circumferential angle of cone from windward generator
ψ	:	angle between wall streamline and freestream direction, see Fig. 4.73

THESIS ABSTRACT

NAME OF STUDENT : *ASAD ASGHAR*

TITLE OF STUDY : *Experimental Investigations of the Vortex Flow Behind a Circular Cone at High Angles of Attack*

MAJOR FIELD : *Mechanical Engineering*

DATE OF DEGREE : *June, 1992*

The vortex flow which develops on a flying aircraft or missile becomes asymmetric at some large incidence. This asymmetric vortex configurations can give rise to significant undesirable side forces and yawing moments.

The vortex-flow asymmetry was experimentally studied on a circular cone in the low-speed wind tunnel of KFUPM, at high angles of attack. Circumferential surface-pressure distributions were measured, at $Re_D = 142{,}000$ *from* $\alpha = 15$ *deg to 35 deg. Asymmetric pressure distribution due to vortex-flow asymmetry occurs on the lee-side, at* $\alpha \geq 17$ *deg. resulting in large side force. Inserting a longitudinal fin between the vortices at* $\alpha = 25$ *deg and 35 deg appreciably reduces the asymmetry of the vortices and the side force.*

The angle of attack, α_{onset}, *at which the lee-side vortex system becomes asymmetric was determined, by smoke-flow visualization, as a function of free-stream Reynolds number* Re_D, *for* Re_D = *5,000 to 202,000 (based on cone base diameter). The results show a clear dependence of* α_{onset} *on* Re_D, *and on surface conditions.*

MASTER OF SCIENCE DEGREE

KING FAHD UNIVERSITY OF PETROLEUM AND MINERALS

Dhahran, Saudi Arabia

June, 1992

ملخص الرسالة

إسم الطالب : أسد أصغر .

عنوان الرسالة : بحث تجريبي حول الدوامات الحاصلة خلف مخروط دائري الشكل وبزوايا إلتقاء عاليه مع الإنسياب .

التخصص : الهندسة الميكانيكية .

تاريخ الرسالة : يونيه ١٩٩٢م .

عندما يتحرك صاروخ أو طائرة في الهواء وبزاوية إلتقاء معينة مع الهواء فإن إضطرابات بشكل دوامات تبدأ في الظهور حول الجسم الطائر . وهذه الدوامات تصبح غير متماثلة عند زوايا الإلتقاء الكبيرة بين الجسم الطائر والهواء ممايعطي بعض النتائج غير المرغوب فيها .

هذه الظاهرة درست في هذا البحث بالنسبة لجسم مخروطي الشكل حيث أن هذا الشكل يمثل بعض الأشكال الموجودة في مقدمات الصواريخ والأجسام الطائرة .

أجريت الدراسات التجريبية في النفق الهوائي الموجود بجامعة الملك فهد للبترول والمعادن حيث تم دراسة الإنسياب حول أجسام مخروطية مختلفة عند سرعات هواء منخفضة وزوايا إلتقاء عالية عن طريق قياس الضغط على سطح الجسم والتقاط صور للتأثيرات الحادثة على الجسم . ولقد درس إنسياب الهواء حول المخروط بقياس توزيع الضغط المحيطي حول السطح عند رقم رينولدز حوالي (١٤٢٠٠٠) وزوايا إلتقاء بين ١٥° إلى ٣٥° .

وحدث عدم تماثل للدوامات عندما كانت زاوية الإلتقاء حوالي ١٧° مما نتج عنه قوى عمودية وجانبية عالية وبإدخال مروحة طولية حول الجانب الخلفي من المخروط عند زاوية إلتقاء ٢٥° و ٣٥° أدى إلى التقليل من الإضطراب الحاصل .

وقد حددت زاوية الإلتقاء الحرجة (α_{onset}) التي عندها تصبح الدوامات غير متماثلة كدالة من رقم رينولدز في المدى من رقم رينولدز = ٥٠٠٠ إلى رقم رينولدز = ٢٠٢٠٠٠ (إعتماداً على قطر قاعدة المخروط) وقد حددت بداية عدم التماثل بإستخدام ضوء الليزر الساقط عموديا على محور المخروط . وقد أظهرت النتائج إعتماداً كبيراً لزاوية الإلتقاء الحرجة مع رقم رينولدز وكذلك استخدمت طريقة الطين الصيني لرؤية الإنسياب حول الجسم في تحديد قيمة زاوية الإلتقاء الحرجة عند رقم رينولدز مساوي (٢٩٠٠٠) وقد وجد أن زاوية الإلتقاء الحرجة تعتمد إعتماداً ظاهريا على عدة عوامل مرتبطة بسطح الجسم وإختلافات أخرى في هندسة التصميم للنموذج المعد للدراسة .

درجة الماجستير في العلوم

جامعة الملك فهد للبترول والمعادن

الظهران - المملكة العربية السعودية

يونيه ١٩٩٢م

CHAPTER 1

INTRODUCTION AND OBJECTIVES

1.1 Introduction

Combat agility requirements in the new generation of fighter aircraft and increased performance requirements for missiles have emphasized the need for controlled flight capability at increasingly high angles of attack, α [1]. An extensive knowledge of the aerodynamics of aircraft and missiles over a large range of angles of attack is therefore required.

Efficient high-speed flight of missiles and aircraft necessitates the use of slender, pointed forebodies for aerodynamic drag minimization. However, these slender pointed bodies characteristically experience abrupt and relatively large lateral aerodynamic loads when pitched to high angles. With degraded control effectiveness also encountered under such conditions, serious handling difficulties can result [1].

The aerodynamics of slender bodies at high angles of attack is especially interesting because of the wide variety of flow phenomena that occur at those flight conditions [2]. At zero incidence the flow is attached and vortex-free. As the angle of attack is increased from zero, a steady, symmetric pair of vortices is observed in the leeward-side flow. With further increase in incidence, the symmetric vortex pair becomes asymmetric, but the flow remains essentially steady in time. At still higher incidence, the steady asymmetric flow becomes

unsteady, and as the angle of attack tends towards 90°, the flow pattern approaches that of a circular cylinder in crossflow [2,3]. The asymmetric disposition of the vortices at high angle of attack gives rise to significant side forces and yawing moments [2]. Figure 1.1 shows a typical variation of side force and vortex patterns with incidence occurring on a typical body of revolution at zero yaw. The magnitude of side force can be larger than the maximum normal force. The strong yawing moments can overwhelm the control surfaces causing the vehicle to lose control. For example, the unpredictable trajectories of missiles launched at high angles of attack are related to the forces generated by the forebody vortices. The critical angle of attack at which symmetric flow gives way to asymmetric flow on slender bodies is called 'onset angle' or α_{onset}.

Side forces and moments at high angle of attack are relatively more severe at low velocities and gradually diminish as the velocity increases to low supersonic values [4, 5, 6].

The asymmetric vortices can be made symmetric or their effects counteracted with external appendages such as strakes [7], fins [8], and body trips [1]. The vortex asymmetry can also be suppressed by base bleed technique [9], nose blunting [10] and by blowing at the apex [11].

There are different geometries of missile and aircraft forebodies, such as hemisphere cylinder and tangent-ogive. However, many noses of aircraft and missiles can quite well be represented by a simple cone [12]. A study of the flow about a cone at incidence will help in the understanding of the fundamental

fluid mechanics of flows around aircraft and missile forebodies. As such, the cone holds a position with respect to flows about the wider class of slender bodies similar to that held by the plane delta wing with respect to flows about slender wings [13]. Therefore, a circular cone has been used as a prototype configuration for our experimental investigation of three-dimensional, separated flows.

1.2 Objectives

Vortex flow behind a circular cone at high angles of attack in low-speed flow was studied in two parts.

1.2.1 Part I

Stahl [8] investigated the influence of a fin on the lee-side vortex flow of a circular cone primarily in a water tunnel by means of flow visualization, at $Re_D = 7{,}800$. He found that the addition of a fin between the vortices suppresses the asymmetry of the vortex flow, present without fin. The present study was performed to carry further the earlier work done by Stahl. Therefore, a quantitative investigation as to the effectiveness of a fin in suppressing vortex flow asymmetry was carried out. To this end, the flow field around the cone in a low-speed air stream ($Re_D = 142{,}000$) was studied by taking pressure measurements on the surface and by vortex-flow visualization. The effect on the flow around the cone of inserting a fin on the lee-side of the cone was studied by taking surface-pressure measurements on the cone with a fin, and on the fin.

1.2.2 Part II

It has been found in earlier investigations of vortex-flow asymmetry behind circular cones [8, result of part I] that the onset of asymmetry occurred at two widely different angles of attack in two different sets of experiments in two different tunnels. It was assumed, that the two largely different values of Reynolds numbers, which prevailed in the two sets (Re_D = 7,800 and 142,000) were influential in the occurrence of the two widely different values of onset angles ($\alpha_{onset} \approx 35$ deg and 16 deg, respectively). Therefore, an experimental investigation was carried out on two geometrically similar circular cones of different size to determine the onset angle of attack of vortex-flow asymmetry as a function of Reynolds number, Re_D , in the range of Re_D = 5,000 to 202,000 (formed with base diameter).

CHAPTER 2

LITERATURE REVIEW

2.1 General

Vortical flow over slender bodies have stirred the minds of experimentalists and numericists alike since early times [14]. Many investigators have contributed to the knowledge of flow past circular cylinders and over inclined bodies of revolution. In the following, we will start with the early work on two-dimensional flow past a cylinder and progress to fully three-dimensional shedding from slender bodies. Both theoretical and experimental work will be covered, although the large amount of literature allows only a limited selection.

2.2 Theoretical Studies

An interesting, early model for an initially symmetric vortex pair behind a two-dimensional circular cylinder in potential flow is that discussed by Föppl [15]. The result of his analysis is a locus of the vortex centers, such that the symmetric vortex pair is stationary relative to the cylinder (equilibrium positions), together with a specific vortex strength for each center location. Föppl also investigated the stability of the symmetrical vortex pair with respect to small symmetric and antisymmetric displacements from the equilibrium positions. He found that the symmetrical vortex configuration is stable for symmetric and unstable for antisymmetric disturbances. He compared the predictions of his mathematical model with an available experimental result, and

found them in good agreement.

The use of discrete vortices to represent a continuous vortex-sheet was first proposed by Rosenhead [16], however, this work was not concerned with vortex-shedding from bodies. The first application of this approach to separation from cylinders was reported by Gerrard [17], but practical computations were first carried out by Sarpkaya [18]. Further improvements in the location of separation points and the strength of the discrete vortices resulted in several usable prediction methods, notably from Deffenbaugh and Marshall [19] and Sarpkaya [20].

2.2.1 Studies on Slender Bodies

The solution of the vortex-shedding problem associated with slender bodies at high angles of attack can be approached by extension of the aforementioned two-dimensional work through the cross-flow analogy. In this approach, the three-dimensional, steady-flow problem is replaced by a two-dimensional, unsteady, separated-flow problem for solution. Numerous implementations of this general model were developed, of which that by Allen and Perkins [21] is particularly well known. The approach was exploited in the work of Thomson and Morrison [22], who used the von Karman vortex-street model of a two-dimensional wake to correlate vortex shedding data on bodies of revolution at high angle of attack. A model of this type requires a large base of empirical information.

An early three-dimensional approach that requires less empirical information is reported by Bryson [23]. He attempted to calculate the flow

around circular cylinders and cones at high incidence. The flow model is a pair of concentrated vortices each connected to the body by a feeding sheet of negligible strength. The vortex strength and position are determined from conditions which require that the separation point is a stagnation point and that there is no net force on the vortex and its feeding sheet. The method of Bryson was extended by Wardlaw [24] to improve the calculation of the vortex strength, using experimentally found separation points.

Wardlaw uses relatively high-strength, concentrated vortices in his method. A different approach is used by Angelucci [25] and Marshall and Deffenbaugh [26], who developed techniques incorporating large numbers of elementary discrete vortices fed into the flow field. Angelucci used the vortex cloud approach coupled with the use of experimental data to specify the separation lines. Marshall and Deffenbaugh used boundary-layer methods to calculate the separation lines on axisymmetric bodies. The symmetric vortex-shedding restriction was removed by Deffenbaugh and Koerner [27], their work permits the asymmetric development of vortices. Mendenhall and Perkins [28] combined and extended several of the preceding methods to develop prediction methods for circular and noncircular bodies with symmetric and asymmetric vortex shedding in subsonic flow.

Recently, there has been some effort to go beyond the crossflow analogy to a full three-dimensional calculation of vortex shedding from bodies at high angles of attack. An approach using a three-dimensional vortex-lattice method for the calculation of separated vortex flows from slender bodies was developed by Almosnino [29]. This approach requires a priori knowledge of the separation

lines on the body, and it uses an iterative calculation procedure.

2.2.2 Studies on Circular Cones

An inviscid model, originally proposed by Bryson [23] to describe the positions and strengths of laterally-symmetric vortices above bodies of revolution at high angle of attack, was extended by Dyer, Fiddes, and Smith [30] to describe vortex flows without lateral symmetry around circular cones. They represented each vortex by a single line-vortex and applied conditions of crossflow stagnation at the postulated separation lines. They showed that asymmetric solutions for the separated vortex flow over a conical slender body could be predicted from the standard line-vortex model, even for symmetric boundary conditions. They found that at low angle of attack the flows were symmetric, but that at a critical angle of attack the solutions exhibited a bifurcation to a non-symmetry.

The original work was followed by more extensive works by Fiddes and Smith [31] and Fiddes [12,32], using a more representative vortex-sheet model, which confirmed the results of the simpler theory. In this improved model, the vortex core is represented by a line-vortex, and the free shear layer from the separation line is replaced by a vortex-sheet of finite extent, with its edge connected to the line vortex by a feeding sheet. This model gave more accurate predictions of vortex positions and strengths, but essentially similar results for the appearance of asymmetries in the flow.

In a recent paper Fiddes and Williams [33] demonstrated that the basic results apply, in modified form, to a wide variety of slender body shapes. Pidd

and Smith [34] presented a detailed study of the existence of symmetric and asymmetric solutions for the vortex flow on circular cones. These solutions illustrate the generation of asymmetric solutions by bifurcation from the symmetric solution as the incidence parameter, $\frac{\alpha}{\delta_N}$, increases above a bifurcation value. They also examined the stability of the solutions to small spatial disturbances and found that the asymmetric solutions are stable, but the symmetric solutions are only stable at values of the incidence parameter below that at which asymmetric solutions occurs. They also demonstrated that the appearance of stable asymmetric solutions coincides with the instability of the symmetric solutions, so that bifurcation occurs "with exchange of stabilities".

2.3 Experimental Studies

The great majority of experimental studies on vortex flows on slender bodies has concentrated on tangent-ogive cylinders. These shapes are characteristic of those in practical use. There has been comparatively little experimental work on purely conical bodies [35].

Rainbird, Crabbe, and Jurewicz [36] have reported besides own work, an early work of Laitone [37] and Fink [38] on cones at low speed. They have also compared theoretical results of Laitone with experimental results of Grimson [39]. Grimson obtained pressure distributions and surface flow results on 3-inch base diameter cones, at Reynolds numbers of 2.2×10^5 and 1.8×10^5 , formed with base diameter for the 12.5 deg and 7.5 deg cones. He noted in his experiments at high angles of attack (between 22.5 deg and 30 deg) that apparently steady, but asymmetric, flows developed. Rainbird and his co-

workers carried out flow-visualization studies on two cones of semi-apex angles 12.5 deg and 7.5 deg at incidences up to about 40 deg in a water tunnel. All these tests were performed at a Reynolds number of about 7×10^3 based on base diameter for the 7.5 deg cone. He measured the angular positions of all separation and attachment lines, and the directions of the "surface streamlines" between such lines. He compared his results with those of Grimson and found them in good agreement. He did not observe asymmetric vortex flow at high angles of attack up to 44 deg and 41 deg for the 12.5 deg and 7.5 deg cones. respectively.

Rainbird [40] also determined pressure distribution and vortex core position for symmetric flow over cones. Mundell [41] as reported by Fiddes and Williams [33] determined the location of separation lines over cones. He used a cone-cylinder model where only the front part of the conical portion of the body was "live" and mounted on a force balance. He found large values of side force and recorded the separation line positions (by using surface-oil visualization) corresponding to these conditions.

Peake, Owen, and Johnson [42] performed experiments with a 5 deg semiangle cone at a Reynolds number of 2.4×10^6 based on the base diameter of the cone. On the cone surface, static and dynamic circumferential pressures were measured and oil-dot flow visualization was performed. They investigated details of the leeward separated flow using laser-light and vapor-screen flow visualization and dual-beam velocimetry. They also demonstrated the effectiveness of surface blowing in suppressing the vortex asymmetry.

Fiddes [12] conducted an experiment in a low-speed wind tunnel to verify the predictions of the vortex-sheet model discussed above. The model used in the experiments was a cone-cylinder combination comprising a nose cone of 10 deg semi-apex angle faired to a cylindrical afterbody. The experimental conditions corresponded to a Reynolds number of 1.1×10^6 based on the base diameter. The model was pitched to 35 deg incidence at zero roll, and the pressures recorded. The model was then rolled, typically in 10 deg intervals, and the pressures were recorded again. The process was repeated until the entire roll range had been covered. Fiddes used the data to show that the high side-force state was associated with a characteristic circumferential pressure distribution that was independent of roll angle, apart from a change of hand. He also ruled out the possibility of association of maximum side-force condition with a large asymmetry on the separation position. He also confirmed that the asymmetric solutions of the vortex-sheet model correspond to the high side-force condition.

Stahl [8] carried out flow-visualization studies in a water tunnel and in a wind tunnel on circular cones of 8 deg semi-apex angles at Reynolds number, formed with base diameter, of 7,800 and 68,100, respectively. The incidence angles were from 15 deg to 50 deg and at 45.5 deg in the water tunnel and wind tunnel, respectively. He investigated the influence of a fin on the lee-side vortex flow and found that the addition of a fin suppresses the asymmetry of the vortex flow present without a fin.

Pidd and Smith [34] used measurements of Fiddes, Lean, and Moir [43] to support the predictions of their theoretical work. The model used in the experiments was a cone-cylinder combination. The semi-apex angle of the cone

was 10 deg. The model was fitted with circumferential pressure tappings in the nose. The pressure measurements were made at angles of attack of 30 deg and 35 deg. They used their data to show that the asymmetric flow over a circular cone can be significantly non-conical with large variations in local side-force coefficient along the length of the cone. At an angle of incidence of 35 deg, an approximately conical flow appears to predominate, but at 30 deg only exceptionally occurs.

Lowson and Ponton [35] tested three cone models having 5 deg, 10 deg, and 20 deg semi-apex angles in a wind tunnel. The models were tested at incidences ranging from 0 deg to 90 deg. The principal flow-visualization medium in their investigation was smoke. They found that asymmetric, but still conical, surface flows can exist on conical bodies, as predicted by theory [34]. They have also reported that the change from symmetric to asymmetric flow occurs at an incidence parameter (the ratio of angle of attack to nose semi-apex angle) of between 2 and 2.5. They also observed the effect of Reynolds number on the onset of flow asymmetry. They, however, did not conduct an extensive study.

CHAPTER 3

EXPERIMENTAL SETUP AND TECHNIQUES

3.1 Testing Equipment

The following equipment was used for experimental investigation of the vortex-flow behind a cone.

3.1.1 Wind Tunnel

The experiments were conducted in the low-speed wind tunnel of the Wind Tunnel Laboratory at the King Fahd University of Petroleum and Minerals (KFUPM). Figure 3.1 shows a schematic and two views of the KFUPM wind tunnel. The low-speed wind tunnel has a closed, horizontal test section of cross-sectional area of 0.8 m x 1.1 m. The test section is 3 m long, and is divided into three equal sections. The side walls of the test-section are made of plexiglass, whereas the floor is made of wood. The top of the test section can be provided with either a plexiglass roof or wooden roof. Maximum wind velocity in the empty test section is $U_\infty \approx$ 35 m/s. The maximum freestream turbulence level of the wind tunnel is 0.1 %. It has a open return circuit.

3.1.2 Pressure Measuring Equipment

Manometers: Two Betz manometers (model 5585 series, manufactured by T.E.M. Engineering Limited, new name Elven Precision Limited) were used for the measurement of surface pressures on the model and other pressures like dynamic and static pressures in the wind tunnel. One manometer has an accuracy in reading of 0.02 mbar and the other of 0.2 mm of H_2O.

Pitot-Static Tube: A pitot-static (Prandtl) tube was used to measure the static and dynamic pressures in the wind tunnel. The tube was placed near the roof of the tunnel, at the entrance of the test section.

3.1.3 Flow Visualization Equipment

Smoke Probe: A NPL (National Physical Laboratory, USA) type "smoke" probe, shown in Fig 3.2, was used to generate smoke. It features a compact, electrically heated, screw-on vaporiser that is fed with a special oil. Vaporization of the oil takes place at the extreme tip with subsequent condensation in the flow. The smoke is emitted directly into the flow upstream of the model.

Supply and Control Unit for Smoke Probe: A supply and control unit (model FVSP204, manufactured by Elven Precision Limited), shown in Fig 3.3, was used for supplying oil to the probe and controlling its flow rate. The voltage for the heating coil can also be regulated by this unit. The smoke probe and supply/control unit form an integrated system.

Laser-Light Source: A helium-neon laser-light source (Spectra Physics, Model 124B) of 15 mW power was used to illuminate the flow. The laser-light beam has a diameter of 1.1 mm. A combination of a cylindrical (f = 5.5 mm) and a spherical (f = 1000 mm) lens was used to produce a light sheet in sections normal to the axis of the model. The arrangement of laser-light source and lenses is shown in Fig. 3.4

Photographic Camera and Film: Photography of the vortex-flow was accomplished with a 35 mm camera (Minolta XD-7). The pictures were taken with the combination of a 50 mm lens and a 2X tele-convertor, at an aperture opening of f 1.4 and shutter speeds of 1/125 to 1/8 secs (depending upon the light conditions). The flow patterns were recorded on Kodak T-Max P 3200 ASA, black and white, film. The films were push-developed to 5,000 ASA.

3.2 Cone Models and Mounting

Three slender circular cone models were used for the investigation. The cones had semi-apex angles of δ_N = 8 deg.

3.2.1 Pressure Model

The cone model, used for measuring the pressures on the surface is shown in Fig. 3.5(a). The length of the cone was L = 500 mm and the base diameter was D = 140.5 mm. The model had four circumferential rings of pressure taps, at sections A, B, C, and D along the axis of the cone, with distances from the apex of X/L = 0.2, 0.4, 0.6, and 0.8, respectively. Each ring consisted of about

18 or 22 pressure taps (ϕ1 mm) with nonuniform angular spacing, as shown in the Fig.3.5(b). On the leeward side of the cone, the pressure taps were closely spaced to enhance measurement resolution in the regions beneath the vortices. The model was of aluminium and was hollow inside, so that the plastic tubes (1.5 mm inner diameter) could be connected to the pressure taps. The plastic tubes were then connected to the manometer, outside the tunnel. The model had a machined surface and no paint coating on it.

The effect of a fin on the asymmetry of vortices was studied by attaching a detachable fin, shown in Fig 3.5(c), of height $H/R_{sectional}=1$ at the leeward generator of the cone. The fin had a length equal to the length of the model. It had pressure taps at four sections, aligned with the sections on the basic cone. with 7 pressure taps on each side along the height.

The model was supported on a hollow, flanged sting, which was screwed onto the cone base and through which the plastic tubes came out. The model sting was mounted on a downstream vertical support, fixed on the test-section floor. The vertical support had adjustable height, so that the model was always approximately in the middle of the test section. Figure 3.5(d) and (e) show the basic cone, and basic cone with fin, installed in the wind tunnel.

All pressure tubes, downstream of the model, were tied to the sting, see the Fig. 3.5(d and e). The tube bundle formed was approximately 50 mm in diameter, and produced little disturbance in the flow.

3.2.2 Flow-Visualization Models

These cones were used to study the vortex flow and carry out surface-flow visualizations. They were manufactured of steel and painted matt black to provide a contrasting background for the transparent coating of china-clay, and to minimize reflections of the laser-light plane. One of them, shown in Fig 3.6(a), had a length of L = 100 mm and a base diameter of D = 28.1 mm. With this cone, Reynolds numbers from 5,000 to 40,000, based on the base diameter, were investigated. The other cone model, shown in Fig 3.6(b) had a length of L = 500 mm and a base diameter of D = 140.5 mm, it was used to cover the Reynolds numbers from 25,000 to 202,000. Both of these models had flanged stings, screwed to the base of the model. The model sting was mounted to the downstream vertical support in a manner similar to the pressure model. Figures 3.6(c) and (d) show the models and support system, installed in the wind tunnel.

3.3 Experimental Techniques and Testing Conditions

Pressure measurements and vortex-flow visualizations carried out in this investigation, are briefly described below :

3.3.1 Pressure Measurements.

Circumferential pressure distributions were measured at four sections of the cone at various angles of attack to get more insight into the flow phenomena and information about forces acting on the body.

The pressure measurements were performed at a free-stream velocity of U_∞ = 15.2 m/s, corresponding to a Reynolds number of 142,000, based on the base diameter. Pressure tubes were connected to the manometer in turn, and the pressures were noted. The angle of attack was varied from 15 deg to 35 deg.

The effect of inserting a fin between the lee-side vortices was studied by measuring the surface pressures on the cone and the fin at angles of attack of $\alpha = 25$ deg and 35 deg at $Re_D = 142{,}000$

3.3.2 Vortex-Flow Visualization

The vortex-flow visualization study was carried out for two purposes:

1) To confirm and supplement the inferences from the pressure distribution measurements. The flow visualization for this purpose was done at a wind speed of U_∞ = 15.2 m/s. The Reynolds number and angles of attack were the same as those for the pressure measurements.
2) To find out the angle of attack of onset of vortex-flow asymmetry, α_{onset}, as a function of Reynolds number. For this purpose, the big model (L = 500 mm) was placed in the tunnel to observe the vortex flow at various wind speeds (or Reynolds numbers). The wind speed was varied from 3 m/s to 22 m/s in order to cover the Reynolds number range from Re_D = 25,000 to 202,000. Angles of attack were from $\alpha = 22$ deg to 33 deg. The vortex-flow patterns were visualized in the whole range of Reynolds numbers and α_{onset} was subsequently determined

The small model (L = 100 mm) was then placed in the wind tunnel and

the procedure used for the big cone was repeated to find α_{onset} at various Reynolds numbers in the range of Re_D = 5,000 to 40,000.

The vortex-flow visualization was performed by introducing smoke in the flow from the smoke probe upstream of the model. The vortex-flow patterns were made visible in laser-light sheets arranged perpendicular to the cone length-axis. A schematic of the vortex-flow visualization set-up used in the experiment is shown in Fig. 3.7. The observations were carried out in two light planes, one at the base and the other one base-diameter upstream of the base. All the observations were made at one fixed roll orientation, at nominally zero yaw. The flow patterns were recorded on ASA 3200, black and white, photographic film.

CHAPTER 4

RESULTS AND DISCUSSION

PART I

4.1 Pressure Measurements

The circumferential pressure distribution on the large circular cone (L = 500 mm) without fin was determined to get insight into the separated flow on the lee-side. The surface pressures were subsequently integrated to give side and normal forces acting on the cone.

Pressure measurements were carried out at free-stream velocity U_∞ = 15.2 m/s, and corresponding Reynolds number (based on cone base-diameter, D), Re_D = 142;000. The angle of attack was varied from $\alpha = 15$ deg to 35 deg, at $\beta \leq 0.2$ deg, and one fixed roll orientation. The value of the Reynolds number gives us reason to expect that a laminar boundary layer is separating near the shoulder of the cone [44]. This is discussed in some detail in section 4.2.

The conventions employed for angles, forces, and sides of cone are shown in Fig. 4.1. The circumferential surface pressure distributions on the circular cone at the four axial sections are presented in Figs. 4.2 to 4.25 at several angles of attack. The regions of suction on the lee-side indicate the presence of the vortices. The minimum surface pressure occurs beneath the vortices due to the

high velocity induced by them, close to the cone surface. At angle of attack of 15 deg, shown in Figs. 4.2 to 4.5, the pressure distribution is nominally symmetric. The small differences that appear between the port and starboard side pressures are either within the resolution of the measurements, or can be explained by small errors in the positions of pressure holes around the circumference, and/or setting of the cone zero roll angle. For larger angles of attack, $\alpha = 17$ deg to 35 deg, asymmetric vortex development is indicated by the asymmetric pressure distributions, shown in Figs. 4.6 to 4.25. At $\alpha = 17$ deg, the pressure distribution is only slightly asymmetric, see Figs. 4.6 to 4.9. The occurrence of asymmetric vortex-flow at $\alpha = 17$ deg, was verified by vortex-flow visualization on the same model in repeated tests around $\alpha = 17$ deg. At the higher angles of attack, with asymmetric pressure distribution, the flow visualizations also confirmed that the higher suction exists beneath the vortex which is closer to the surface. In this test, the vortex on the starboard side was always closer to the surface. This bias of the vortex flow might be attributed to an asymmetry which might have been developed on the model surface during manufacturing, possibly near the tip. The leeward suction peak beneath the primary vortex on the starboard side increased from $|C_p| \approx 0.15$ to 1 and on the port side from 0.15 to 0.4 with increase in angles of attack from $\alpha = 15$ deg to 35 deg. The suction beneath the primary vortex on the port side at large α is not very prominent, as the vortex is too remote from the surface.

Figure 4.26 shows a typical circumferential pressure distribution on the circular cone in cartesian coordinates with conjectured features marked on it. It should be pointed out, that due to the wide spacing of the pressure holes (

$\Delta\varphi = 15$ deg), the interpretations are of somewhat speculative nature. Figure 4.27 shows in a schematic sketch, a corresponding vortex system on the starboard side of the cone. For all angles of attack, flow from the free-stream attaches to the cone at the windward generator, A_1, $\varphi_{A_1} \approx 180$ deg, and gives rise to a positive pressure. This positive pressure on the windward side increases with increase in incidence. These overpressures around the windward generator generally decrease with axial distance from the tip in downstream direction. The decrease in pressure at section A, B, and C (x/L = 0.2, 0.4, and 0.6, respectively) is small, but large at section D (x/L = 0.8). This might be attributed to the influence of base.

From the windward side, the pressure generally decreases to a minimum between the angles $\varphi_{min} \approx 80$ deg - 90 deg and 265 deg - 275 deg, followed by a pressure rise, causing boundary layer flow separation at S_1, see Table 4.1. There is a minor deviation to this behaviour at $\alpha = 15$ deg: at section C, pressure minimum occurs at $\varphi_{min} = 282$ deg on starboard side; and at section D, it occurs at $\varphi_{min} = 73$ deg and 281 deg on port and starboard side, respectively.

The angular location of primary separation, φ_{S_1}, can be conjectured as the point where the pressure distribution flattens out after the adverse circumferential-pressure gradient. Although the determination of the separation point from the pressure distribution is difficult, especially, because of the wide spacing of the pressure taps, it can fairly well be estimated in most of the cases. Table 4.1 gives the estimated points of primary separation; it is obvious from the results, that the points of primary separation, S_1, on starboard and port

Table 4.1 Approximate positions of minimum pressure on leeward side; secondary separation; primary separation; and minimum pressure before separation on cone without fin

	Section	Port side				Starboard side			
α[°]		φ_{v_1}	φ_{s_2}	φ_{s_1}	φ_{min}	φ_{v_1}	φ_{s_2}	φ_{s_1}	φ_{min}
15	A	37	*	49+	79	330	316	287	273
	B	20	38	56	86	334	325	299+	270
	C	18	27	56	86	*	*	296	282
	D	*	*	58	73	*	*	296	281
17	A	37	*	49+	79	330	316	287	273
	B	20	38	71	86	334	325	299	270
	C	18	37+	71	86	334	315	296	267
	D	29	39	73	87	337	327	296	266
20	A	37	*	49+	79	330	*	287+	273
	B	20	38	71	86	334	325	299	270
	C	18	37+	71	86	334	315	296	267
	D	29	39	73	87	337	*	296+	266
25	A	37	49	64	79	330	316	287	273
	B	20	28	71	86	334	325	299	270
	C	*	*	71	86	334	315	296	267
	D	29	39	73	87	337	327	296	266
30	A	37	49	64	79	345	316	287	273
	B	*	*	71+	86	344	325	285	270
	C	*	*	71+	86	351	324	282	267
	D	29	39+	73+	87	337	327	281	266
35	A	25	49	64	79	330	316	287	273
	B	20	*	*	86	344	325	285	270
	C	18	*	*	86	343	324	282	267
	D	29	39	*	87	348	*	*	266

+-Not well defined
*-Not possible to measure

side are not symmetrically located, even for nominally symmetrical vortex flow (at $\alpha = 15$ deg). The difference between the angular locations of the points of separation, at $\alpha = 15$ deg, is $\Delta\varphi_{S_1} \approx 6$ deg; and, at higher angles of attack, is $\Delta\varphi_{S_1} \approx 9$ deg. At $\alpha = 17$ deg, the difference between the locations of the separation points is large, although the pressure distribution is only slightly asymmetric. The same difference in separation position is present at $\alpha = 20$ deg and 25 deg, where the pressure distribution is clearly asymmetric. The separation position on the starboard side, with the vortex close to the surface, is further leeward than on the port side at $\alpha = 17$ deg, 20 deg, and 25 deg. Presumably this is caused by rotation of this vortex towards the leeward generator. The rotation towards lee-side generator, of the vortex closer to the surface, was also observed during the vortex-flow visualization on a similar cone, using smoke and laser light. At $\alpha = 15$ deg, the separation position on the port side is further leeward than that on the starboard side. At $\alpha = 30$ deg and 35 deg, the separation position on the starboard side has shifted towards the windward side.

The boundary layer flows merge at S_1 from windward side and leeward side and separate from the cone surface forming a vortex sheet. This vortex sheet then rolls up and forms the primary vortex V_1, on the lee-side.

After the pronounced low pressure region on the leeward side, a recovery of pressure occurs around the leeward generator and a local high pressure region, A_2, is observed. This high pressure region indicates the position of attachment of downward flow from the saddle point formed by the flow from the starboard

and port side over the vortices. At $\alpha = 15$ deg, 17 deg, and 20 deg the point A_2 is on the starboard side, near the vortex close to the surface; at $\alpha = 25$ deg it is on the leeward generator; and at $\alpha = 30$ deg and 35 deg it shifts towards the port side, away from the vortex close to the surface.

The leeward surface flow downward from A_2 ($\varphi \approx 0$ deg) separates at S_2, slightly windward of the suction peak under the primary vortex V_1 , after encountering an adverse pressure gradient. The values of φ_{S_2} for various angles of attack are given in Table 4.1. The vortex sheet formed rolls up into a relatively weak, secondary vortex, V_2, of opposite sense to the primary vortex. This vortex sheet is also fed from the opposite side of S_2 by the new boundary layer developing from A_3, the tertiary attachment line formed by the secondary vortex, V_2. The boundary layer developing downward from A_3 feeds the separating boundary layer at S_1. The positions of A_3 and V_2, on Figs. 4.26 and 4.27, are only the most probable positions of them. They are difficult to estimate from the pressure distribution, because differences of the pressures are within the resolution of the measurements.

4.2 State of the Boundary Layer

Circumferential pressure distribution can be used to get some inference about the state of the boundary layer developing around the cone at incidence. One feature which has been noted in all of the pressure distributions (Figs. 4.2 to 4.25) is that there is a small pressure recovery prior to flow separation, on both sides of the body. By qualitatively comparing the measured pressure

distributions with those found over two-dimensional, circular cylinders [2,45] it can be seen that these distributions are consistent with laminar boundary layers over the body up to the separation lines. If the boundary layers were turbulent, there would be large pressure recoveries ahead of the separations lines. Such feature was not found in the current test results, indicating separations of laminar boundary layers.

A laminar boundary layer flow on two-dimensional cylinder is characterized by early separation at $\varphi' \approx 80$ deg from the windward generator ($\varphi' = 0$ deg). In our tests, for all incidences, the conjectured separation occurred between the angles of $\varphi'_{s_1} \approx 101$ deg and 124 deg, which suggests the presence of turbulent flow before separation of the boundary layer. In view of these contradictory facts, a literature search was done from which, it was found that laminar boundary layer occurs on cones and ogive noses at the Reynolds number ($Re_D = 142{,}000$) of the present study [12,46]. Furthermore, it was found from surface-flow visualization tests of Rainbird et al [37], on a circular cone ($\delta_N = 7.5$ deg) in a water tunnel ($Re_D = 7{,}000$), that a laminar boundary layer on a cone can separate as far back as $\varphi'_{s_1} \approx 125$ deg from the windward generator.

4.3 Side and Normal Forces

The circumferential surface-pressure distribution obtained on our circular cone, was integrated to find sectional side- and normal-force at each measuring section.

4.3.1 Side Force

Figure 4.28 shows the variation of sectional side-force coefficient, C_y , with angle of attack, α . The nominally symmetric pressure distribution at $\alpha = 15$ deg, shown in Figs. 4.2 to 4.5, produced (negligibly) low side forces. The side force at $\alpha = 17$ deg is slightly higher than that at $\alpha = 15$ deg, due to differences in the pressure distribution on the port side and the starboard side of the cone, at $\alpha = 17$ deg. At $\alpha = 15$ deg, the pressure profiles exhibit minima that are relatively symmetric in both position and magnitude. At higher incidence, the asymmetric pressure distribution produces significant side forces, whereby this pressure distribution is, in turn, generated by asymmetric vortex-patterns on the lee side. The sectional side-forces increase with increase in angle of attack (except for section A at high angles). When the vortices start to show asymmetry in their positions, the pressure on the starboard side, under the vortex closer to the surface, decreases more rapidly than that on the port side. The side force arises as a result of the differences in the pressures on the two sides of the cone, and this comprises the attached flow ahead of separation, as well as the differential suction under the vortices. The direction of this side force is towards the side featuring the vortex closer to the surface.

Variation of sectional side-force with axial distance is shown in Fig. 4.29. The plot does not show a well defined trend of increase or decrease of sectional side-force, C_y , with axial distance. At section A, the values of C_y are somewhat higher than those at the other three sections. The reason for these high values possibly is that, at section A, the pressure tapping at $\varphi = 208$ deg was blocked, increasing area, during integration, on which the suction pressure of next

tapping is assumed acting. This is somewhat misleading, because physical consideration clearly shows that the sectional side-force should be lower. Since the vortex-flow pattern along the axial length of the model remained constant, the direction of the side force also remained constant.

4.3.2 Normal Force

Figure 4.30 presents the variation of sectional normal-force, C_n , with angle of attack, α . The magnitude of the sectional normal-force increases with the increase in angle of attack. This increase in the normal force is due to the decrease in pressure occurring under the lee-side vortices, particularly under the vortex closer to the surface, as well as due to the increase in overpressure on the windward side. As the flow asymmetry increases, the pressure in the lee of the body decreases, causing the sectional normal-force to become larger. Figure 4.31 shows the variation in sectional normal-force with axial distance. Similar to the sectional side-force behaviour, no well defined trend of increase or decrease of sectional normal-force exists. But, they all have a similar behaviour. At section A, for all α , covered in this test, the normal force is less than that at section B or C because of missing pressure tapping at $\varphi = 208$ deg, as discussed in 4.3.1.

Comparison of Figs. 4.28 and 4.30 show a general relation between sectional side- and normal-force. Both the side force and the normal force increase with the increase of angle of attack; however, the increase of the side force is more rapid than that of the normal force. The side force can attain magnitudes similar to those of the normal force. This may be seen from Figs. 4.32 and 4.33

where their ratios C_y / C_n are plotted versus angle of attack and distance along the cone, respectively. The sectional side-force becomes almost as high as the sectional normal-force.

4.4 Effect of a Fin on Vortex Asymmetry

Stahl [8] investigated the influence of a fin on the lee-side vortex flow of a circular cone primarily in a water tunnel by means of flow visualization, at $Re_D = 7{,}800$. He found that the addition of a fin between the vortices suppresses the asymmetry of the vortex flow, present without fin. As the asymmetric flow gives rise to a side force on the body, a quantitative investigation as to the effectiveness of a fin in suppressing vortex flow asymmetry and associated side force was carried out.

After the completion of the tests on the basic cone-model, a longitudinal fin was attached along the lee-side generator of the cone. The length of the fin was equal to the length of the model, and the height above the cone surface at any axial section was equal to the local radius of the cone ($H/R_{sectional} = 1$). The fin was pressure-tapped at four axial sections, with each section housing 7 holes on each side along the height. The sections on the fin were aligned with the sections on the basic cone. The cone with the fin may be seen, for example, in Fig. 3.5(c).

4.4.1 Pressure Measurements on the Cone with a Fin

Pressure measurements were made on the cone and fin at $\alpha = 25$ deg and 35 deg, and $Re_D = 142{,}000$. Figures 4.34 to 4.41 present the circumferential pressure distribution at four axial sections on the cone with the fin present. The pressure on the cone, under the fin, at the leeward generator ($\varphi = 0$ deg) was obtained by taking the average value of the pressures at the base of either side of the fin.

At $\alpha = 25$ deg, the pressure distribution on the cone, at all four axial sections, is nominally symmetric. The large asymmetry in the pressure distribution on the basic cone without fin, observed at $\alpha = 25$ deg, has now disappeared. Thus, the fin is found to be highly effective at $\alpha = 25$ deg in suppressing asymmetry of the vortex flow. At $\alpha = 35$ deg, the pressure distribution shows a slight degree of asymmetry; but, this asymmetry is much less than that on the basic cone without fin at the same incidence. Thus, the fin loses some of its effectiveness at this high angle of attack, in eliminating asymmetry of the vortex flow. The decline in performance of the fin might be attributed to an insufficient height of the fin. The effectiveness of the fin might, therefore, be improved by increasing the height of the fin above $H/R_{sectional} = 1$. The appearance of some vortex-flow asymmetry at $\alpha = 35$ deg shows that the fin delayed the formation of asymmetric vortex-flow from $\alpha = 17$ deg to $\alpha \approx 35$ deg.

The trend of the pressure distribution shown in these plots is generally similar to that on the cone without the fin at same α and asymmetric flow. Around the windward generator, $\varphi = 180$ deg, the overpressures are essentially

the same in magnitude, for both cases. From the position of the first pressure minimum, φ_{min} on windward side through to the leeward generator ($\varphi = 0$ deg), the magnitude of pressures on the starboard and port sides of the cone with fin are intermediate of those on the two sides of the basic cone without fin.

The positions of the lee-side vortices, φ_{V_1} ; pressure minimum on the windward side, φ_{min} ; the primary separation, φ_{S_1} ; and the secondary separation, φ_{S_2} are given in Table 4.2. The comparison of Table 4.2 with Table 4.1 shows that the positions of the suction peaks under the leeward vortices, φ_{V_1} and the secondary separation, φ_{S_2} are generally different for the vortex flows on the cone with and without fin, with asymmetric vortex flow. However, the position of the minimum pressure on the windward side, φ_{min} , and primary separation, φ_{S_1} are generally the same in both cases. This indicates that the presence of the fin on the leeward generator is felt by the flow after separation. The effect of the fin on the changes in the position of the minimum pressures and separation points for the cone with and without fin are not well defined.

The pressure distribution on the cone with fin also indicates the separation of a laminar boundary layer. The position of separation point in this case is $\varphi'_{S_1} \approx 108$ from the windward generator.

4.4.2 Normal and Side Forces on the Cone with a Fin

Figures 4.42 and 4.43 show the variation of sectional side-force on the cone with fin. The side force on the cone with fin has now reduced to a low value; at

Table 4.2 Approximate positions of minimum pressure on leeward side; secondary separation; primary separation; and minimum pressure before separation on cone with fin

	Section	Port side				Starboard side			
$\alpha[°]$		φ_{v_1}	φ_{s_2}	φ_{s_1}	φ_{min}	φ_{v_1}	φ_{s_2}	φ_{s_1}	φ_{min}
25	A	25	37	64	79	330	316	300	273
	B	20	48	71	86	334	317	285	270
	C	18	37	71	86	334	315	282	267
	D	19	*	*	58	337	316	281	266
35	A	25	49	64	79	330	316	*	*
	B	28	48	71	86	325	317	285	270
	C	18	45	71	86	334	305	282	267
	D	19	29	*	*	337	316	281	266

+-Not well defined
*-Not possible to measure

$\alpha = 25$ deg, it is approximately two times the value on the cone without fin at $\alpha = 15$ deg, a nominally (naturally) symmetric vortex flow case, at all stations except near the base, where it is high. At $\alpha = 35$ deg, it is approximately three times the value of the naturally symmetric case, and again larger near the base, see Fig. 4.44. However, since the values of the side force on the basic cone at $\alpha = 15$ deg (i.e. in the naturally symmetric case) are negligibly small, the absolute values of the side force at $\alpha = 25$ deg and 35 deg on the cone with fin can also be considered as negligibly small.

When comparing the side forces on the cone without fin with those on the cone with fin at the same incidence, $\alpha = 25$ deg or 35 deg, Fig. 4.45, one realizes that the fin performs well, reducing the side force by an order of magnitude. Thus, the fin is effective in alleviating the vortex-induced side force, more at $\alpha = 35$ deg, than at $\alpha = 25$ deg.

Sectional normal-force acting on the cone with fin are presented in Figs. 4.46 and 4.47. The magnitude of the normal force on the cone with fin is essentially the same as that on the basic cone without fin. This indicates that the underpressures acting on the lee side of the cone with fin (with symmetric vortex pattern) are average of the underpressures acting on the starboard and the port side of the cone without fin (with asymmetric flow).

The effectiveness of inserting a longitudinal fin on the lee side of a cone is further illustrated by Figs. 4.48 and 4.49. The fin reduces the ratio of the side force and normal force on the cone with fin to the ratio of the side force and normal force on the basic cone without fin at $\alpha = 15$ deg, i.e. to the ratio of a naturally symmetric vortex-flow case.

4.5 Pressure and Force Distributions on the Fin

In this test, surface pressures were also measured on the fin, attached to the lee side of the circular cone. There were 7 pressure tappings on each side of the fin at four cross sections aligned with the sections on the basic cone model. Figures 4.50 to 4.57 show the pressure distribution on both the sides of the fin at $\alpha = 25$ deg and 35 deg at all the four sections. At section A, the pressure data close to the cone surface, on the starboard side of the fin, was not available due to some blocked pressure holes, there. The pressure distribution at all four sections shows a general trend of high suction on the fin near the cone surface. The pressure, progressively, increases towards the top of the fin. This indicates the presence of a vortex structure within the high-suction region, only. The increase of pressure from bottom to top is gradual and less prominent at $\alpha = 25$ deg, but steep and obvious at $\alpha = 35$ deg. Figures 4.54 to 4.57 show that, at $\alpha = 35$ deg, the effect of the vortices extend up to $H/R_{sectional} \approx 0.55$. This was further confirmed by smoke-flow visualizations on the cone , carried out under the same conditions. In general, flow observations revealed that the cores of the vortices were tucked well into the corners formed by the fin and the cone surface. This may be seen in Fig. 4.58, which shows the schematic of vortex flow on the cone with fin, and the downward flow of air above the fin. It can also be seen from the plots that at $\alpha = 35$ deg, suction is much higher than at $\alpha = 25$ deg. This suggests that the vortices are distinctly stronger or/and located closer to the fin at $\alpha = 35$ deg. The pressures near the top of the fin are nominally the same for $\alpha = 25$ deg and 35 deg. Comparing the pressure distribution on both sides of the fin one observes that the pressure distribution is largely symmetric at $\alpha = 25$

deg, and slightly asymmetric at $\alpha = 35$ deg. The suction, at $\alpha = 35$ deg, on the starboard side of the fin is generally higher than that on the port side. It should be noted that, on the cone without the fin, the starboard side always had higher suction on the cone surface, due to the vortex lying closer to the surface.

The pressure distribution on the fin was integrated to obtain the pressure force normal to the fin, i.e. side force on the fin and the centre of pressure on each section of the fin, see Figs. 4.59 and 4.60. Figure 4.59 shows that the magnitude of the side force is small, and varies somewhat randomly, along the axial length of the cone. The force acts on the fin towards the starboard side. The side force is higher at $\alpha = 35$ deg than at $\alpha = 25$ deg. Figure 4.60 shows that the points of application of forces are not constant, they vary rather randomly. At section A, the position of the centre of pressure is misleading because of the missing pressure data near the bottom of the fin.

PART II

4.6 Dependance on Reynolds Number of Onset of Vortex Asymmetry

It has been found in earlier investigations of vortex-flow asymmetry behind circular cones [8] that the onset of asymmetry occurred at two widely different angles of attack in two different sets of experiments in two different tunnels. It was assumed, that the two largely different values of Reynolds numbers, which prevailed in the two sets (Re_D = 7,800 and 142,000) were influential in the occurrence of the two widely different values of onset angles ($\alpha_{onset} \approx 35$ deg and 16 deg respectively) ; although other factors may play a role (as different tip geometries, free-stream turbulence and noise levels, model surface roughness). Therefore, an experimental investigation was carried out on two geometrically similar circular cones of different size to determine the onset angle of attack of vortex-flow asymmetry as a function of Reynolds number, Re_D , in the range of Re_D = 5,000 to 202,000 (formed with base diameter).

The two cone models had lengths L = 100 mm and 500 mm, respectively, to cover the range of Reynolds numbers. The changeover from symmetric to asymmetric vortex configuration was observed visually in laser-light planes normal to the cone axis, with smoke introduced upstream of the model. The observations were carried out in two light planes, one at the base and the other one base-diameter upstream of the base (but not simultaneously). All the observations were made at one fixed roll orientation, at nominally zero yaw.

4.6.1 Onset Angle of Attack

The effect of Reynolds number on the onset angle of attack, α_{onset}, is shown in Figs. 4.61 and 4.62. With the small model the range of Reynolds numbers covered is from Re_D = 5,000 to 40,000 and with the big model Re_D = 25,000 to 202,000. The results show an obvious trend of increase in α_{onset} with decrease in Reynolds number. The onset of asymmetry occurs between $\alpha = 23$ deg and 28 deg for the big cone and between $\alpha = 32$ deg and 37 deg for the small cone. The plots of α_{onset} versus Re_D show that the variation occurs in various steps, this might be accentuated by the rather large increments in angle of $\Delta\alpha = 1$ deg. Minor changes in vortex flow occur for small changes in α. These variations in vortex flow are difficult to perceive, therefore, $\Delta\alpha$ was kept relatively large. The trend in variation of α_{onset} with Re_D is practically the same for the vortex flow observed at the base and one base-diameter upstream of the base. Minor discrepancies between the α_{onset} at the base and one base-diameter upstream might be attributed to the influence of the base, as the wake may interfere with the vortices near the base. Our results on the small cone show that, at Re_D = 8,000, the onset of vortex-flow asymmetry occurs at $\alpha_{onset} = 37$ deg. This result is in reasonable agreement with the result of the tests conducted by Stahl [8] in a water tunnel on a similar cone ($\delta_N = 8$ deg, L = 200 mm), where $\alpha_{onset} \approx 35$ deg was found.

The behaviour of the vortices below Re_D = 5,000 was not studied, due to poor quality of the smoke plume at low flow velocities.

4.6.2 Onset Angle of Attack in the Region of Overlapping Reynolds Numbers

The flow-visualization studies, carried out on the big cone and the small cone, have a range of Reynolds numbers, Re_D = 25,000 to 40,000, which is common between them. The vortex flows observed on the two cones, at same values of Reynolds number, exhibit a distinct difference in α_{onset} : on the small cone α_{onset}=32 deg, while on the big cone α_{onset}=28 deg. This means, that there is a difference in the flow field, at a given α, in the tests with the two geometrically similar models of different lengths, at same Reynolds numbers. This appears to conflict with the principle of flow similarity. The discrepancy might be attributed to small differences in the geometry of the tips of the models. It has been reported that nose bluntness can greatly reduce flow-field asymmetry [10,47]. It was found, using a microscope, that the tip of our big cone was distinctly less blunt, more like a streamlined nose (e.g. of an aircraft) while the small-cone tip was quite blunt with a thickness estimated to be about 0.4 mm. Figure 4.63 clearly illustrates this difference between the tips of the small model and the big model. This may have delayed the onset of vortex asymmetry. Small differences in surface finish and geometrics of the two models may also contribute to the inconsistency in α_{onset}.

4.6.3 Vortex-Flow Pattern

Various changes in the vortex-flow patterns behind the cones have been observed when varying Reynolds number and angle of attack; they can be seen in Figs. 4.64 to 4.67. These changes are generally only small; therefore, the

decision to assign certain attributes to a particular vortex configuration might be subjective. Furthermore, on the small cone, the sizes of the vortices formed are obviously also small. The visual observation of these small vortices, embedded in the smoke plume, is generally difficult, which adds to the subjective nature of these observations. Considering the way a change of incidence has to be carried out, it is not unlikely that between each change of α , there might have been introduced a minute deviation in yaw angle, β . When changing α , this has been checked and found to be typically $\Delta\beta \leq 0.2$ deg for a change $\Delta\alpha \approx 1$ deg (if it occurred at all).

The abbreviations used in the legends of Figs. 4.64 to 4.67 are given in the following table and are explained in the subsequent text.

SSV	Stationary symmetric vortices
WLHS	Weak left-hand-side configuration
WRHS	Weak right-hand-side configuration
SLHS	Strong left-hand-side configuration
SRHS	Strong right-hand-side configuration
USV	Unsteady symmetric vortices

The symmetric vortices found at lower values of angles of attack and Reynolds numbers are basically stationary (SSV): fluctuations in their heights above the surface and their sizes are small. At low Reynolds numbers (within the respective Re_D range covered for each cone) , asymmetric vortices on the big cone appear at $\alpha_{onset} \approx 28$ deg and on the small cone at $\alpha_{onset} \approx 37$ deg. The asymmetry, when it is initially generated, is weak: the differences in sizes of the

vortices and their heights above the cone surface are small. The asymmetric vortex pair is either in a left-hand configuration, WLHS (vortex on left, looking from the apex downstream, is higher and bigger than vortex on right) or right-hand configuration, WRHS.

As the cone is pitched from α_{onset} to higher incidence, a sequence of asymmetric vortex-flow fields develops. The differences in the sizes of the vortices and their heights above the surface increase (SLHS or SRHS). In many cases, especially true for the big cone, when the vortex asymmetry has reached a certain maximum degree, the asymmetry of the vortices diminishes. During their decline, the vortices momentarily take on an unsteady, on the average symmetric pattern, USV. This type of symmetry of the vortices is entirely different from the symmetric flow which occurs below α_{onset}. The latter is steady. while the former is highly unsteady. The sizes, positions, and configuration of the vortices fluctuate rapidly, but, on the average, the vortices are symmetric. When the incidence is further increased, the vortex pair again becomes asymmetric. The configuration of the vortices may or may not be the same as before. The asymmetry of the vortices, either with same or reversed configuration, then increases gradually and becomes quite distinct at high α. Whereas, the reversal of the vortex-flow configuration was frequent on the big cone (i.e. in the high Re_D -range), it was only occasional on the small cone (i.e. low Re_D -range). The phenomenon of formation of unsteady symmetric vortex-pairs, as described above, was observed on the small cone only at large Re_D and there at few incidences. Figures 4.68 and 4.69 show the typical vortex-flow patterns on the big cone and the small cone, respectively. A rather similar trend in variation of

vortex patterns exists for the two cones at moderate and large Reynolds numbers, except that now the onset of asymmetry occurs at lower incidence. Figures 4.70 and 4.71 show the development of the vortex-flow patterns with increase in angles of attack, on the big cone at $Re_D = 172{,}000$ and on the small cone at $Re_D = 11{,}000$.

The variation in vortex-flow patterns, at a certain fixed α, with changes in Reynolds number has a very similar trend. The vortices are weakly asymmetric at the onset. The degree of their asymmetry increases with increase in Re_D, and reaches a large maximum value. This large asymmetry then gradually decreases, with further increase in Reynolds numbers, to a small degree of asymmetry, before acquiring an unsteady symmetric configuration of the type described above. This symmetric pattern exists for a small range of Reynolds numbers. Subsequently, it becomes weakly asymmetric again, but now, usually, the asymmetry is reversed. This asymmetry of vortices then grows and becomes strong as Reynolds numbers are further increased. Figure 4.72 shows the development of the vortex pattern with increase in Re_D, at $\alpha = 33$ deg.

The trends in the development of the vortex-flow patterns with α and Re_D are practically the same for the vortex flows observed at the base and one base-diameter upstream of the base. There are a few minor discrepancies. The reason for them might be that the observation of the vortex flow in the two sections, for a certain α, were not made simultaneously, but at different runs of the test. The cone surface was wiped with tissue paper between the runs to remove any oil film due to smoke visualization from the surface, which may have formed during the previous run. It was indeed observed that the presence

of an oil film on the surface affects the vortex flow appreciably. It randomly causes, decreases, or suppresses vortex asymmetry. However, the effect of the presence of an oil film on the cone surface was not systematically studied.

4.7 Effect of Surface Conditions on Onset of Vortex Asymmetry

From pressure measurements on our large (L = 500 mm) cone model, with circumferential rings of (ϕ 1 mm) pressure taps at four stations along the model's axis, as well as from smoke-flow visualization on the same model, we found that α_{onset} was 16 deg at Re_D = 142,000. In contrast to this, we found by smoke-flow visualization on the corresponding model with a solid and black-painted surface, that α_{onset} occurred at 24 deg at the same Reynolds number. This large discrepancy in α_{onset} might be caused by the differences in surface conditions of the model with pressure holes and the model with solid surface. However, we can not exclude differences in the models' tip geometry, which might influence the vortex-flow behaviour.

From surface-flow visualization on the small cone, using the China-clay method [48,49], we found that $\alpha_{onset} \approx 22$ deg at Re_D = 29,000, whereas on the same model, without China-clay coating, using smoke-flow visualization, we found $\alpha_{onset} = 32$ deg. This wide difference in α_{onset} is conjectured to be due to the difference in surface conditions of the model for the two tests.

Furthermore, it was observed, during smoke-flow visualization, that the presence of an oil film on the surface affects the vortex flow appreciably, it randomly causes, decreases, or suppresses vortex asymmetry.

4.8 Reynolds Number Based on Effective Length

The pressure measurement and flow-visualization results, presented in the previous sections, were given for Reynolds numbers based on the base diameter of the cone. This Reynolds number, Re_D is the one generally found in the technical literature, for presenting the results of studies, done on slender bodies such as cones, ogives, and missiles at angles of attack. Though appropriate in certain cases, it does not truly represent an effective Reynolds number for the boundary layer flow on a body. Such an effective Reynolds number is formed with some representative of the wetted length on which the boundary layer develops. In a three-dimensional flow over a circular cone at a certain incidence, the determination of such a characteristic length is important for evaluating the state of the boundary layer and understanding the asymmetry of vortices.

Surface-flow visualization photographs from various investigators [8, 11, 36, 50, 51, 52, 53] show that at high angles-of-attack, the streamlines that feed separation are turned against the freestream through an angle ($\psi = \sigma - \alpha - \delta_N$), see Fig. 4.73. The feeding streamlines are largely contained in the intersection between the slender body and a plane inclined at an angle σ to the windward generator on the body.

On our circular cone, the development of the boundary layer is determined by the flow following the more or less elliptical path around the cone from the windward attachment line to the separation line. In the present study, surface-flow visualization, using a mixture of oil and clay powder, was tried to obtain surface-flow angles and the separation line on the cone. However, the method

did not work properly. Therefore, an estimate of the direction of the surface streamlines was made using photographs, available in the literature, of surface-flow visualization on various slender bodies. Figures 4.74 and 4.75 show the trend in surface-flow inclination with changes in incidence for various slender bodies: cones and ogives. A linear curve was fitted to some of these data to interpolate or extrapolate the values of surface-flow inclination (see Figs.4.76 and 4.77). Finally an average of the linear curves for $\delta_N = 8$ deg cone/ogive and $\delta_N = 7.5$ deg cone was then obtained, see Fig. 4.78. Figure 4.79 compares this estimated average inclination of streamlines on the cones/ogive with the inclination of the streamlines on a circular cylinder, obtained by using incompressible potential-flow theory [2], given by

$$\sigma = \tan^{-1}(2\tan\alpha) \tag{4.1}$$

The figure shows that the trends are similar on both bodies except that on the slender bodies the inclination, σ, is higher.

The inclination of the streamlines was then used to approximate the effective length or characteristic length, l_{eff}, on the cone, representative of the wetted length of the elliptical path (see Fig. 4.80), using

$$l_{eff} = D_{sec} \times \frac{\cos\delta_N}{\sin\sigma} \tag{4.2}$$

with D_{sec} the local cone diameter. Figure 4.81 shows the variation with angle of attack of the ratio of the Reynolds number based on estimated effective length, $Re_{l,eff}$, to the Reynolds number based on base diameter, Re_D.

The relationship, shown in Fig. 4.81 for the ratio of the Reynolds number based on effective length to the Reynolds number based on base diameter, was

subsequently used to obtain the variation of α_{onset} with $Re_{l,eff}$ and the variation in vortex-flow pattern with changes in angle of attack and $Re_{l,eff}$, see Figs. 4.82 to 4.87. The plots show a shift in the onset of vortex asymmetry towards a lower Reynolds number. The shift is large for high α, and is less for low α.

CHAPTER 5

CONCLUSIONS AND RECOMMENDATIONS

5.1 Conclusions

The asymmetric vortex flow behind a circular cone at high angles of attack in low-speed flow has been studied experimentally. The study was carried out in two parts. In the first part, the effect on asymmetric vortex flow of a longitudinal fin, inserted at the leeward generator of the cone, was quantitatively investigated. In the second part, dependence on Reynolds number of onset of vortex asymmetry behind the cone was investigated.

Surface pressure measurements were made on the cone without fin at a freestream velocity of U_∞ = 15.2 m/s, corresponding to Reynolds number based on the base diameter of Re_D = 142,000. The angle of attack was varied from α = 15 deg to 35 deg. The surface-pressure measurements and subsequent verifications with smoke-flow visualization, showed that the flow was symmetric at α = 15 deg, but was slightly asymmetric at α = 17 deg. The asymmetry increased with increase in angle of attack from α = 17 deg to 35 deg. The sectional side-force and normal-force, obtained by integration of pressure measurements, increased with increase in angle of attack from α = 15 deg to 35 deg. The sectional side-force was negligibly small at α = 15 deg, but became almost as high as the normal force at α = 35 deg.

The effect of the fin was studied at two angles of attack, namely $\alpha = 25$ deg and 35 deg, where the vortices were strongly asymmetric, without the fin. The pressure measurements with fin showed that the fin was effective at $\alpha = 25$ deg and 35 deg in suppressing the vortex-flow asymmetry, present on the cone without fin. The fin reduced sectional side-force by an order of magnitude, and to negligibly small values. The side force on the fin was found to be small.

Vortex-flow visualizations, carried out on the cones, in the Reynolds number range of $Re_D = 5{,}000$ to 202,000, showed that onset angle of attack of vortex asymmetry increased with decrease in Reynolds number. The values of α_{onset} on the small cone, in the Reynolds-number range of $Re_D = 5{,}000$ to 40,000, was between $\alpha_{onset} = 32$ deg and 37 deg. On the big cone, in the Reynolds-number range of $Re_D = 25{,}000$ to 202,000, α_{onset} was found between 23 deg and 28 deg. α_{onset} in the range of Reynolds number, common to the two cones, had two different values. The discrepancy might be attributed to small differences in the geometry of the tips of the models and/or to surface finish and geometries of the two models.

The vortex-flow patterns, observed in this study, showed various configurations. The vortices were symmetric at low α and low Reynolds number, within the range covered for each cone. The asymmetry, when it occurred at a given α and Reynolds number, was weak in the beginning, but developed into strong asymmetry with increase in either incidence α or Reynolds number. The phenomenon of switching of vortex configuration from left-hand side to right-hand side or vice versa was observed: more frequently on the big

cone, and less on the small cone.

It was also observed that the onset angle of attack was largely affected by surface conditions of the model.

5.2 Recommendations

1. The effect of changes in angle of attack, on surface pressures can be investigated at various Reynolds numbers to confirm vortex-flow visualizations.
2. The effect of various heights of the fin, on alleviation of vortex-flow asymmetry can be systematically studied to utilize the forces developed on the fin due to asymmetric vortex flow.
3. The effect of deviating the fin by small angles from the zero roll angle can be studied.
4. The pressure holes on the pressure-measurement model can be used to study the effect of blowing and suction on the vortex-flow asymmetry.
5. The detailed structure of the leeward vortex-flow can be studied by velocity measurements within the vortices.
6. The effect of changes in roll angle of the cone, on vortex flow can be studied by smoke-flow visualizations and combined with the study of dependence on Reynolds number of onset of vortex asymmetry.
7. The influence of tip and other nose shapes, on vortex flow can be investigated in detail.
8. Surface-flow visualization, by means of oil-flow and China-clay methods can be used to obtain surface-flow pattern, which reveal a general picture

of state of boundary layer, location of separation and attachment lines, and location of vortices on the lee-side of the cone.

9. The influence of wind-tunnel turbulence level and structure on vortex-flow patterns could be investigated.

10. Mathematical modelling and subsequent development of prediction method for strength and location of lee-side vortices could be done based on observed flow characteristics.

REFERENCES

[1] Rao, D. M., "Side-Force Alleviation on Slender, Pointed Forebodies at High Angles of Attack," ***J. Aircraft***, Vol. 16, No. 11, 1979, pp. 763-768.

[2] Ericsson, L. E. and Reding, J. P., "Asymmetric Vortex Shedding from Bodies of Revolution," ***Progress in Astronautics and Aeronautics: Tactical Missile Aerodynamics***, edited by M. J. Hemsch and J. N. Nielsen, Vol. 104, AIAA, New York, 1986, pp. 243-296.

[3] Degani, D., "Effect of Geometrical Disturbance on Vortex Asymmetry," ***AIAA Journal***, Vol. 29, No. 4, 1991, pp. 560-566.

[4] Daniels, P., "Ogive-Cylinder Modified for Near-Minimum Side Moment," ***J. Spacecraft and Rockets***, Vol. 17, No. 3, 1980, pp. 161-162.

[5] Yanta, W. J. and Wardlaw, A. B., "Flowfield about and Forces on Slender Bodies at High Angles of Attack," ***AIAA Journal***, Vol. 19, No. 3, 1981, pp. 296-302.

[6] Keener, E. R. and Chapman, G. T., "Similarity in Vortex Asymmetries over Slender Bodies and Wings," ***AIAA Journal***, Vol. 15, No. 9, 1977, pp. 1370-1372.

[7] Keener, E. R. and Chapman, G. T., "Onset of Aerodynamic Side Forces at Zero Sideslip on Symmetric Forebodies at High Angles of Attack," ***AIAA Paper No. 74-770***, Aug. 1974.

[8] Stahl, W. H., "Suppression of Vortex Asymmetry Behind Circular Cones," *AIAA Journal*, Vol. 28, No. 6, 1990, pp. 1138-1140.

[9] Williams, D. R. and Papazian, H., "Forebody Vortex Control with the Unsteady Bleed Technique," *AIAA Journal*, Vol. 29, No. 5, 1991, pp. 853-855.

[10] Ericsson, L. E. and Reding, J. P., "Alleviation of Vortex-Induced Asymmetric Loads," *J. Spacecraft and Rockets*, Vol. 17, No. 6, 1980, pp. 546-553.

[11] Skow, A. and Peake, D. J. "Control of the Forebody Vortex Orientation by Asymmetric Air Injection," *High Angle-of-Attack Aerodynamics*, AGARD Lecture Series No. 121, Paper 10, Dec. 1982.

[12] Fiddes, S. P., "Separated Flow About Cones at Incidence-- Theory and Experiment," *Studies of Vortex Dominated Flows*, edited by M. Y. Hussaini and M. D. Salas, Springer, New York, 1985, pp.285-310.

[13] Stallings, R. L., "Low Aspect Ratio Wings at High Angles of Attack," *Progress in Astronautics and Aeronautics:Tactical Missile Aerodynamics*, edited by M. J. Hemsch and J. N. Nielsen, Vol. 104, AIAA, New York, 1986, pp. 89-128.

[14] Lugt, H. J., *Vortex Flow in Nature and Technology*, John Wiley & Sons, New York, 1983.

[15] Föppl, L., "Wirbelbewegung hinter einem Kreiszylinder," Sitz.ber., Konigl. Bay. Akademie d. Wissenschaften, Math.-Phys. Klasse, Jg. 1913, Munchen, Jan.1913.

[16] Rosenhead, L., "Formation of Vortices from a Surface of Discontinuity," ***Proceedings of the Royal Society of Aeronautics***, Vol. 143, 1931, pp. 170-192.

[17] Gerrard, J. H., "Numerical Computation of the Magnitude and Frequency of the Lift on a Circular Cylinder," ***Philosophical Transactions of the Royal Society, London***, Ser. A, Vol. 261, No 1118, Jan 1967, pp. 134-162.

[18] Sarpkaya, T., "An Analytical Study of Separated Flow About Circular Cylinders," ***J. Basic Engineering***, Vol. 90, Dec. 1968, pp. 511-520.

[19] Deffenbaugh, F. D. and Marshall, F. J., "Time Development of the Flow about an Impulsively Started Cylinder," ***AIAA Journal***, Vol. 14, No. 7, 1976, pp. 908-913.

[20] Sarpkaya, T., "An Inviscid Model of Two Dimensional Vortex Shedddding for Transient and Asymptotically Steady Separated Flow Over a Cylinder," ***AIAA Paper No. 79-0281***, Jan 1979.

[21] Allen, H. J. and Perkins, E. W., "A Study of Effects of Viscosity on Flow Over Slender Inclined Bodies of Revolution," ***NACA Report 1048***, 1951.

[22] Thomson, K. D. and Morrison, D. F., "The Spacing, Position, and Strength of Vortices in the Wake of Slender, Cylindrical Bodies at large Incidence," ***J. Fluid Mechanics***, Vol. 50, 1971, pp. 751-783.

[23] Bryson, A. E., "Symmetric Vortex Separation on Circular Cylinders and Cones," ***J. Applied Mechanics***, Vol. 26, Dec. 1959, pp. 643-648.

[24] Wardlaw, A. B., "Prediction of Normal Force, Pitching Moment, and Yawing Force on Bodies of Revolution at Angles of Attack upto 50 Degrees Using a Concentrated Vortex Flow-Field Model," ***NOL TR 73-209***, Oct. 1973.

[25] Angelucci, S. B., "A Multivortex Method for Axisymmetric Bodies at Angle of Attack," ***J. Aircraft***, Vol. 8, No. 12, 1971, pp. 959-966.

[26] Marshall, F. J. and Deffenbaugh, F. D., "Separated Flow Over Bodies of Revolution Using an Unsteady Discrete-Vorticity Cross Wake. Part I-Theory and Applications," ***NACA CR-2414***, June 1974.

[27] Deffenbaugh, F. D. and Koerner, W. G., "Asymmetric Wake Development and Associated Side Force on Missiles at High Angles of Attack," ***J. Spacecraft and Rockets***, Vol. 14, No. 3, 1977, pp. 155-162.

[28] Mendenhall, M.R. and Perkins, S. C., "Vortex Cloud Model for Body Vortex Shedding and Tracking," ***Progress in Astronautics and Aeronautics: Tactical Missile Aerodynamics***, edited by M. J. Hemsch and J. N. Nielsen, Vol. 104, AIAA, New York, 1986, pp. 519-571.

[29] Almosnino, D., "High Angle-of-Attack Calculations of the Subsonic Vortex Flow on Slender Bodies," ***AIAA Journal***, Vol. 23, No. 8, 1985, pp. 1150-1156.

[30] Dyer, D. E., Fiddes, S. P., and Smith, J. H. B., "Asymmetric Vortex Formation From Cones at Incidence- A Simple Inviscid Model," ***Aeronautical Quarterly***, Vol. 33, No. 11, 1982, pp. 293-312.

[31] Fiddes, S. P. and Smith, J. H. B., "Asymptotic Separations from Slender Cones at Incidence," ***Boundary Layer Separation***, edited by F. T. Smith and S. N. Brown, Springer,1987.

[32] Fiddes, S. P., "A Theory of the Separated Flow Past a Slender Elliptic Cone at Incidence," ***AGARD Conference Proceedings No. 291***, Paper 30, Oct. 1980.

[33] Fiddes, S. P. and Williams, A. L., "Recent Developments in the Study of Separated Flows Past Slender Bodies at Incidence," Paper 31 in ***The Prediction and Exploitation of Separated Flow***, Royal Aeronautical Society, London, April 1989.

[34] Pidd, M. and Smith, J. H. B., "Asymmetric Vortex Flow Over Circular Cones," Paper 18, ***AGARD Meeting on Vortex Flow Dynamics***, Oct, 1990.

[35] Lawson, M. V. and Ponton, A. J. C., "Symmetric and Asymmetric Vortex Flows at High Angle of Attack," ***AIAA Paper No. 91-0276***, Jan. 1991.

[36] Rainbird, W. J., Crabbe, R. S., and Jurewicz, L. S., "A Water Tunnel Investigation of the Flow Separation about Circular Cones at Incidence," ***NRCC Aeronautical Report LR-385***, September 1963.

[37] Laitone, E. V., "Experimental Measurement of Incompressible Flow Along a Cylinder with a Conical Nose," ***J. Applied Physics***, Vol. 22, No. 1, 1951, pp.63-64.

[38] Fink, P. T., "Some Low Speed Aerodynamic Properties of Cones-Experiments Done in the Imperial College Aeronautical Laboratory," ***ARC 17***, 632, Perf. 1363, Feb. 1955.

[39] Grimson, J., "An Investigation into Flow Separation from Cones at Low Speeds," ***Unpublished College of Aeronautics Experimental Thesis***, Cranfield Institute of Technology, June 1958.

[40] Rainbird, W. J., "The External Flow about Yawed Circular Cones," Paper 19 in ***AGARD CP 30***, 1968.

[41] Mundell, A. R. G., ***RAE Unpublished***, 1978.

[42] Peake, D. J., Owen, F. K., and Johnson, D. A., "Control of Forebody Vortex Orientation to Alleviate Side Forces," ***AIAA Paper No. 80-0183***, Jan. 1980.

[43] Fiddes, S. P., Lean, D. E., and Moir, I. R. M., "Experimental Investigation of the Separated Flow Past Slender Bodies in the RAE 5-Metre Low-Speed Pressurised Tunnel," ***RAE, to be published***, 1991.

[44] Roos, F. W. and Kegelman, J. T., "Aerodynamic Characteristics of Three Generic Forebodies at High Angles of Attack," ***AIAA Paper No. 91-0275***, Jan. 1991.

[45] Hoerner, S. F., "Mechanism of Flow Separation," in ***Fluid-Dynamic Drag***, 2nd Edition, Published by the Author, New York, 1965, pp. 3-3.

[46] Lamont, P. J., "Pressures Around an Inclined Ogive Cylinder with Laminar, Transitional, or Turbulent Separation," ***AIAA Journal***, Vol. 20, No. 11, 1982, pp. 1492-1499.

[47] Moskovitz, C. A., Hall, R. M., and DeJarnette, F. R., "Effects of Surface Perturbations on the Asymmetric Vortex Flow Over a Slender Body," ***AIAA Paper No. 88-0483***, Jan. 1988.

[48] Moir, I. R. M., "Recent Experience in the RAE 5 Metre Wind Tunnel of a China-Clay Method for Indicating Boundary Layer Transition," ***Aeronautical Journal***, Vol. 90, No.1, 1986, pp. 6-9.

[49] Abdul Jabbar, F. M. H. and Al-Khalifah, N. I. "Experimental Investigations for Angle of Onset of Asymmetry of Vortex Flow Behind Circular Cone," ***Senior Project II***, Mechanical Engineering Department, KFUPM, Jan. 1992.

[50] Peake, D. J., Owen, F. K., and Higuchi, H. "Symmetrical and Asymmetrical Separations About a Yawed Cone," ***NASA-TM-78532***, September 1978.

[51] Keener, E. R., "Oil Flow Separation Patterns on an Ogive Forebody," *AIAA Journal*, Vol. 21, No. 4, 1983, pp. 550-556.

[52] Wang, K. C., "Separation Patterns of Boundary Layer over an Inclined Body of Revolution," *AIAA Journal*, Vol. 10, No. 8, 1972, pp. 1044-1050

[53] Deane, J. R. "Missile Body Vortices and Their Interaction with Lifting Surfaces," *High Angle-of-Attack Aerodynamics*, AGARD Lecture Series No. 121, Paper 12, Dec. 1982.

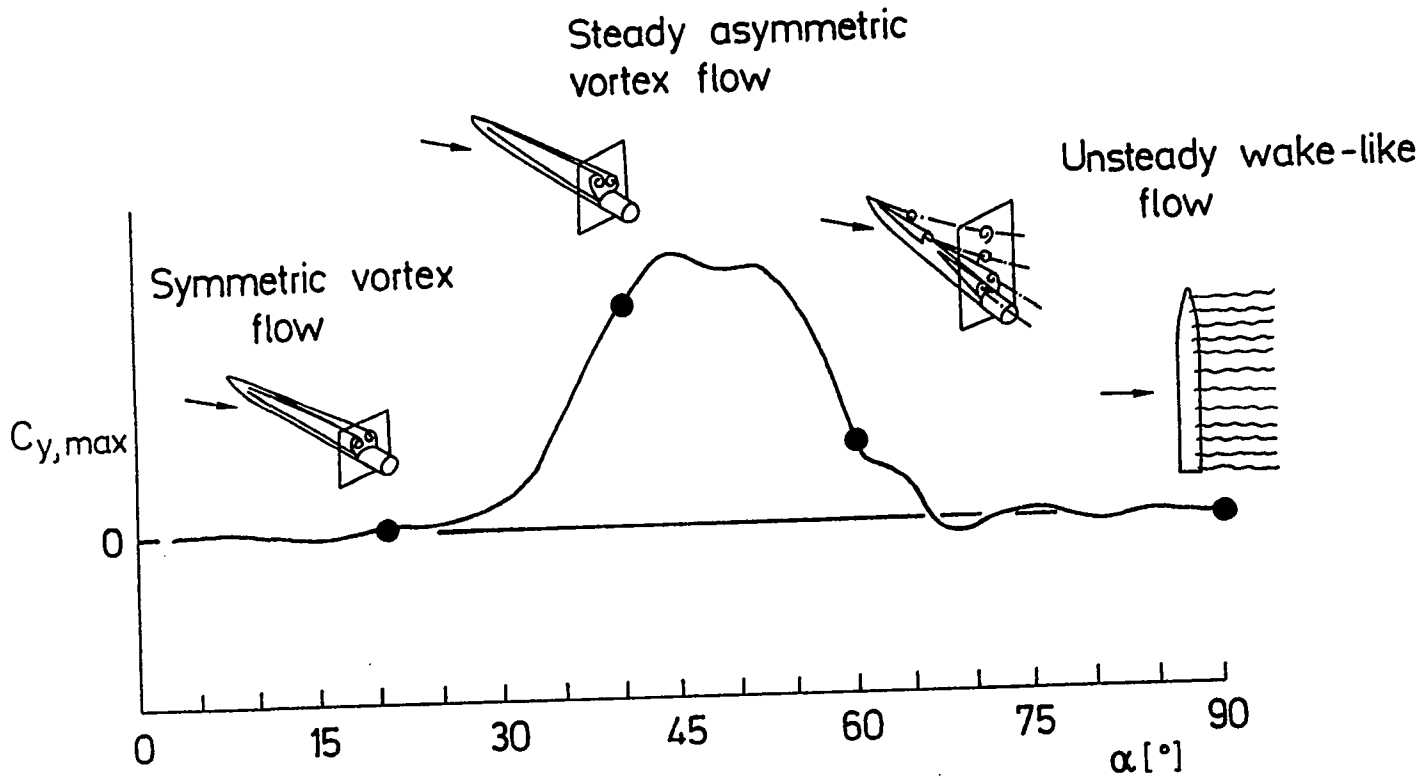

Fig. 1.1 Typical variations of side force and vortex patterns with incidence of body of revolution at zero yaw.

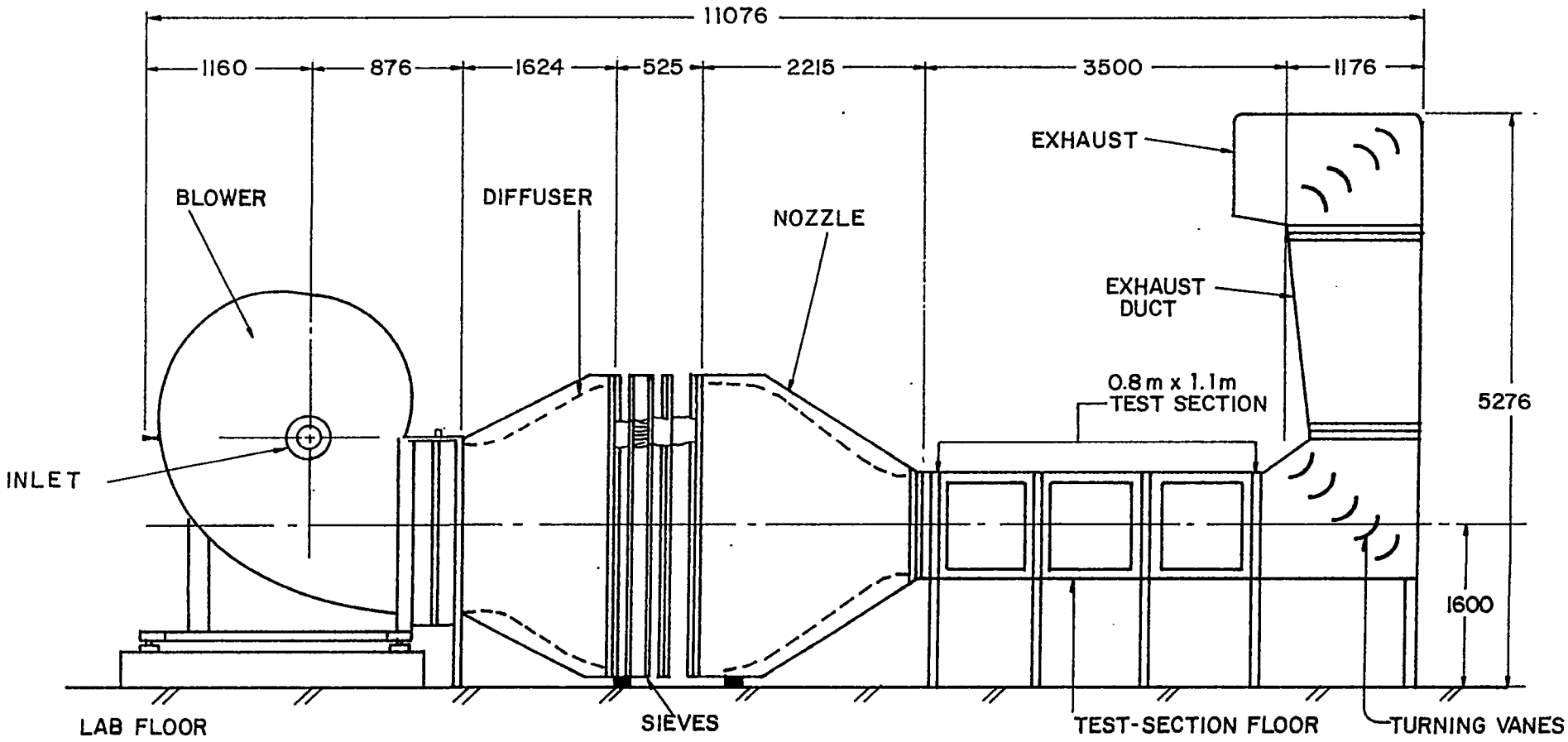

(a) schematic of the wind tunnel

Fig. 3.1 KFUPM 0.8 m x 1.1 m wind tunnel

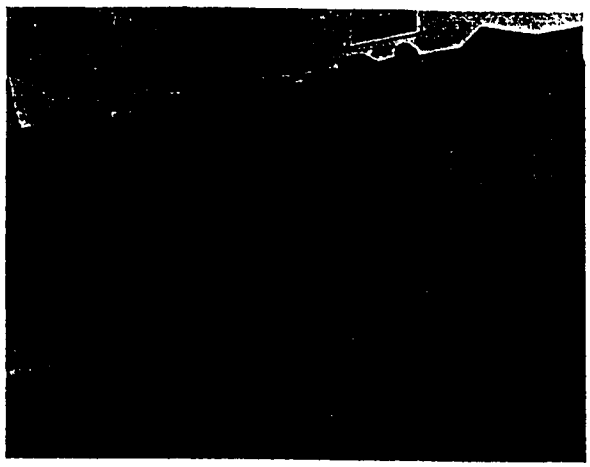

(b) test section of the wind tunnel

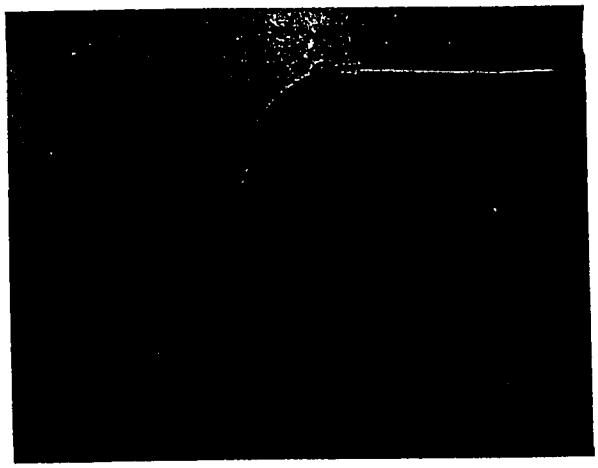

(c) blower and diffuser of the wind tunnel

Fig 3.1 Concluded

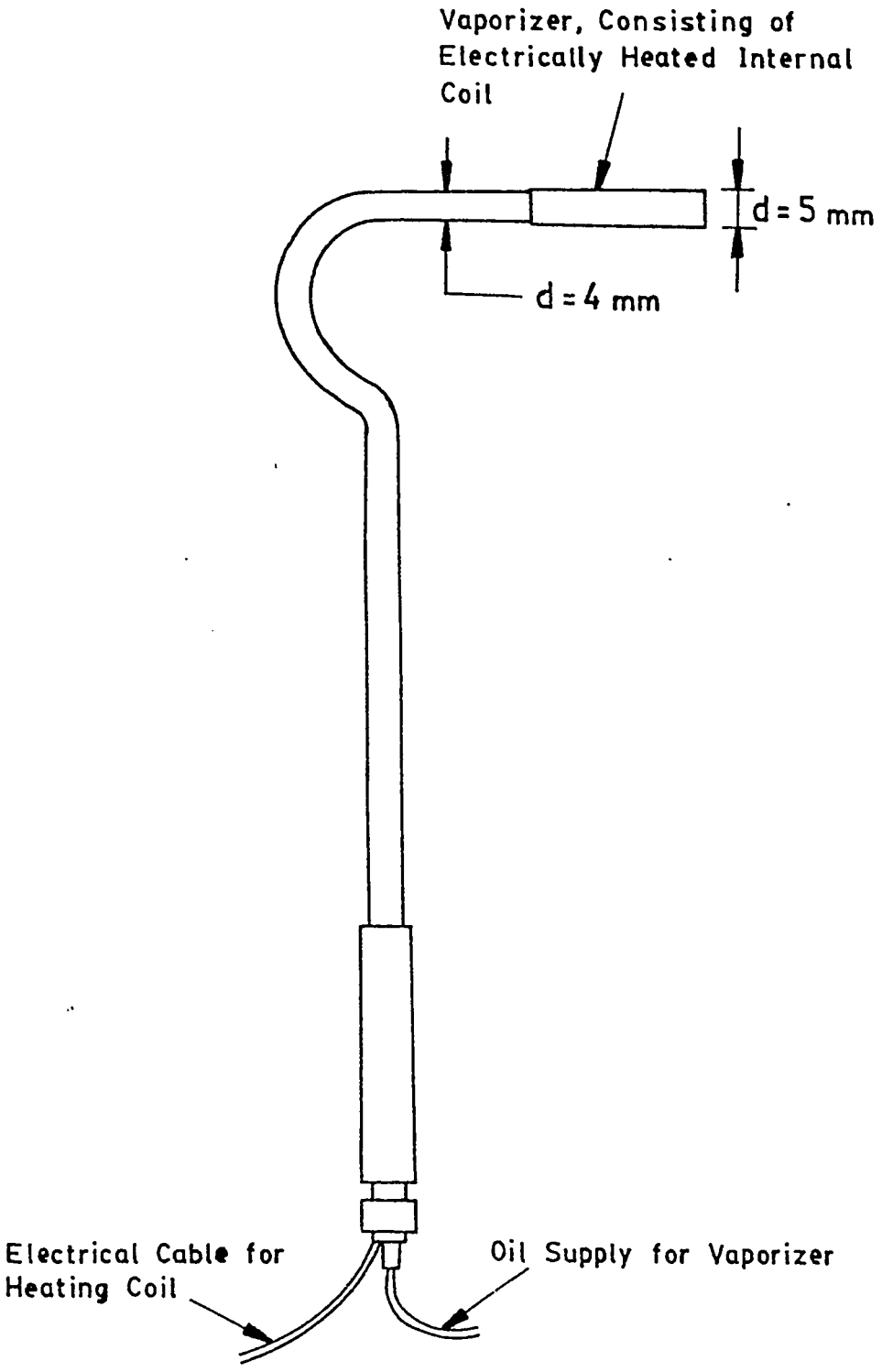

Fig. 3.2 Smoke probe

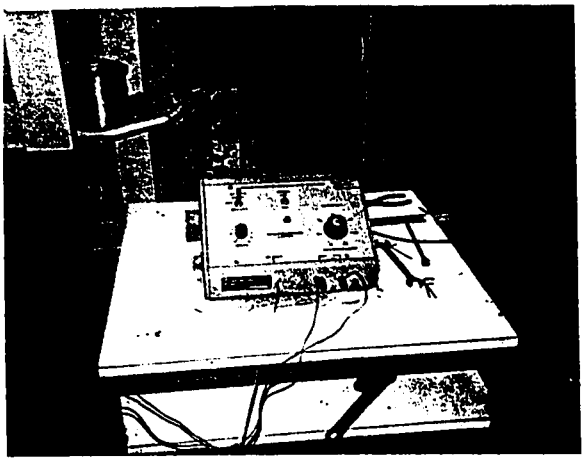

Fig 3.3 Oil supply and control unit for smoke generating probe

Fig 3.4 Laser-light source and optical arrangement

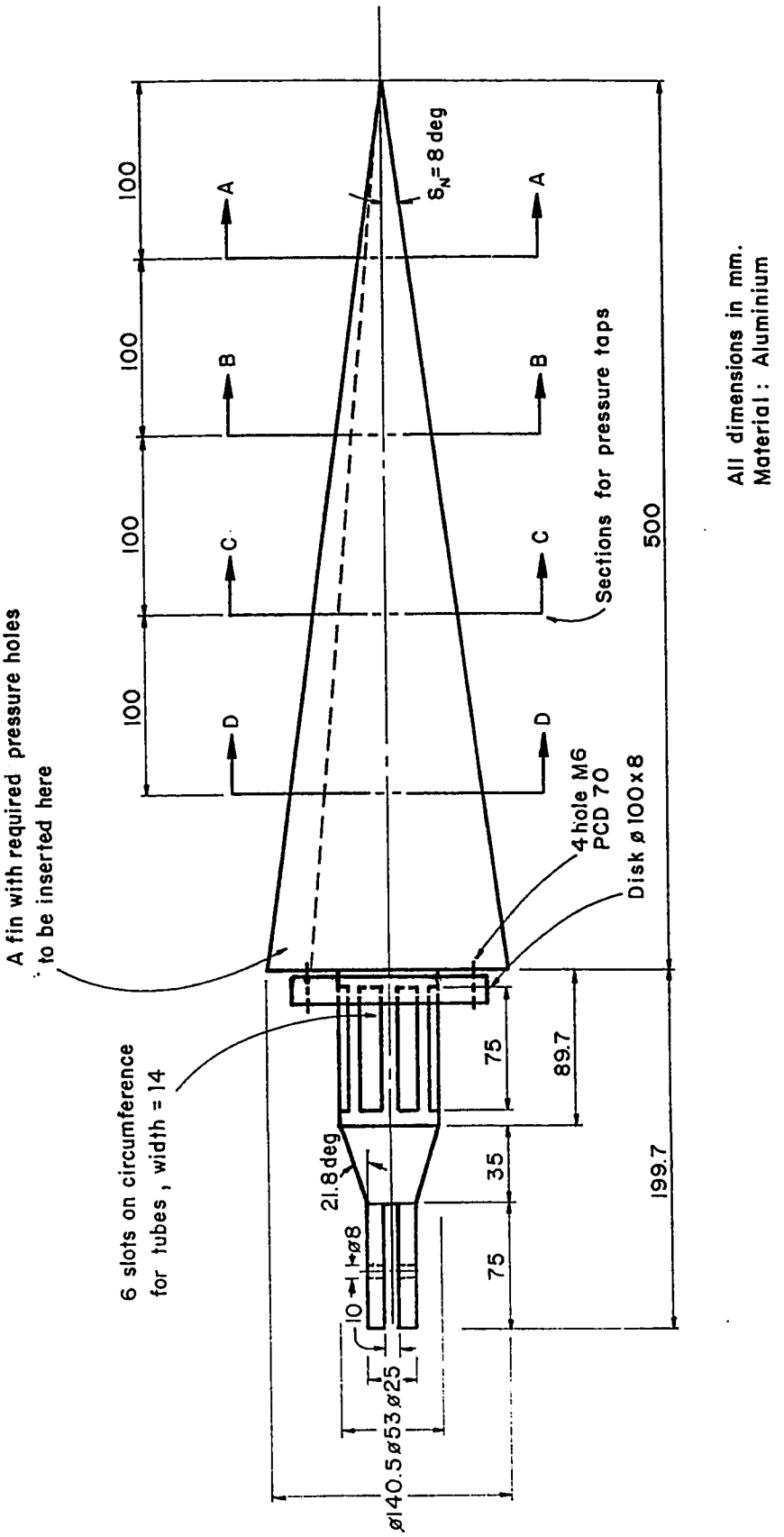

(a) plan view of the cone and sting

Fig. 3.5 Surface-pressure measurement model and mounting

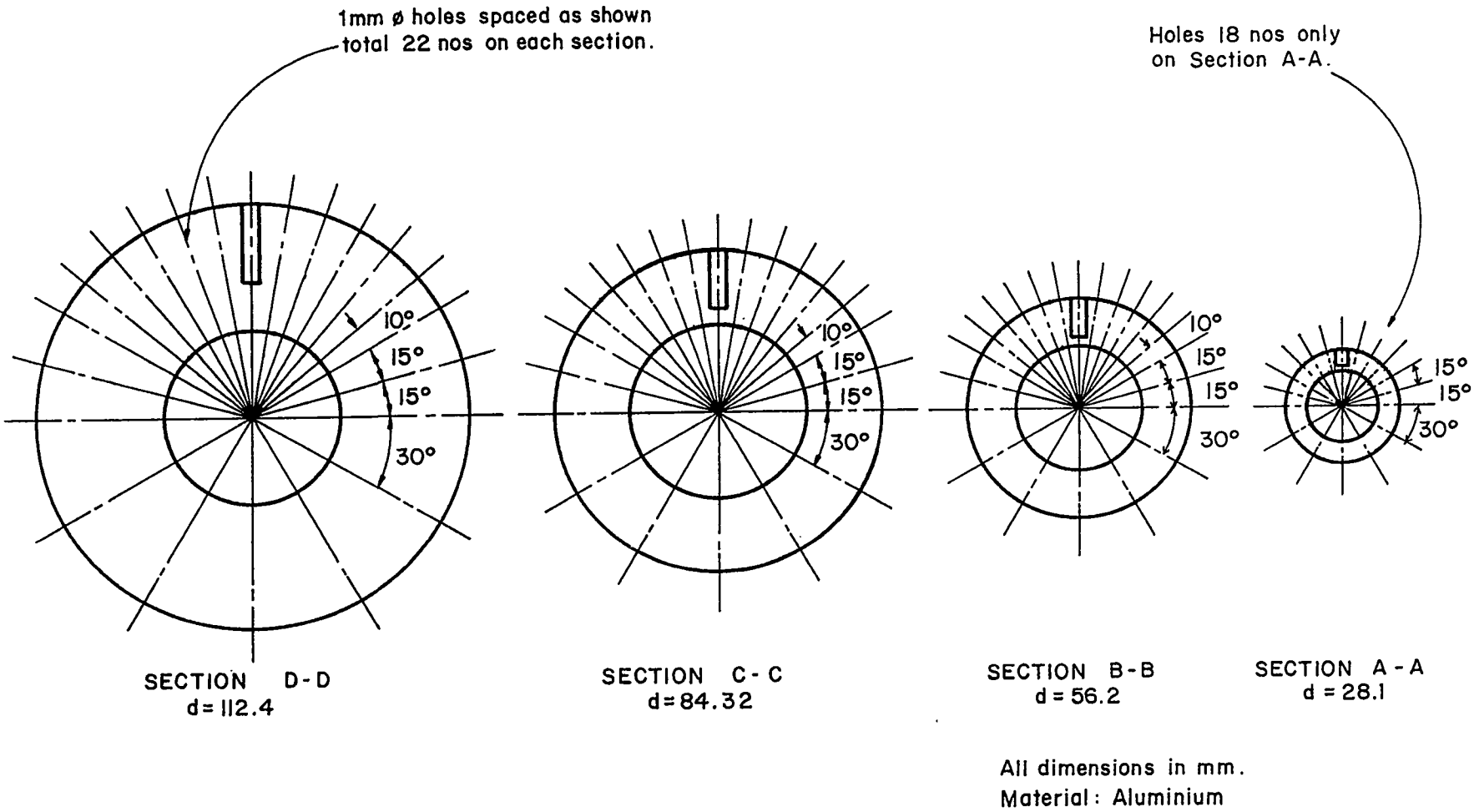

(b) pressure-tap positions at A, B, C, and D sections

Fig. 3.5 Continued

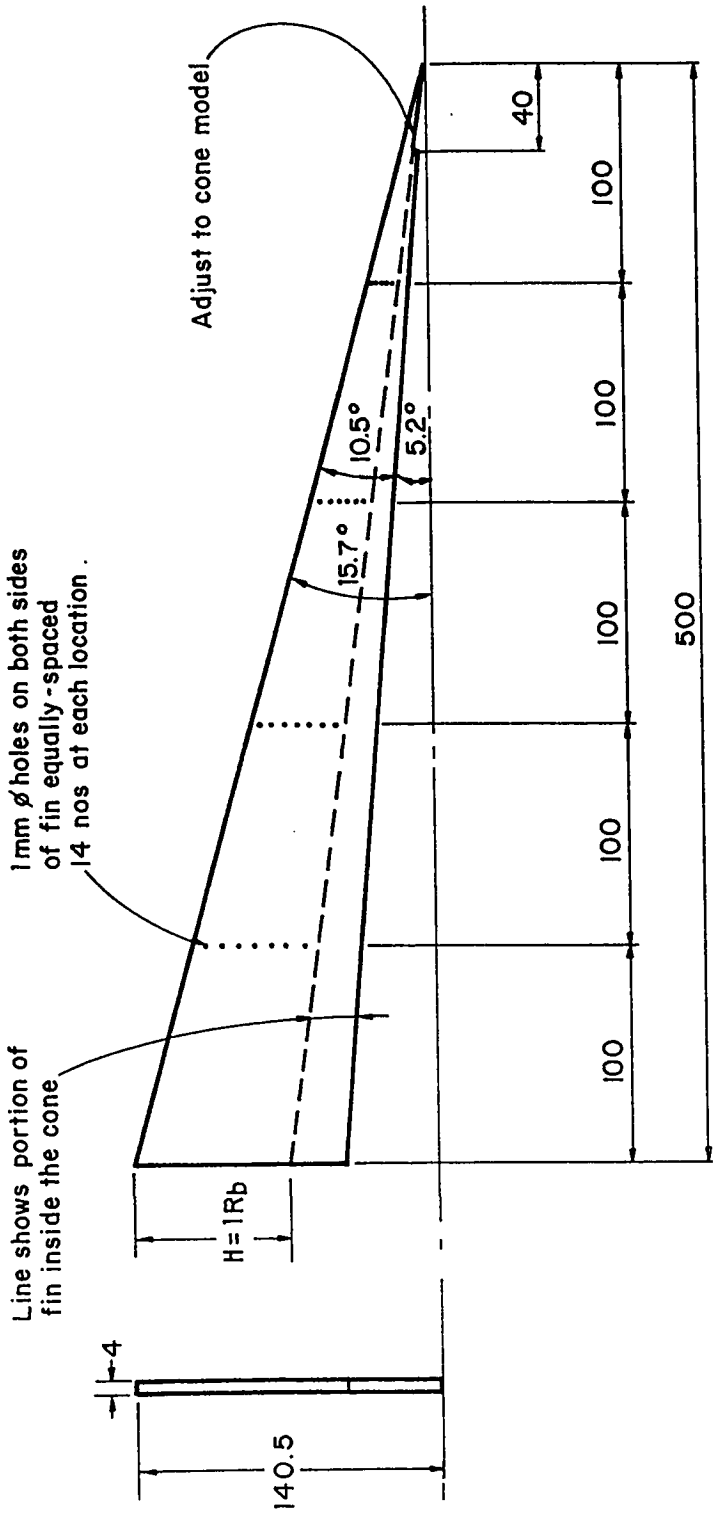

All dimensions in mm.
Material : Wood

(c) Fin

Fig. 3.5 Continued

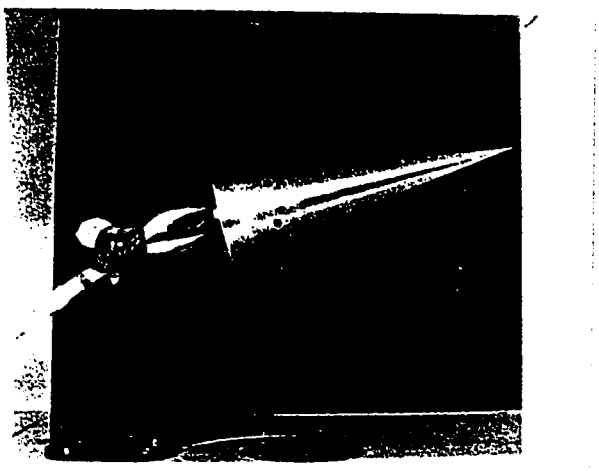

(d) pressure-measurement cone in the wind tunnel

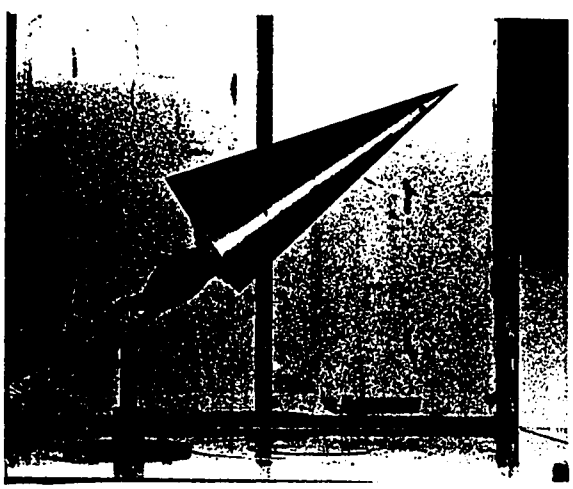

(e) pressure-measurement cone with fin in the wind tunnel

Fig 3.5 Concluded

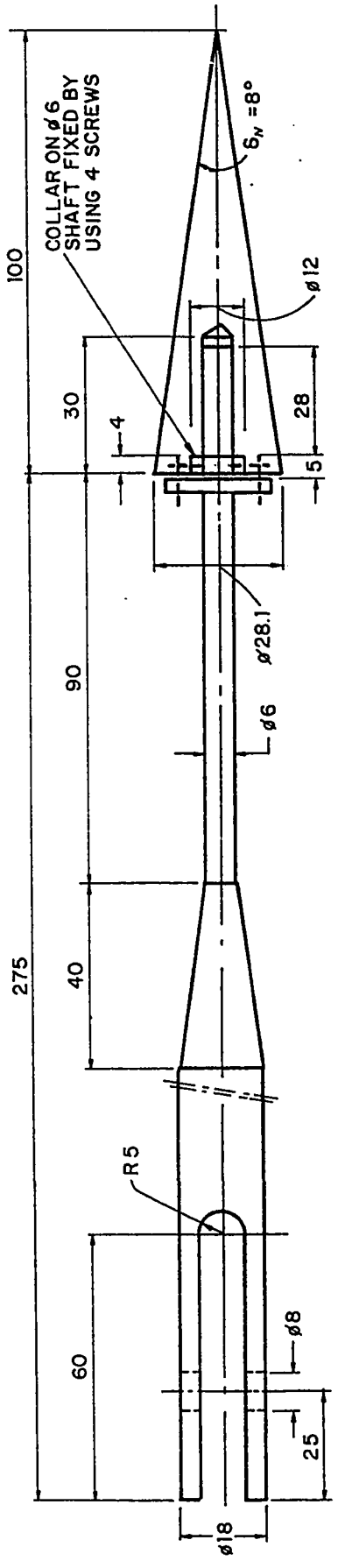

(a) plan view of the small cone (L = 100 mm) with sting

Fig. 3.6 Flow-visualization models and mounting

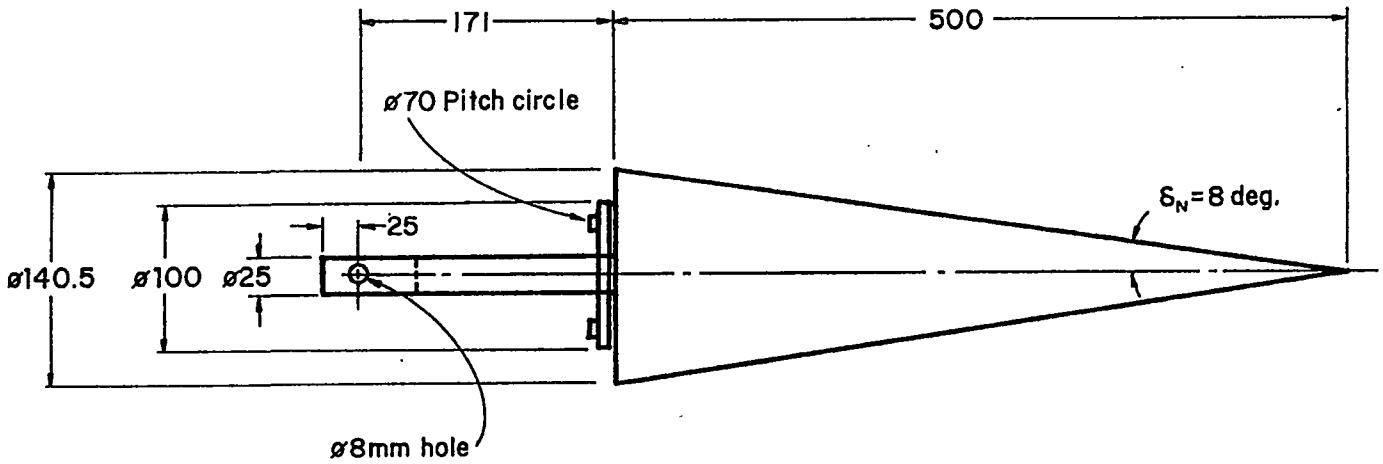

All dimensions in mm.
Material: Steel

(b) plan view of the big cone (L = 500 mm) with sting

Fig. 3.6 Continued

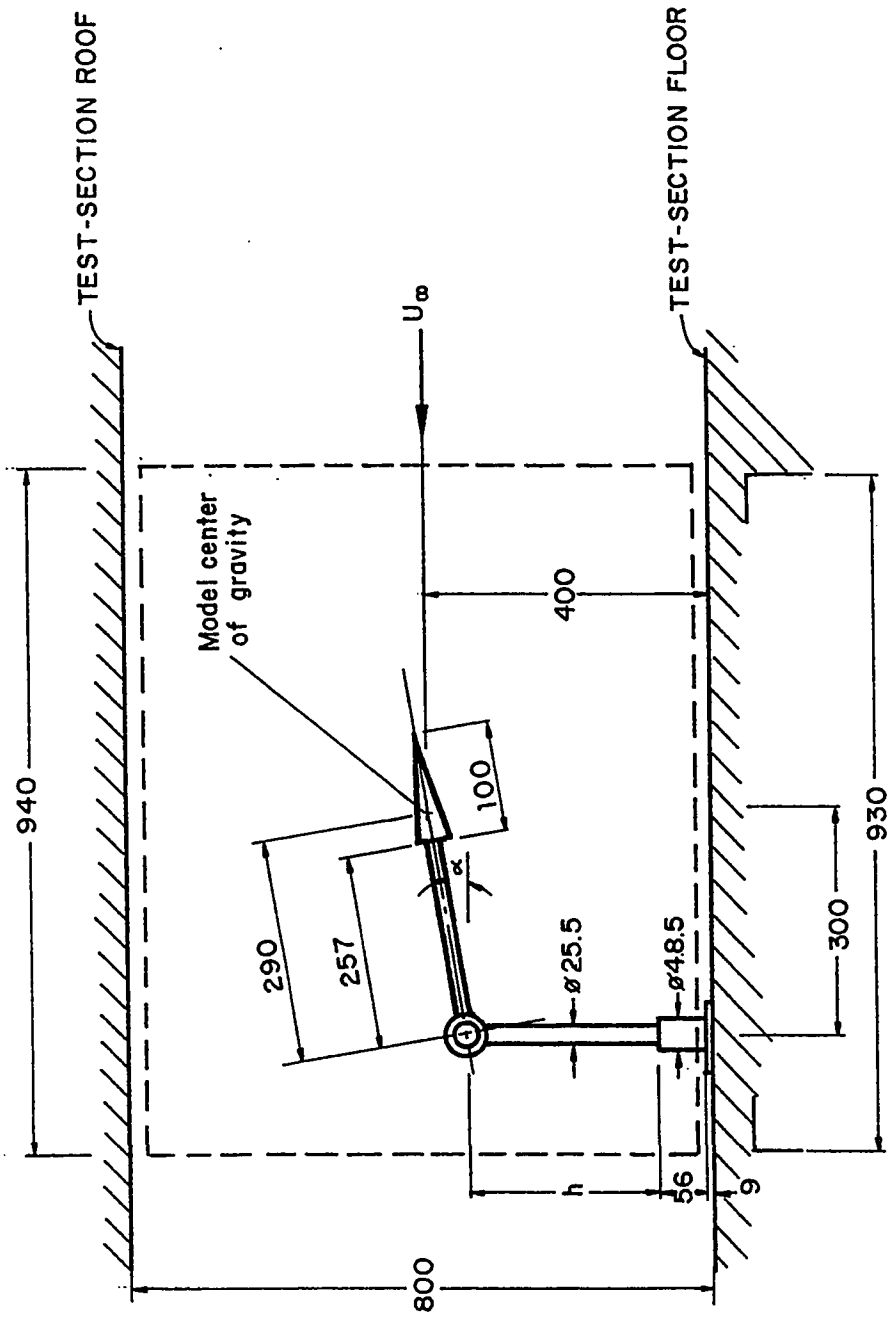

(c) schematic of the small cone installation in the wind tunnel

Fig. 3.6 Continued

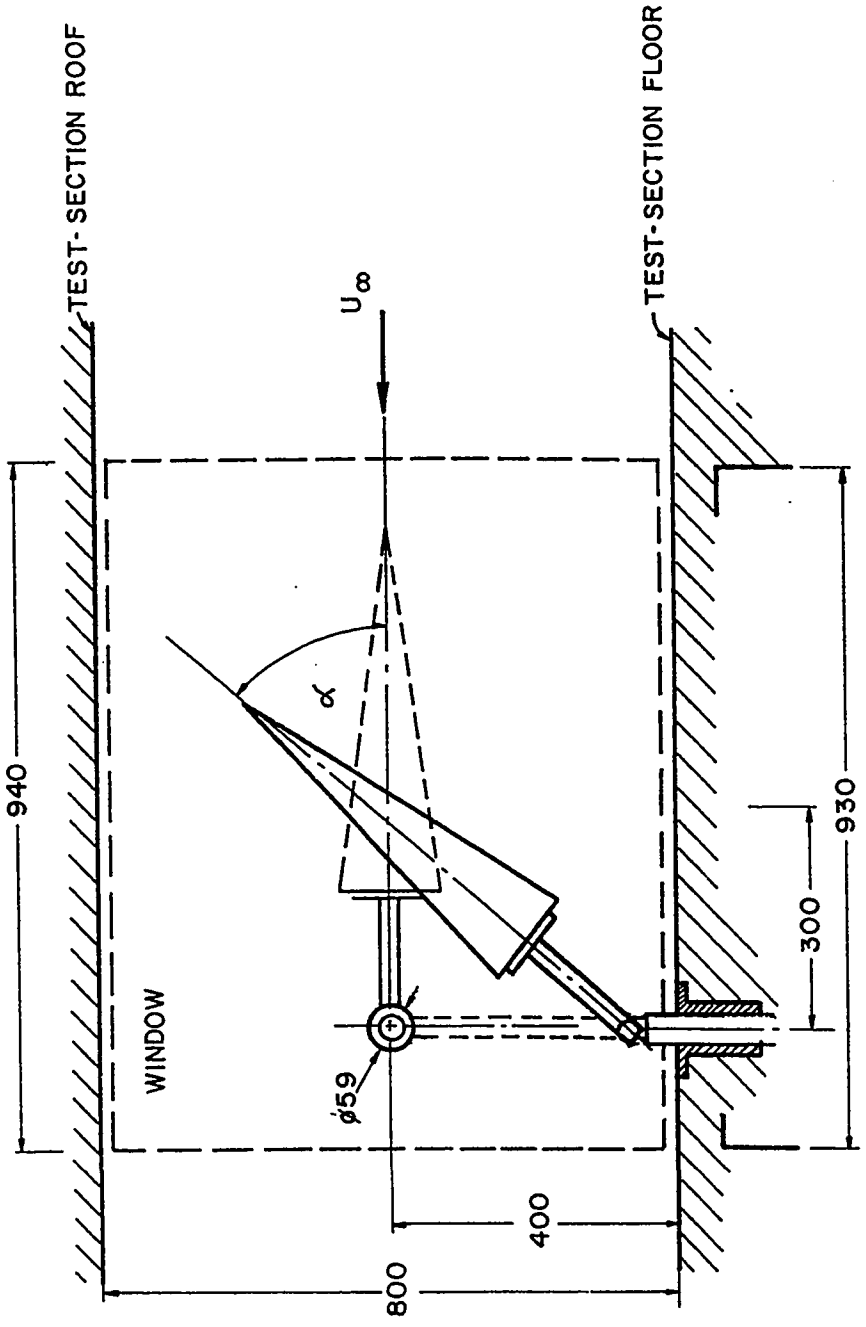

(d) Schematic of big cone installation in the wind tunnel

Fig. 3.6 Concluded

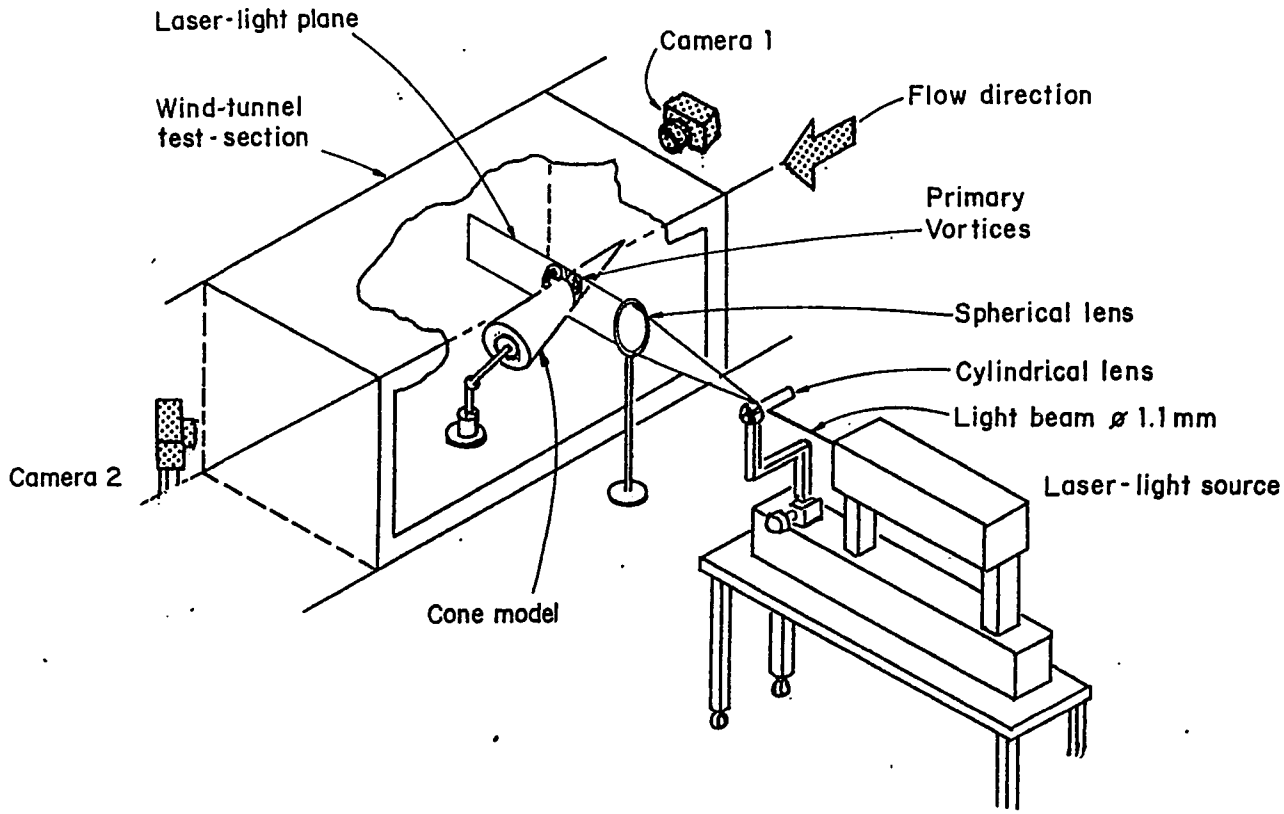

Fig. 3.7 Schematic of vortex-flow visualization set-up in wind tunnel

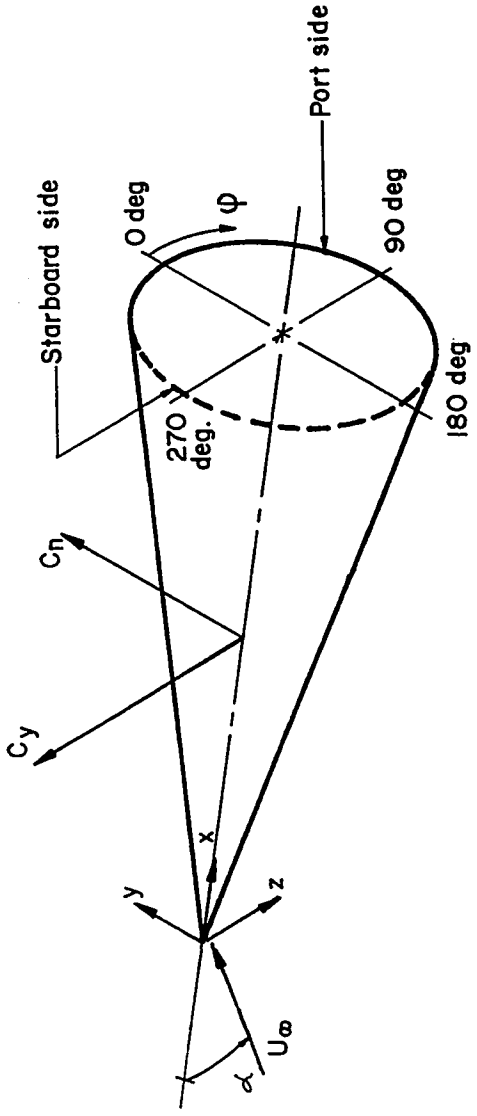

Fig. 4.1 Variables and sign conventions

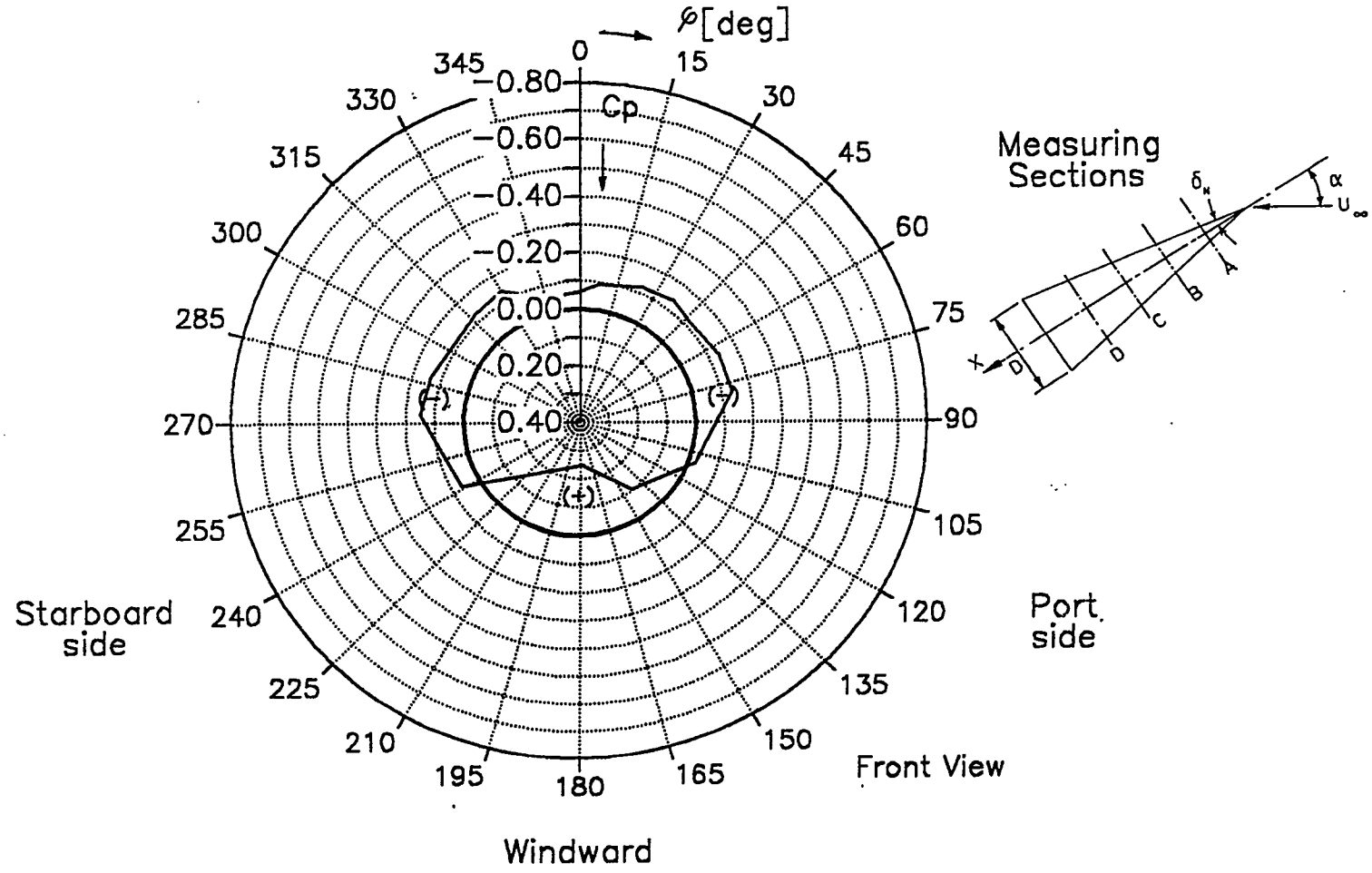

Fig. 4.2 Circumferential pressure distribution on circular cone δ_N=8 deg, without fin, Re_D = 142,000, α=15 deg, section A

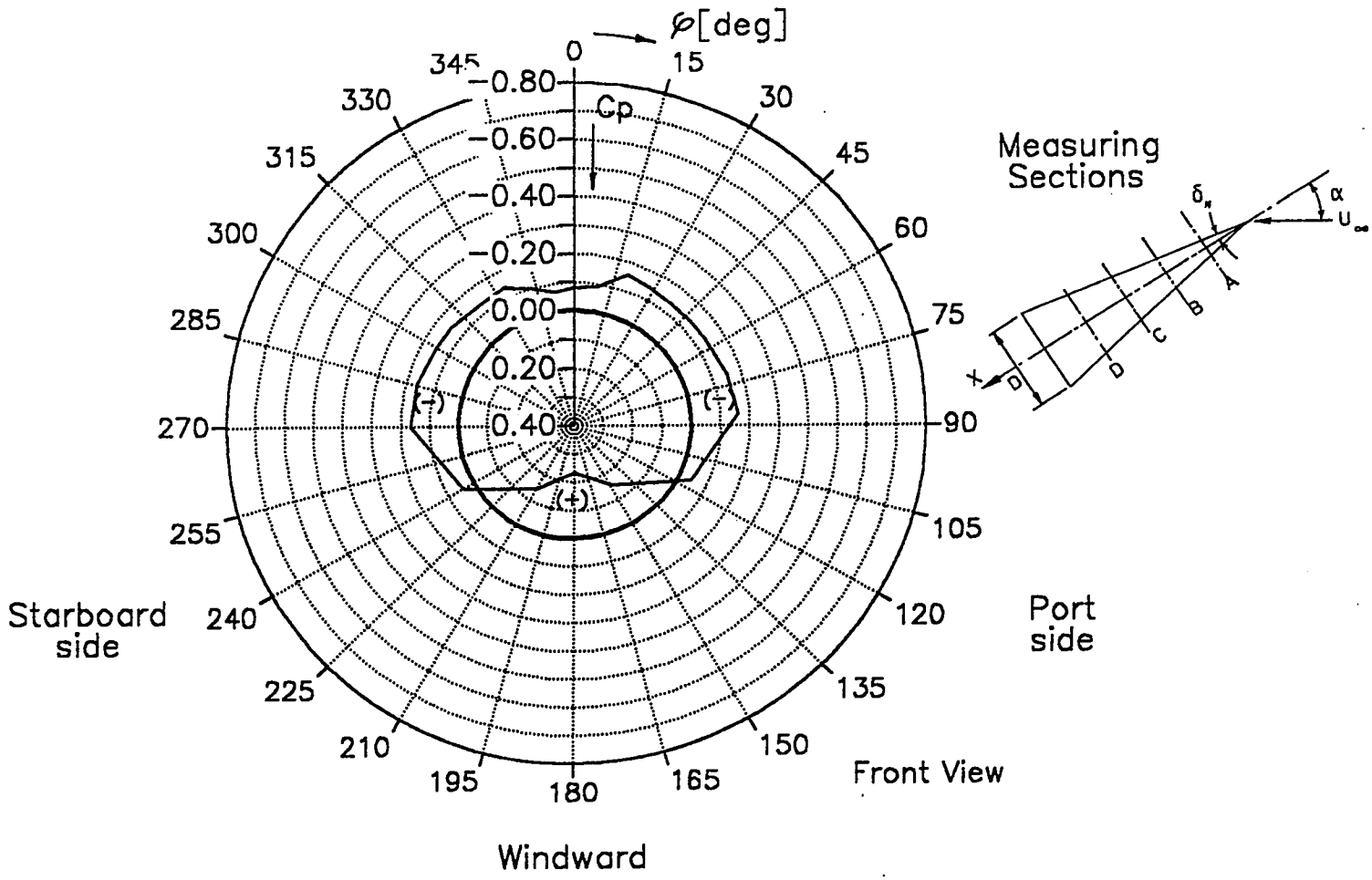

Fig. 4.3 Circumferential pressure distribution on circular cone, δ_N=8 deg, without fin, Re_D = 142,000, α=15 deg, section B

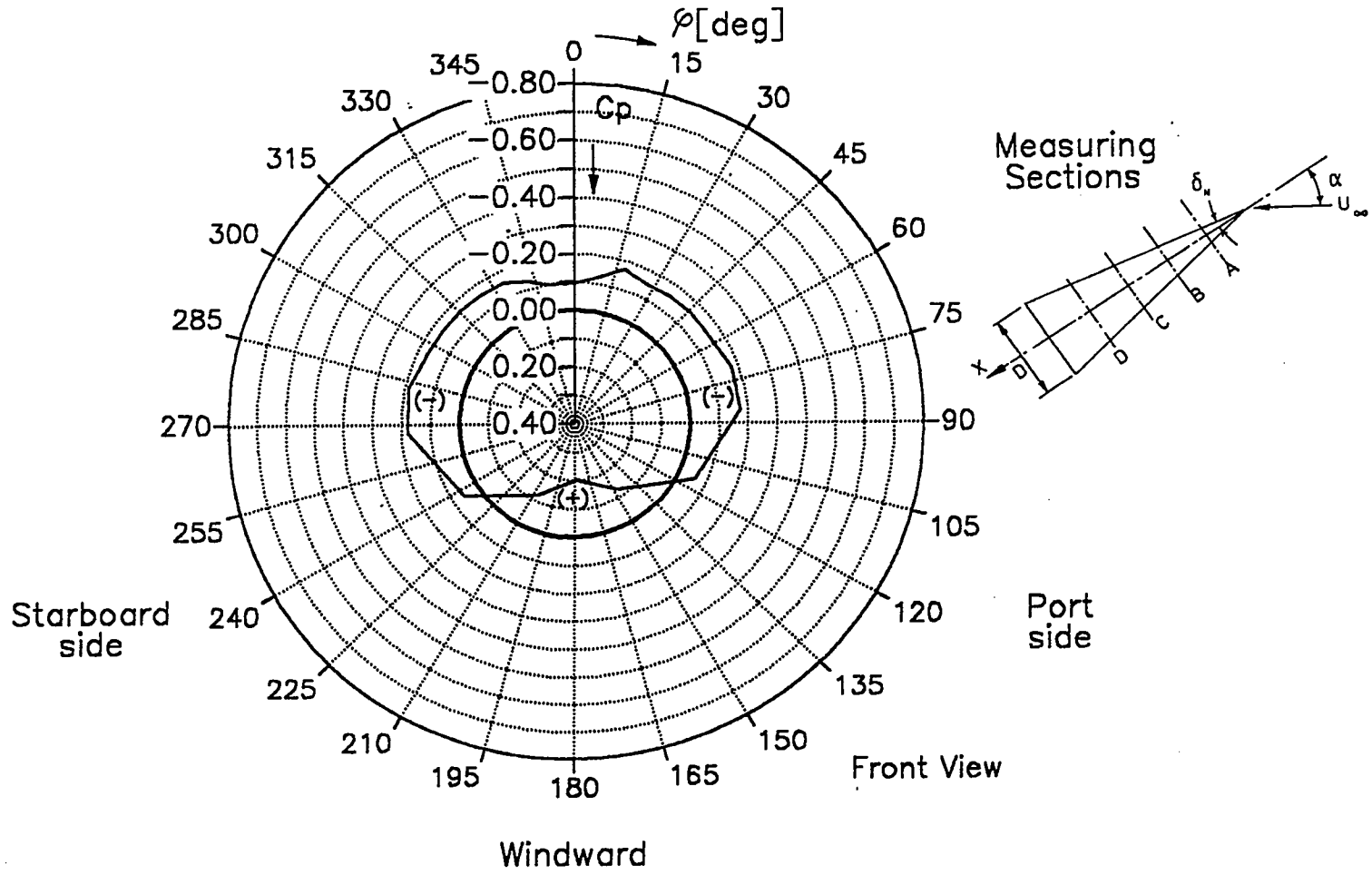

Fig. 4.4 Circumferential pressure distribution on circular cone, $\delta_N = 8$ deg, without fin, $Re_D = 142{,}000$, $\alpha = 15$ deg, section C

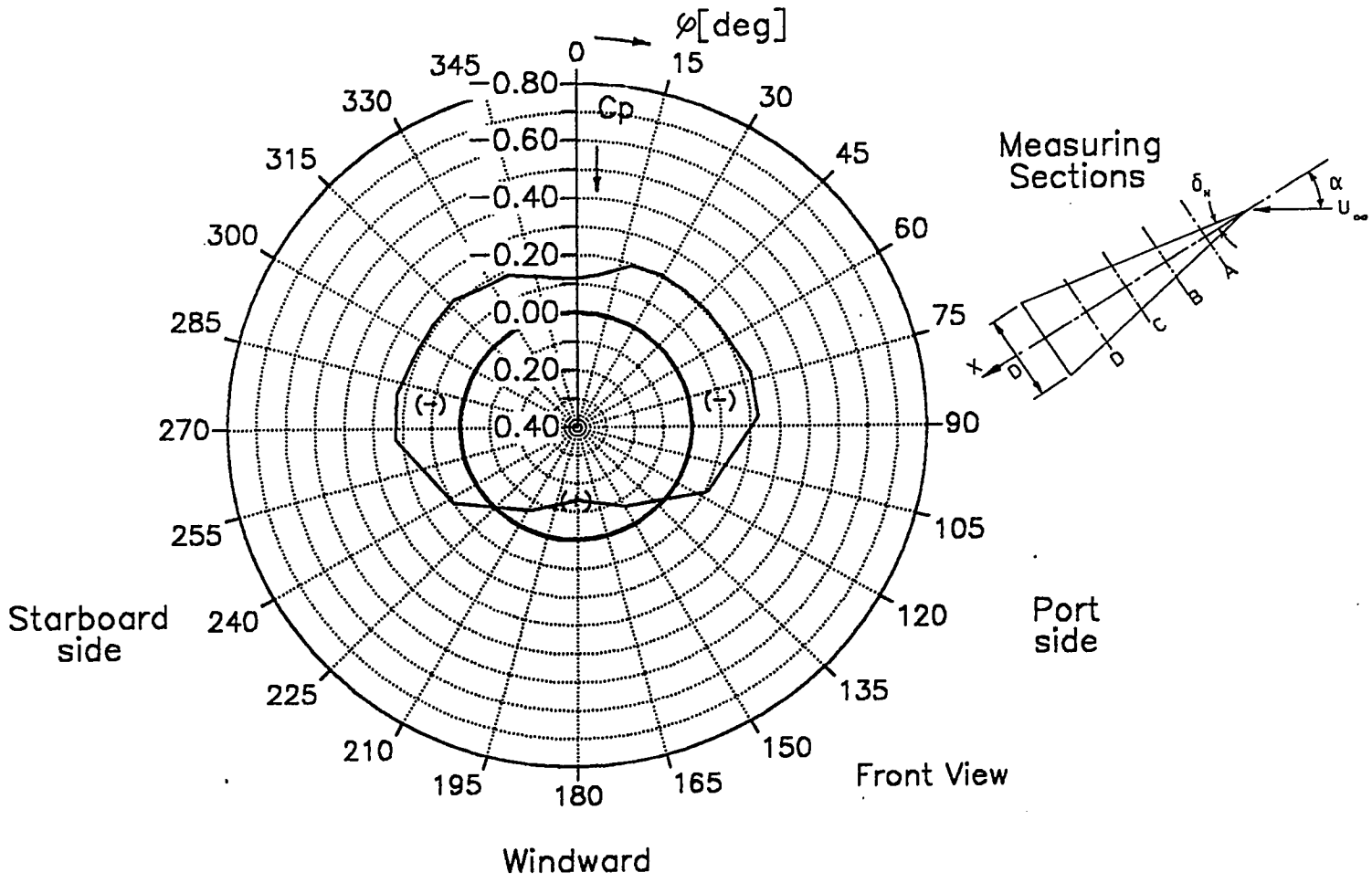

Fig. 4.5 Circumferential pressure distribution on circular cone, $\delta_N = 8$ deg, without fin, $Re_D = 142{,}000$, $\alpha = 15$ deg, section D

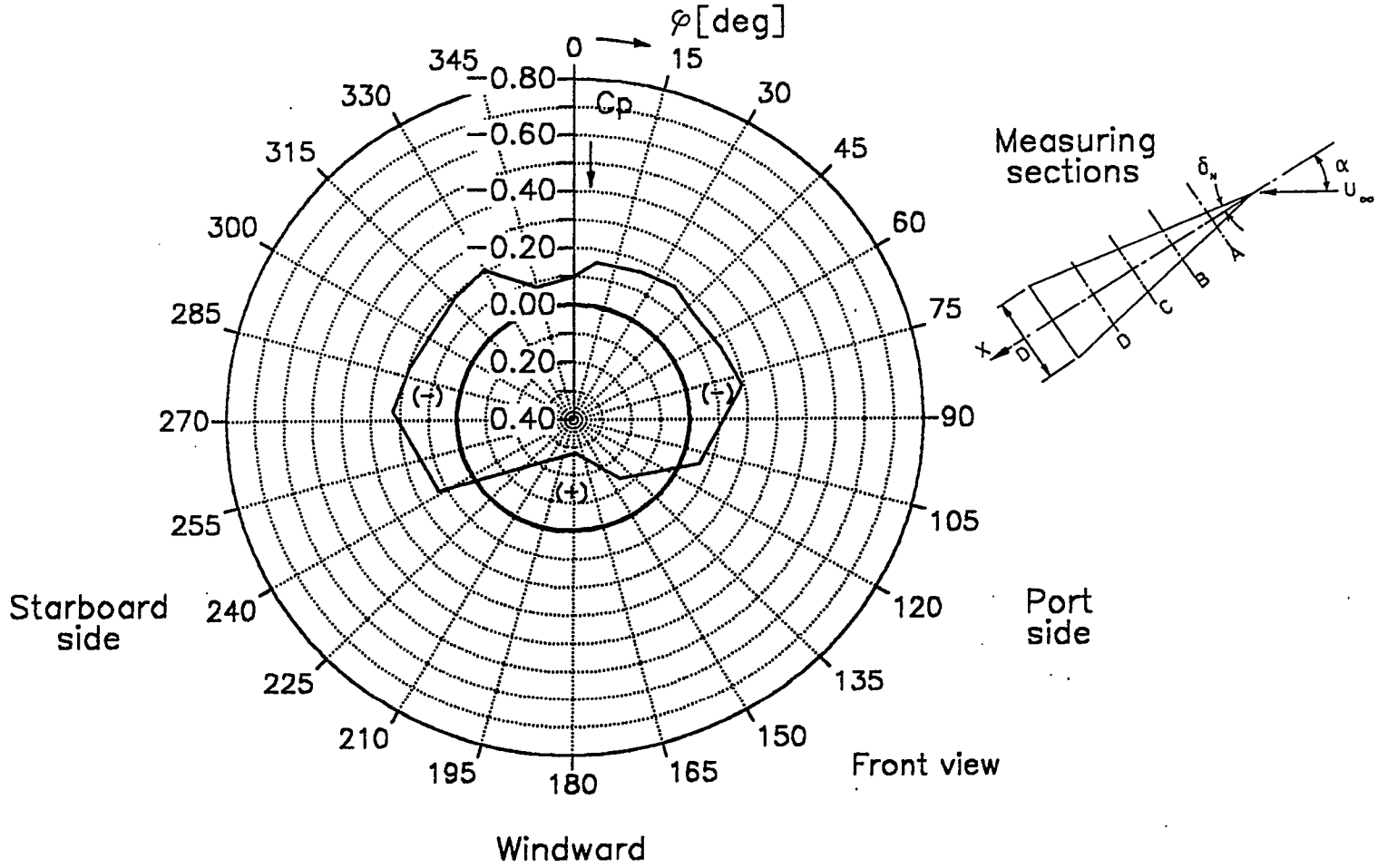

Fig. 4.6 Circumferential pressure distribution on circular cone δ_N=8 deg, without fin, Re_D = 142,000, α=17 deg, section A

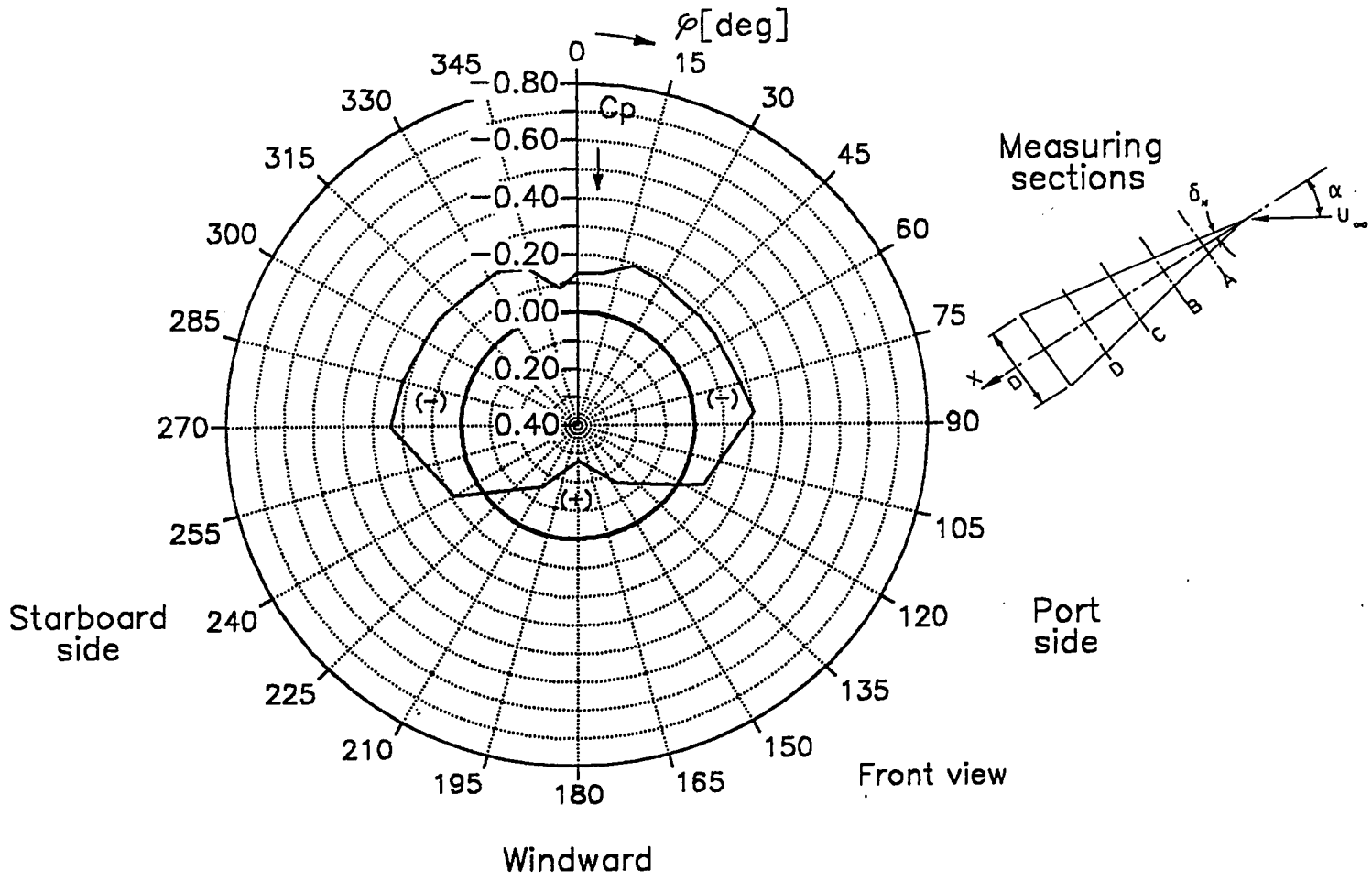

Fig. 4.7 Circumferential pressure distribution on circular cone δ_N=8 deg, without fin, Re_D = 142,000, α=17 deg, section B

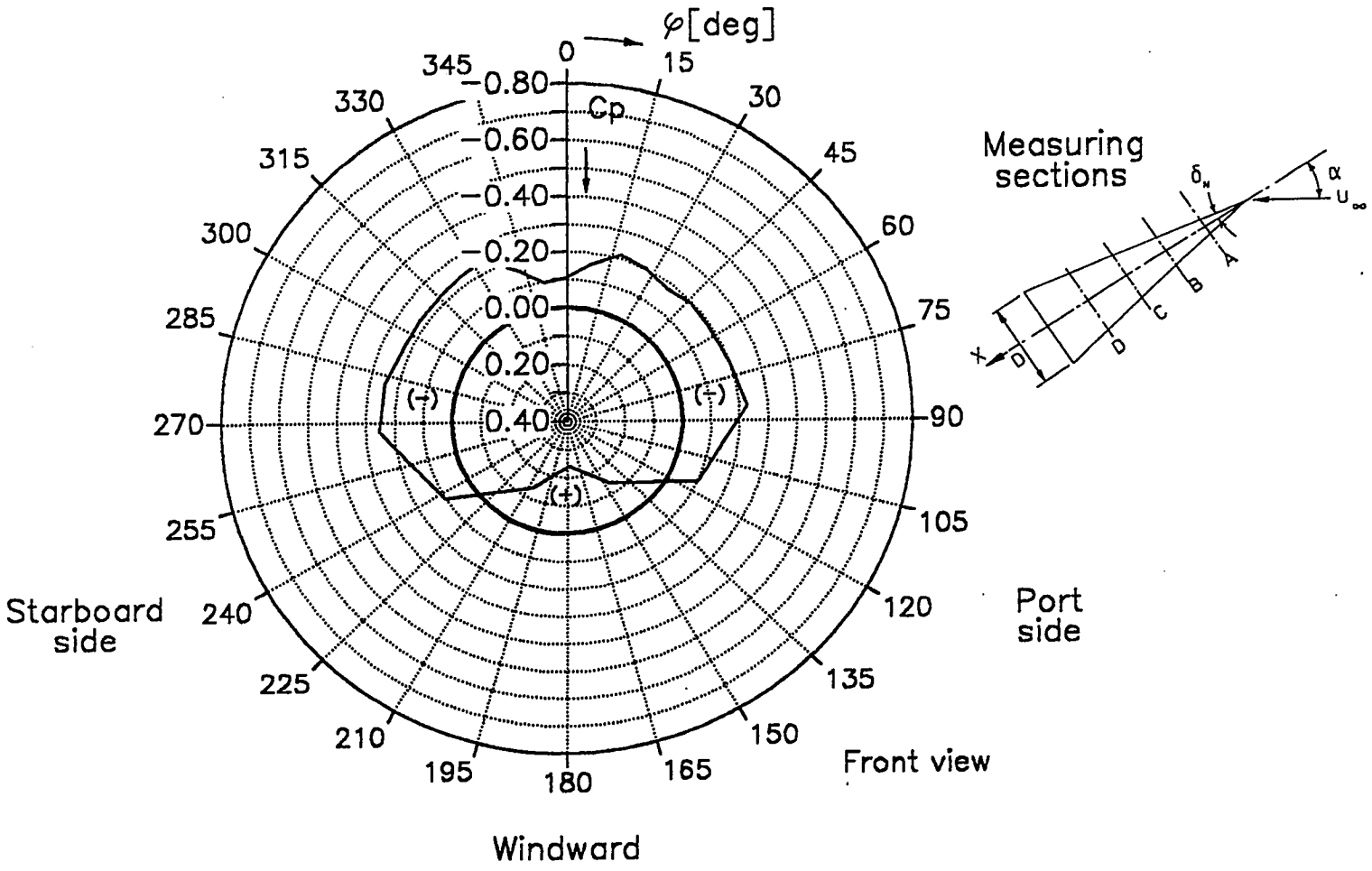

Fig. 4.8 Circumferential pressure distribution on circular cone $\delta_N = 8$ deg, without fin, $Re_D = 142{,}000$, $\alpha = 17$ deg, section C

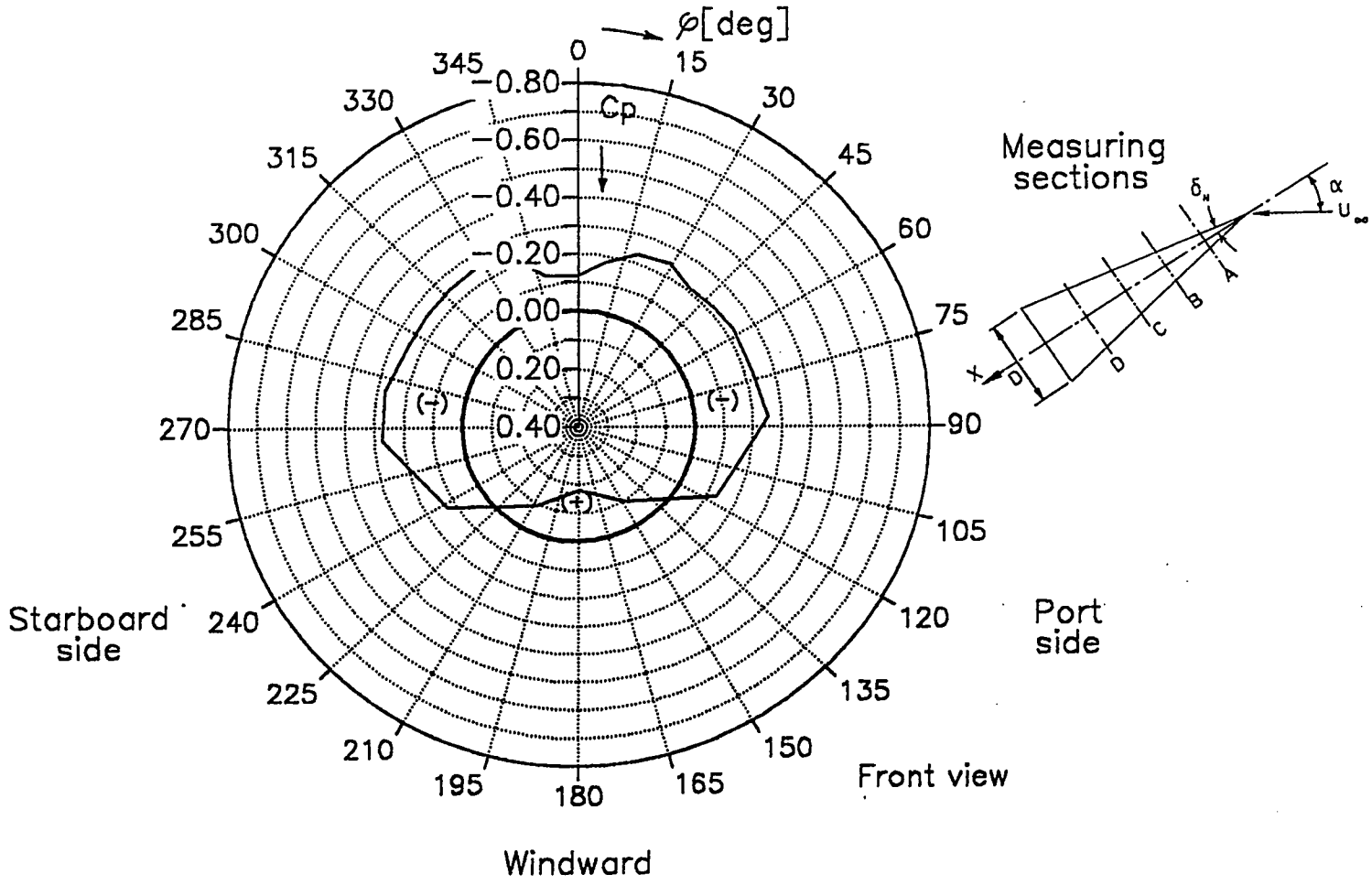

Fig. 4.9 Circumferential pressure distribution on circular cone $\delta_N = 8$ deg, without fin, $Re_D = 142{,}000$, $\alpha = 17$ deg, section D

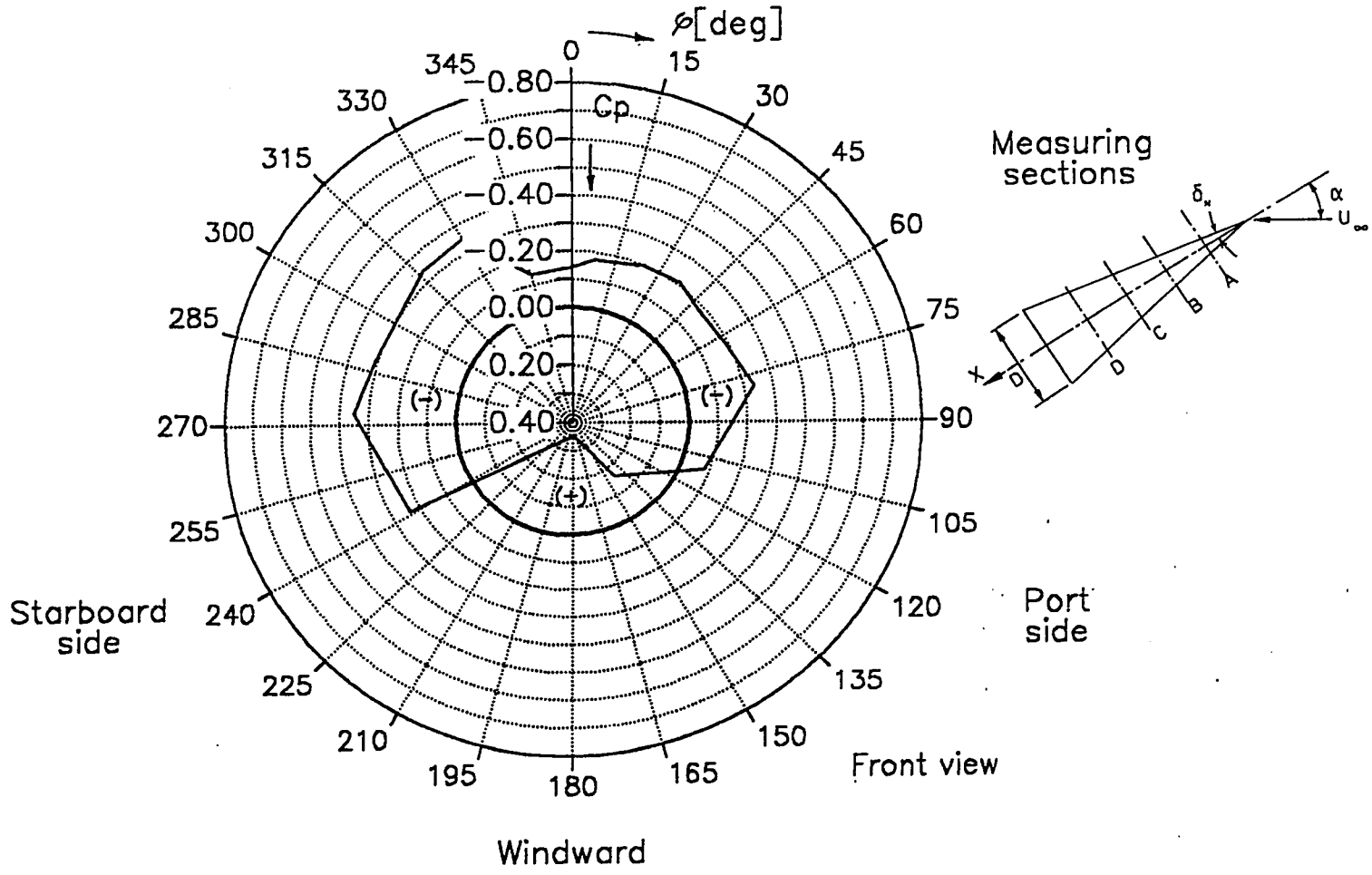

Fig. 4.10 Circumferential pressure distribution on circular cone δ_N=8 deg, without fin, Re_D = 142,000, α=20 deg, section A

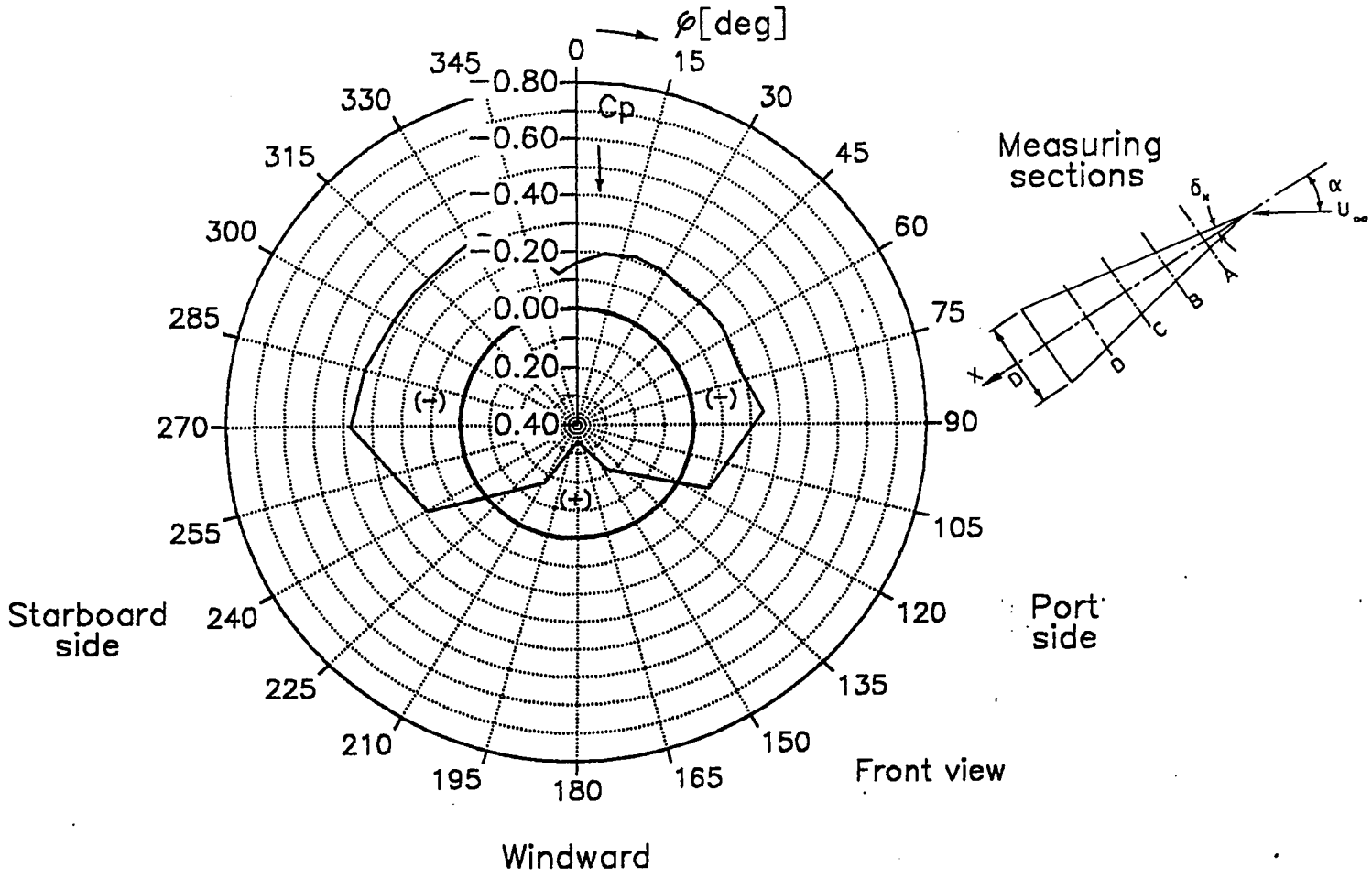

Fig. 4.11 Circumferential pressure distribution on circular cone $\delta_N = 8$ deg, without fin, $Re_D = 142{,}000$, $\alpha = 20$ deg, section B

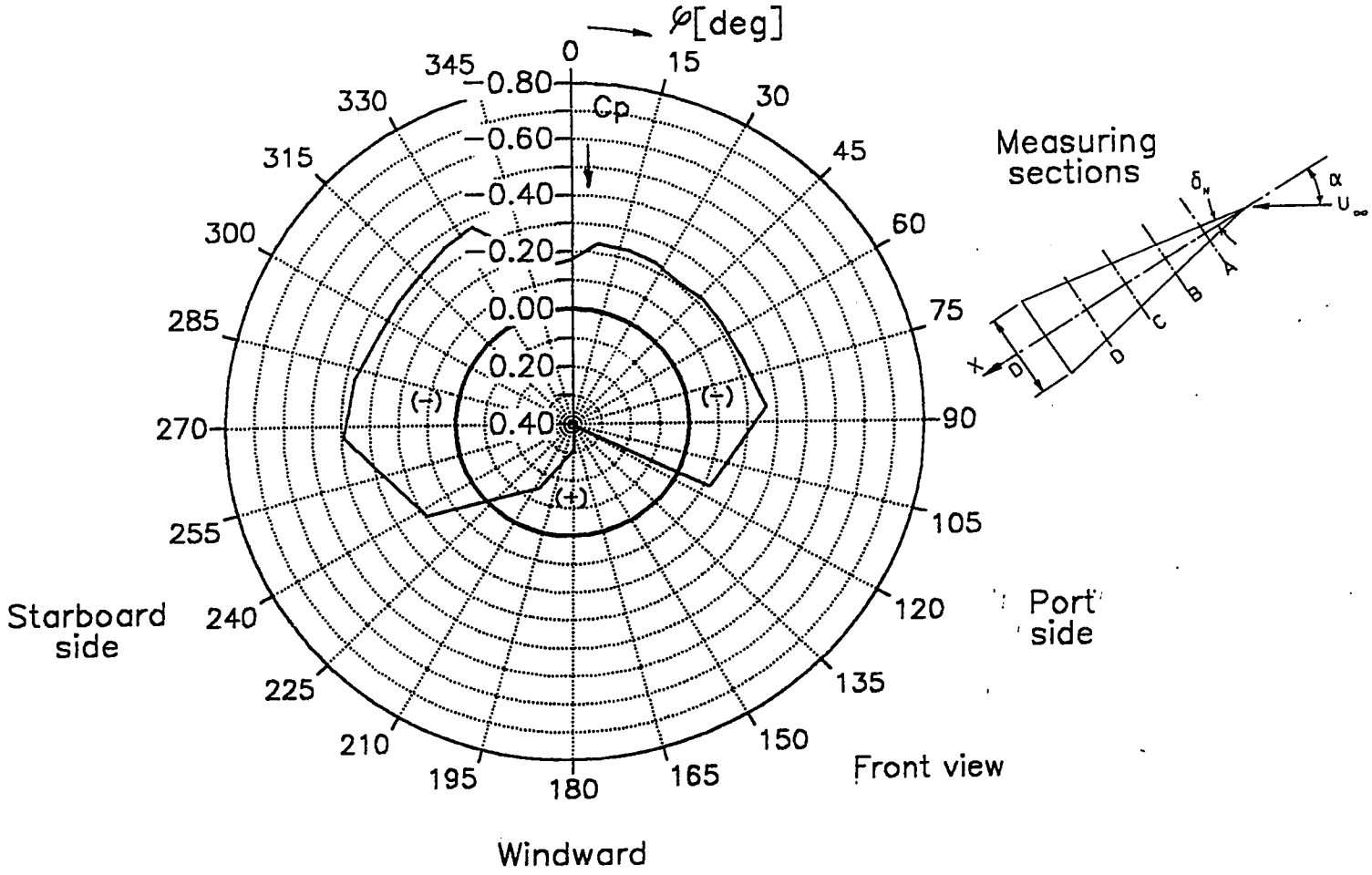

Fig. 4.12 Circumferential pressure distribution on circular cone $\delta_N = 8$ deg, without fin, $Re_D = 142{,}000$, $\alpha = 20$ deg, section C

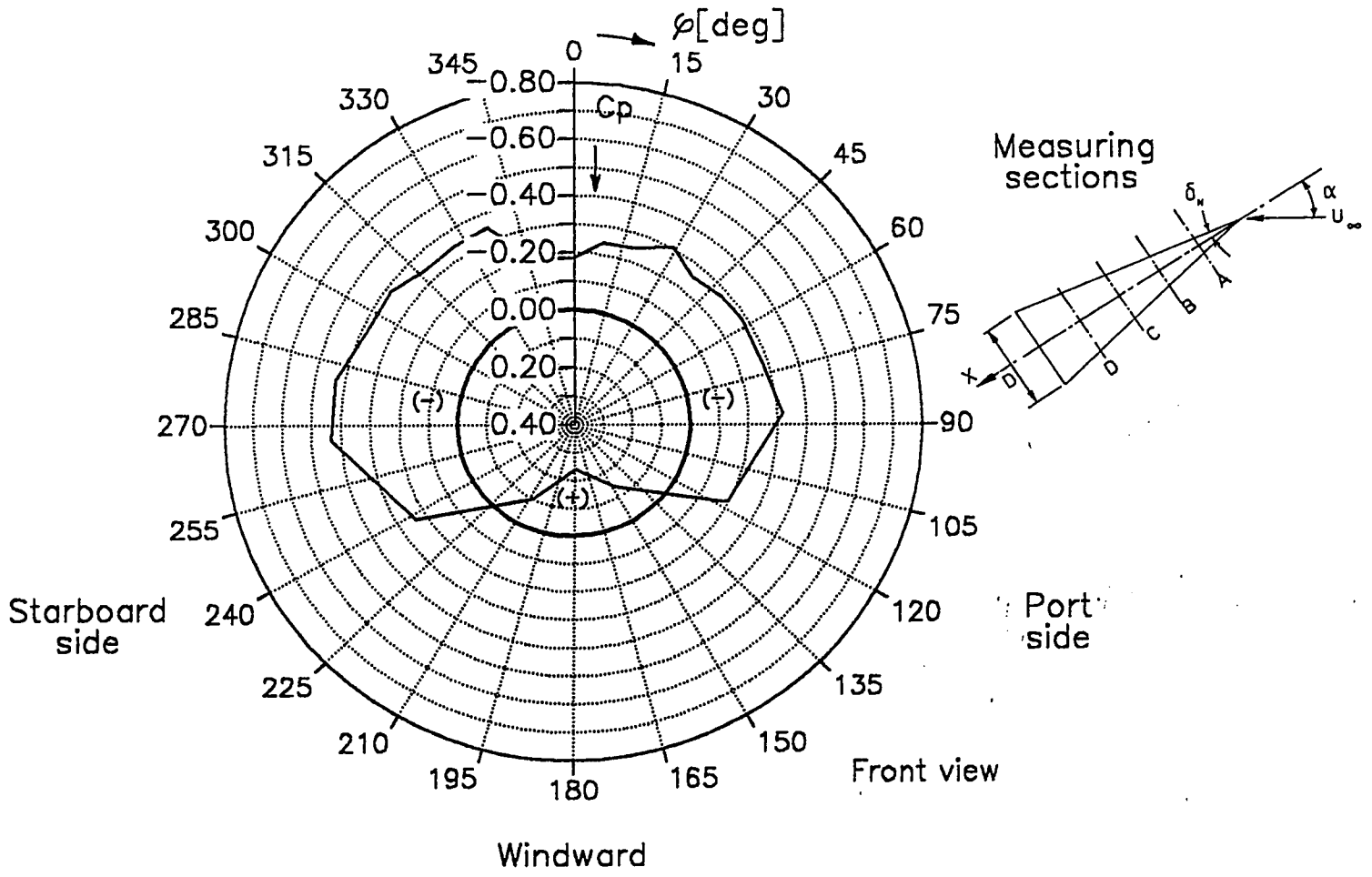

Fig. 4.13 Circumferential pressure distribution on circular cone $\delta_N = 8$ deg, without fin, $Re_D = 142{,}000$, $\alpha = 20$ deg, section D

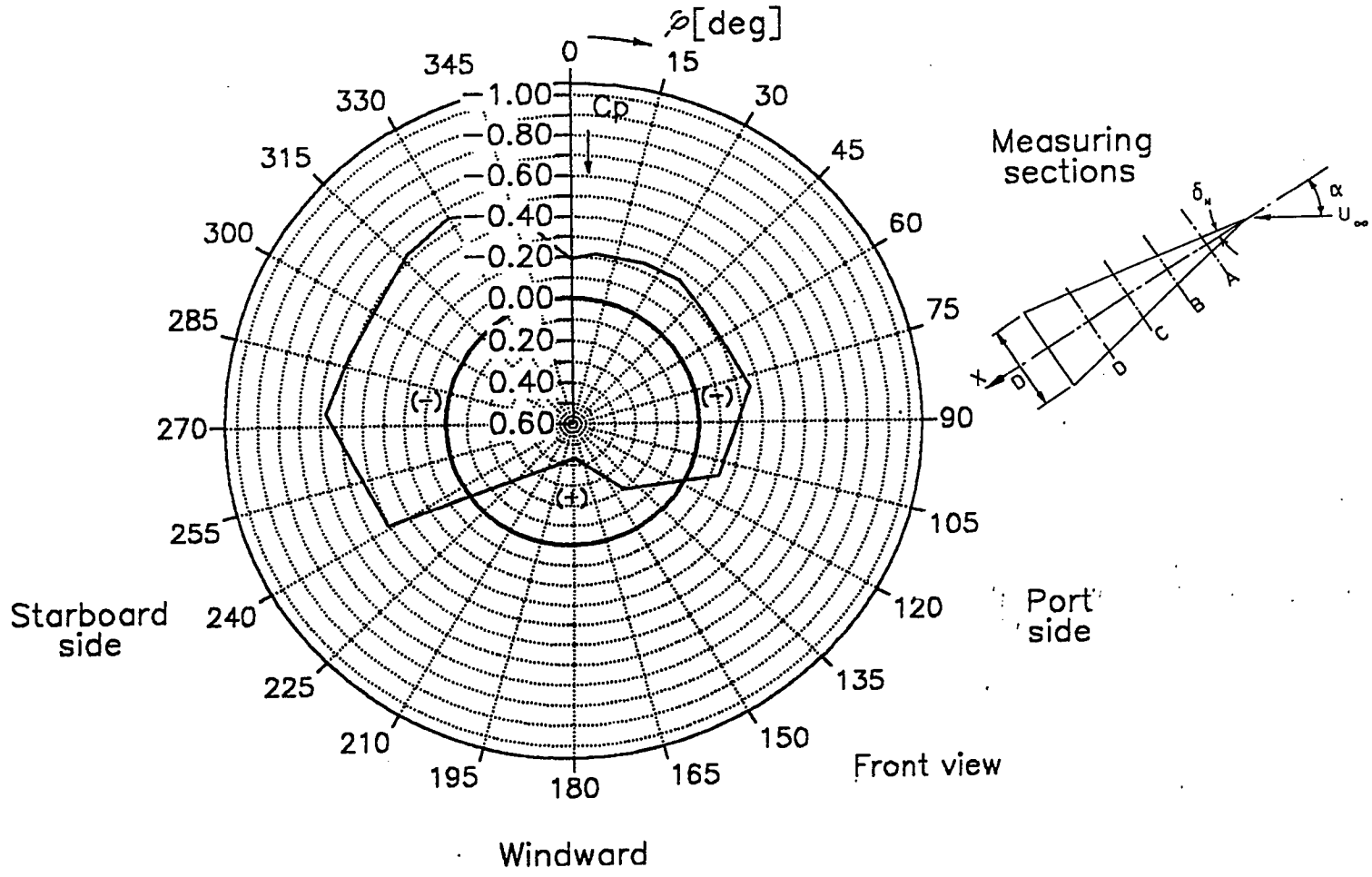

Fig. 4.14 Circumferential pressure distribution on circular cone δ_N=8 deg, without fin, Re_D = 142,000, α=25 deg, section A

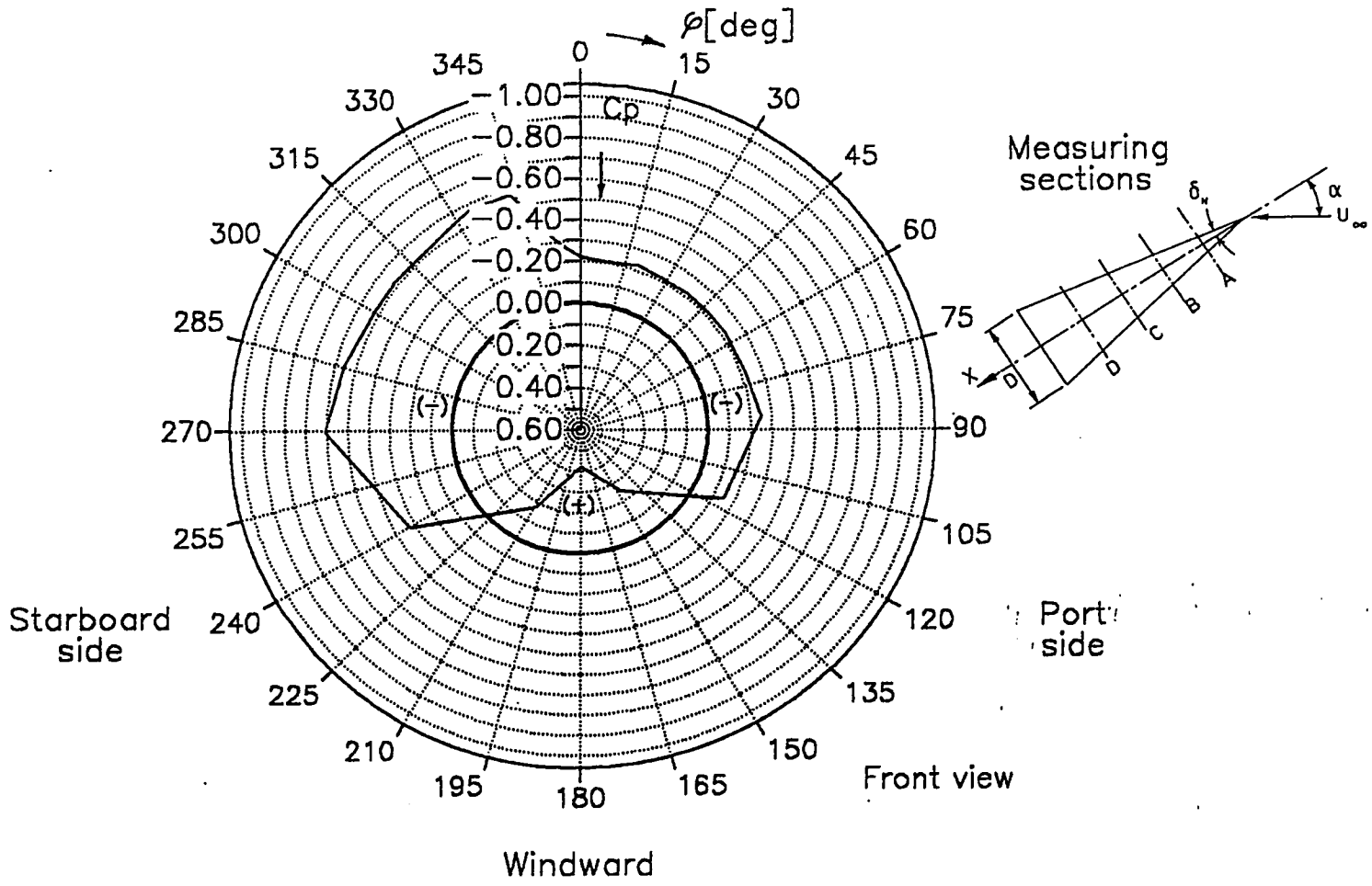

Fig. 4.15 Circumferential pressure distribution on circular cone $\delta_N = 8$ deg, without fin, $Re_D = 142{,}000$, $\alpha = 25$ deg, section B

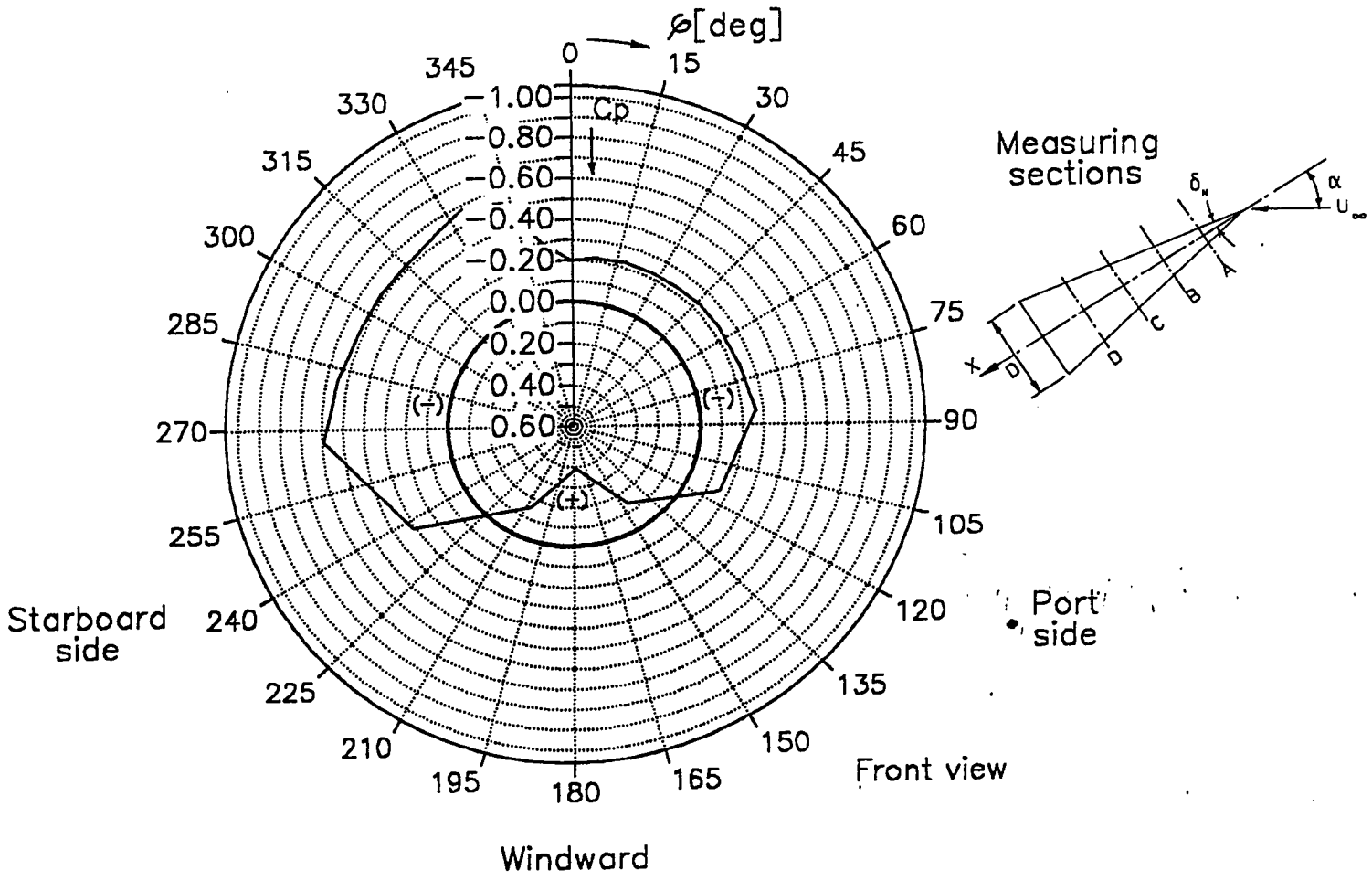

Fig. 4.16 Circumferential pressure distribution on circular cone δ_N=8 deg, without fin, Re_D = 142,000, α=25 deg, section C

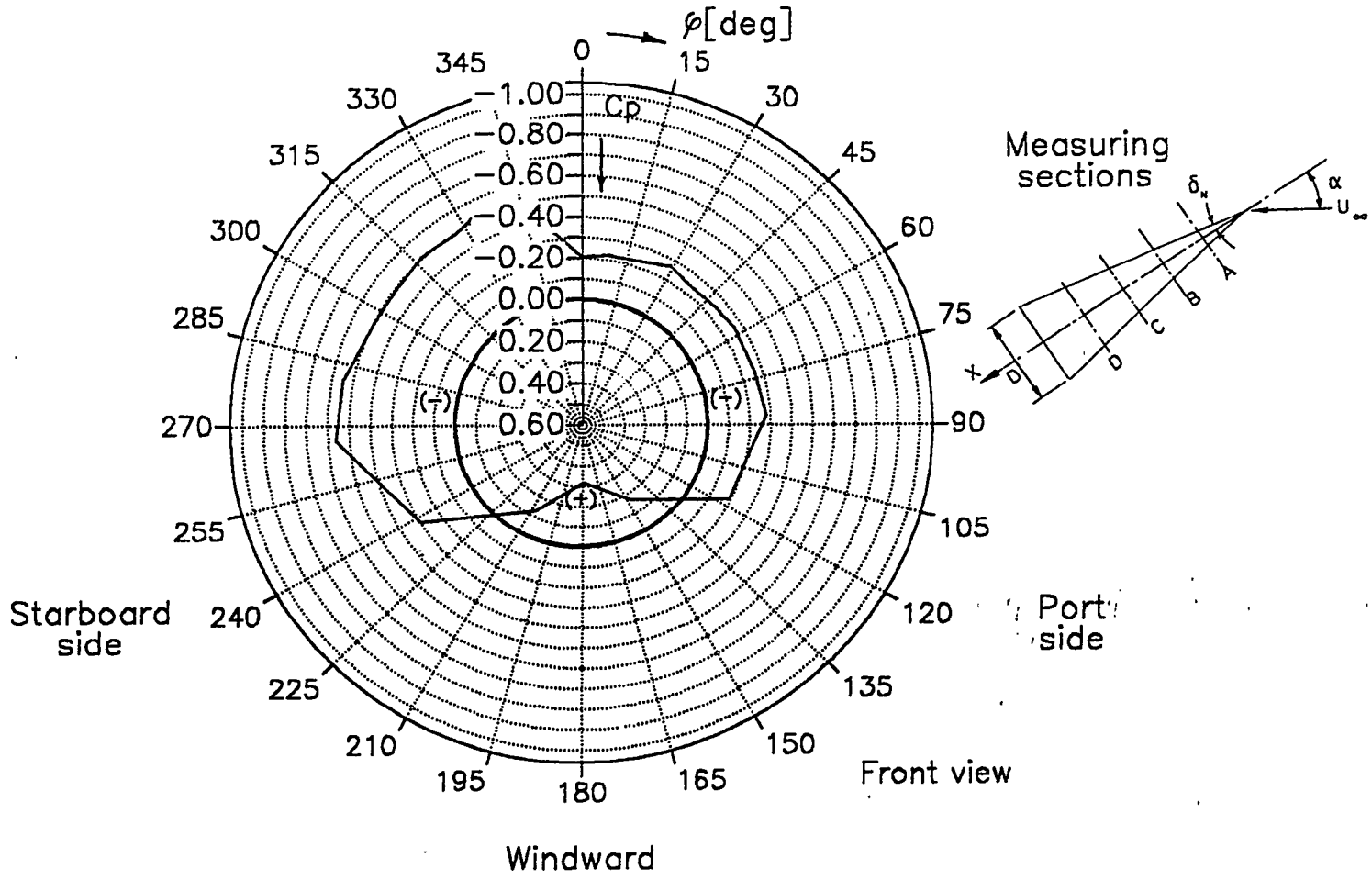

Fig. 4.17 Circumferential pressure distribution on circular cone δ_N=8 deg, without fin, Re_D = 142,000, α=25 deg, section D

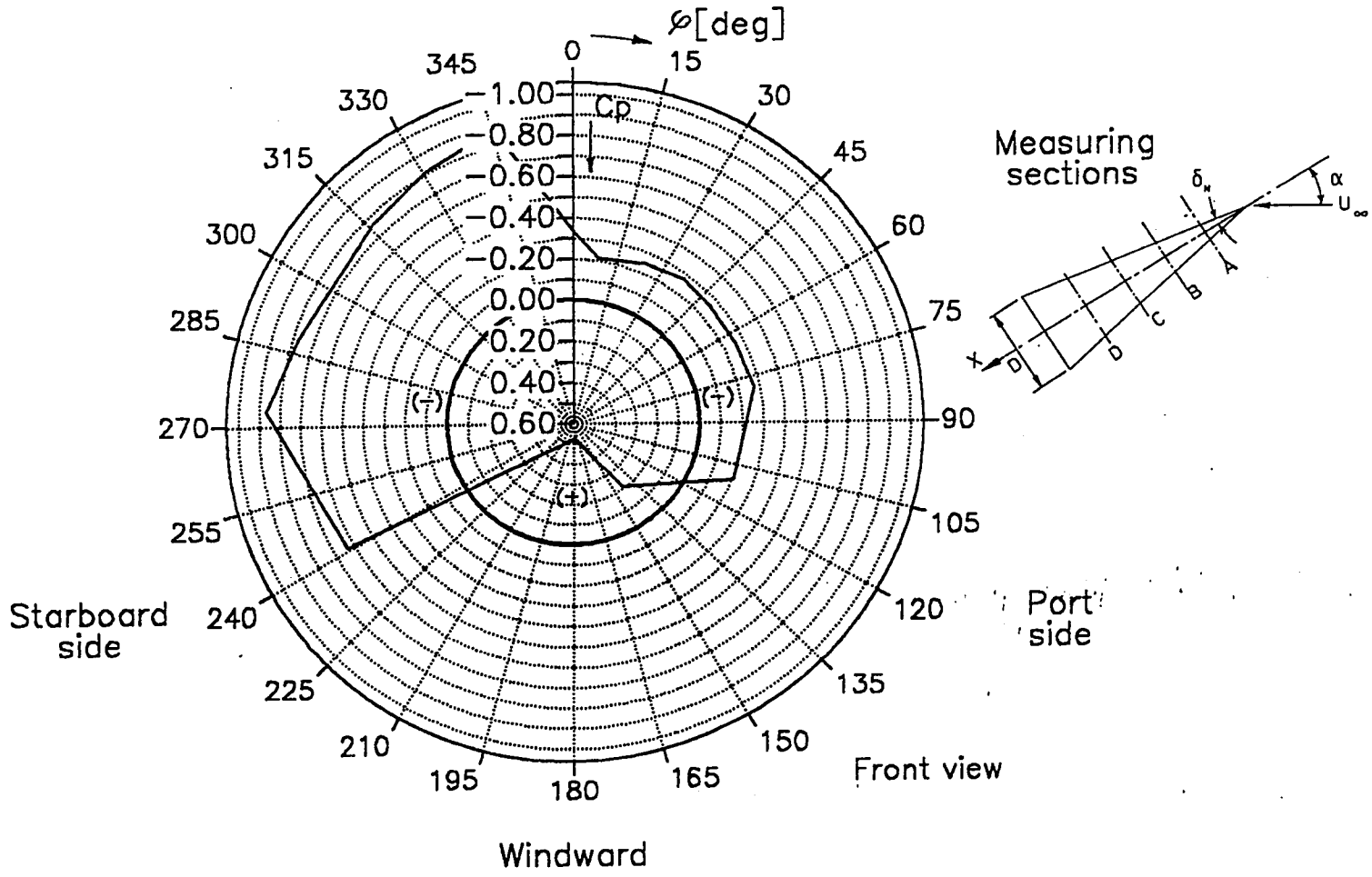

Fig. 4.18 Circumferential pressure distribution on circular cone δ_N=8 deg, without fin, Re_D = 142,000, α=30 deg, section A

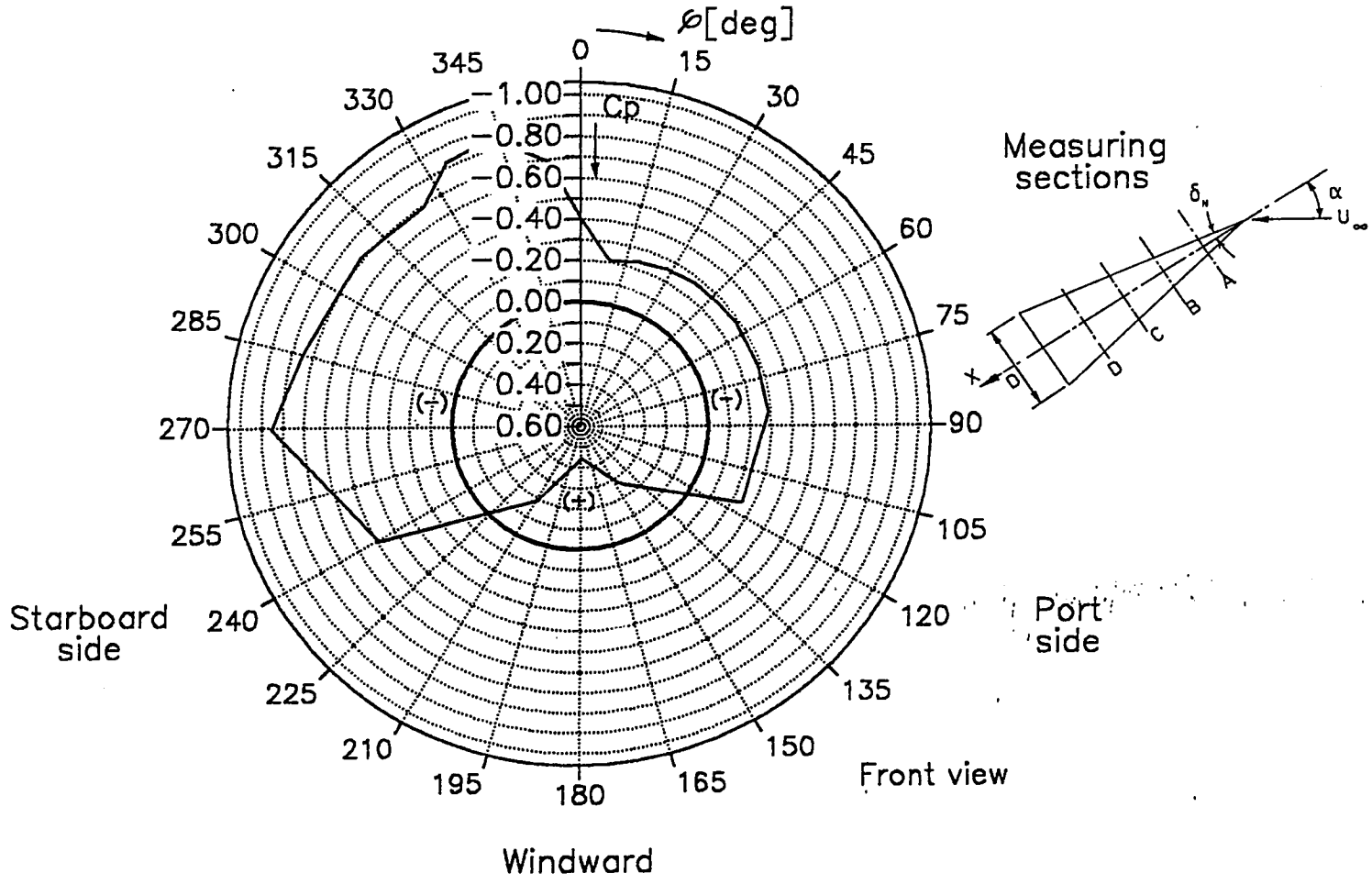

Fig. 4.19 Circumferential pressure distribution on circular cone δ_N=8 deg, without fin, Re_D = 142,000, α=30 deg, section B

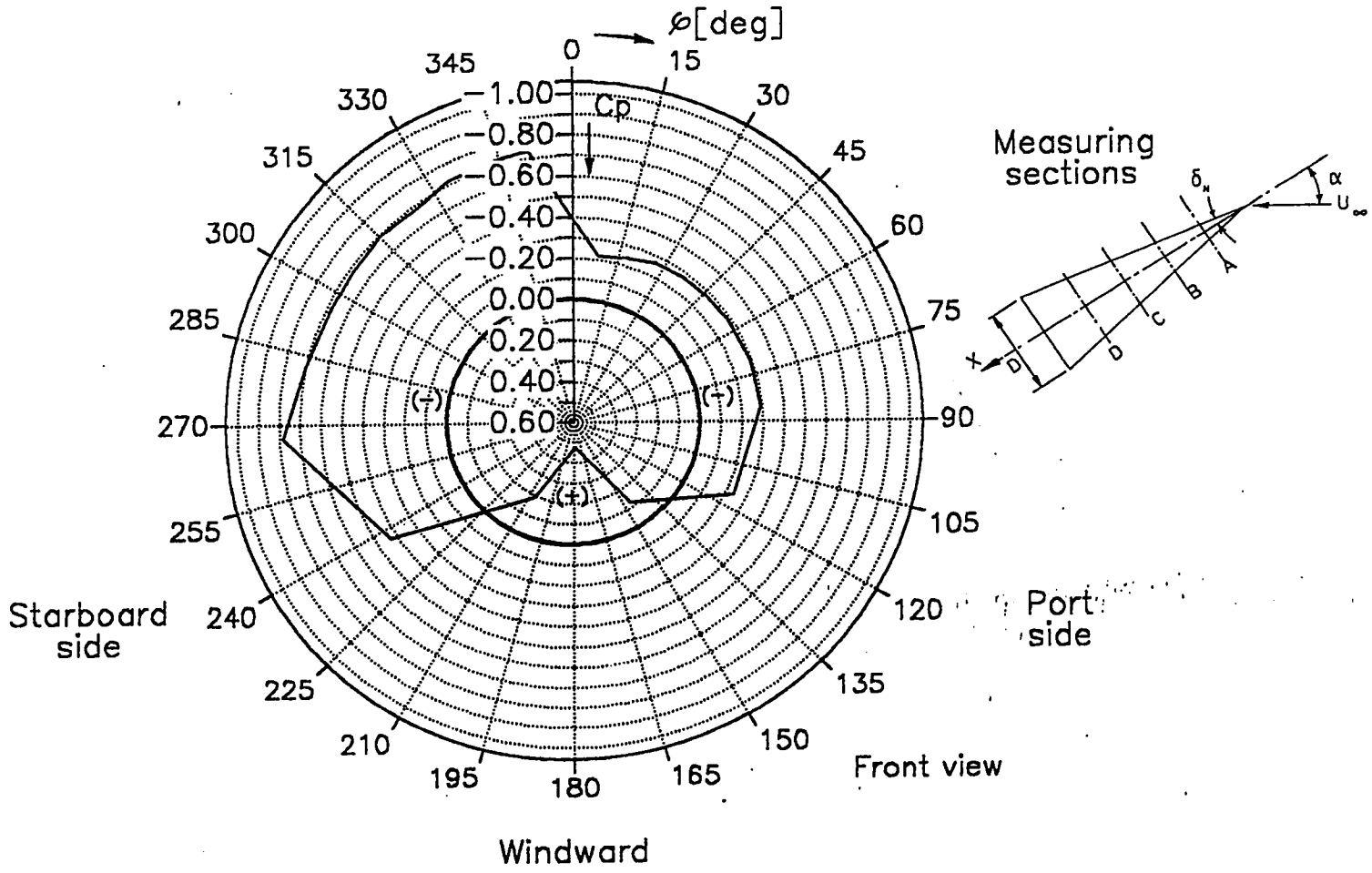

Fig. 4.20 Circumferential pressure distribution on circular cone δ_N=8 deg, without fin, Re_D = 142,000, α=30 deg, section C

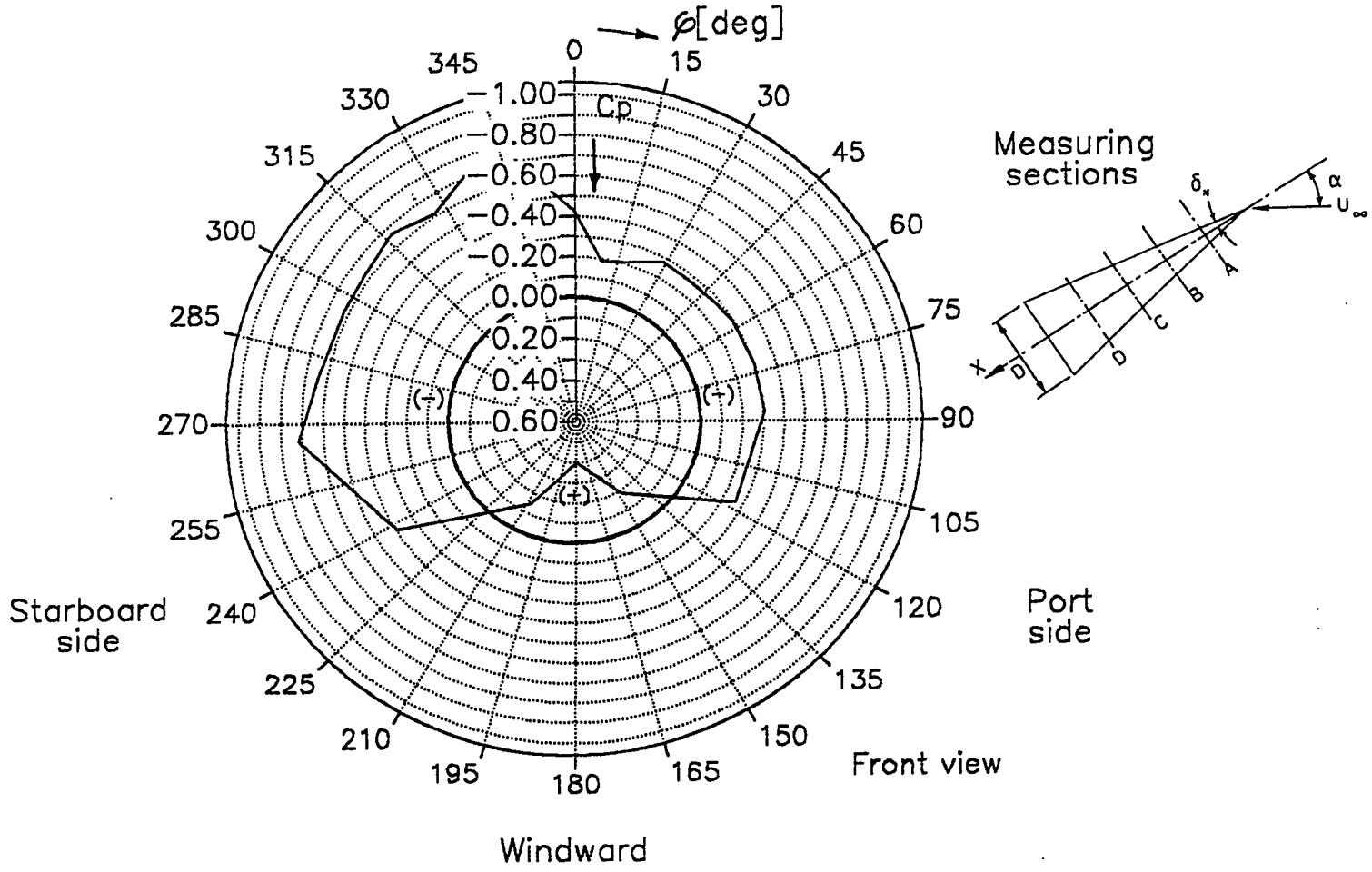

Fig. 4.21 Circumferential pressure distribution on circular cone δ_N=8 deg, without fin, Re_D = 142,000, α=30 deg, section D

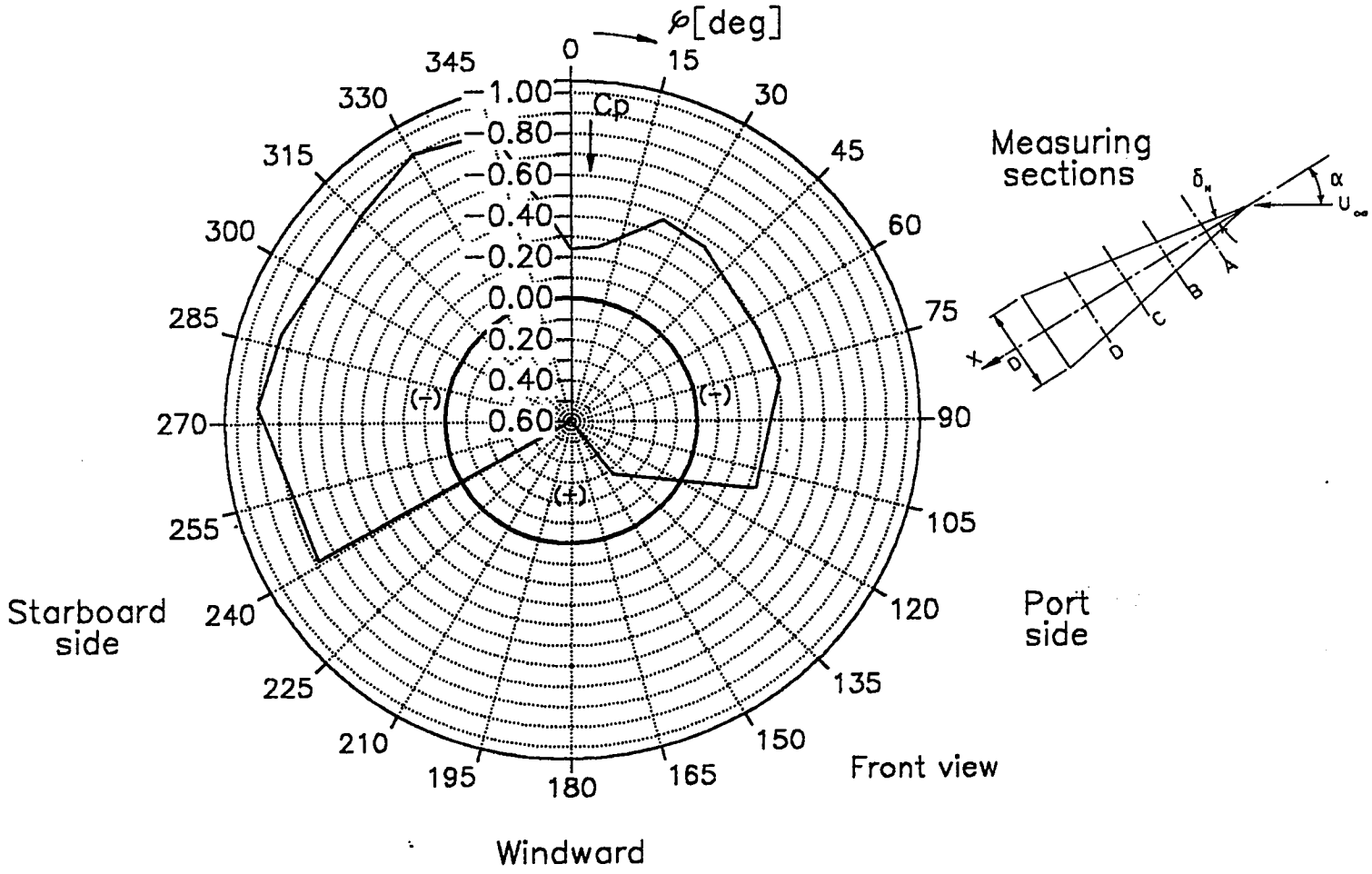

Fig. 4.22 Circumferential pressure distribution on circular cone δ_N=8 deg, without fin, Re_D = 142,000, α=35 deg, section A

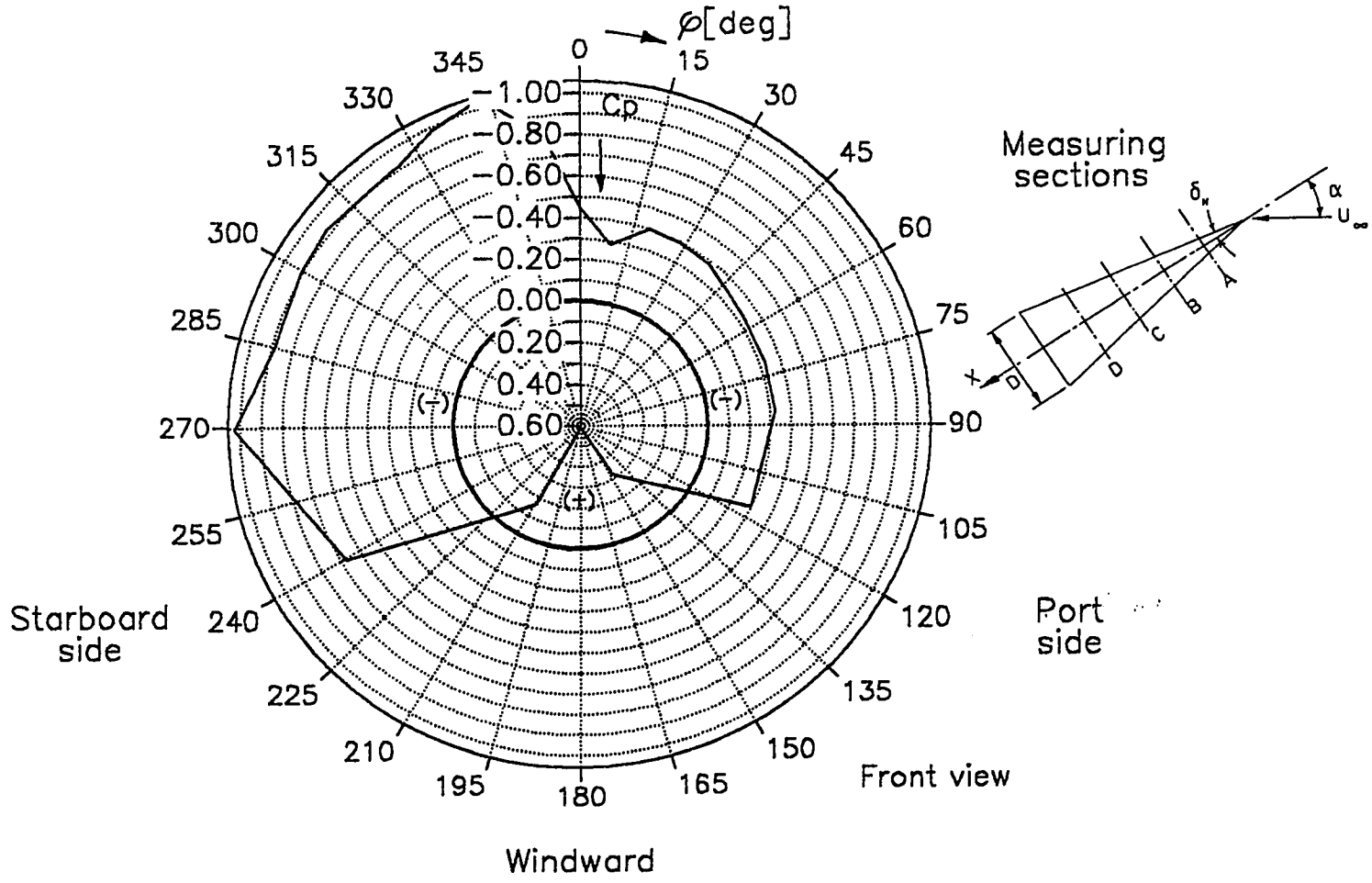

Fig. 4.23 Circumferential pressure distribution on circular cone δ_N=8 deg, without fin, Re_D = 142,000, α=35 deg, section B

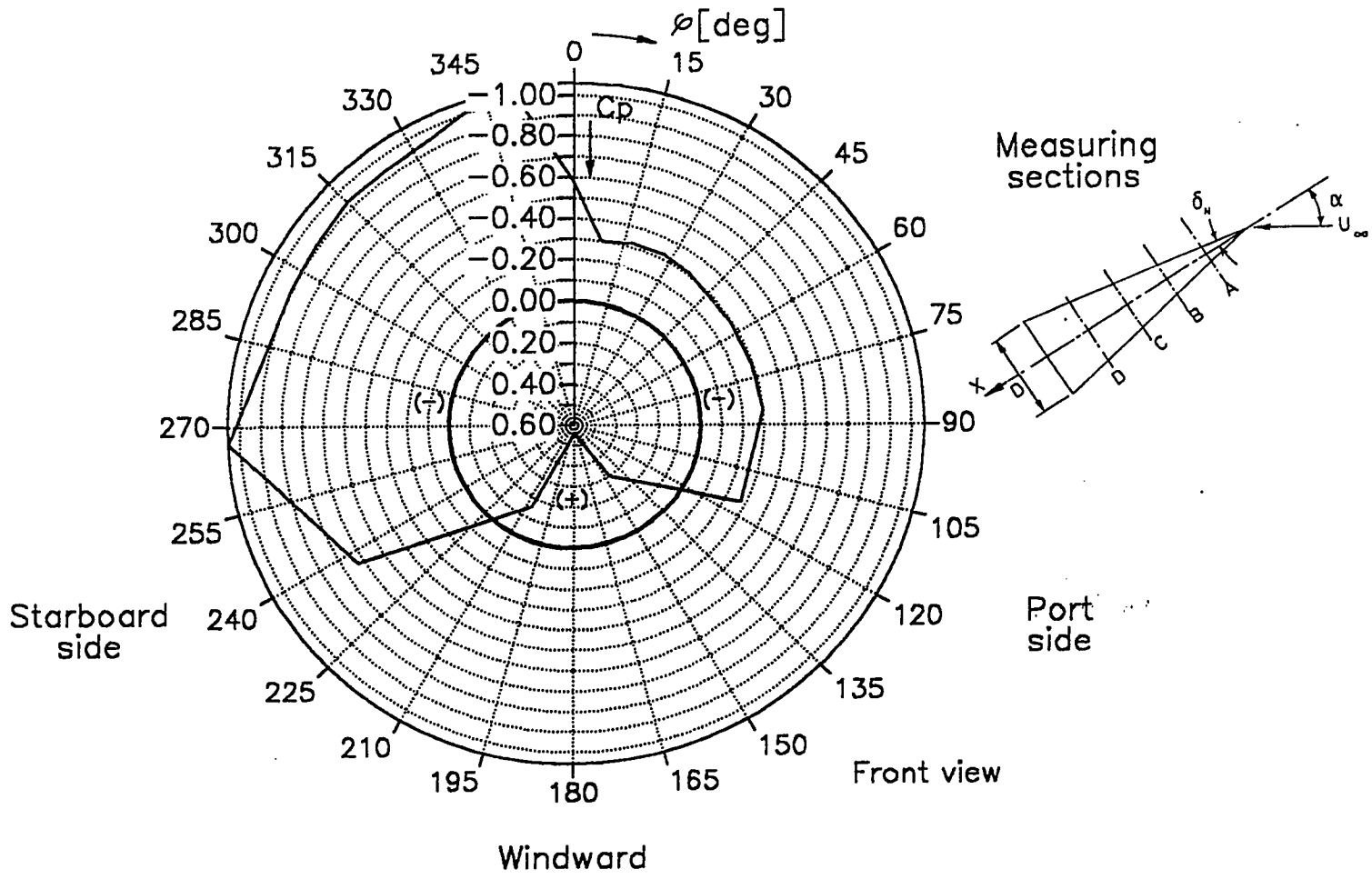

Fig. 4.24 Circumferential pressure distribution on circular cone $\delta_N = 8$ deg, without fin, $Re_D = 142{,}000$, $\alpha = 35$ deg, section C

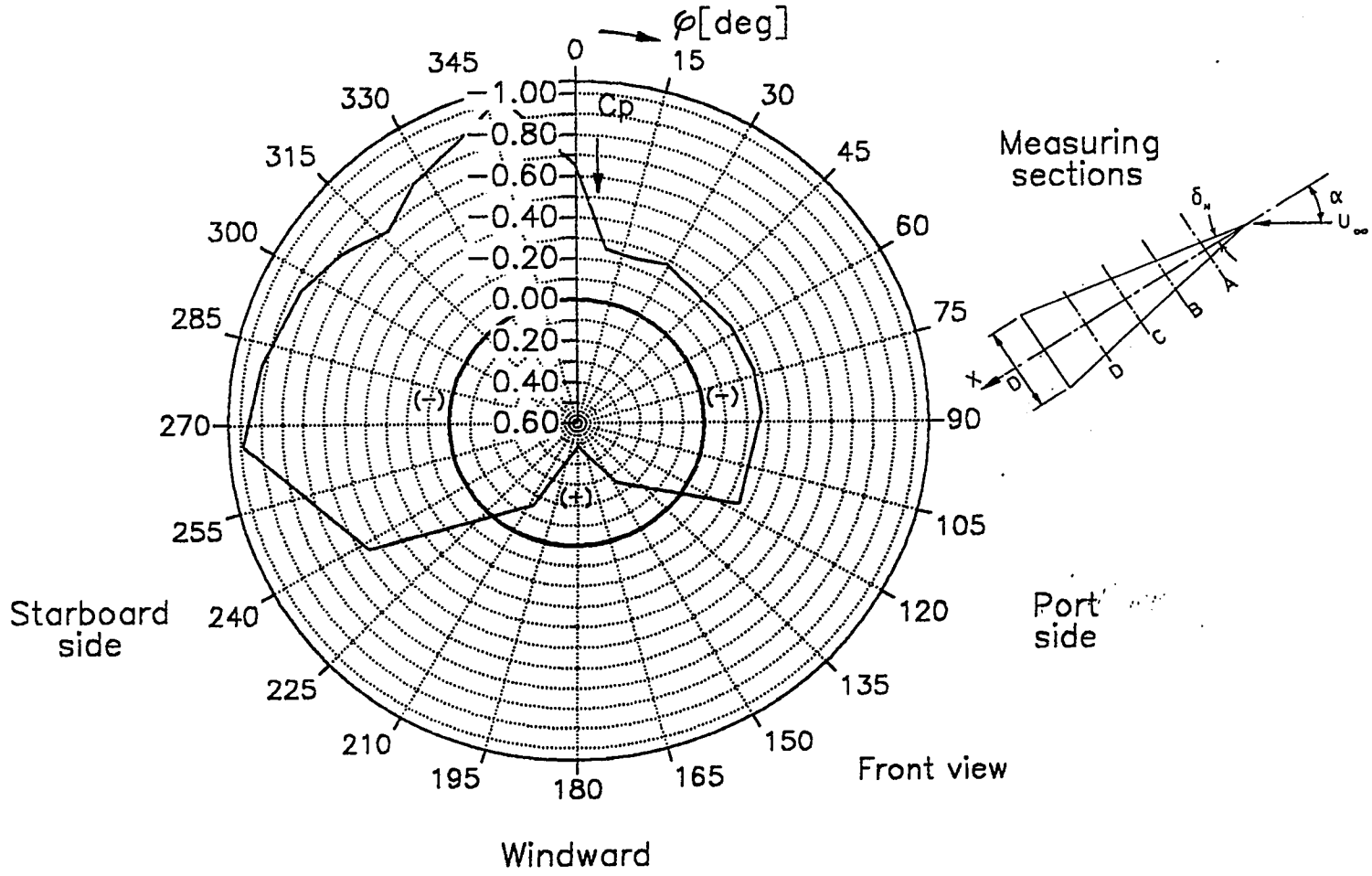

Fig. 4.25 Circumferential pressure distribution on circular cone δ_N=8 deg, without fin, Re_D = 142,000, α=35 deg, section D

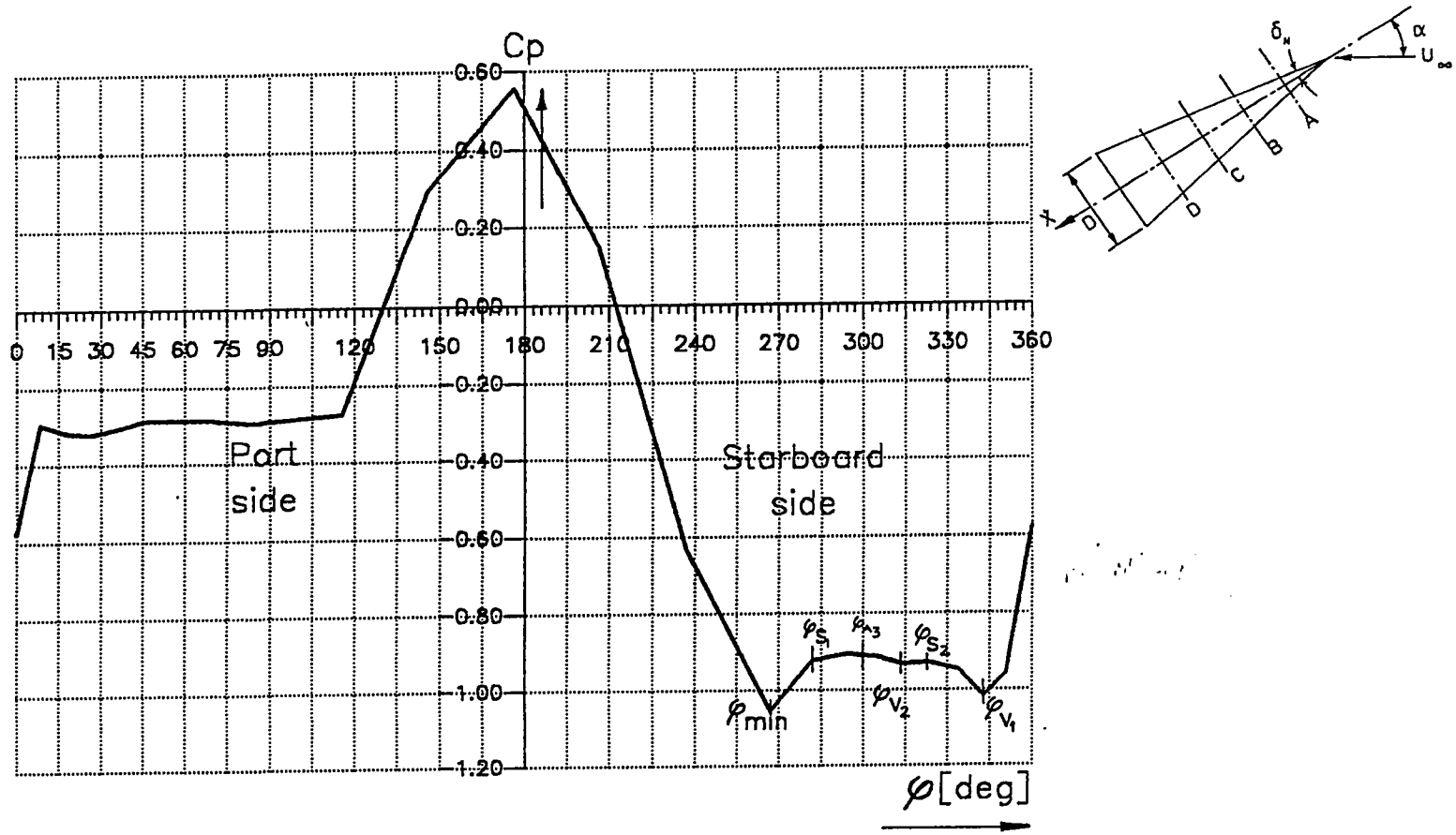

Fig. 4.26 Typical circumferential pressure distribution on circular cone $\delta_N = 8$ deg without fin at $\alpha = 35$ deg $Re_D = 142{,}000$, section C

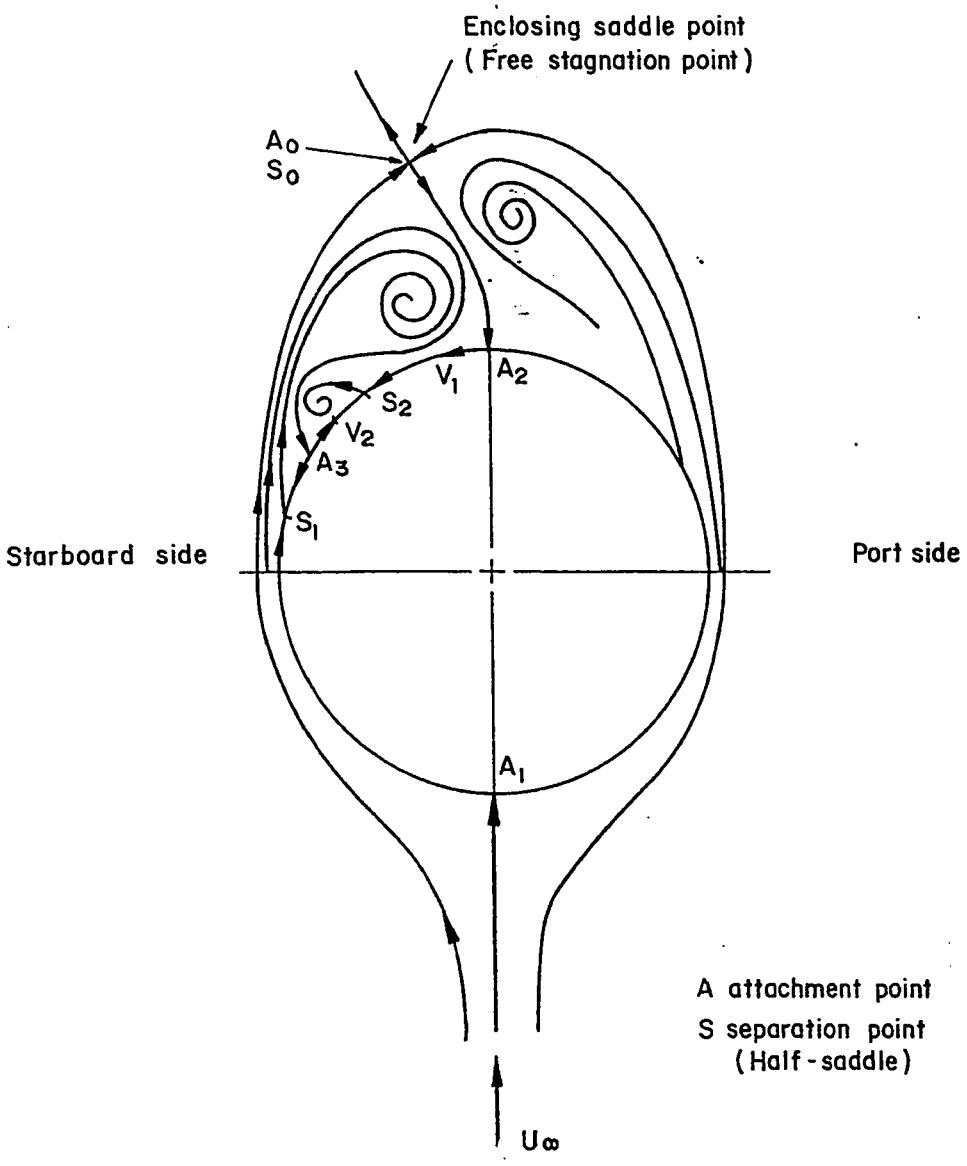

Fig. 4.27 Schematic of leeward vortex-flow on starboard side of circular cone corresponding to pressure distribution at $\alpha = 35$ deg, section C

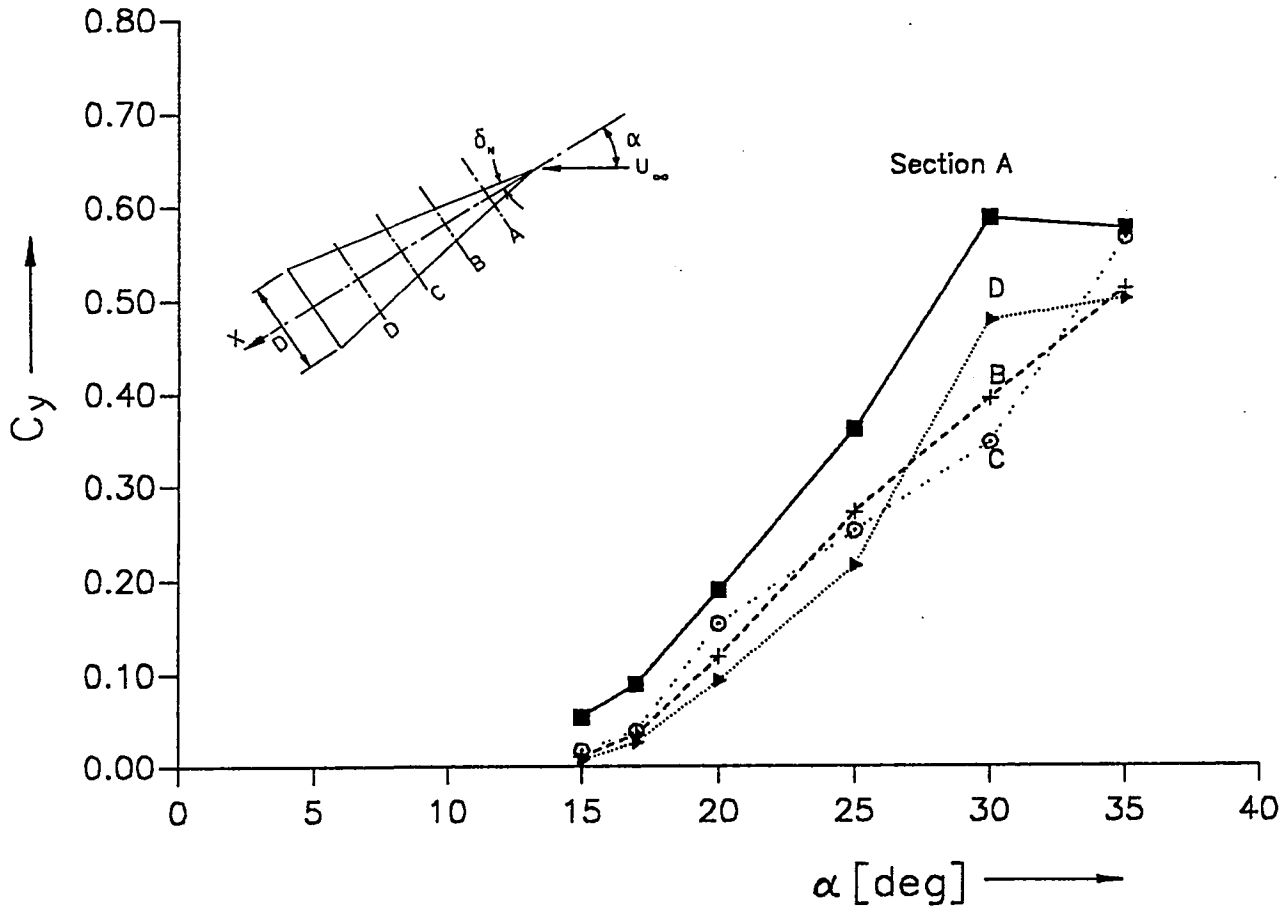

Fig. 4.28 Sectional side-force vs. angle of attack for circular cone without fin at four axial sections, Re_D = 142,000, δ_N = 8 deg

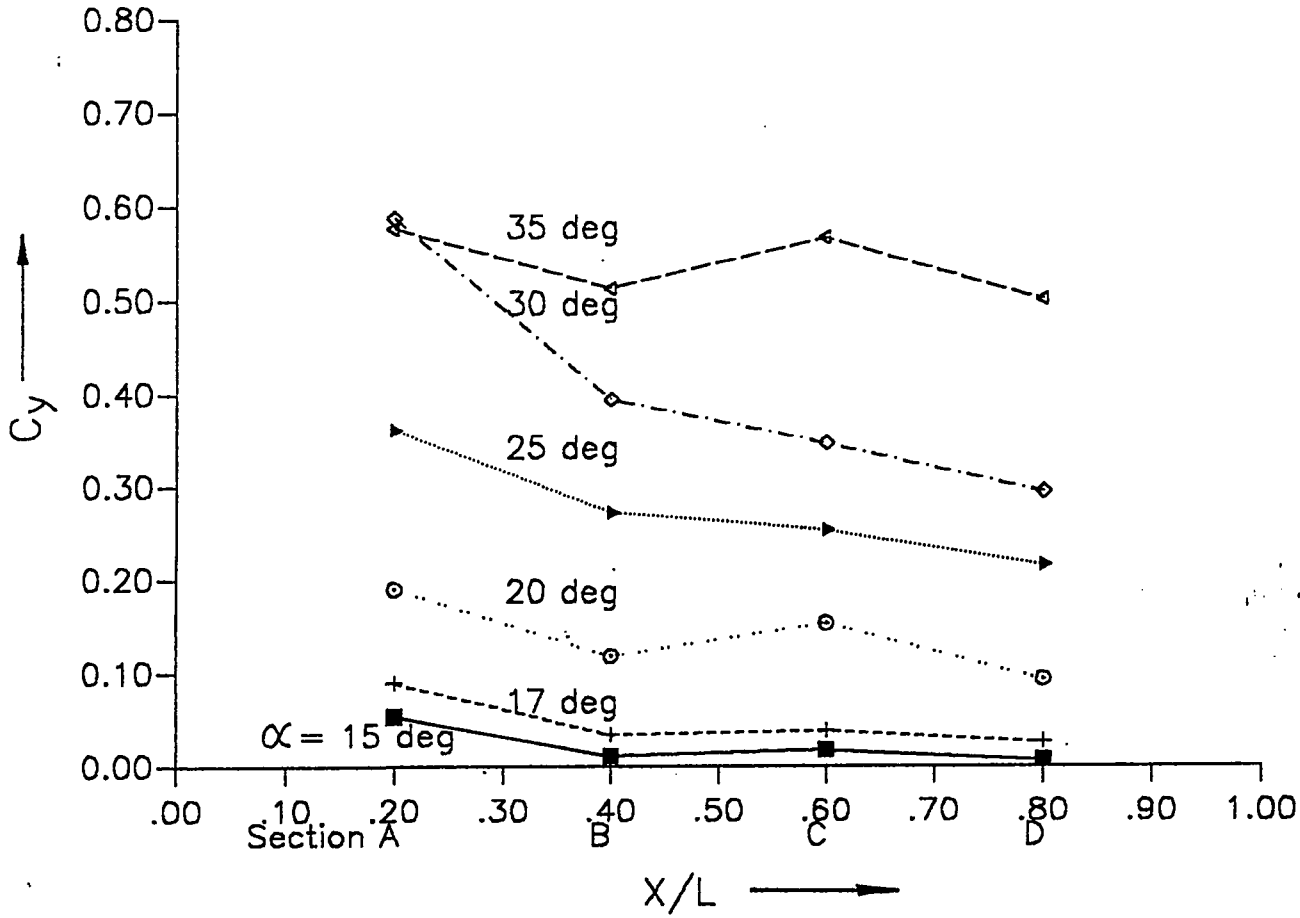

Fig. 4.29 Sectional side-force vs. length for circular cone without fin at various angles of attack, $Re_D = 142{,}000$, $\delta_N = 8$ deg

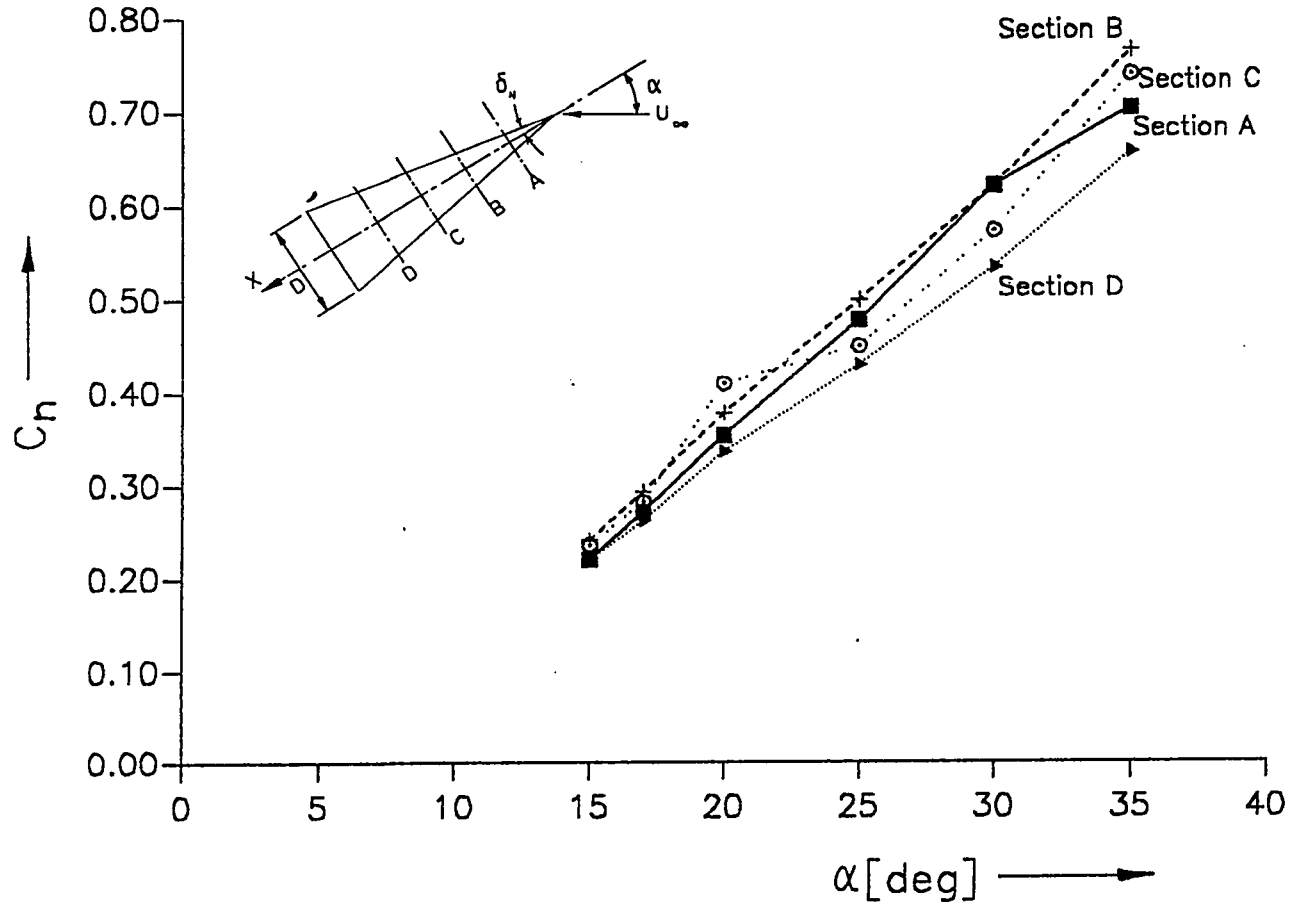

Fig. 4.30 Sectional normal-force vs. angle of attack for circular cone without fin at four axial sections, Re_D = 142,000, δ_N = 8 deg

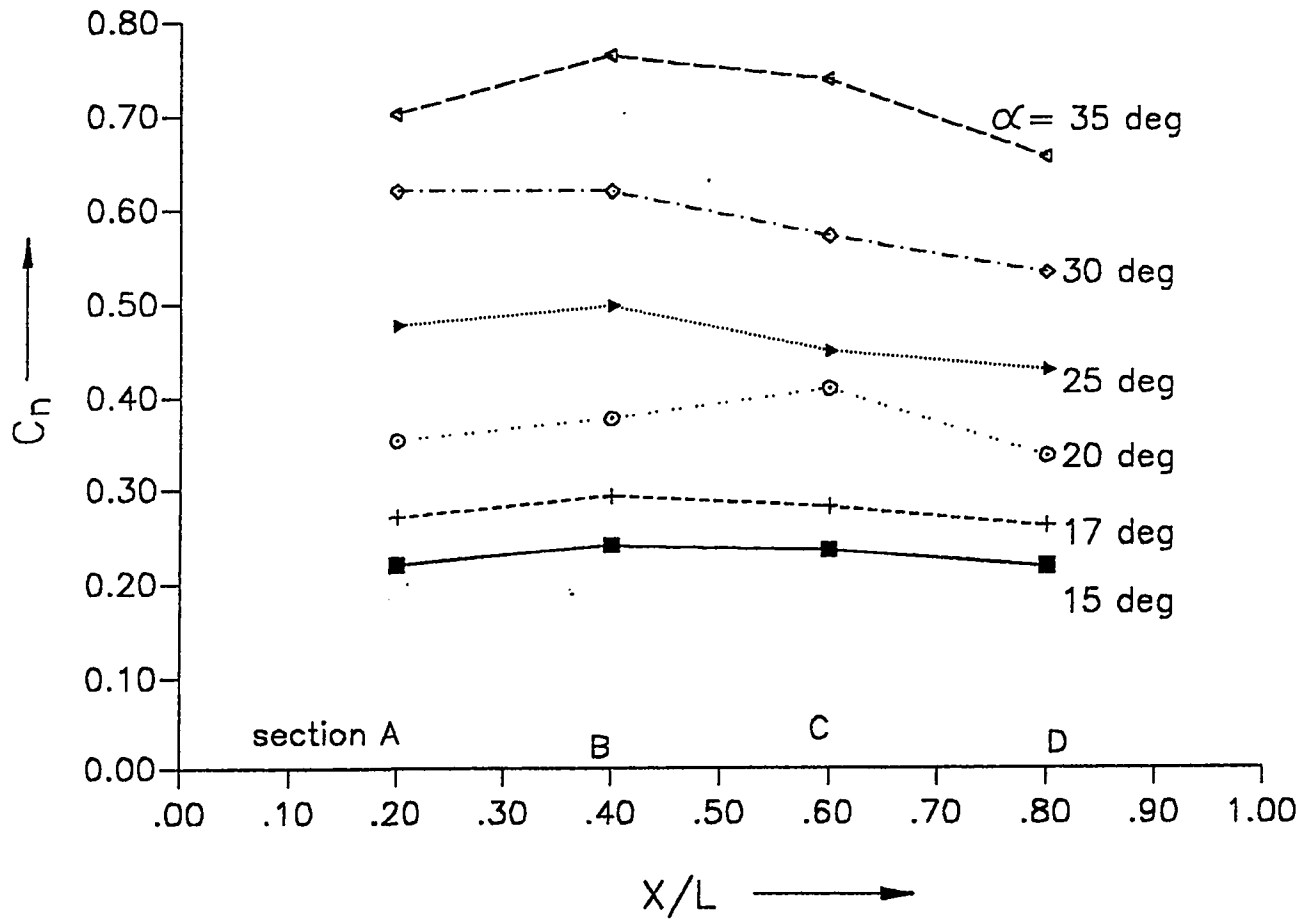

Fig. 4.31 Sectional normal-force vs. length for circular cone without fin at various angles of attack, Re_D = 142,000, δ_N = 8 deg

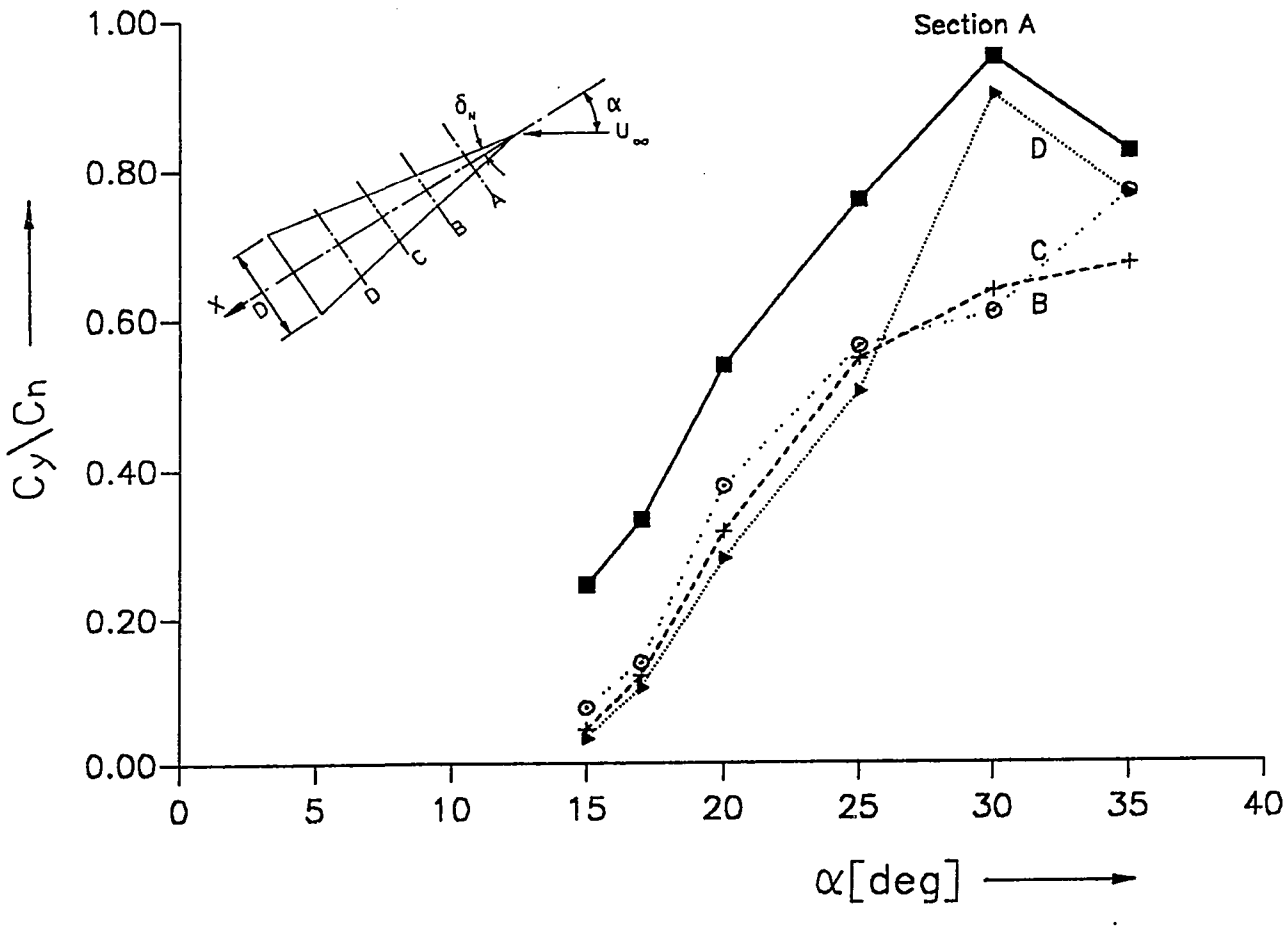

Fig. 4.32 Ratio of side force and normal force on a circular cone without fin vs. angle of attack, at various sections along the length of the cone, $Re_D = 142{,}000$, $\delta_N = 8$ deg

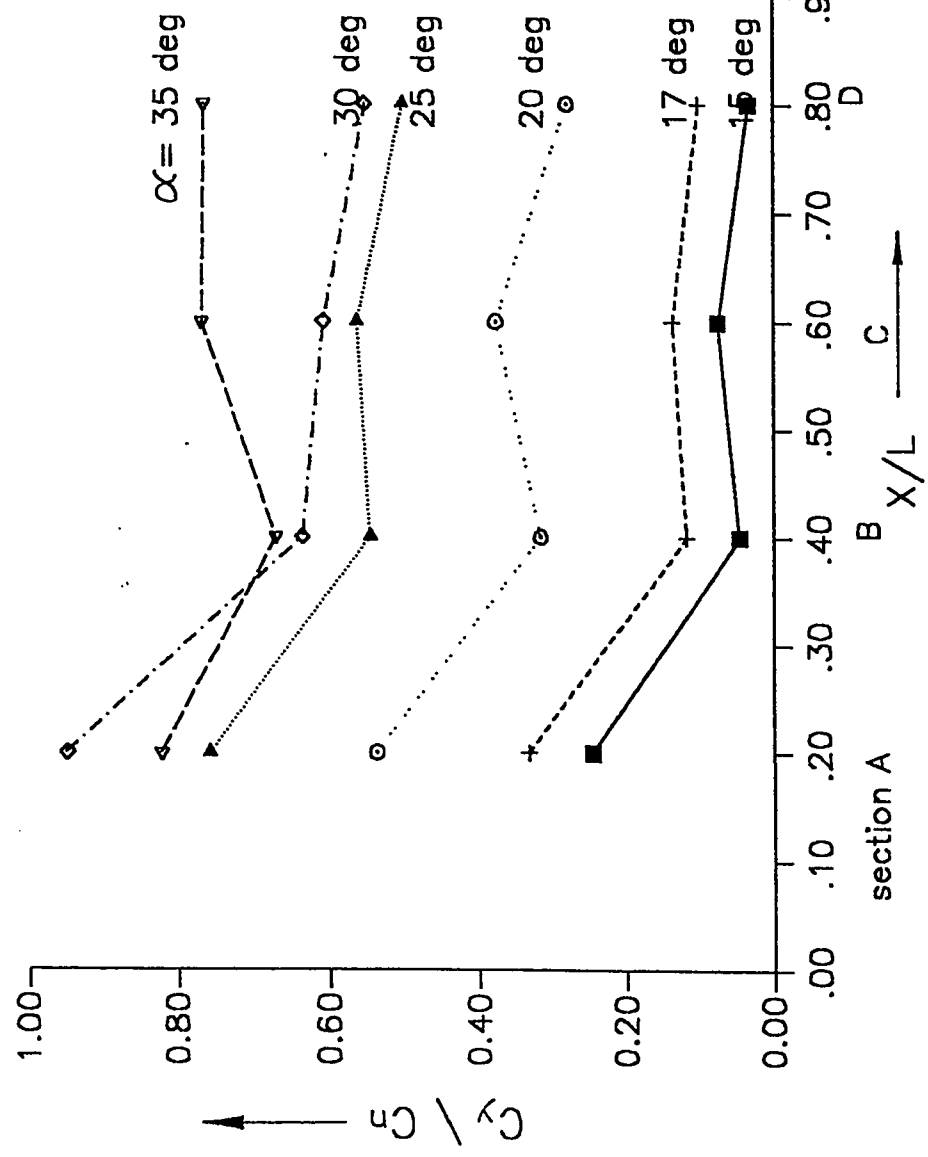

Fig. 4.33 Ratio of side force and normal force vs. length along the circular cone without fin for various angles of attack, $Re_D = 142{,}000$, $\delta_N = 8$ deg

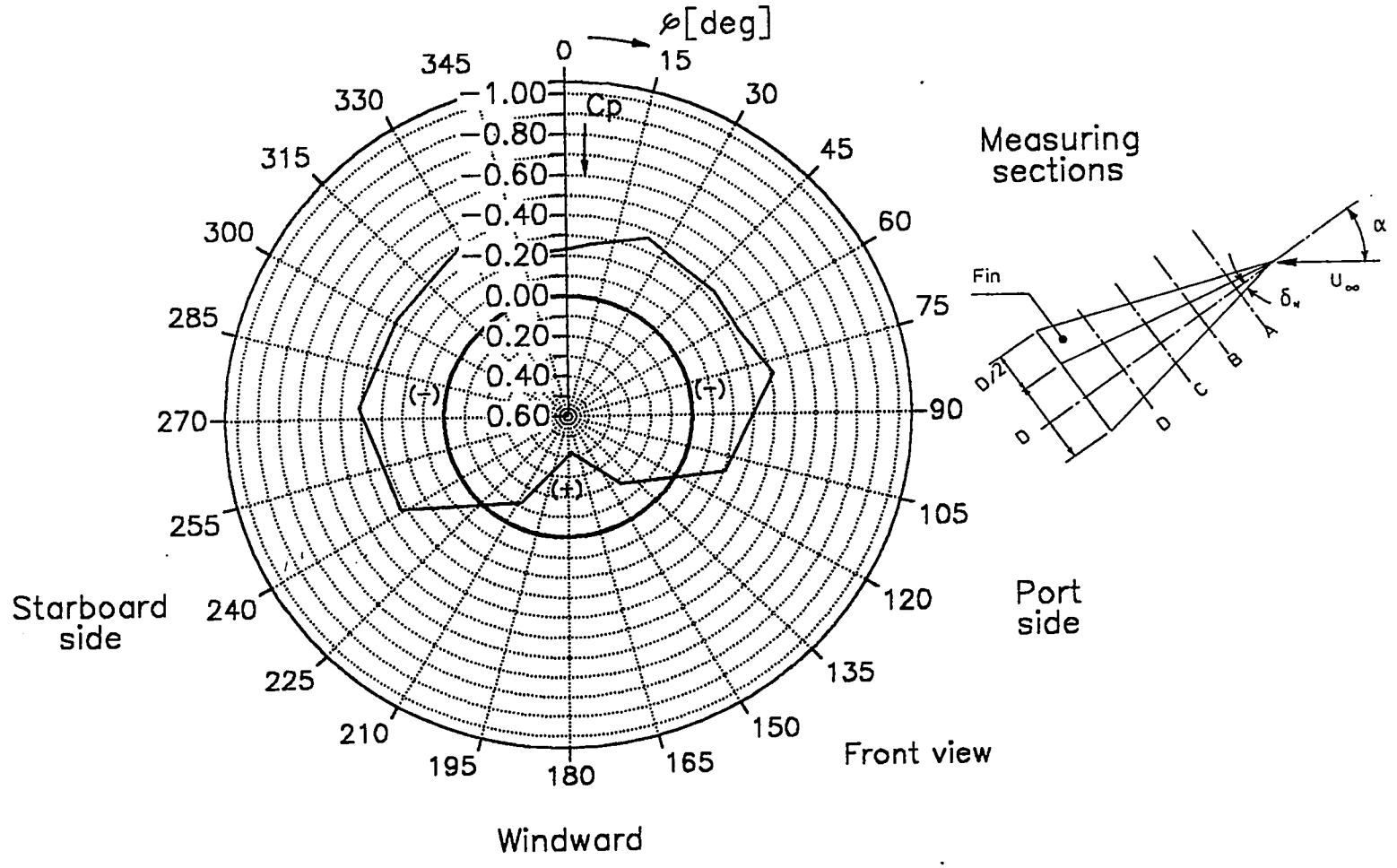

Fig. 4.34 Circumferential pressure distribution on circular cone with fin, Re_D = 142,000, δ_N=8 deg, α=25 deg, section A

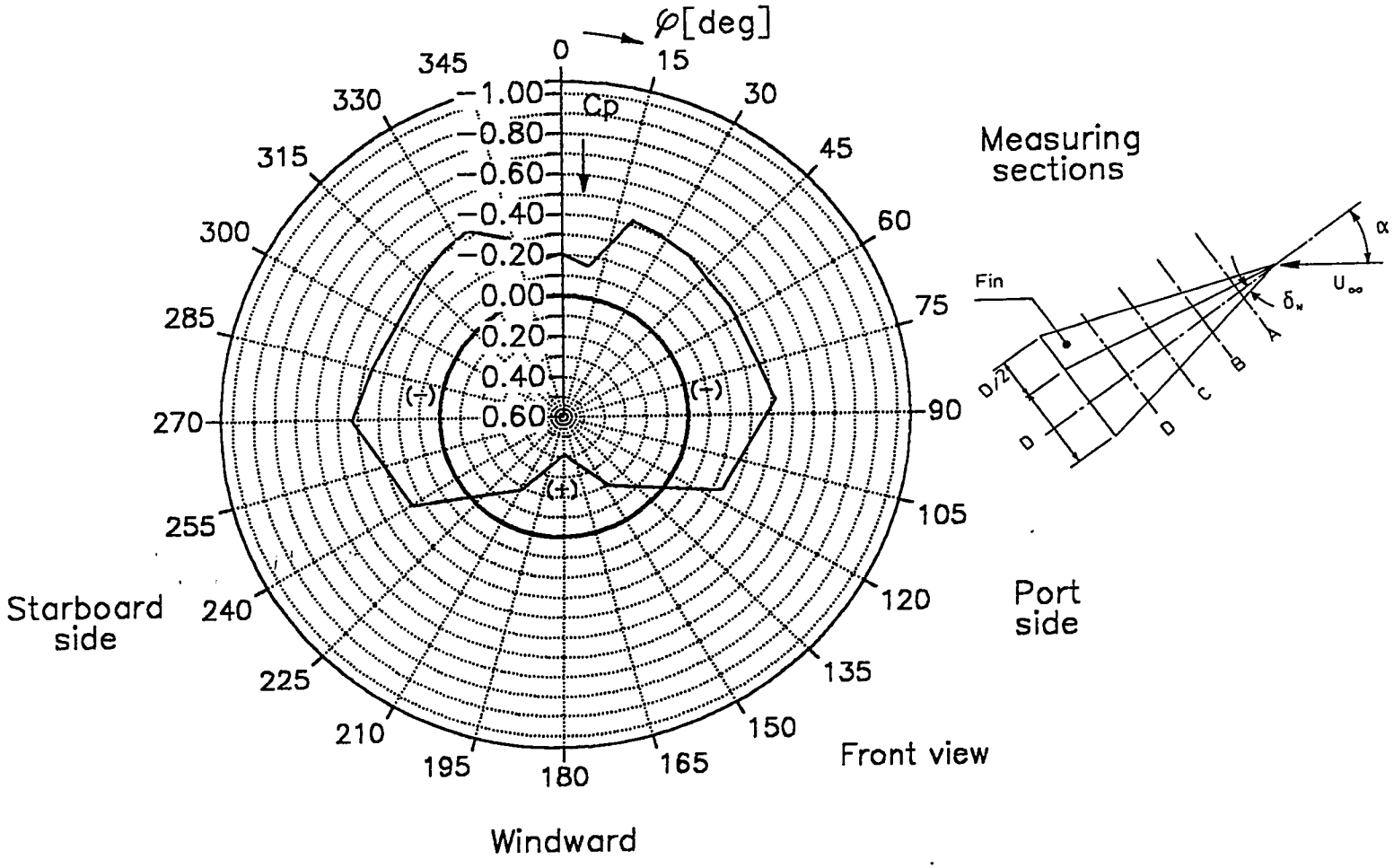

Fig. 4.35 Circumferential pressure distribution on circular cone with fin, $Re_D = 142{,}000$, $\delta_N = 8$ deg, $\alpha = 25$ deg, section B

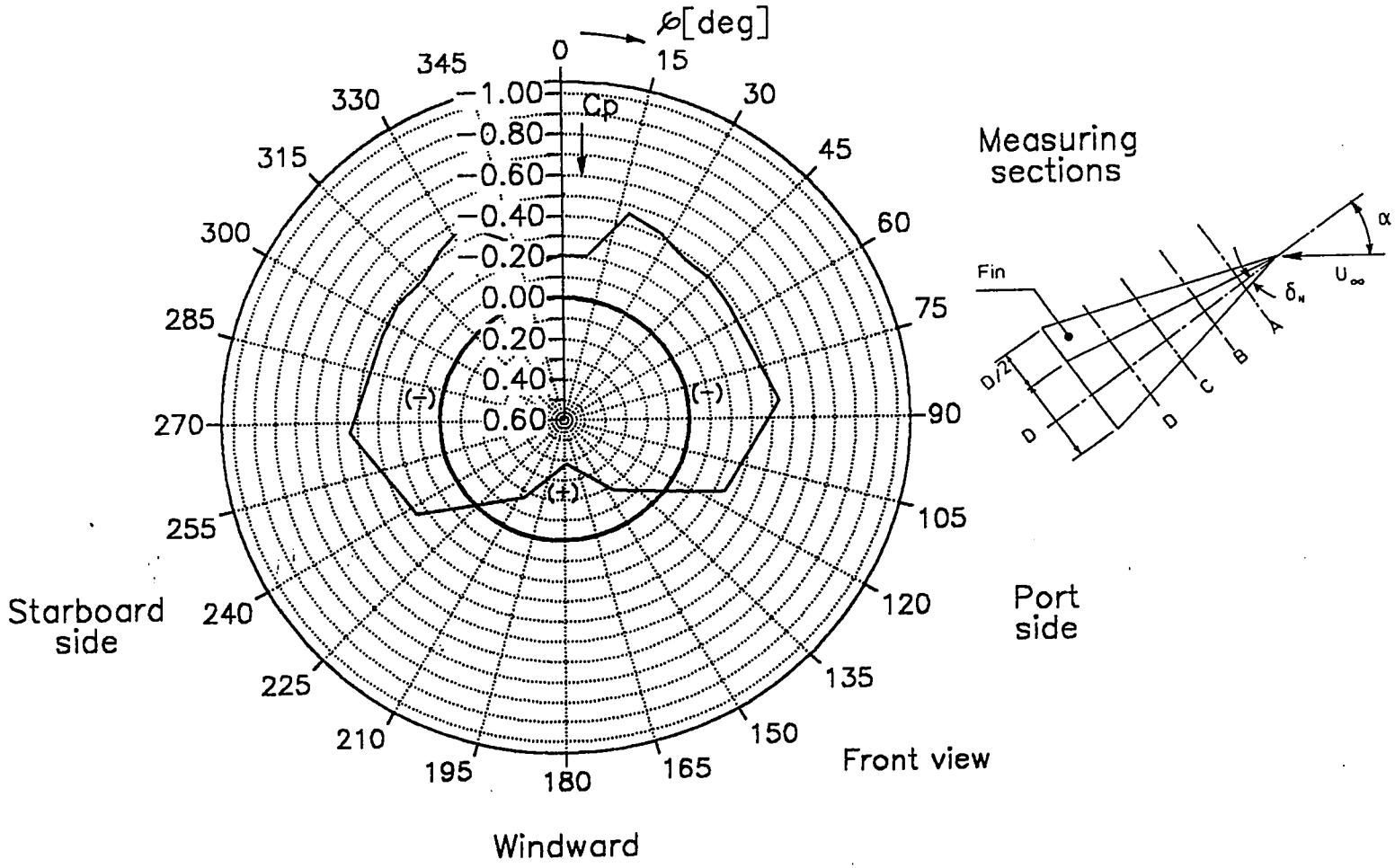

Fig. 4.36 Circumferential pressure distribution on circular cone with fin, Re_D = 142,000, δ_N=8 deg, α=25 deg, section C

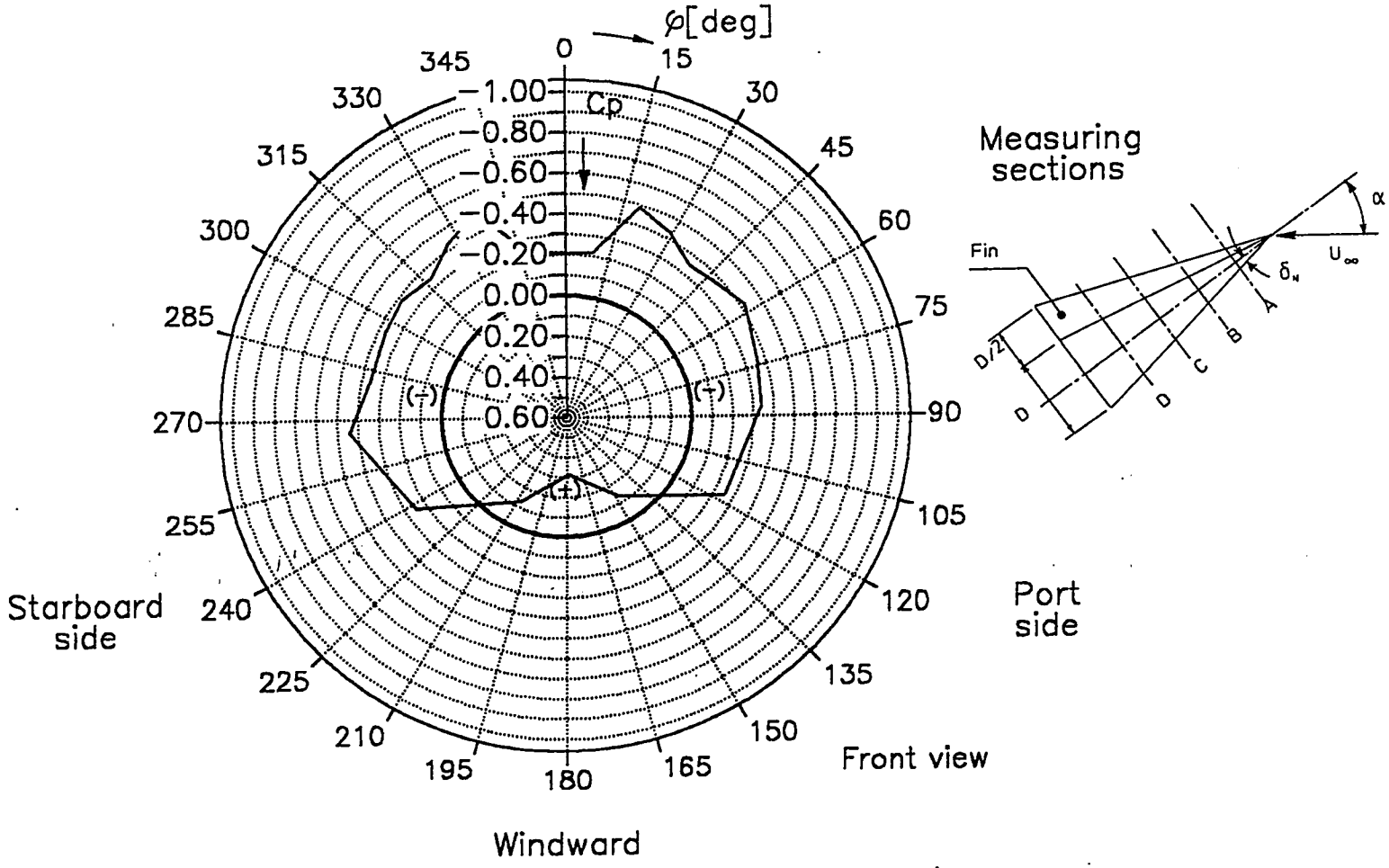

Fig. 4.37 Circumferential pressure distribution on circular cone with fin, Re_D = 142,000, δ_N=8 deg, α=25 deg, section D

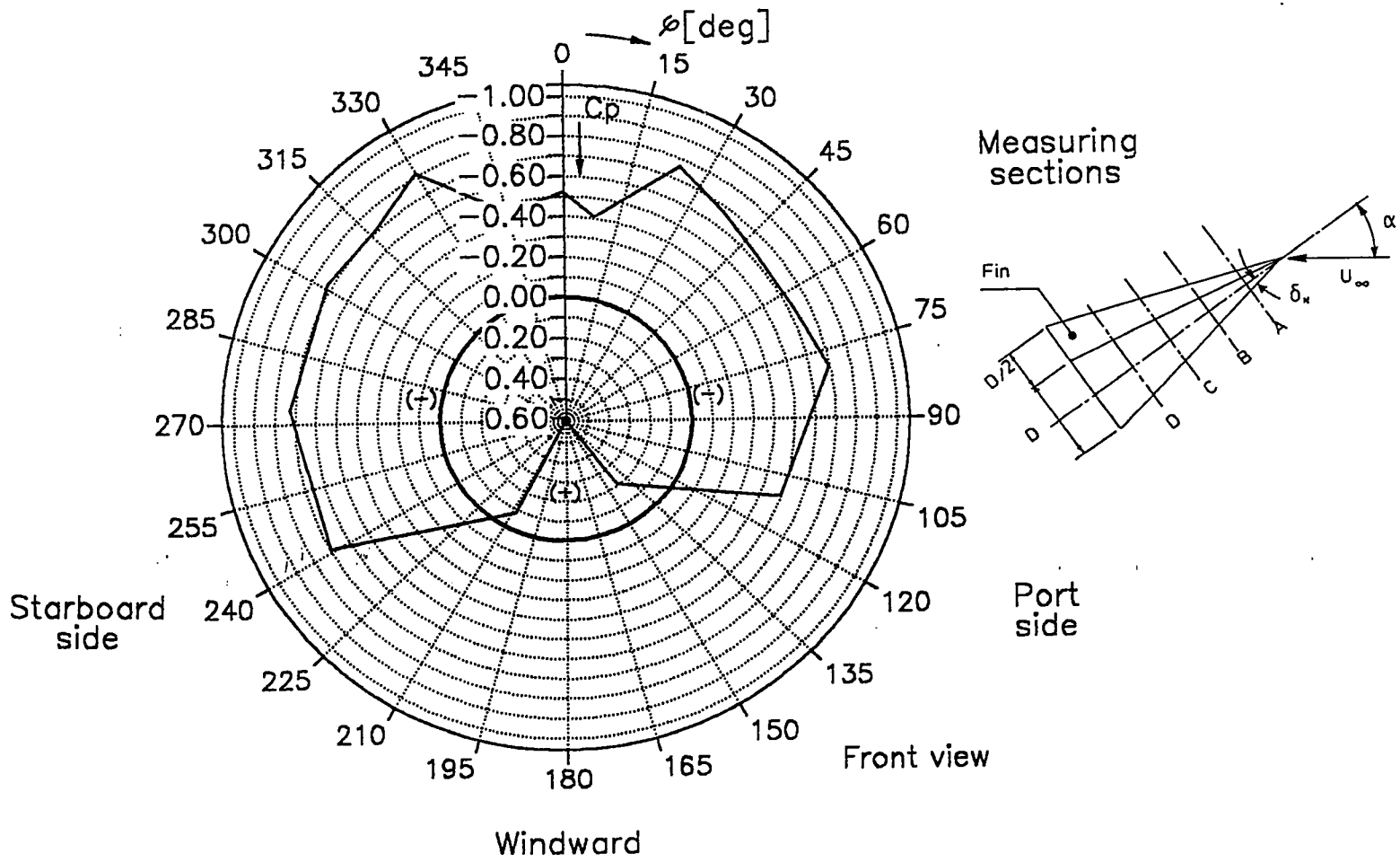

Fig. 4.38 Circumferential pressure distribution on circular cone with fin, Re_D = 142,000, δ_N=8 deg, α=35 deg, section A

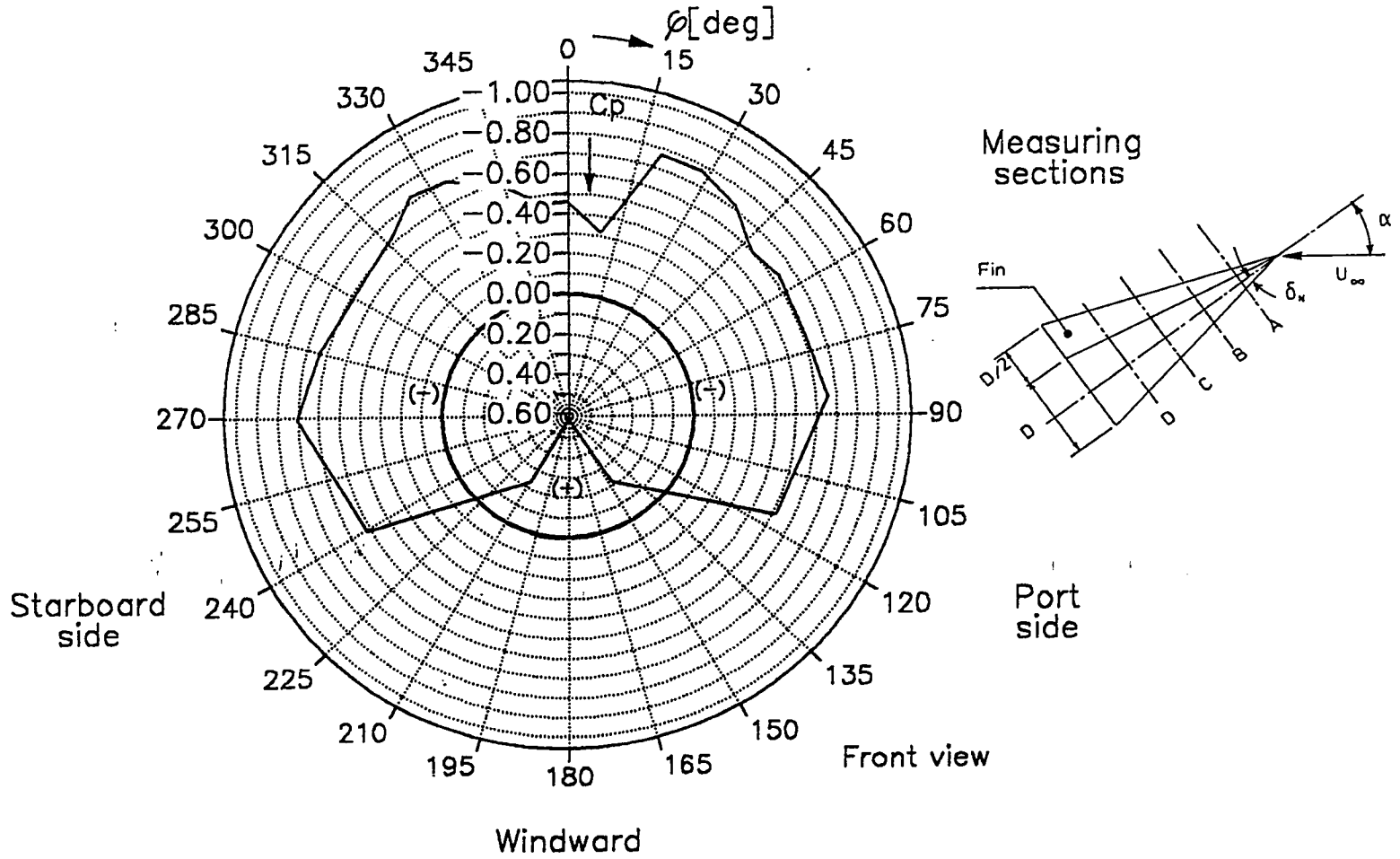

Fig. 4.39 Circumferential pressure distribution on circular cone with fin, Re_D = 142,000, δ_N = 8 deg, α = 35 deg, section B

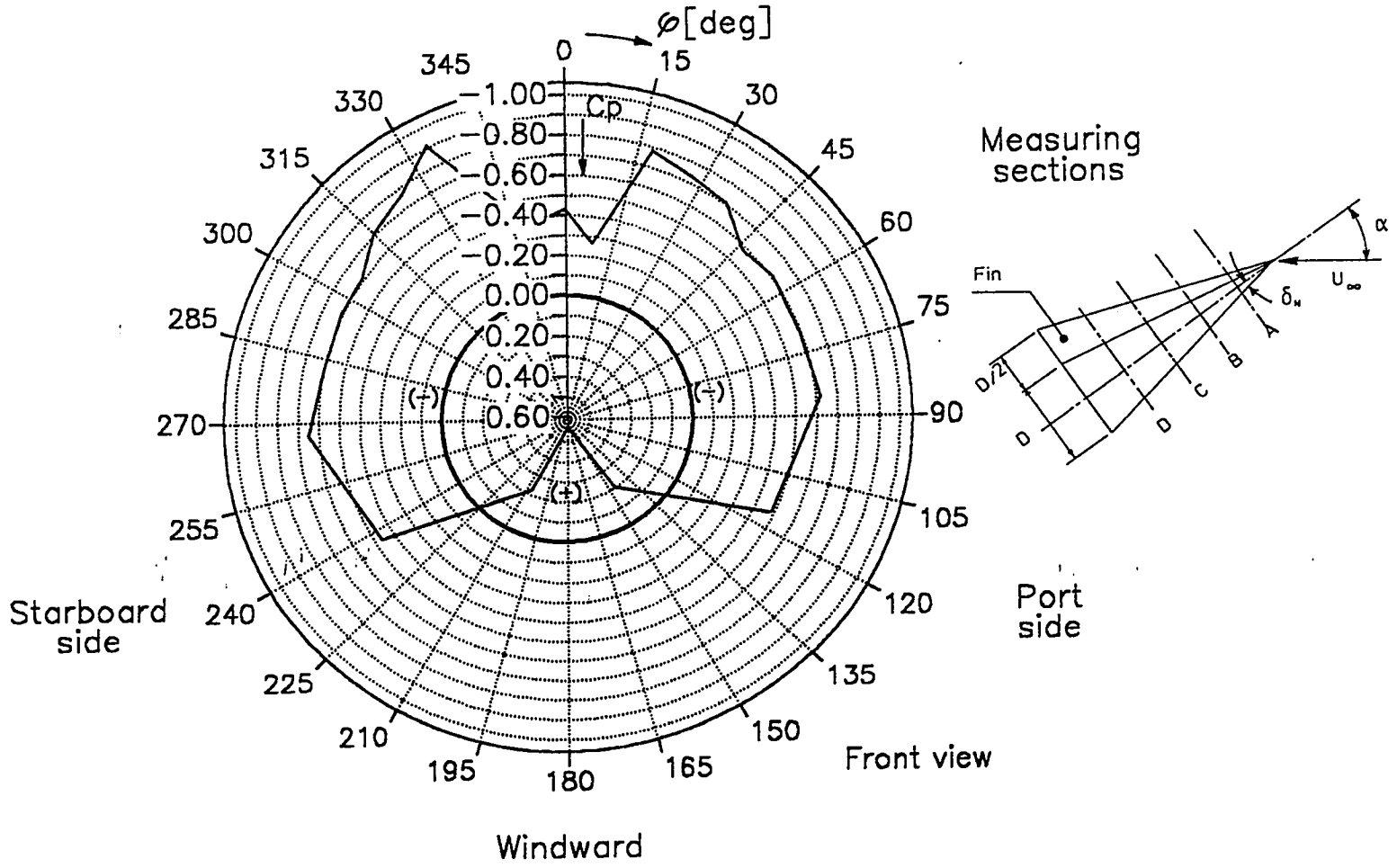

Fig. 4.40 Circumferential pressure distribution on circular cone with fin, Re_D = 142,000, δ_N=8 deg, α=35 deg, section C

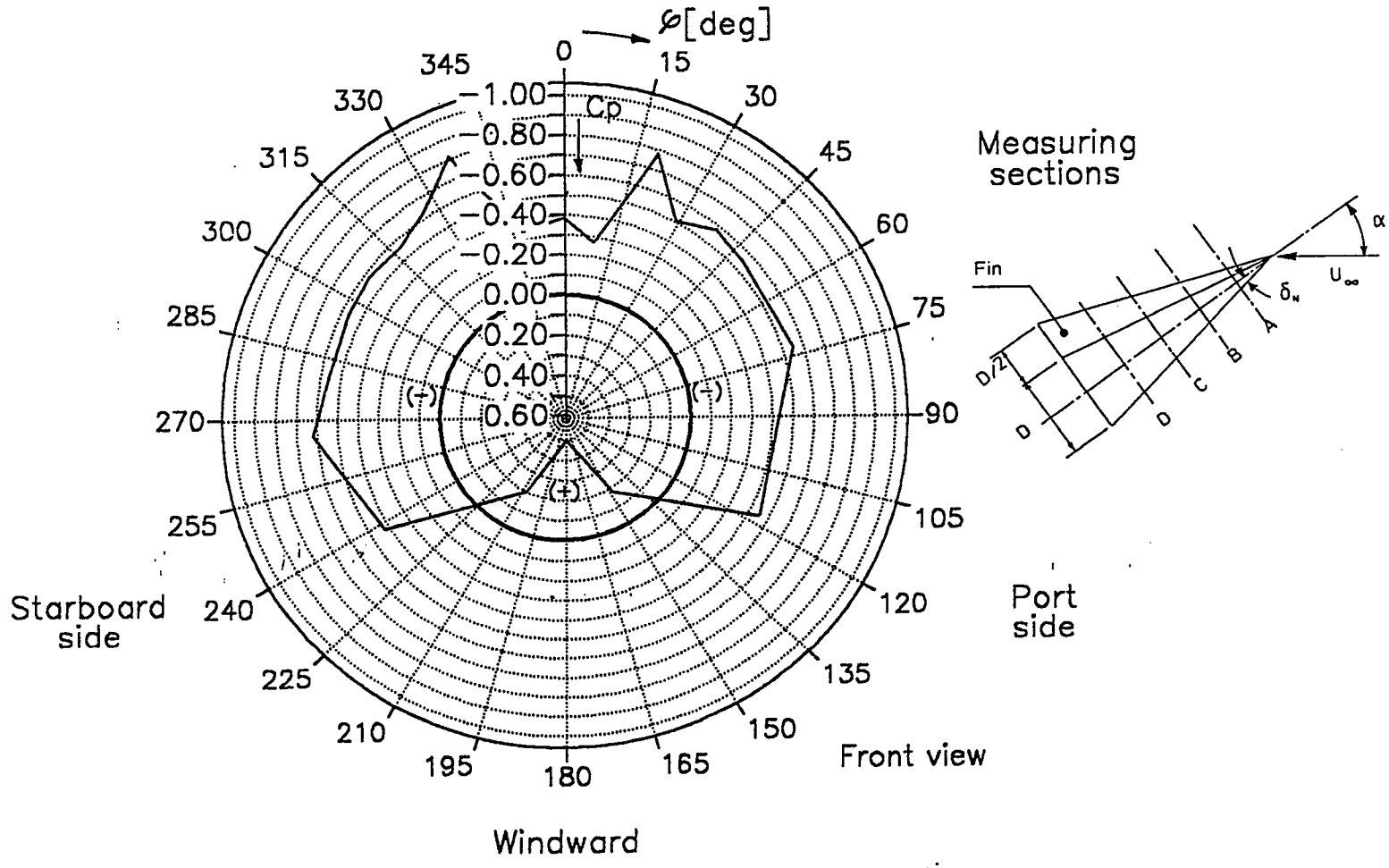

Fig. 4.41 Circumferential pressure distribution on circular cone with fin, Re_D = 142,000, δ_N=8 deg, α=35 deg, section D

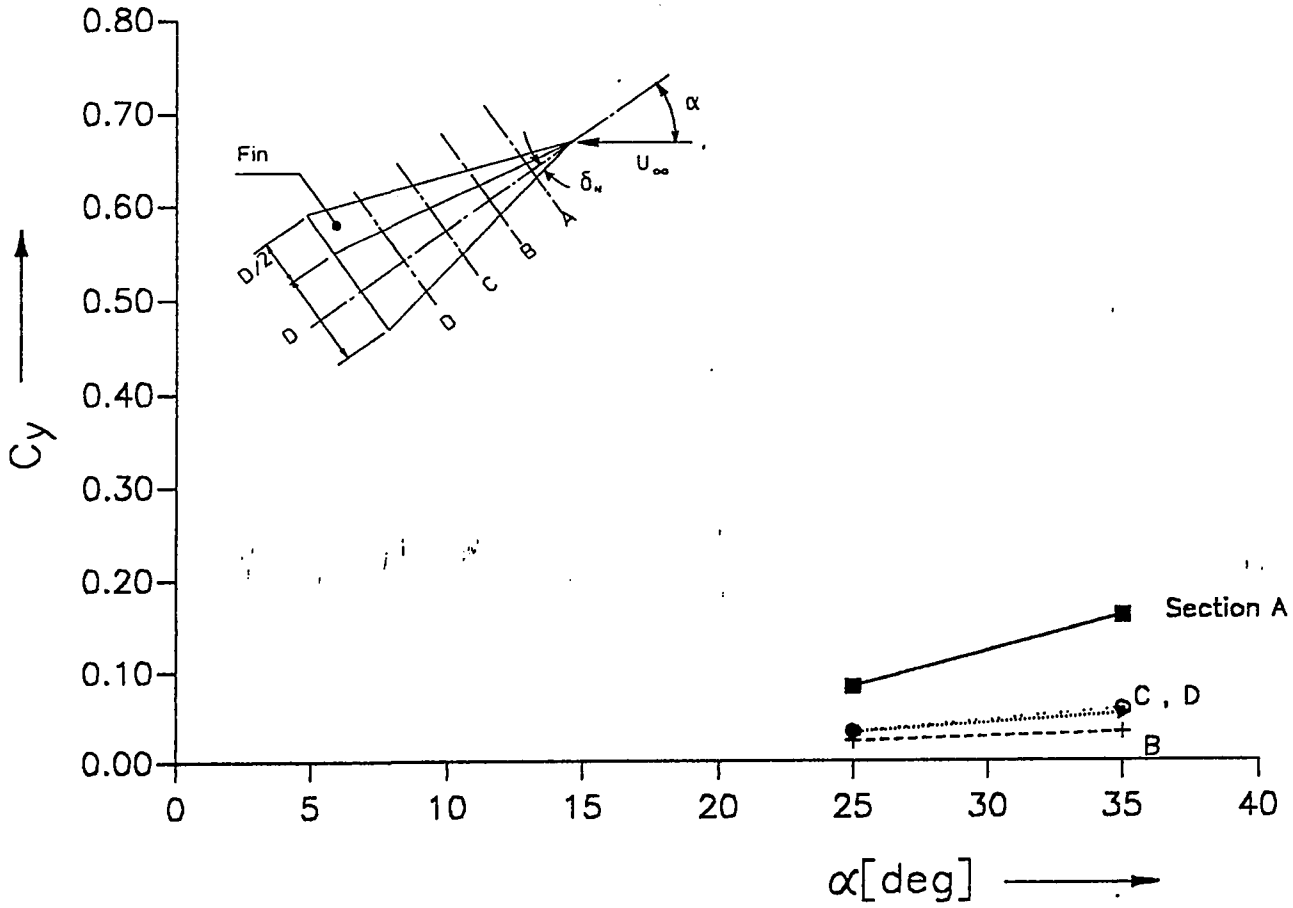

Fig. 4.42 Sectional side-force vs. angle of attack for circular cone with fin at four axial sections, Re_D = 142,000, δ_N = 8 deg

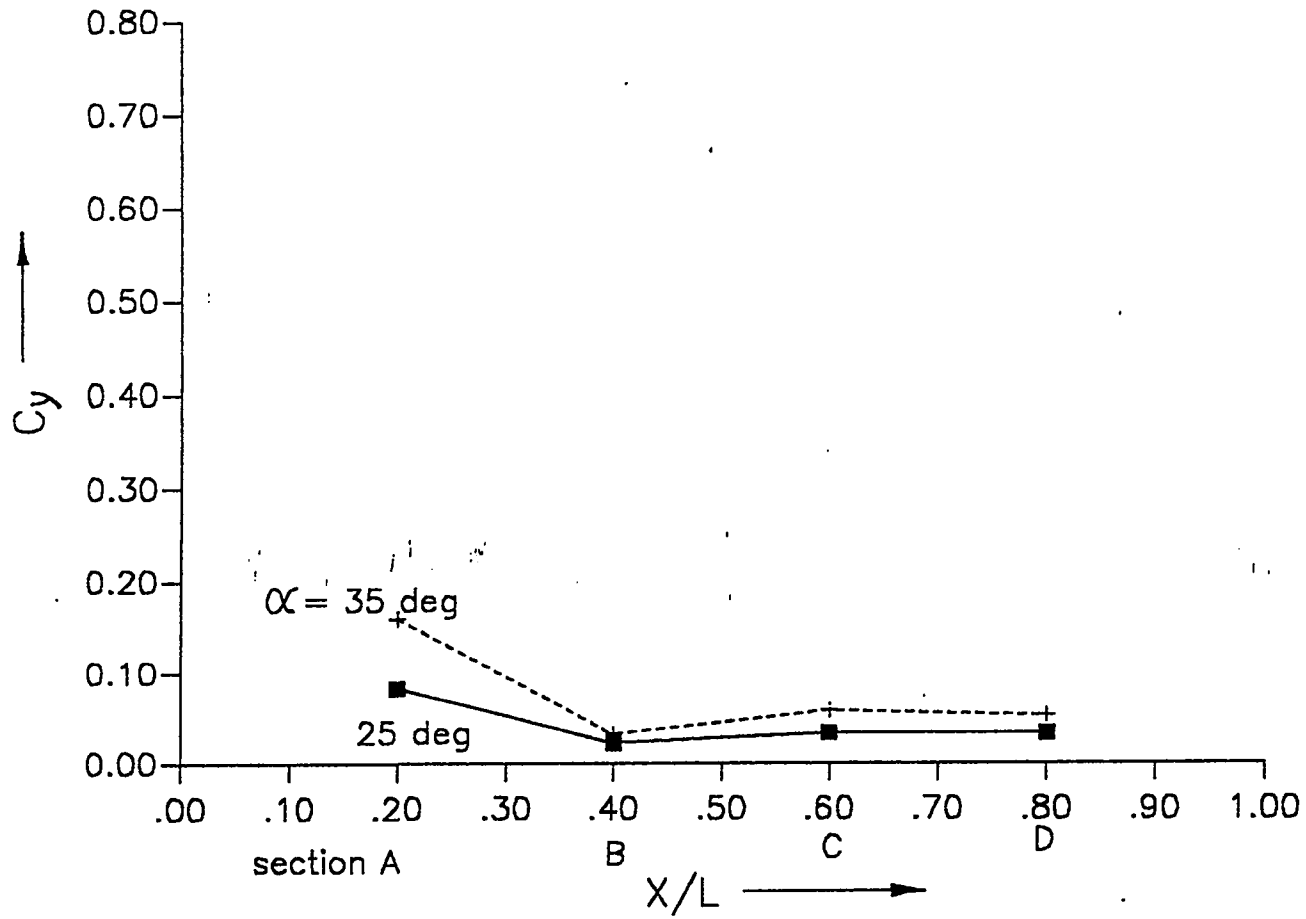

Fig. 4.43 Sectional side-force vs. length for circular cone with fin at two angles of attack, $Re_D = 142{,}000$, $\delta_N = 8$ deg

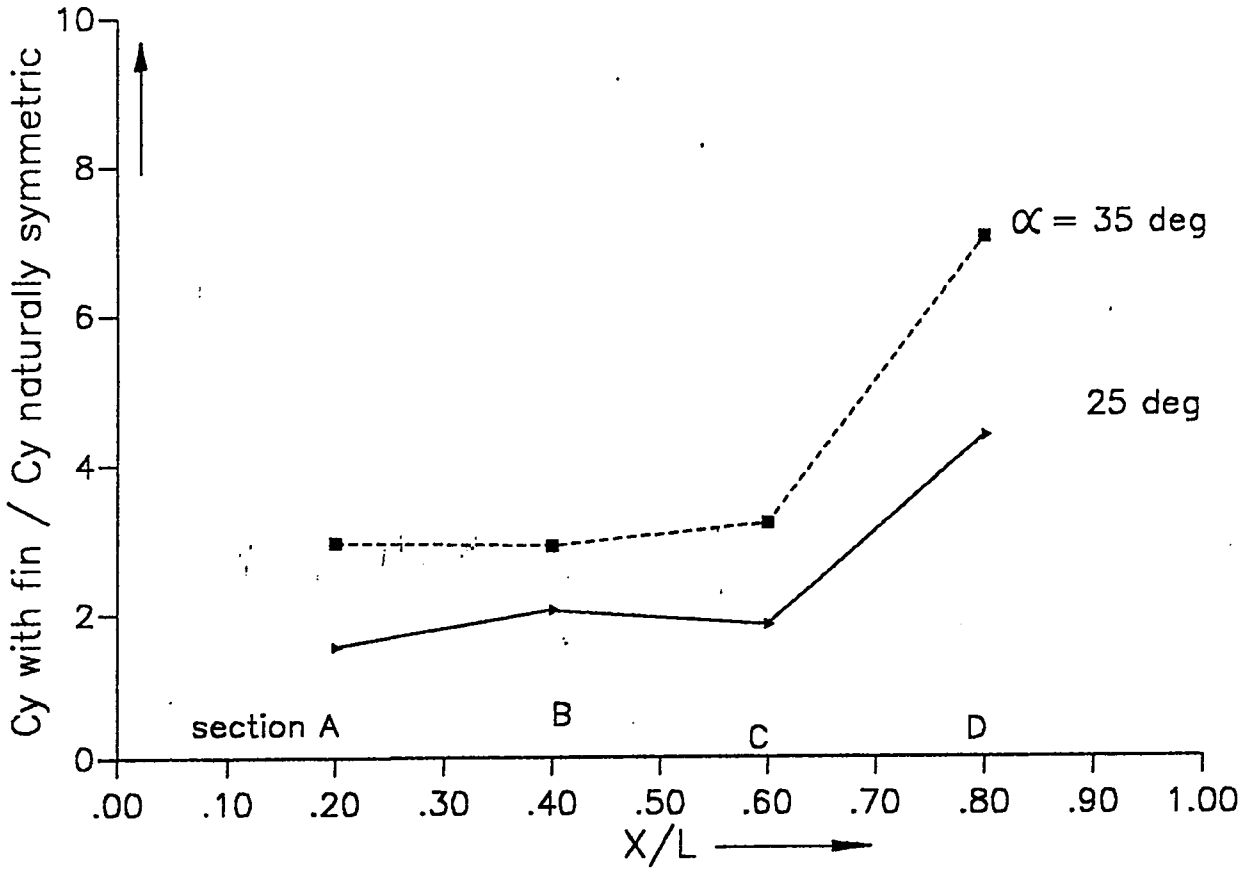

Fig. 4.44 Ratio of side force on cone with fin to the side force on cone without fin at $\alpha = 15$ deg (nominally symmetric vortex flow case), $Re_D = 142{,}000$, $\delta_N = 8$ deg

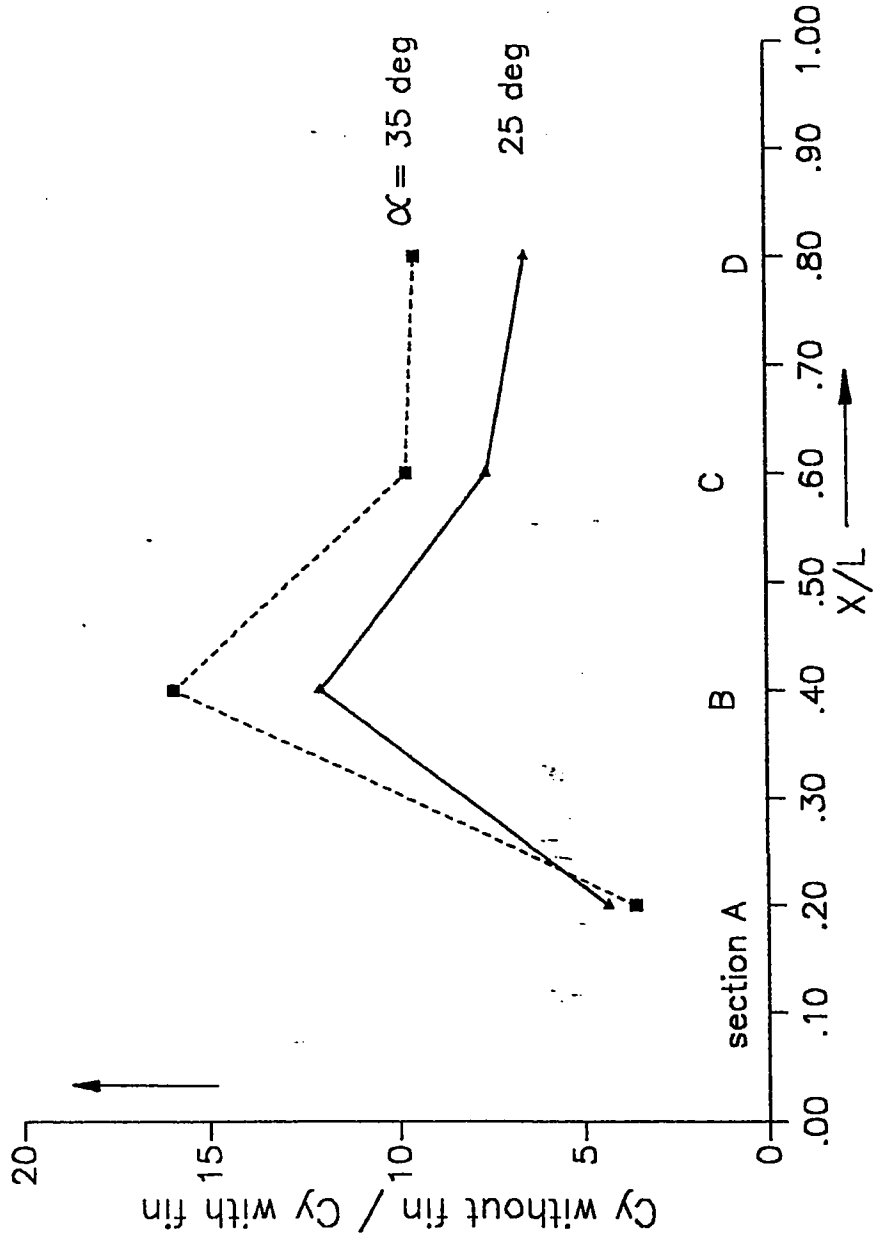

Fig. 4.45 Ratio of sectional side-force on cone without fin to the sectional side-force on cone with fin, at $\alpha = 25$ deg and 35 deg, $Re_D = 142{,}000$, $\delta_N = 8$ deg

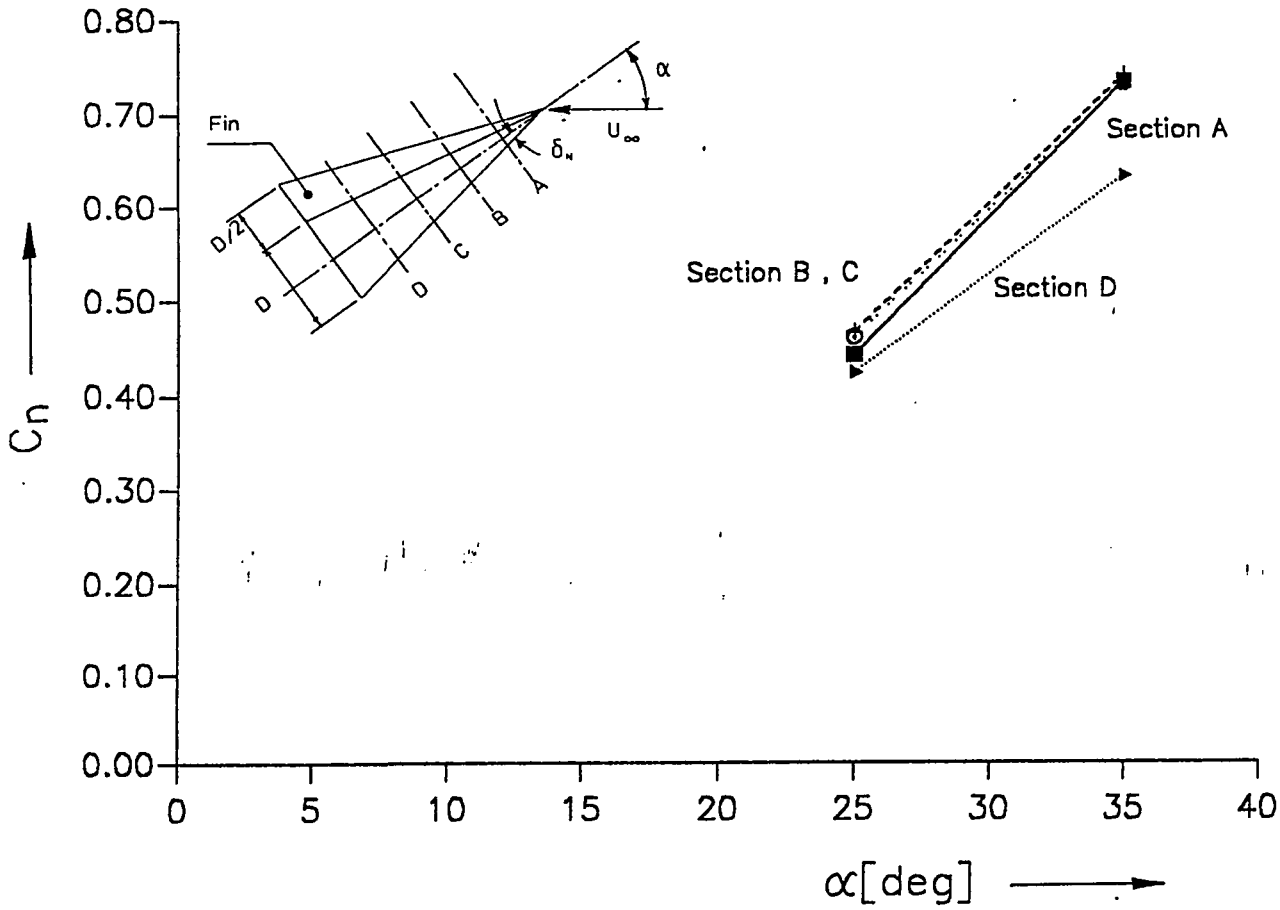

Fig. 4.46 Sectional normal-force vs. angle of attack for circular cone with fin at four axial sections, Re_D = 142,000, δ_N = 8 deg

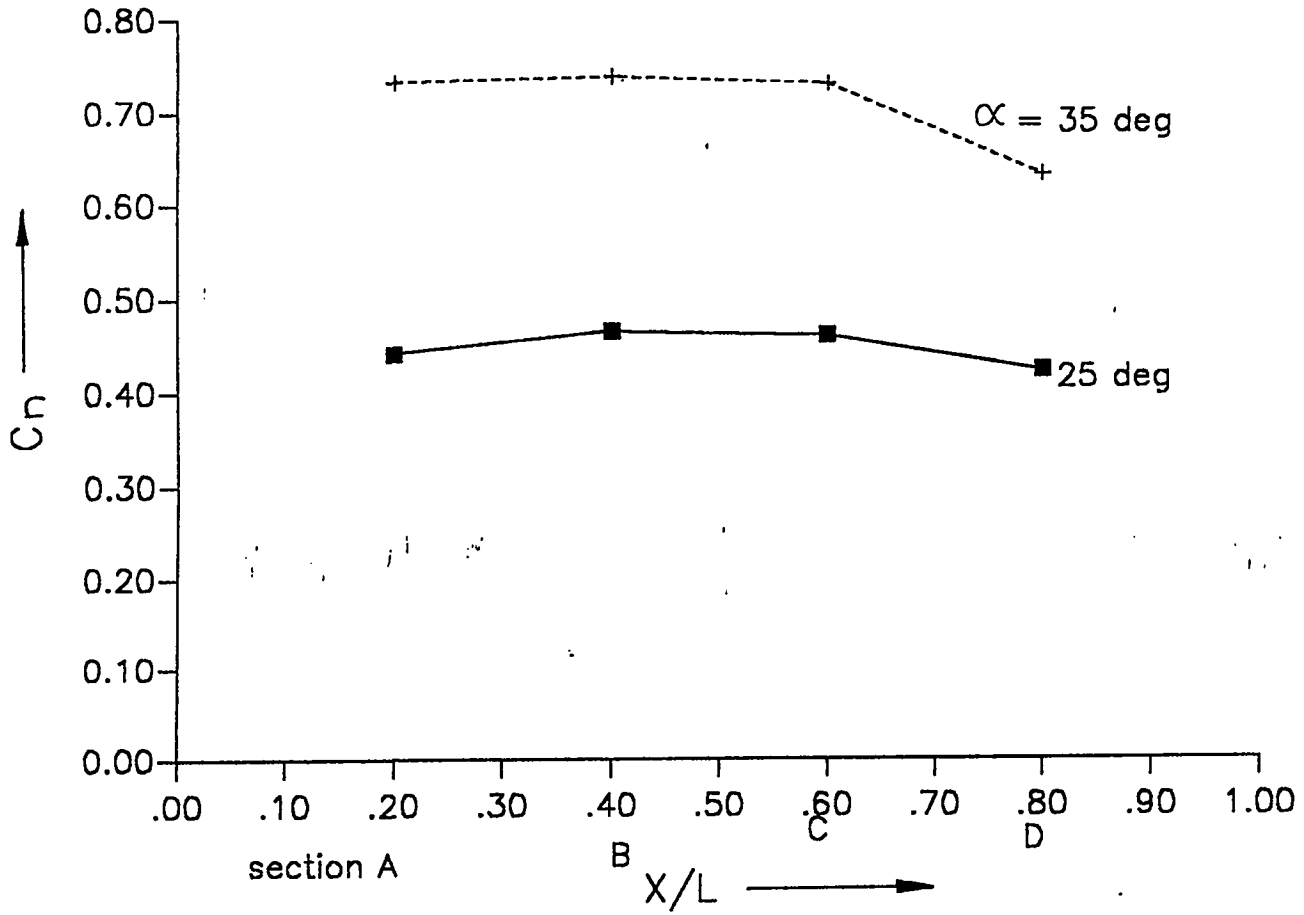

Fig. 4.47 Sectional normal-force vs. length for circular cone with fin at two angles of attack, Re_D = 142,000, δ_N = 8 deg

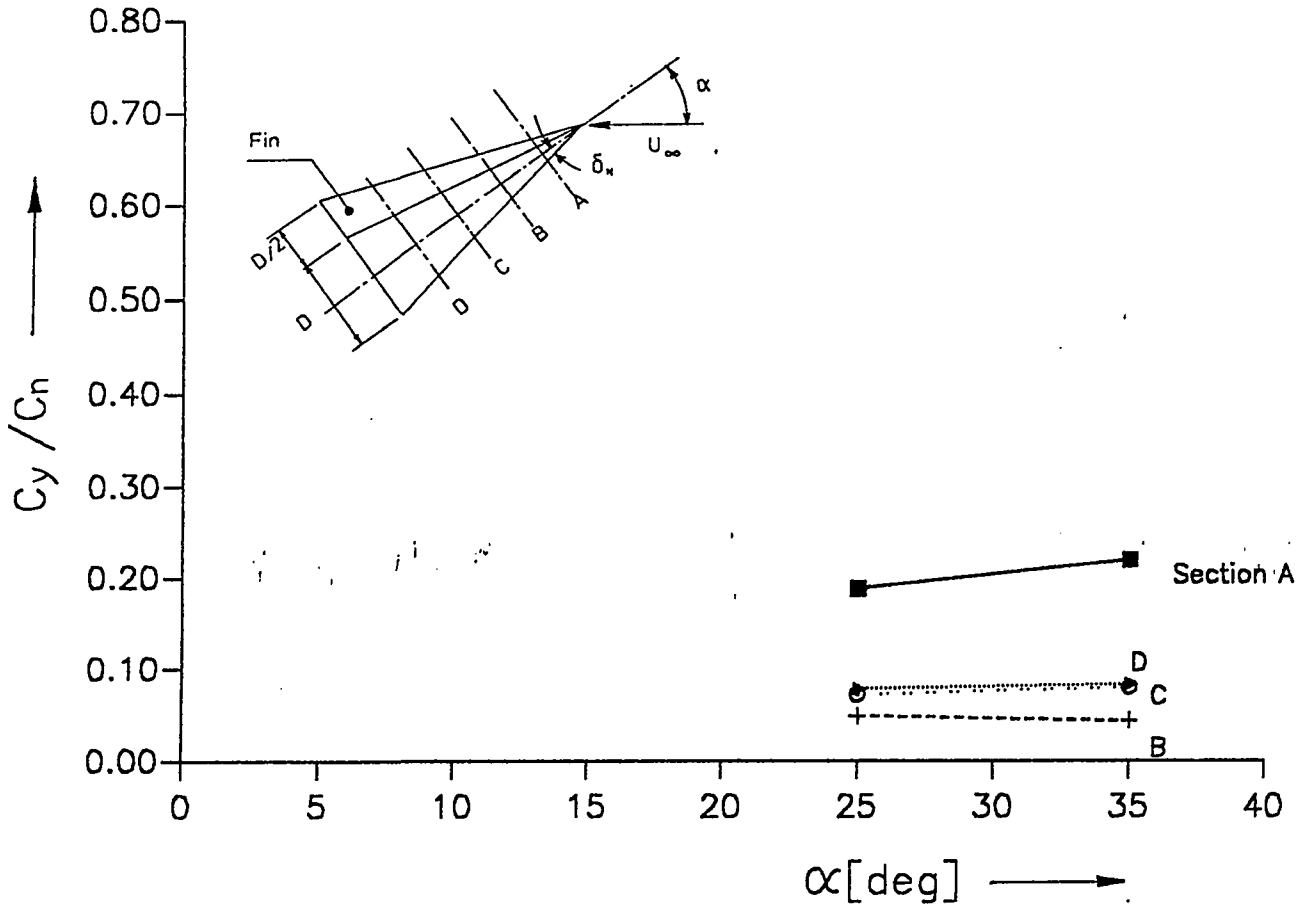

Fig. 4.48 Ratio of side force and normal force on a circular cone with fin, at two angles of attack, for various sections along the length, $Re_D = 142{,}000$ $\delta_N = 8$ deg

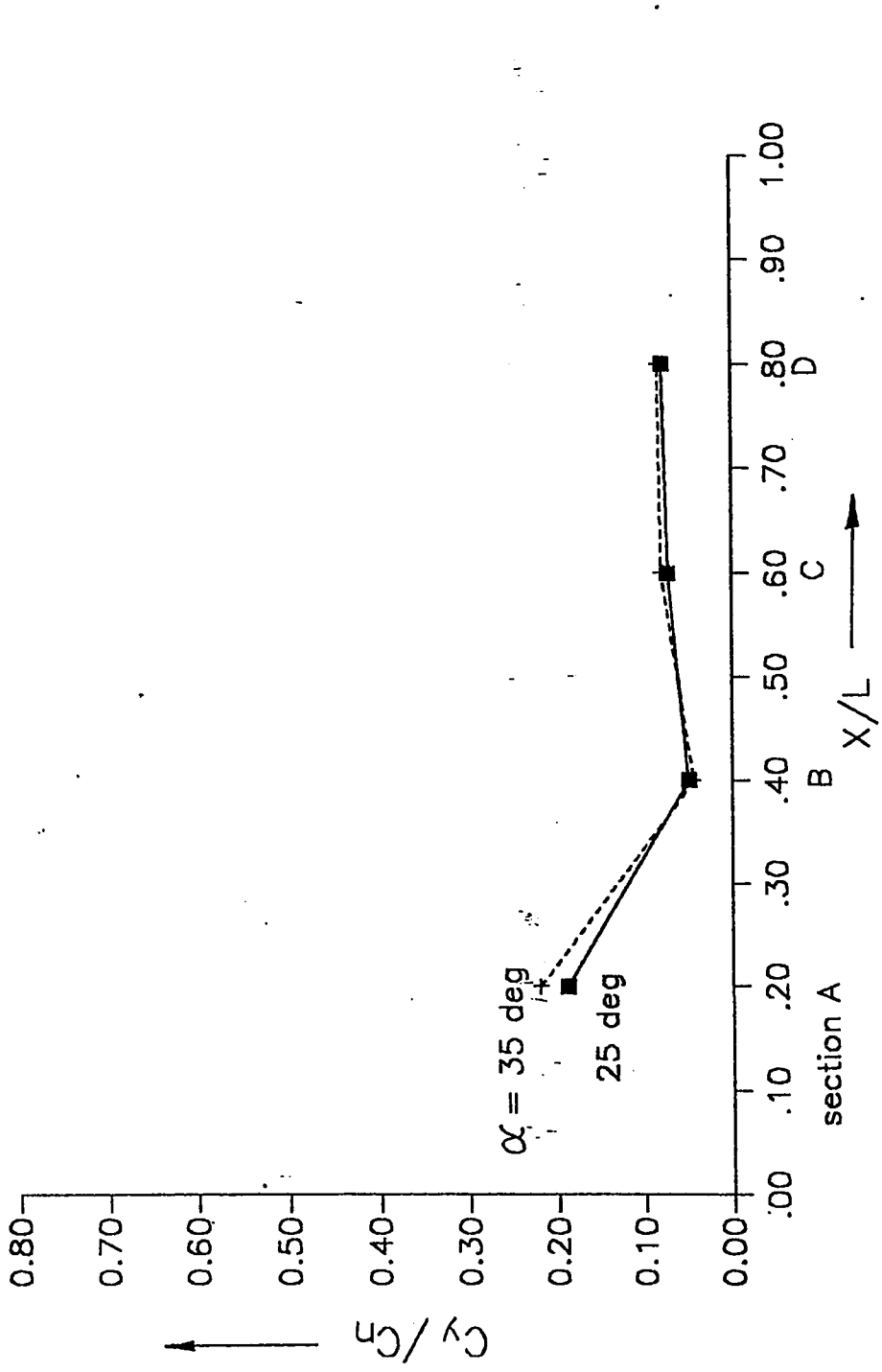

Fig. 4.49 Ratio of side force and normal force along the length of the cone with fin for various angle of attack, Re_D = 142,000, δ_N = 8 deg

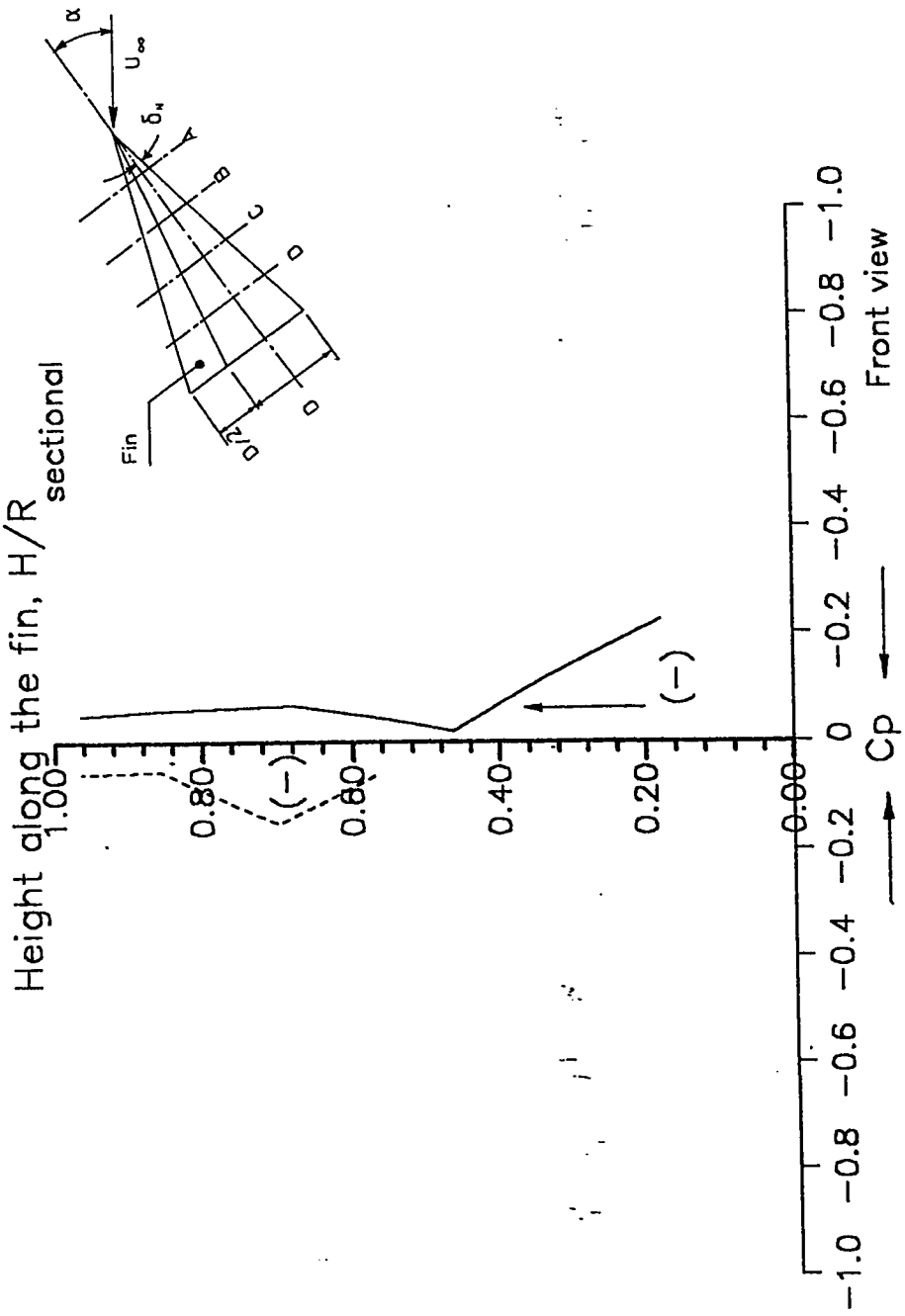

Fig. 4.50 Pressure distribution on the fin, attached to the circular cone at $\alpha = 25$ deg, section A, $Re_D = 142{,}000$

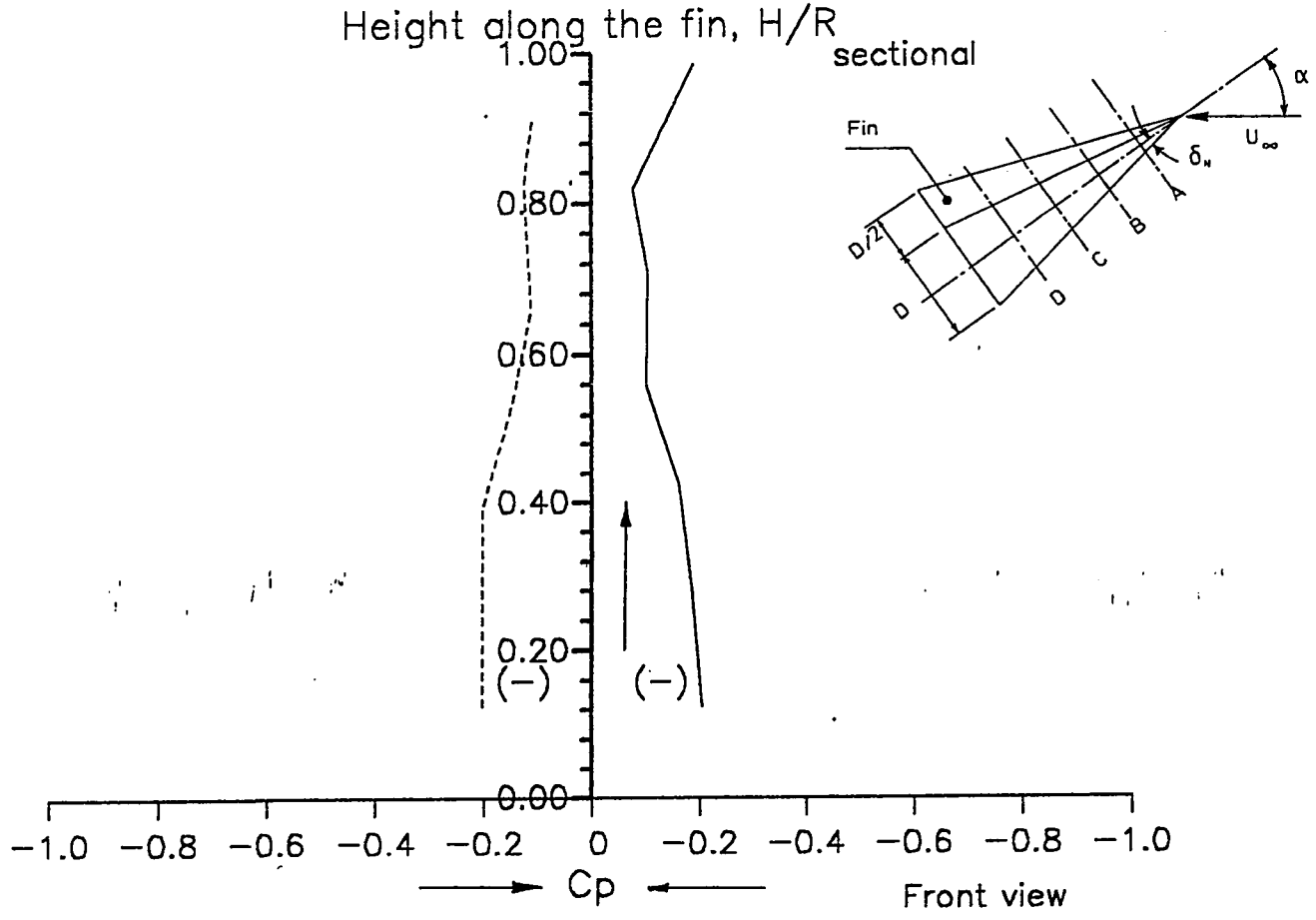

Fig. 4.51 Pressure distribution on the fin, attached to the circular cone at $\alpha = 25$ deg, section B, $Re_D = 142{,}000$

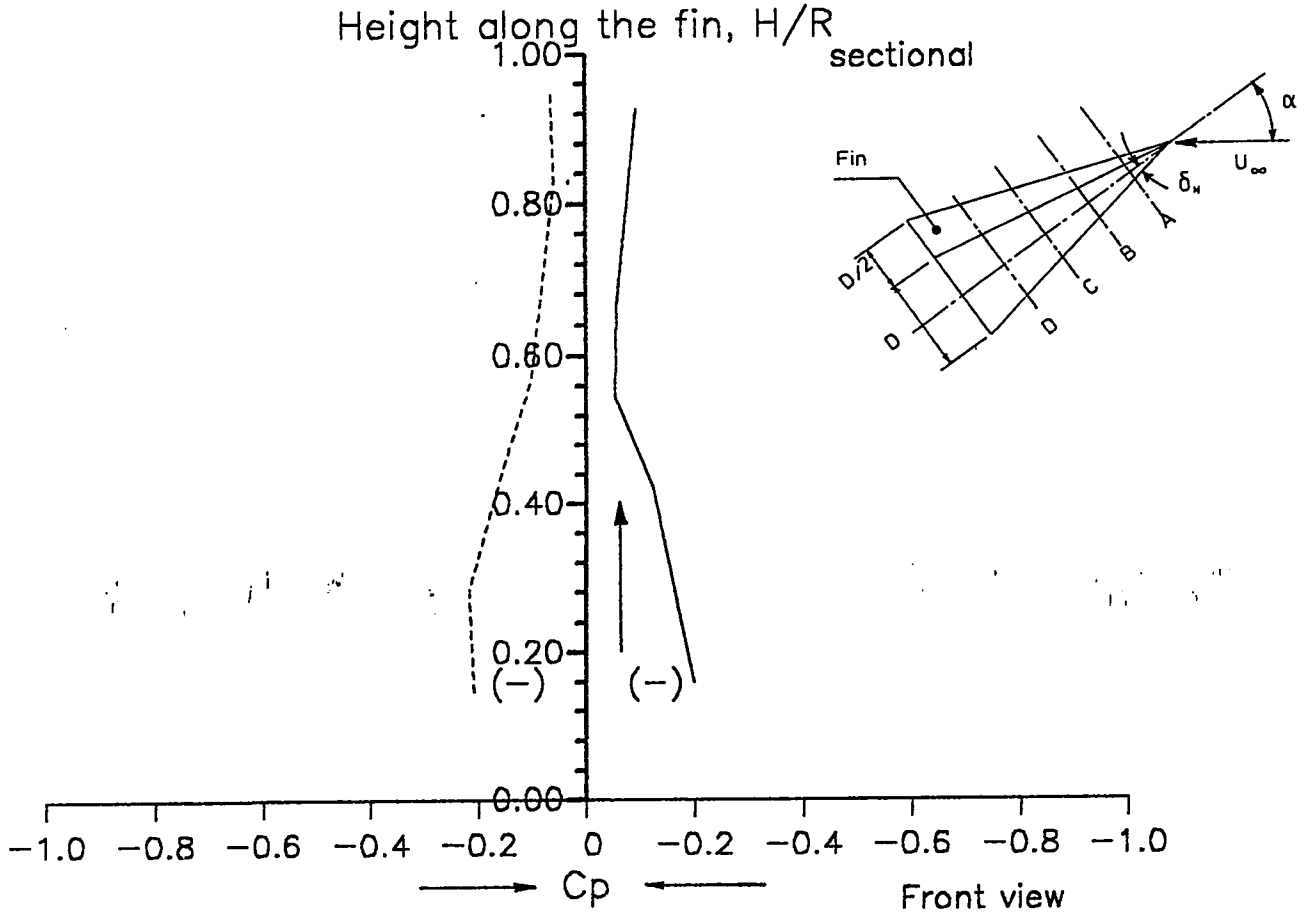

Fig. 4.52 Pressure distribution on the fin, attached to the circular cone at $\alpha = 25$ deg, section C, $Re_D = 142{,}000$

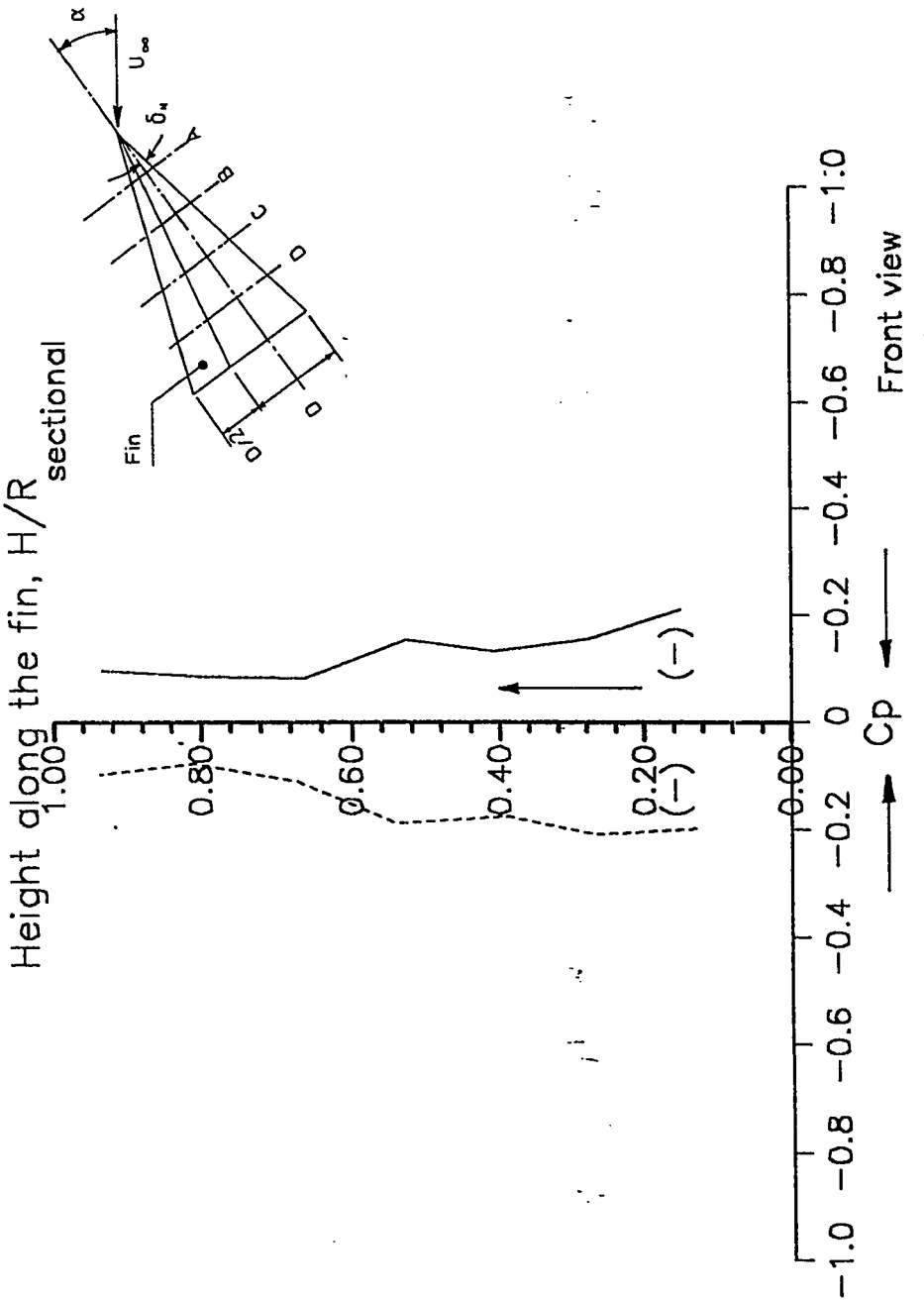

Fig. 4.53 Pressure distribution on the fin, attached to the circular cone at $\alpha = 25$ deg, section D, $Re_D = 142{,}000$

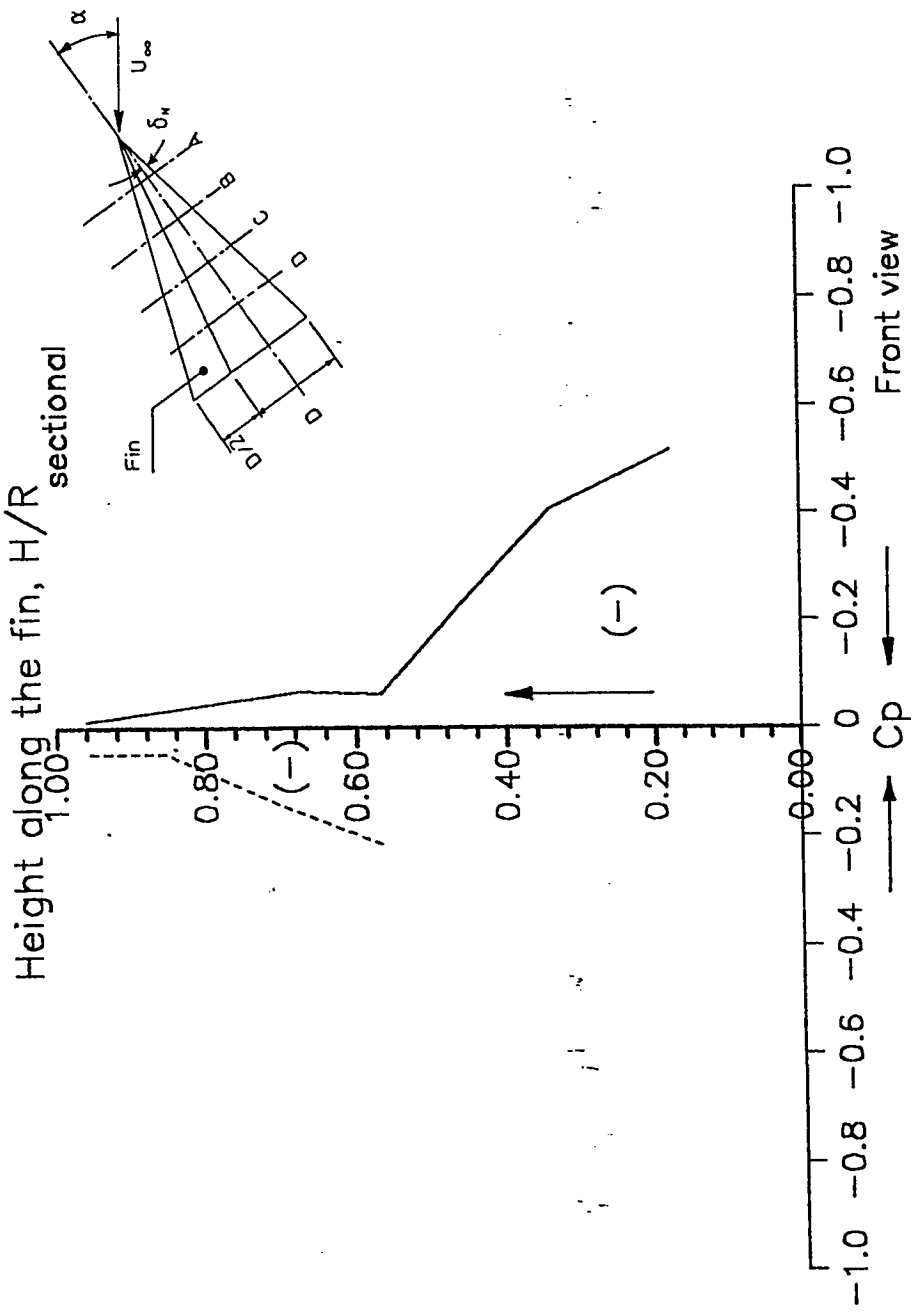

Fig. 4.54 Pressure distribution on the fin, attached to the circular cone at $\alpha = 35$ deg, section A, $Re_D = 142{,}000$

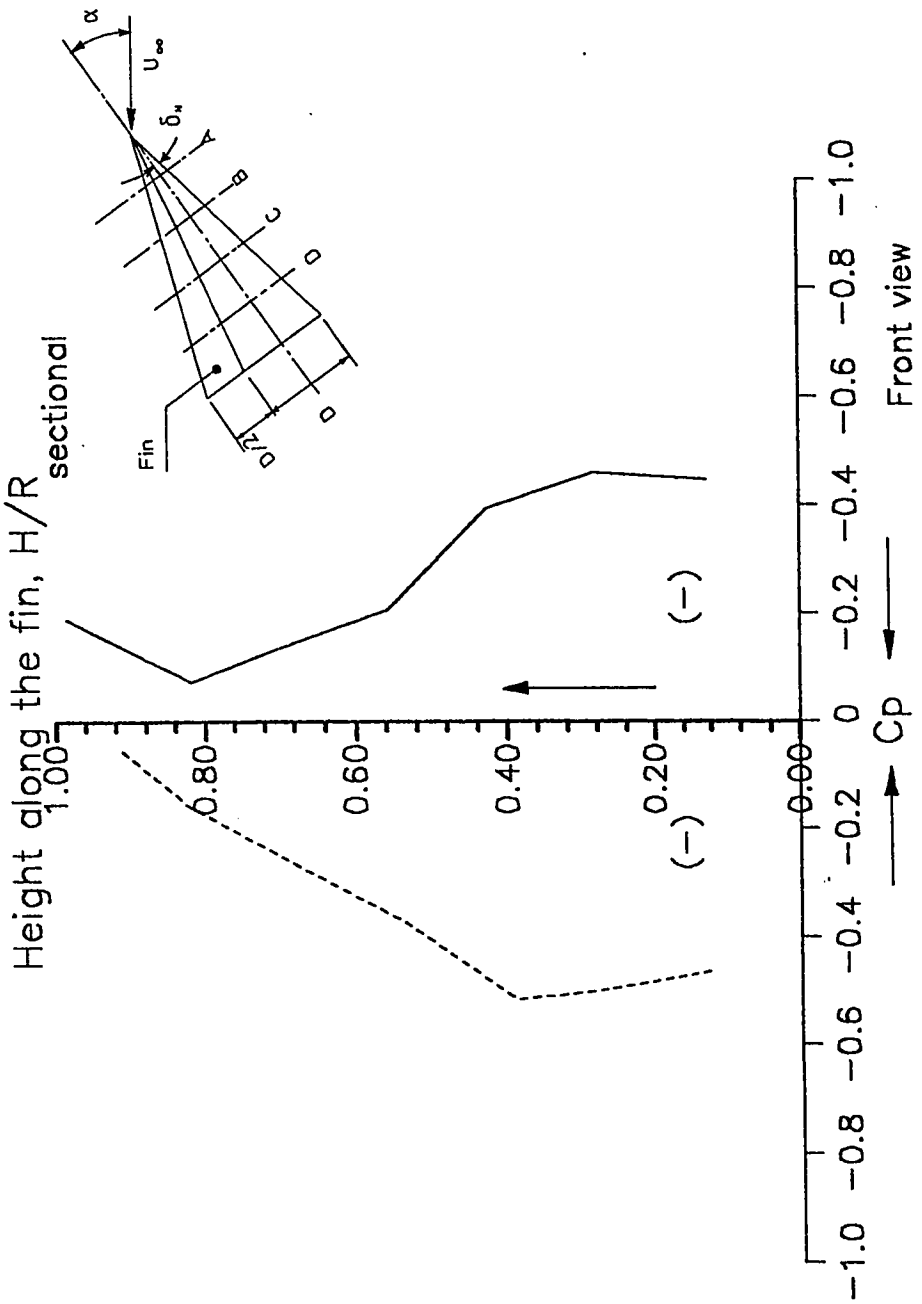

Fig. 4.55 Pressure distribution on the fin, attached to the circular cone at $\alpha = 35$ deg, section B, $Re_D = 142{,}000$

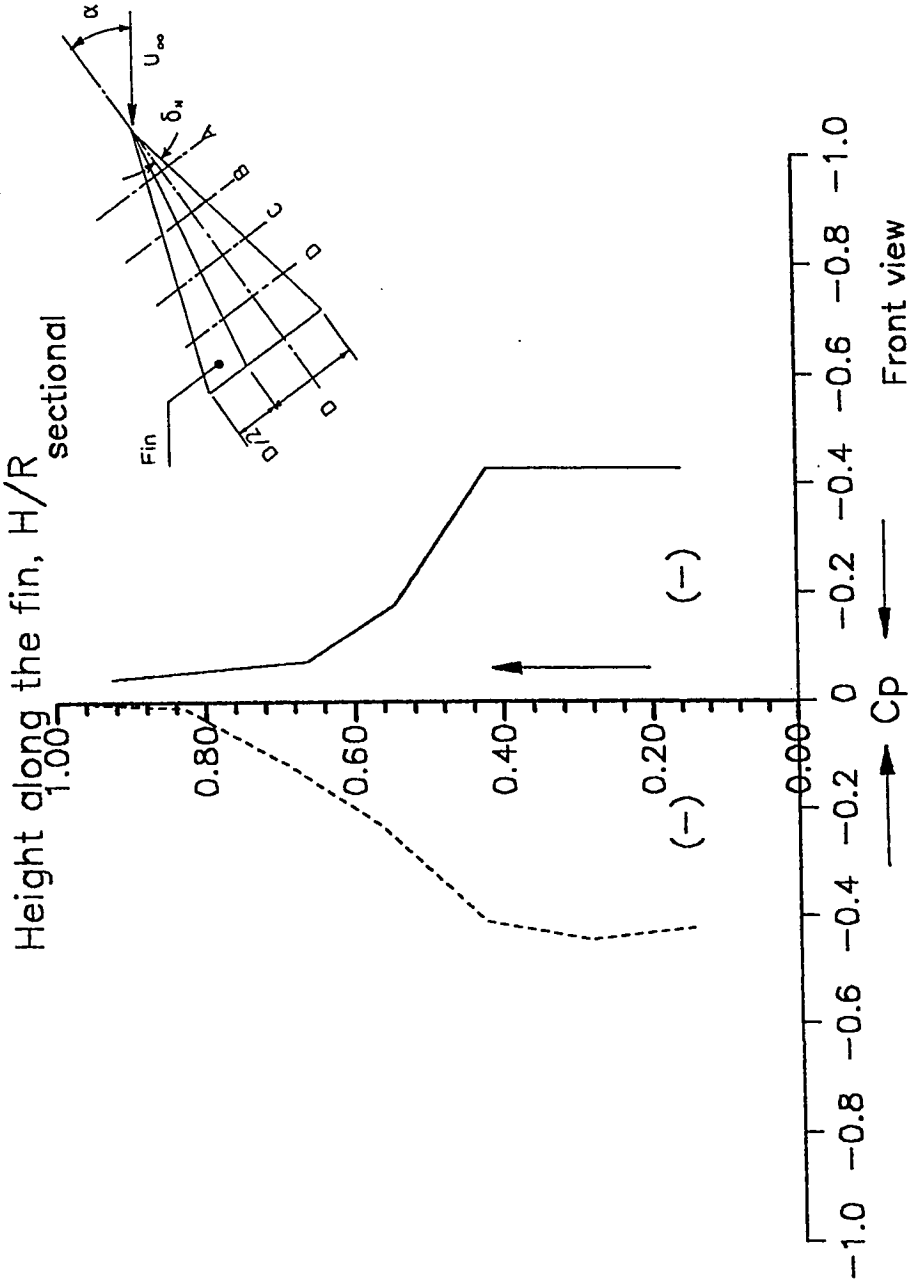

Fig. 4.56 Pressure distribution on the fin, attached to the circular cone at $\alpha = 35$ deg, section C, $Re_D = 142{,}000$

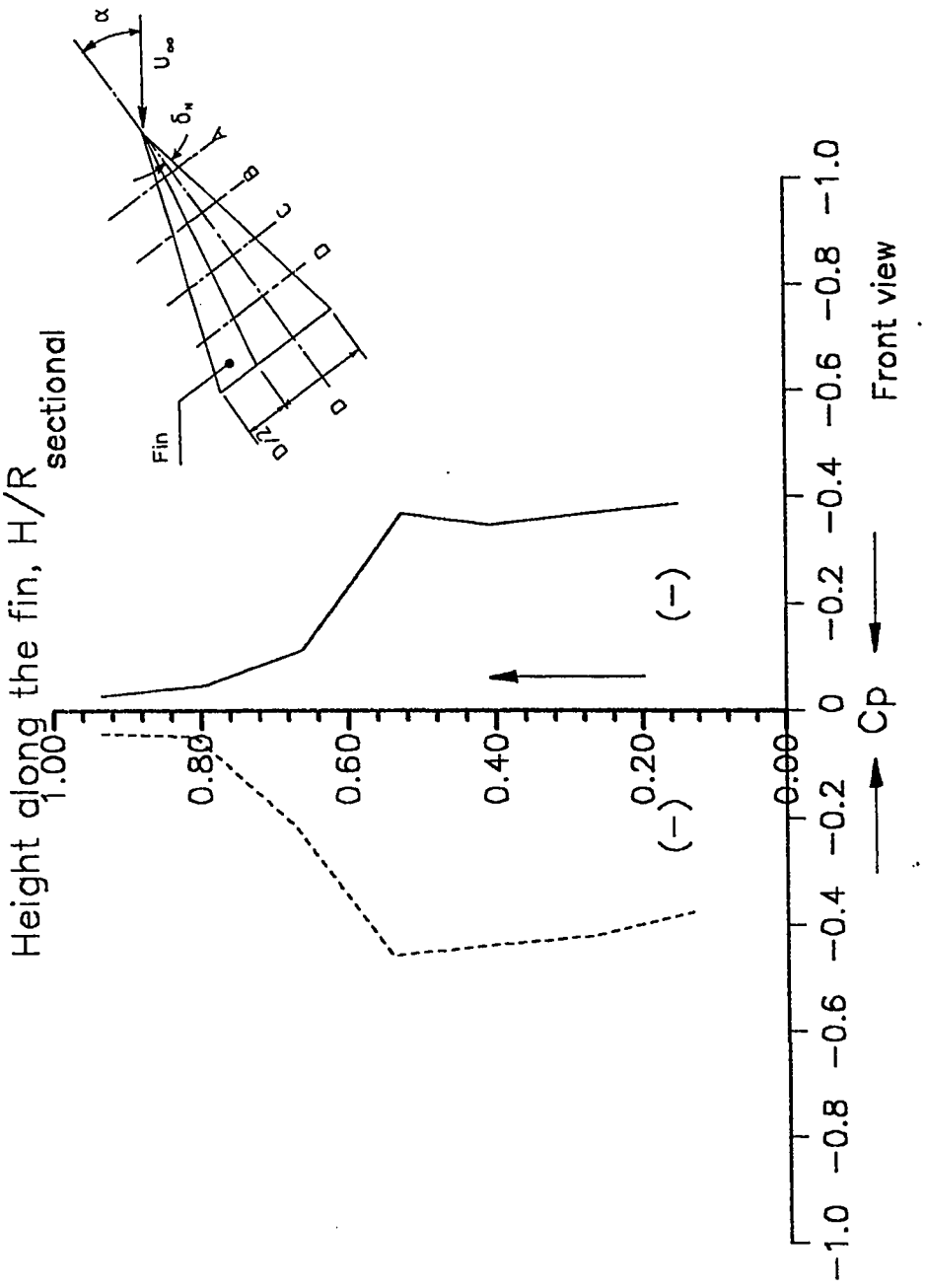

Fig. 5.57 Pressure distribution on the fin, attached to the circular cone at $\alpha = 35$ deg, section D, $Re_D = 142{,}000$

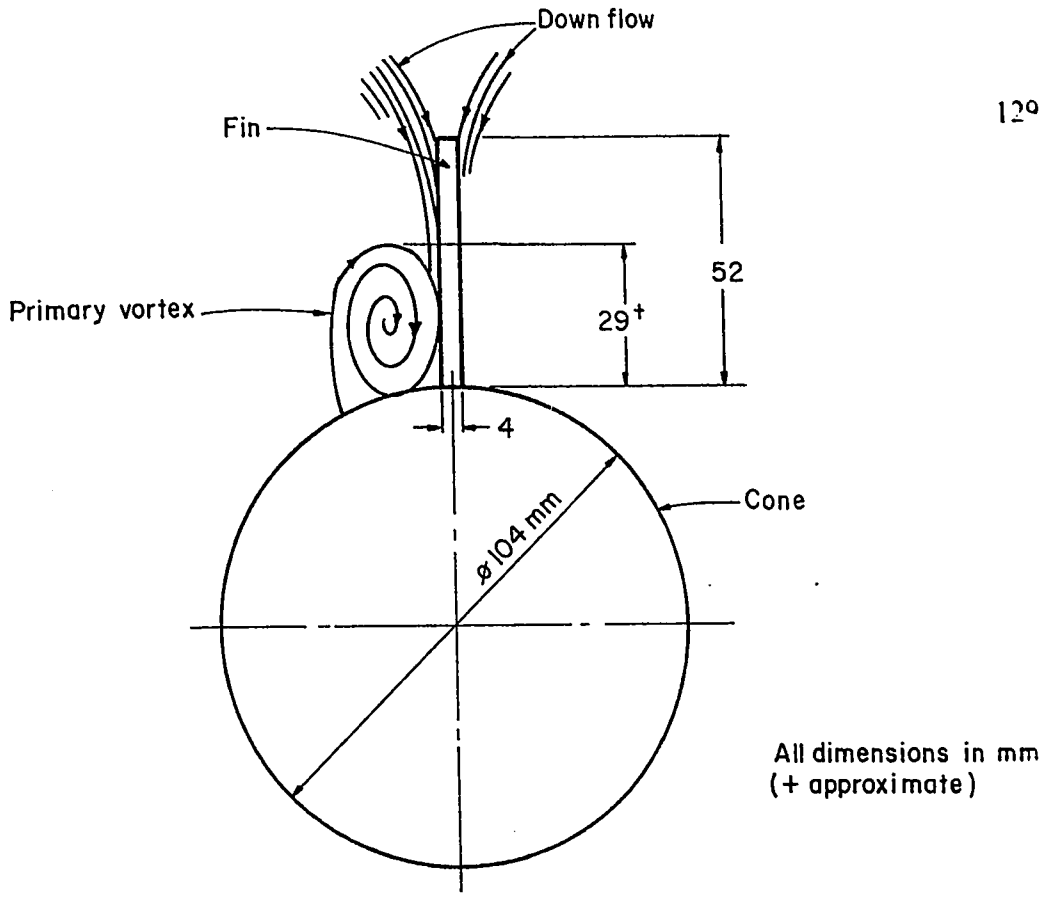

(a) schematic of vortex flow on cone with fin

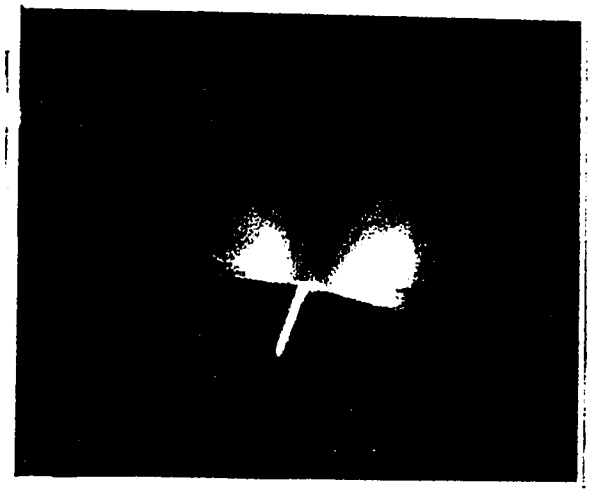

(b) downflow of air above fin

Fig 4.58 Vortex flow on cone with fin, $\alpha = 35$ deg, $Re_D = 142{,}000$, $\delta_N = 8$ deg

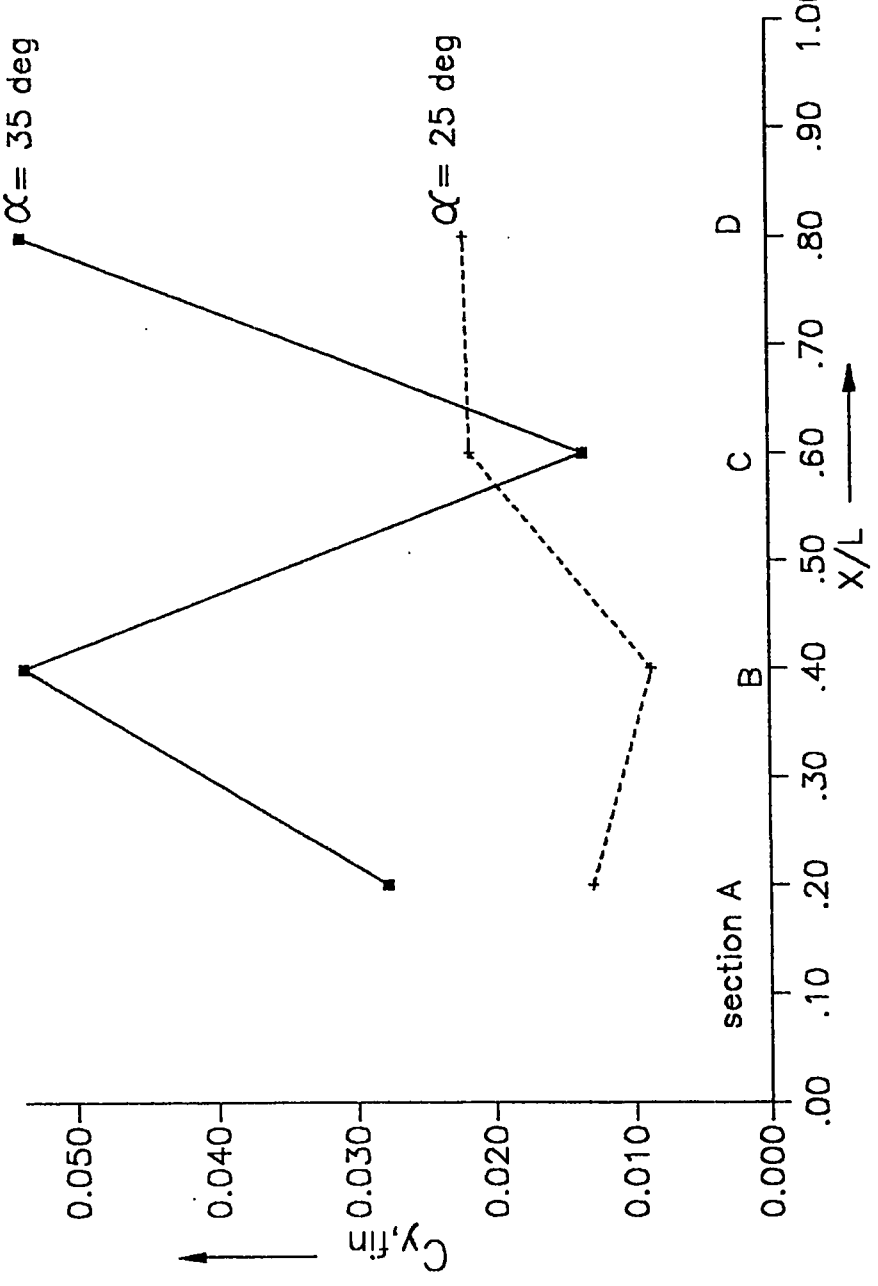

Fig. 4.59 Side force at four axial sections on the fin attached to the circular cone, at $\alpha = 25$ deg and 35 deg, $Re_D = 142,000$

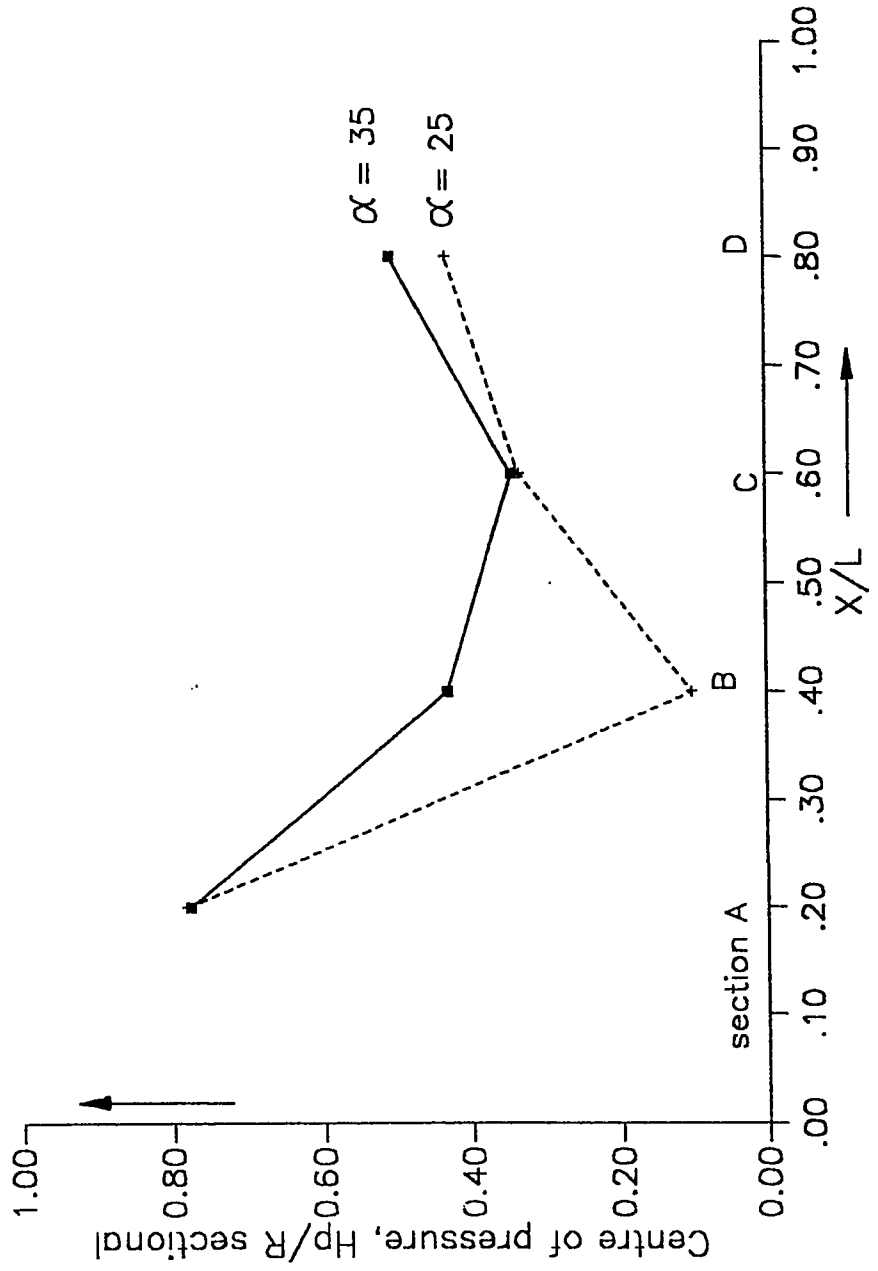

Fig. 4.60 Centre of pressure at four axial sections on a fin attached to the circular cone, at $\alpha = 25$ deg and 35 deg, $Re_D = 142,000$

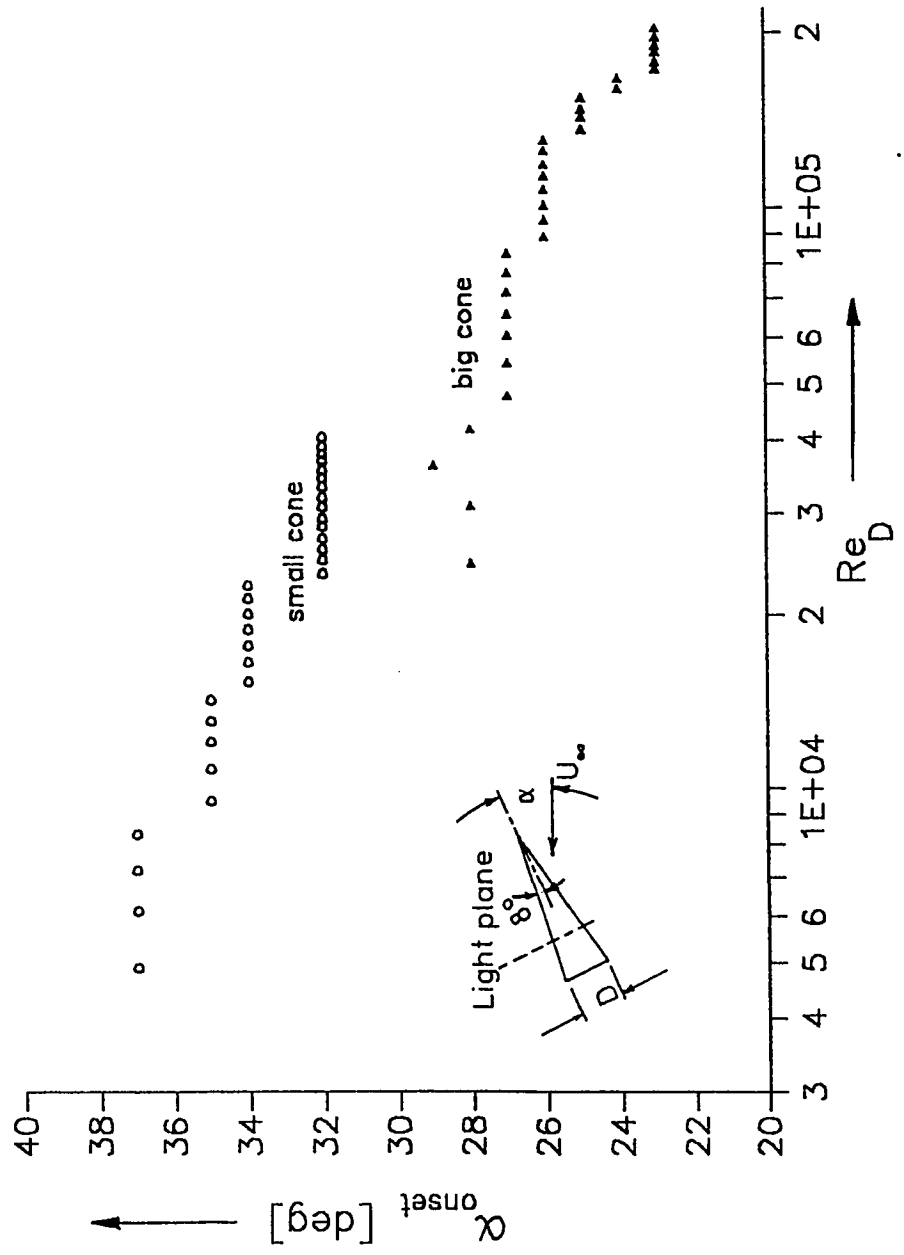

Fig. 4.61 Variation of onset angle of attack with Reynolds number based on base diameter, at one base-diameter upstream

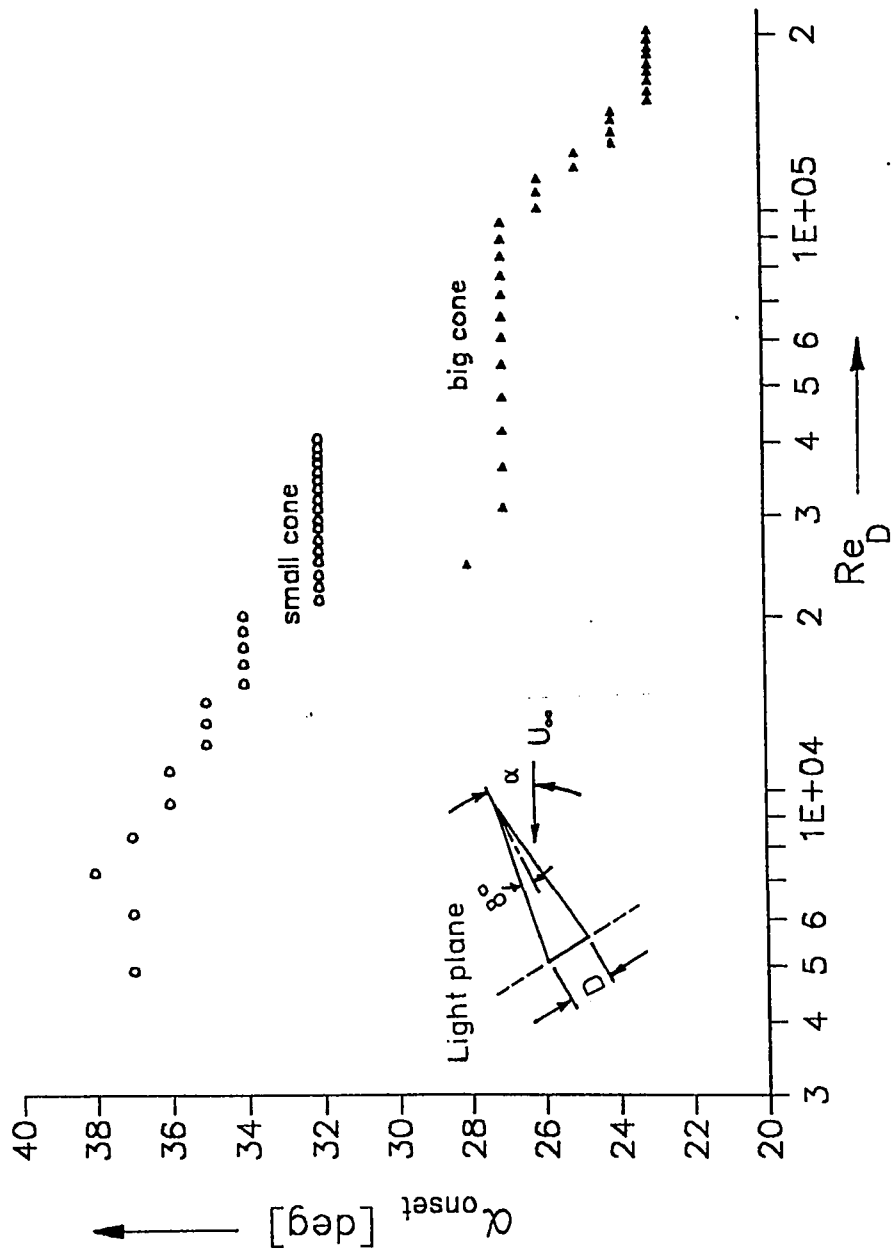

Fig. 4.62 Variation of onset angle of attack with Reynolds number based on base diameter, at the base

Fig 4.63(a) Tip of small cone, viewed under the microscope (Magnification, X84)

Fig 4.63(b) Tip of big cone, viewed under the microscope (Magnification, X84)

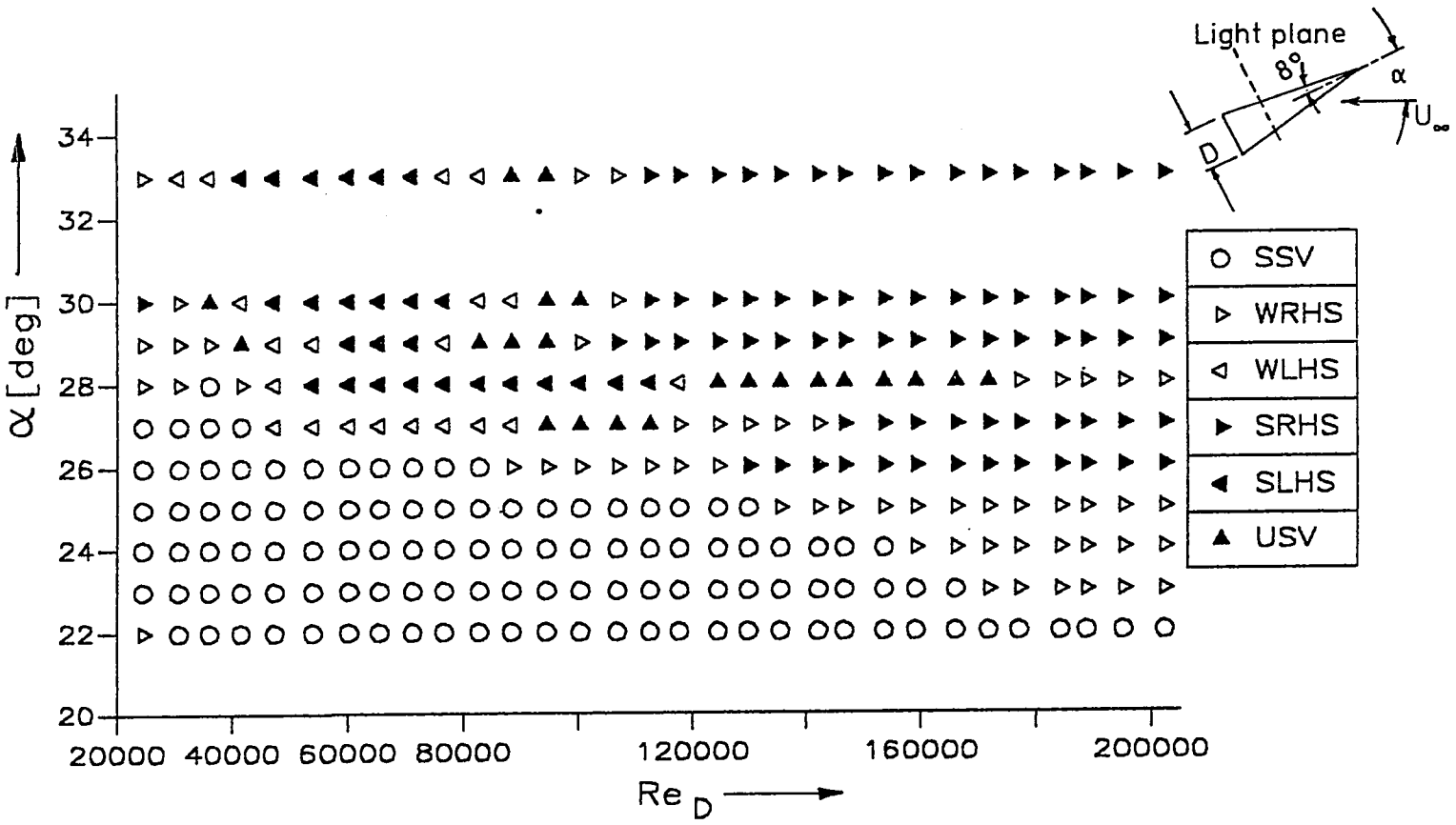

Fig. 4.64 Vortex flow patterns with variation in angle of attack and Reynolds number based on base diameter for circular cone, L = 500 m, one base-diameter upstream (looking from tip to base)

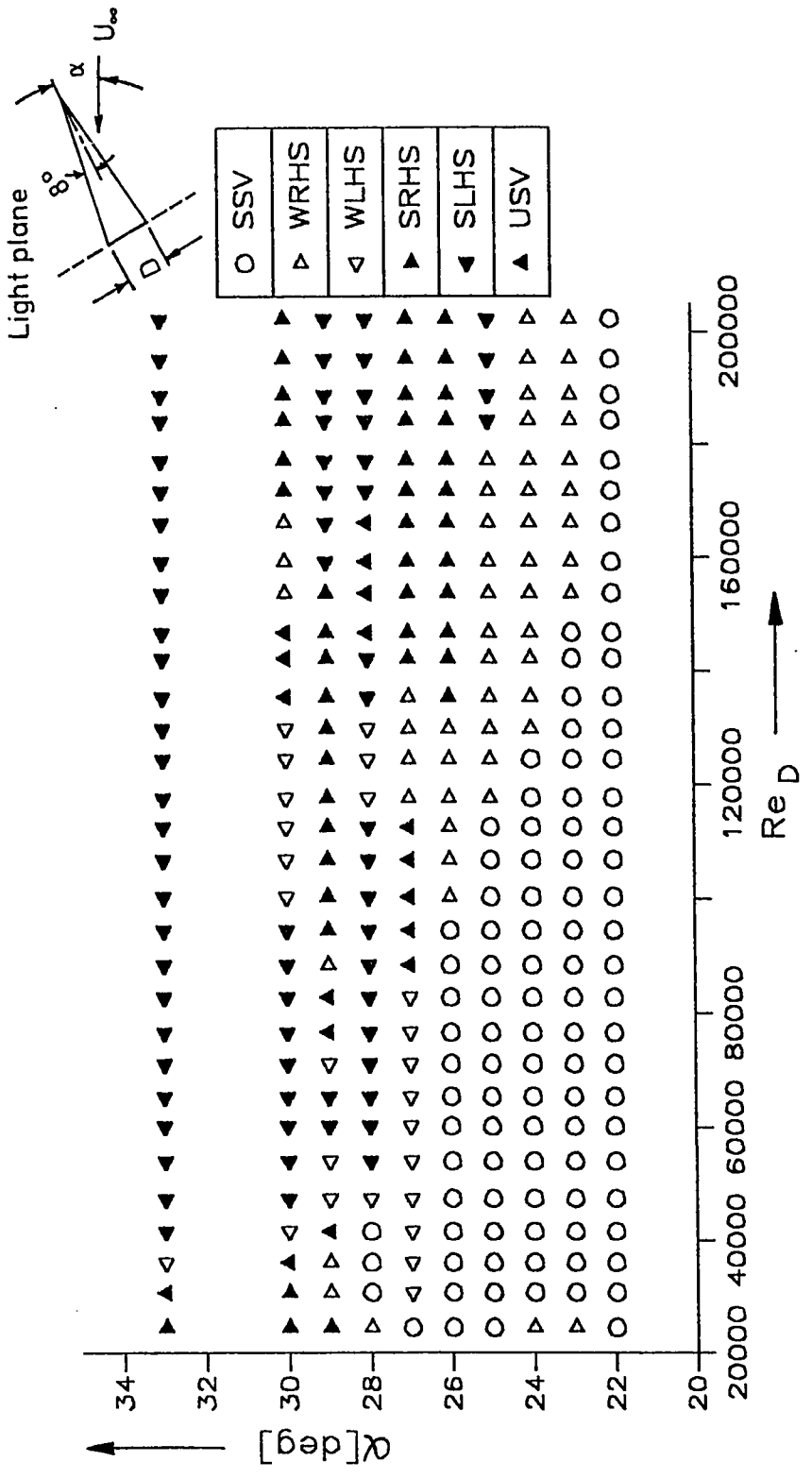

Fig. 4.65 Vortex flow patterns with variation in angle of attack and Reynolds number based on base diameter for circular cone, L = 500 mm, at the base,(looking from tip to base)

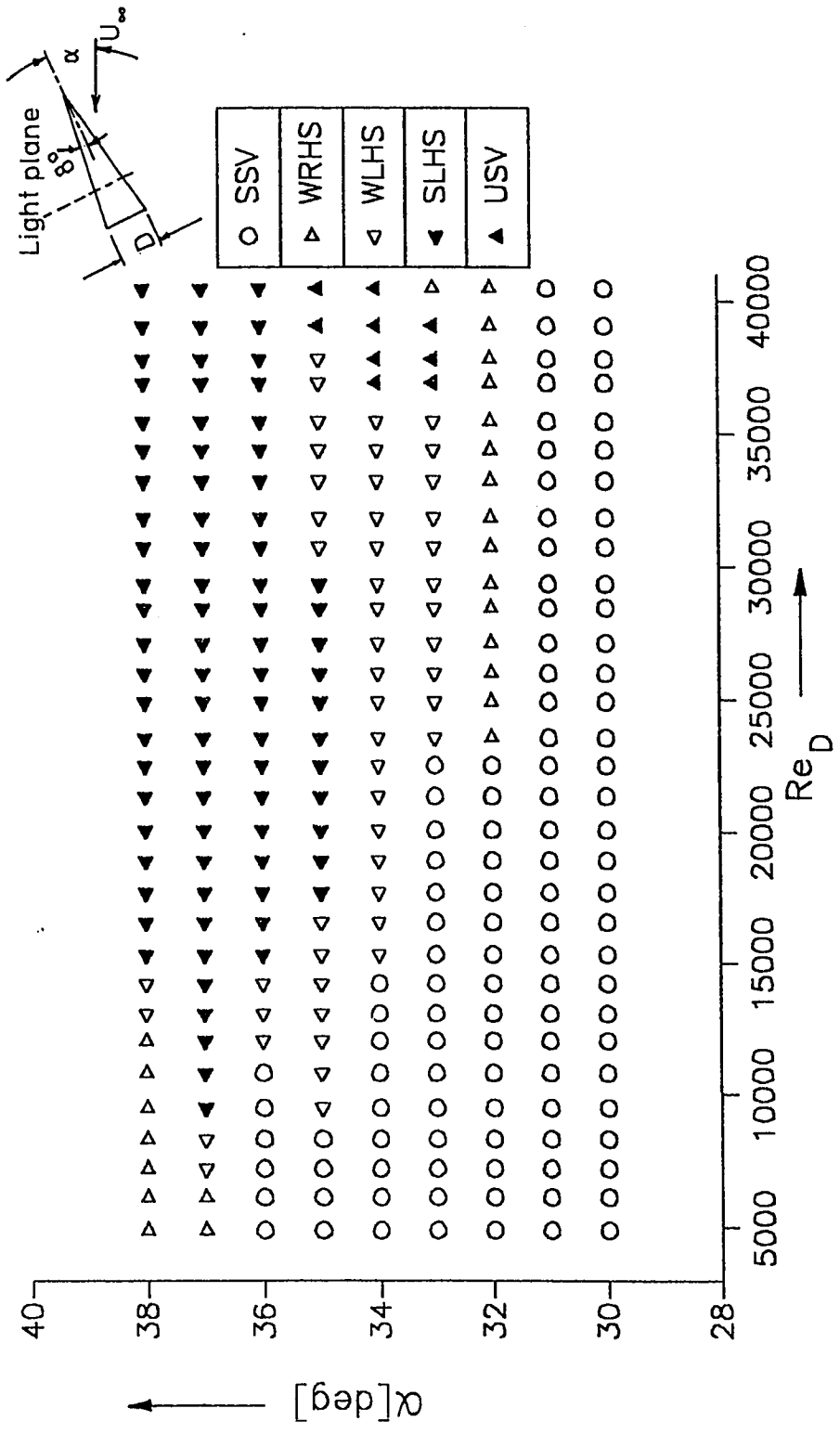

Fig. 4.66 Vortex flow patterns with variation in angle of attack and Reynolds number based on base-diameter for circular cone, L = 100 mm, one base-diameter upstream,(looking from tip to base)

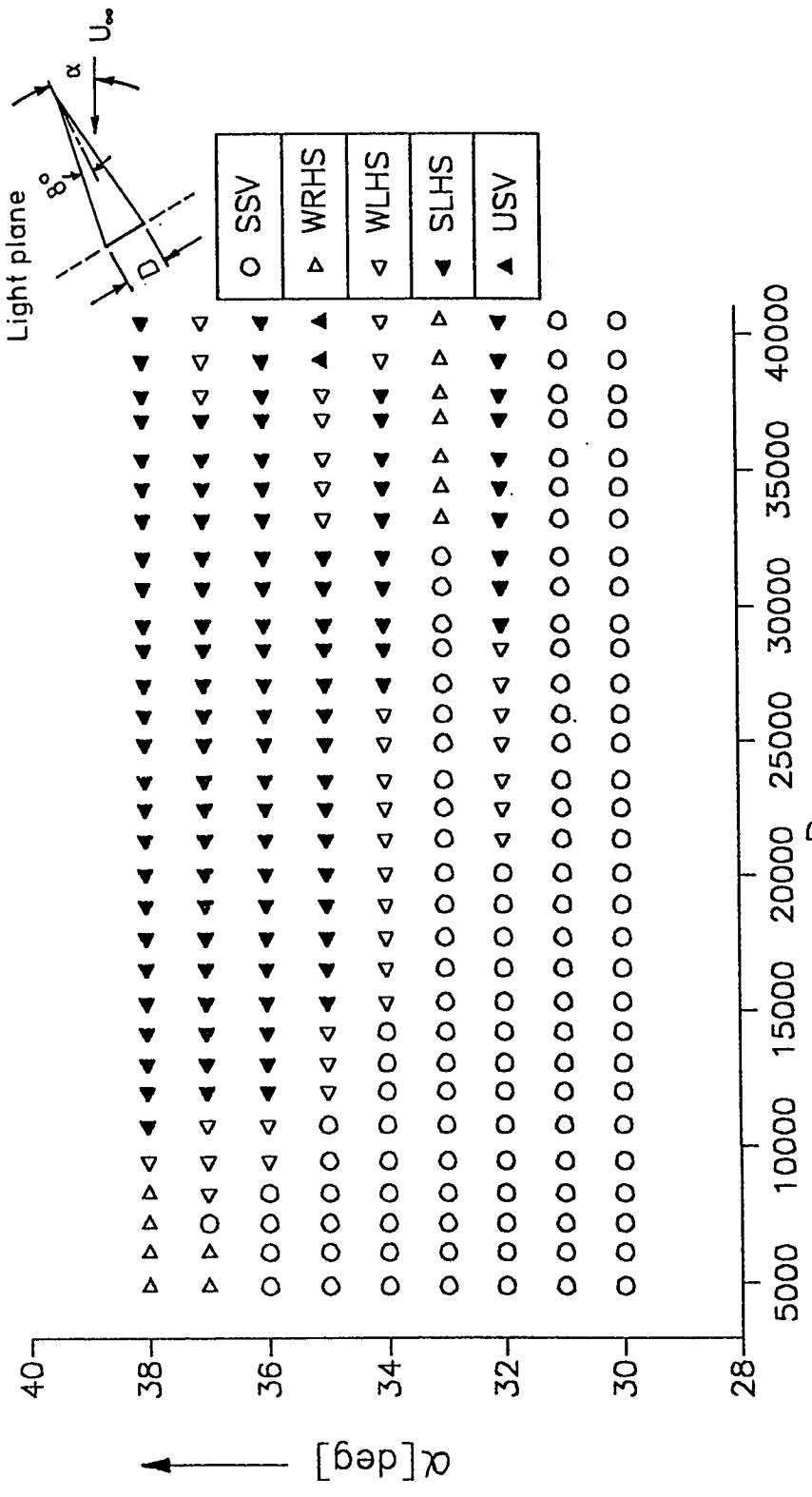

Fig. 4.67 Vortex flow patterns with variation in angle of attack and Reynolds number based on base diameter for circular cone, L = 100 mm, at the base,(looking from tip to base)

(a) Stationary symmetric vortices

$\alpha = 22$ deg, $Re_D = 65{,}000$, at one base-diameter upstream of the base

Fig 4.68 Typical vortex-flow patterns on big cone,looking from tip to base: a) stationary symmetric vortices; b) weak right-hand-side configuration; c) weak left-hand-side configuration; d) strong right-hand-side configuration; e) strong left-hand-side configuration

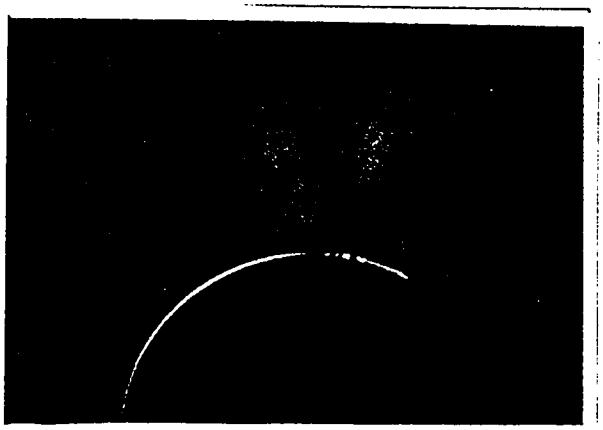

(b) Weak right-hand-side configuration,

$\alpha = 27$ deg, $Re_D = 125{,}000$, at one base-diameter upstream of the base

(c) Weak left-hand-side configuration,

$\alpha = 27$ deg, $Re_D = 54{,}000$, at one base-diameter upstream of the base

Fig 4.68 Continued

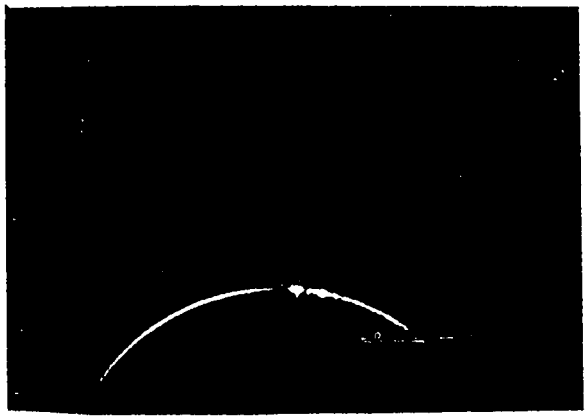

(d) strong right-hand-side configuration,
$\alpha = 29$ deg, $Re_D = 113{,}000$, at the base

(e) strong left-hand-side configuration,
$\alpha = 29$ deg, $Re_D = 54{,}000$, at the base

Fig 4.68 Concluded

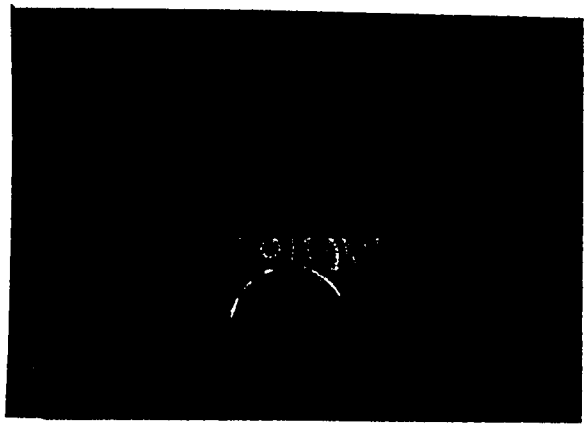

(a) stationary symmetric vortices,
$\alpha = 33$ deg, $Re_D = 5{,}000$, at the base

(b) Weak right-hand-side configuration,
$\alpha = 37$ deg, $Re_D = 5{,}000$, at one base-diameter upstream of the base

Fig 4.69 Typical vortex-flow patterns on small cone,looking from tip to base: a) stationary symmetric vortices; b) weak right-hand-side configuration; c) weak left-hand-side configuration; d) strong left-hand-side configuration

(c) weak left-hand-side configuration,
$\alpha = 35$ deg, $Re_D = 13{,}000$, at the base

(d) strong left-hand-side configuration,
$\alpha = 36$ deg, $Re_D = 40{,}000$, at the base

Fig 4.69 Concluded

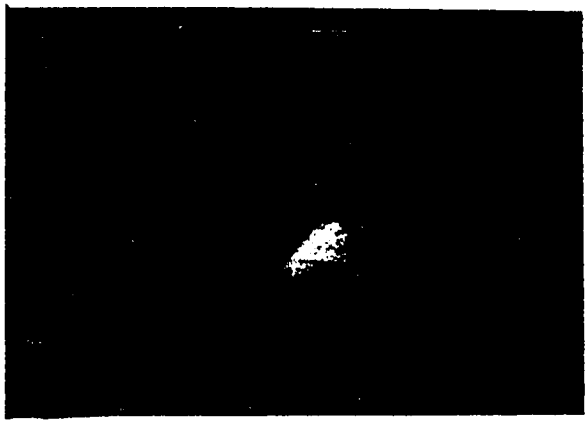

(c) $\alpha = 29$ deg, looking from base to tip, SRHS

(b) $\alpha = 27$ deg, looking from tip to base, SRHS

(a) $\alpha = 25$ deg, looking from tip to base, WRHS

Fig 4.70 Development of vortex-flow pattern with increase in angles of attack, on big cone at $Re_D = 172{,}000$, at one base-diameter upstream

(c) $\alpha = 38$ deg, looking from tip to base, SLHS

(b) $\alpha = 37$ deg, looking from tip to base, WLHS

(a) $\alpha = 36$ deg, looking from tip to base, WLHS

Fig 4.71 Development of vortex-flow pattern with increase in angles of attack, on small cone at $Re_D = 11{,}000$, at the base

(c) $Re_D = 125{,}000$, looking from base to tip, SRHS

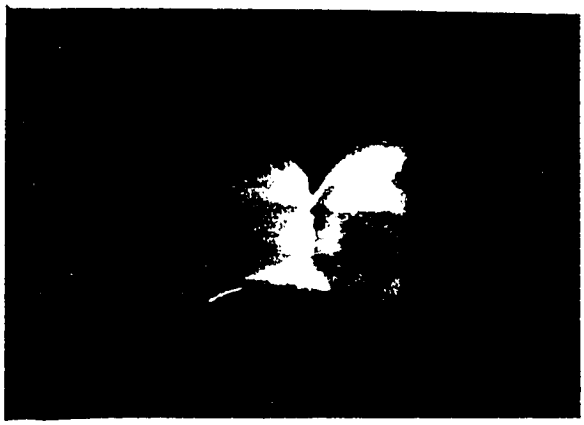

(b) $Re_D = 77{,}000$, looking from base to tip, USV

(a) $Re_D = 65{,}000$, looking from base to tip, SLHS

Fig 4.72 Development of vortex-flow pattern with Reynolds numbers, on big cone at $\alpha = 33$ deg, one base-diameter upstream of base

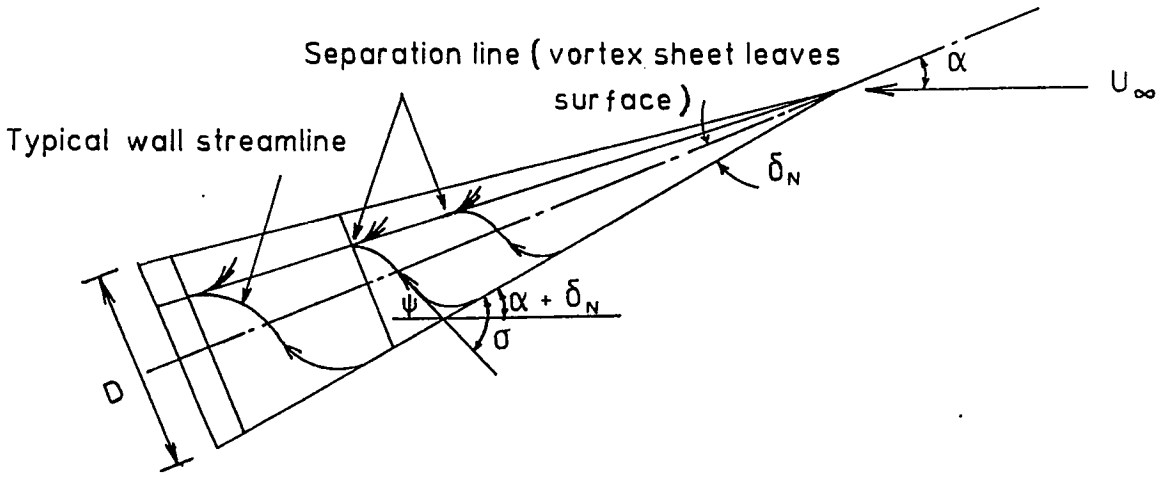

Fig. 4.73 Typical wall streamlines on a circular cone at incidence

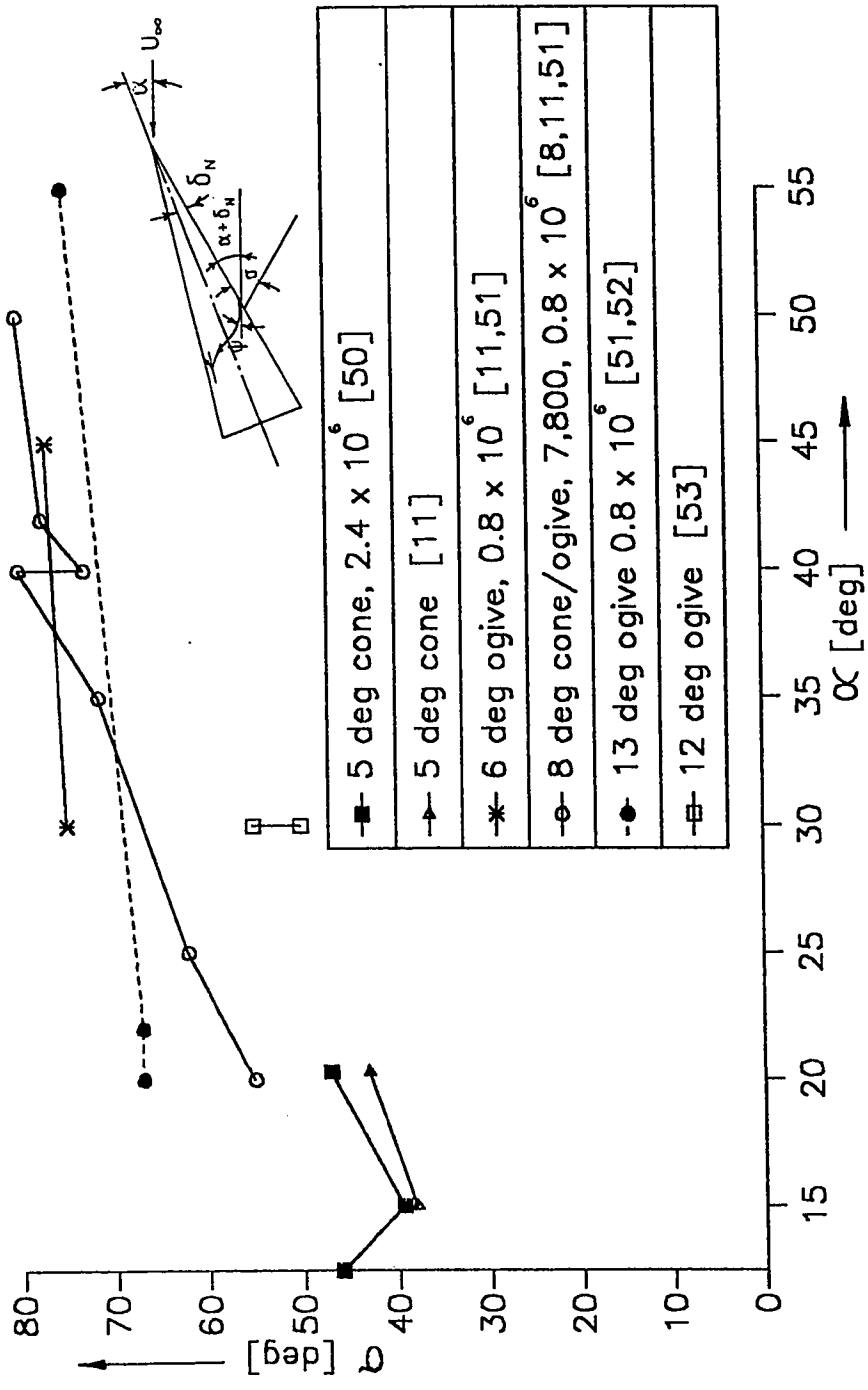

Fig. 4.74 Variation in surface-flow inclination with angle of attack on various slender bodies

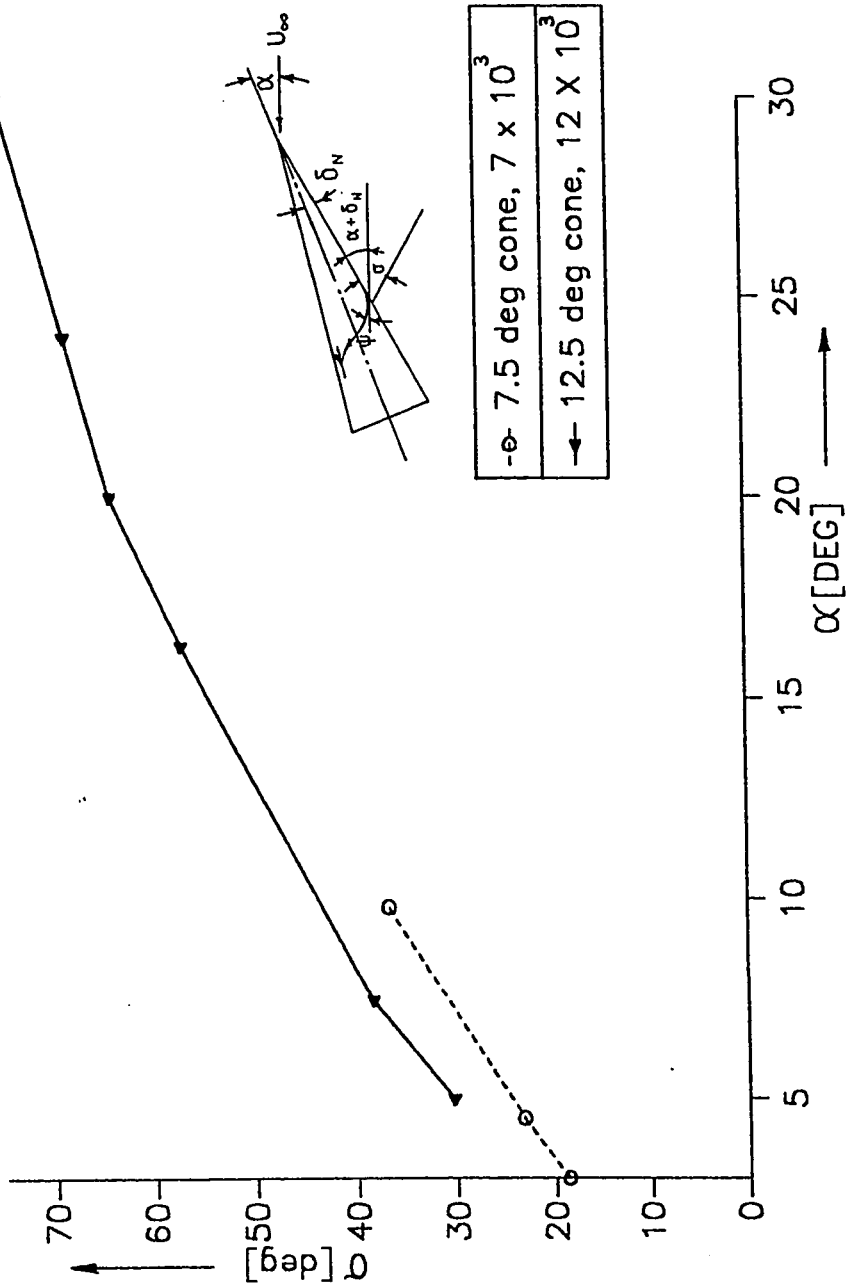

Fig. 4.75 Variation in surface-flow inclination with angle of attack on two circular cones, $\delta_N = 7.5$ deg, and $\delta_N = 12.5$ deg, [36]

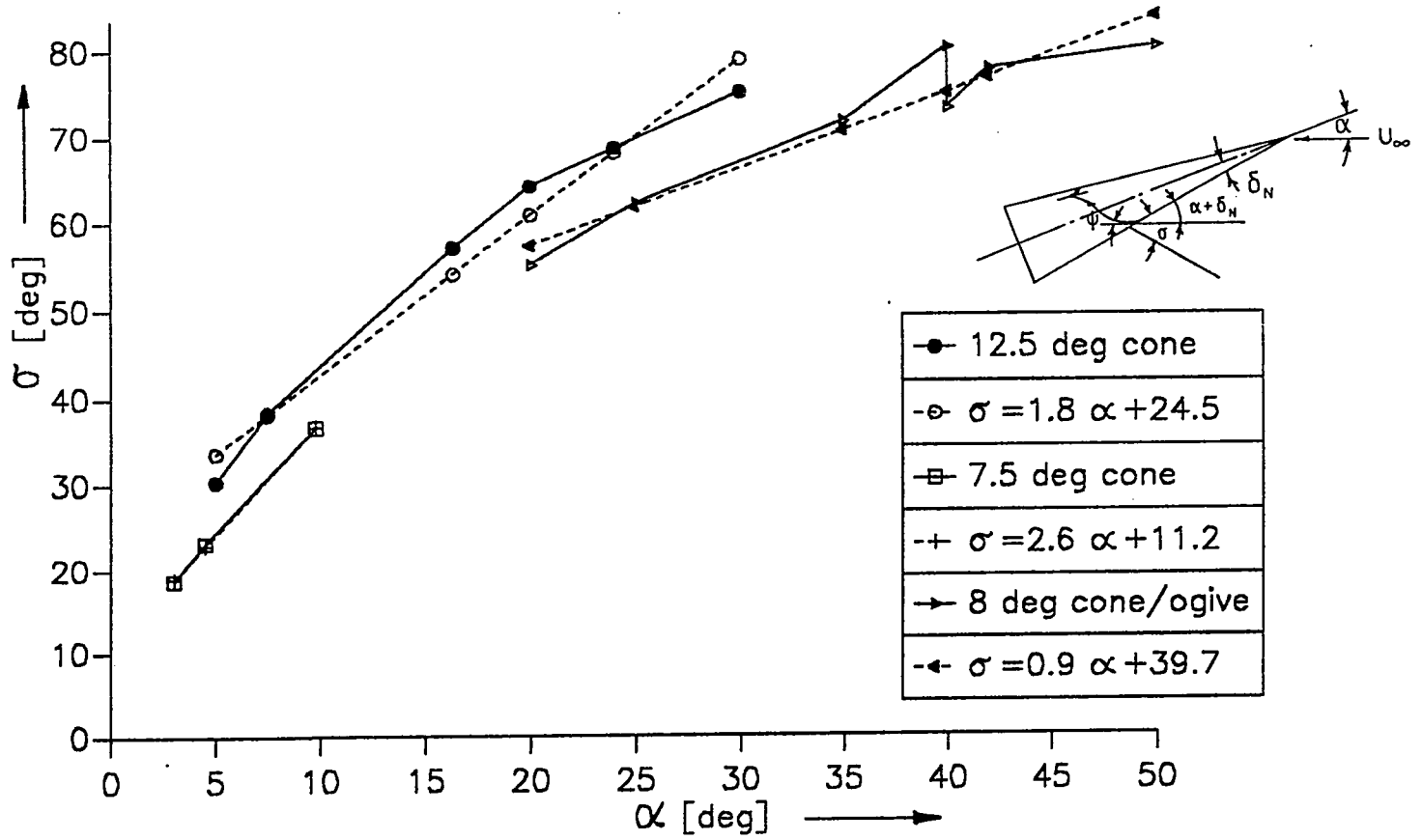

Fig. 4.76 Surface-flow inclination on slender bodies. Values from experiments and from linear curves, fitted to experimental values

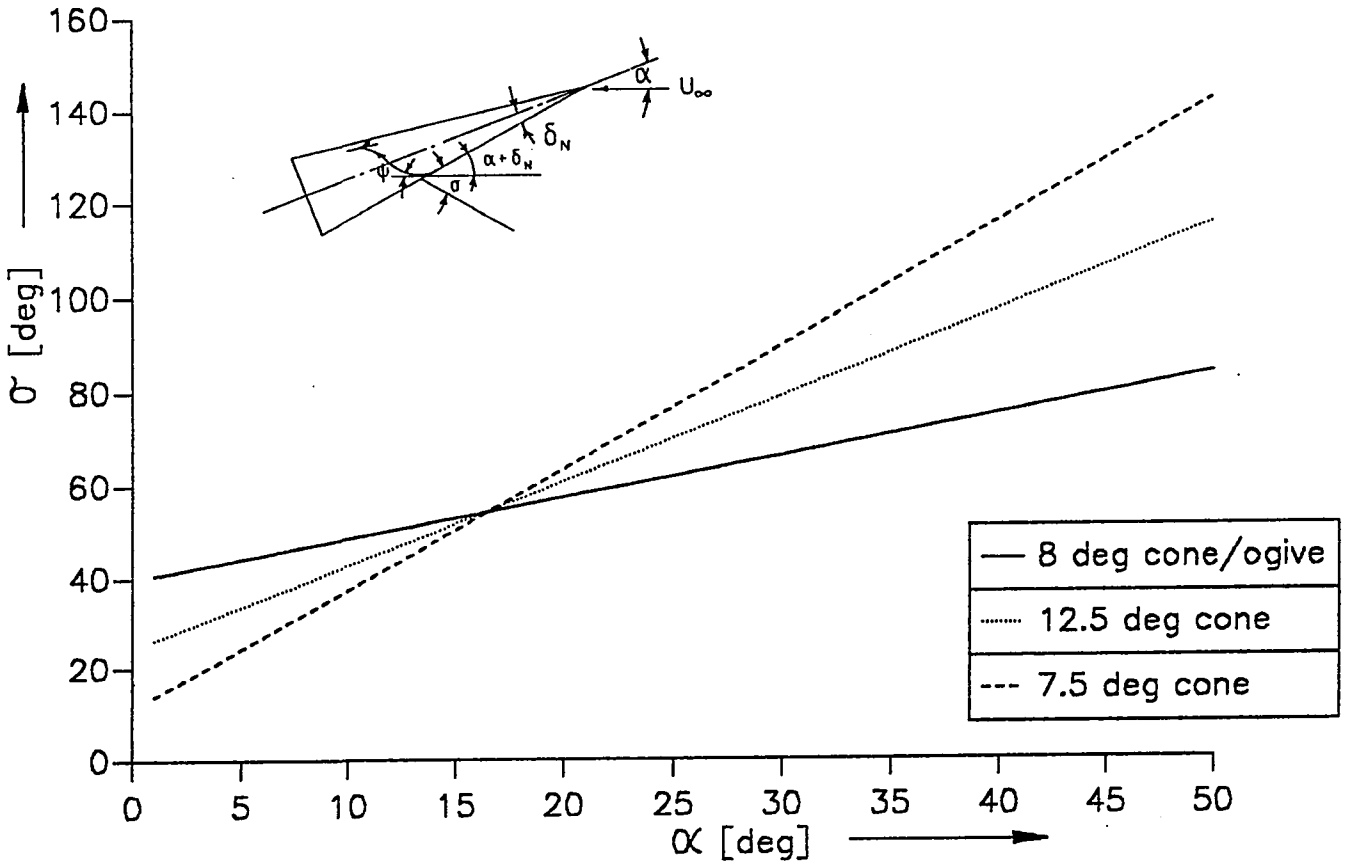

Fig. 4.77 Surface-flow inclination on slender bodies, using linear relationship obtained by curve fitting of experimental values of various slender bodies

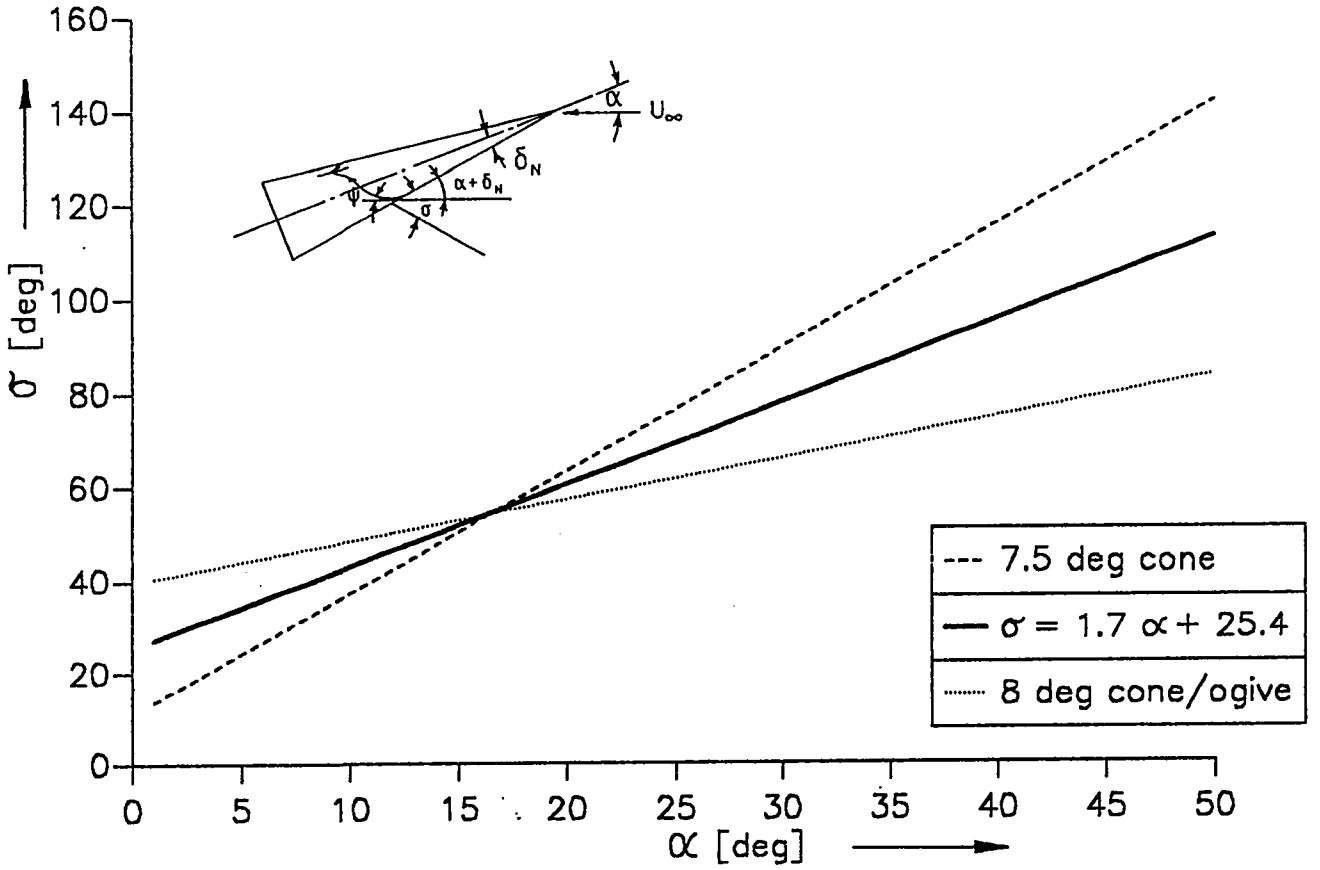

Fig. 4.78 Surface-flow inclination on slender bodies, obtained by taking average of calculated values of $\delta_N = 7.5$ deg cone and $\delta_N = 8$ deg cone/ogive

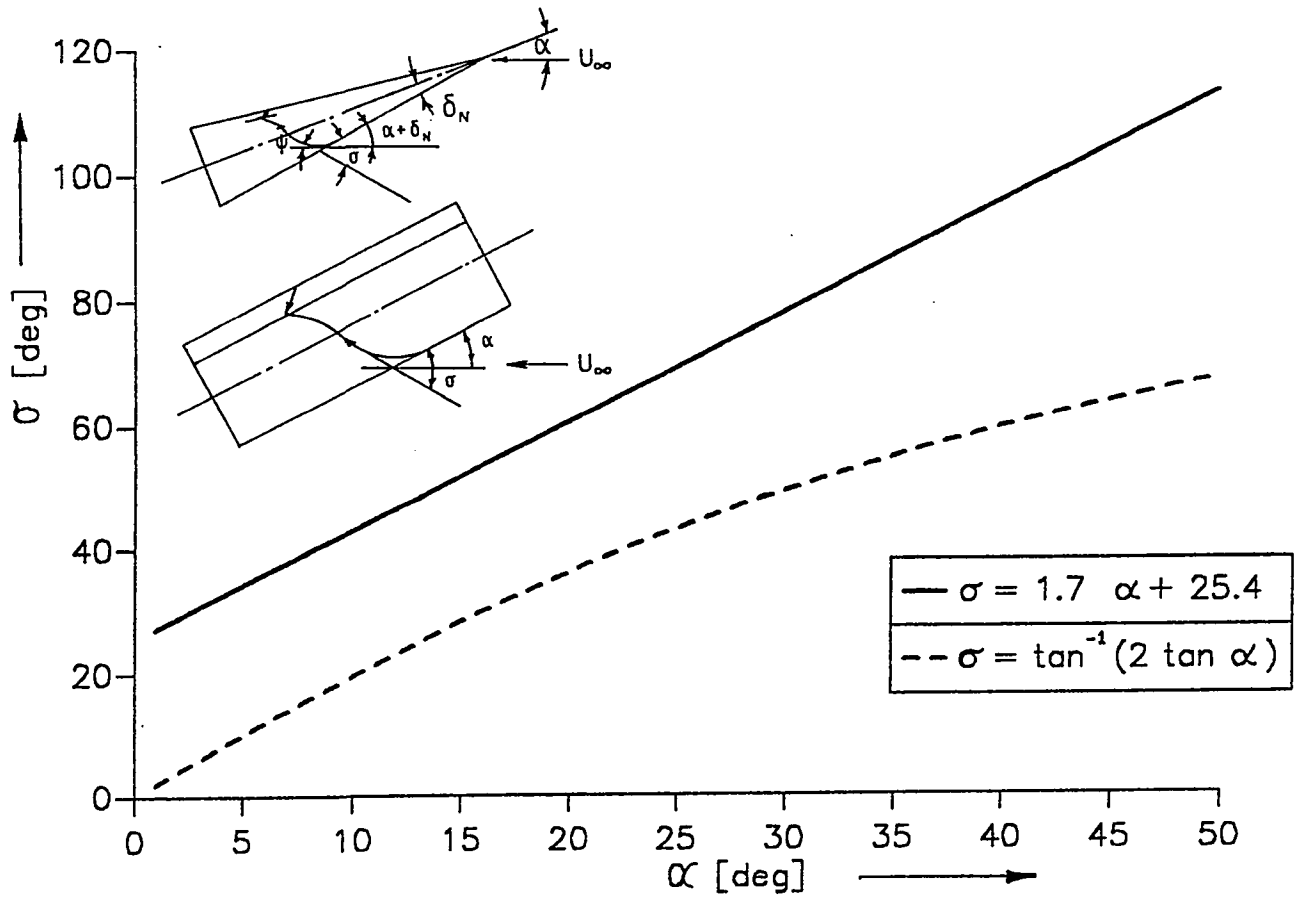

Fig. 4.79 Comparison of estimated surface-flow inclination on pointed slender bodies and on a circular cylinder (using incompressible potential flow theory, $\sigma = \tan^{-1}(2\tan\alpha)$) [2]

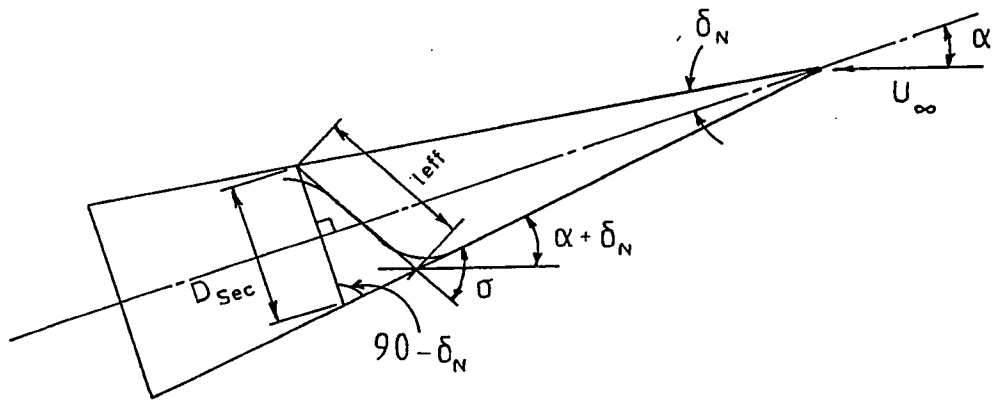

Fig. 4.80 Characteristic length, l_{eff}, on circular cone at incidence, $l_{eff} = D_{sec} \times \frac{\cos\delta_N}{\sin\sigma}$

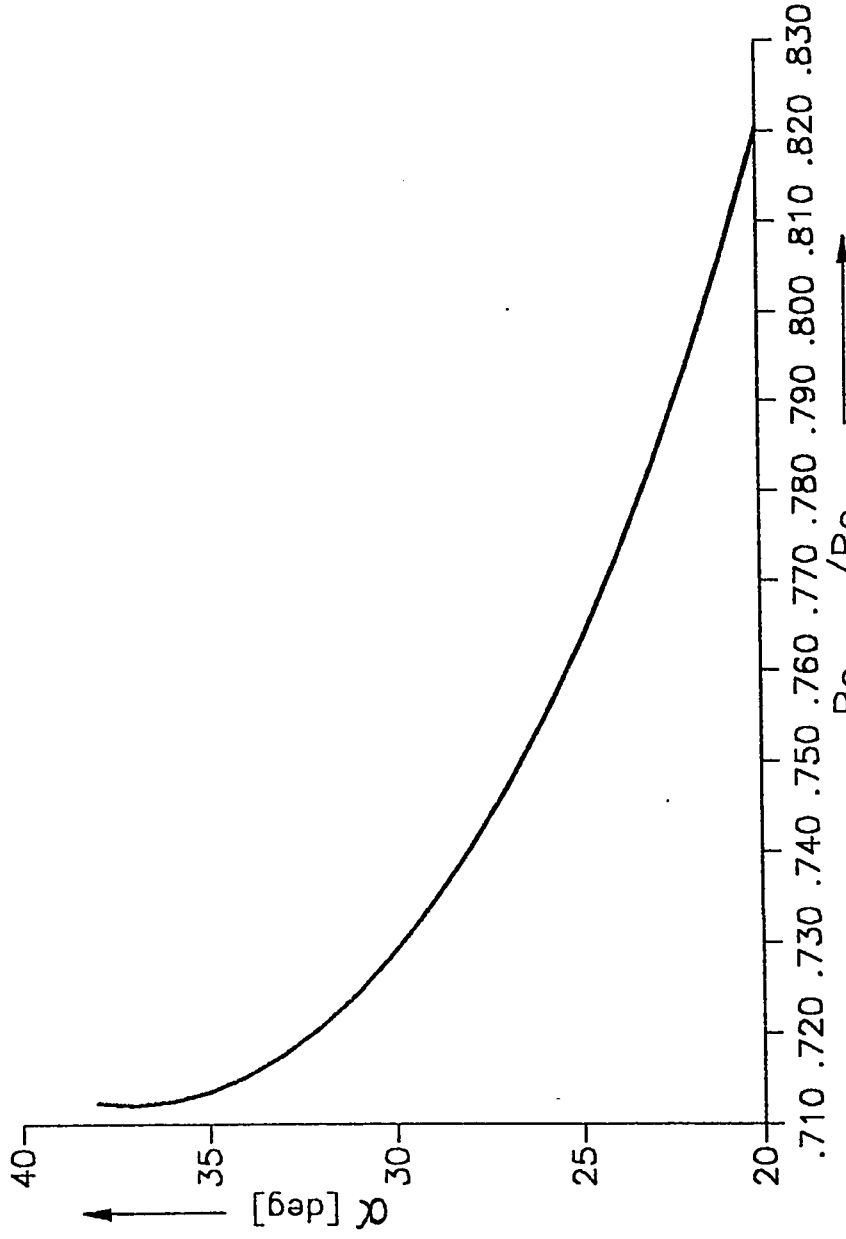

Fig. 4.81 Variation of effective Reynolds number with angle of attack. Effective length calculated using surface flow inclination $\sigma = 1.7\,\alpha + 25.4$

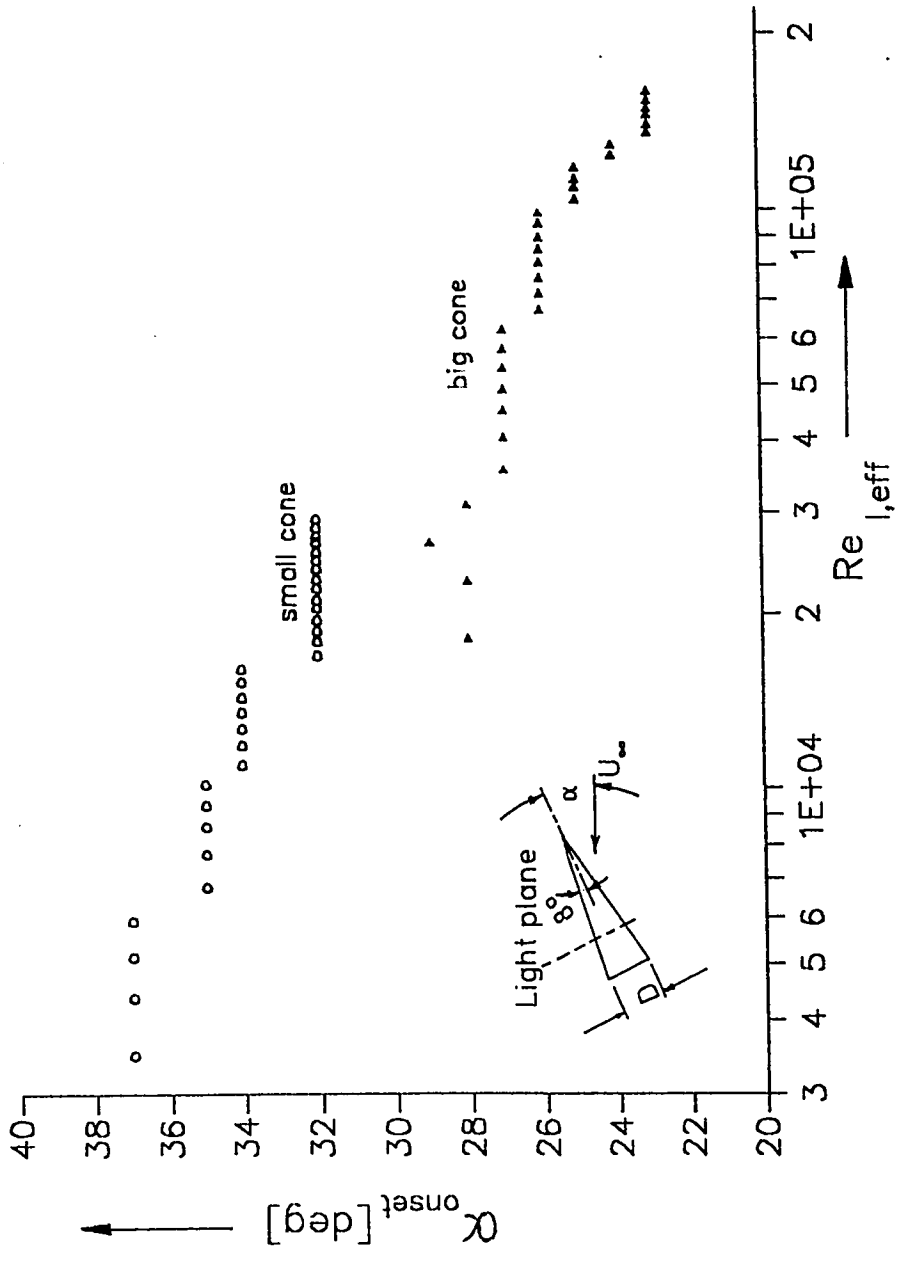

Fig. 4.82 Variation of onset angle of attack with effective Reynolds number on circular cone, at one base-diameter upstream of base

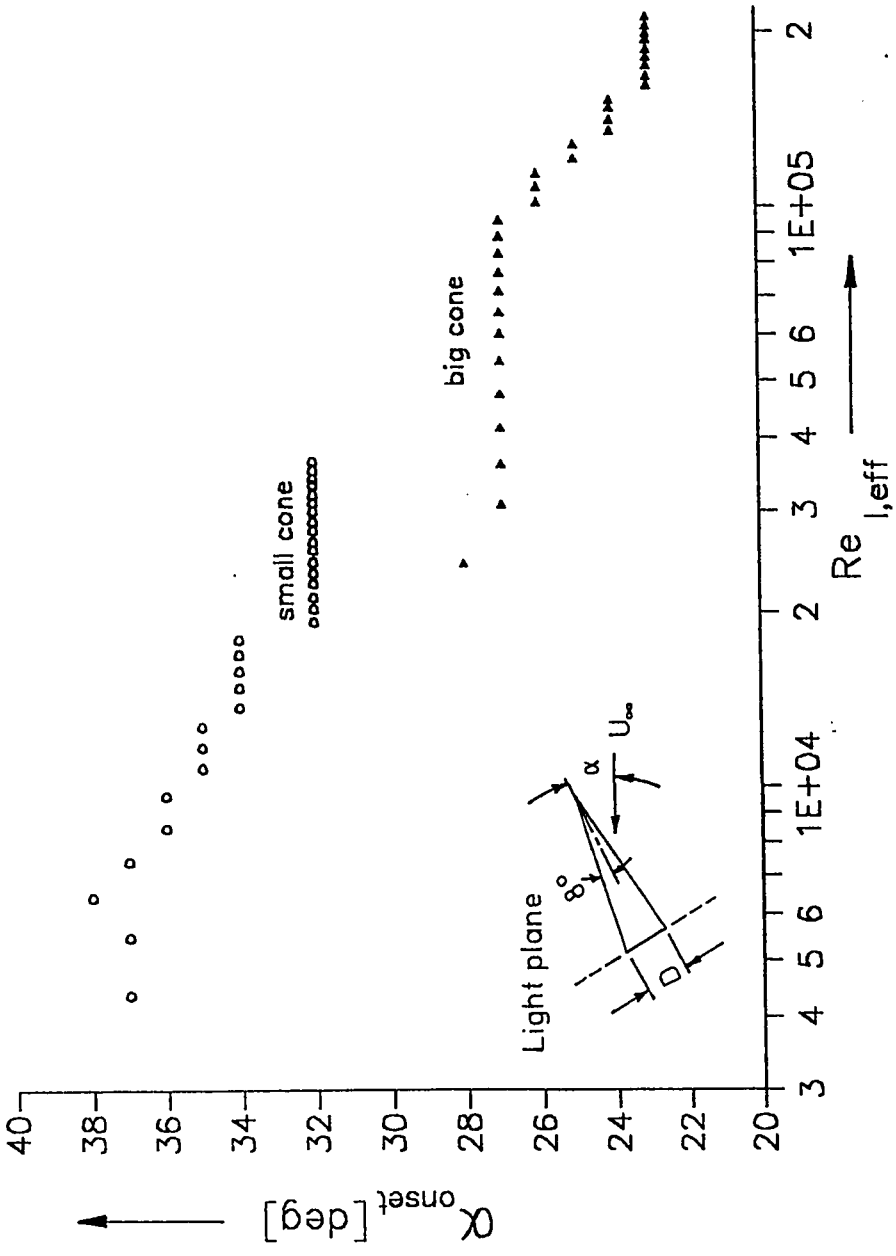

Fig. 4.83 Variation of onset angle of attack with effective Reynolds number on circular cone, at the base

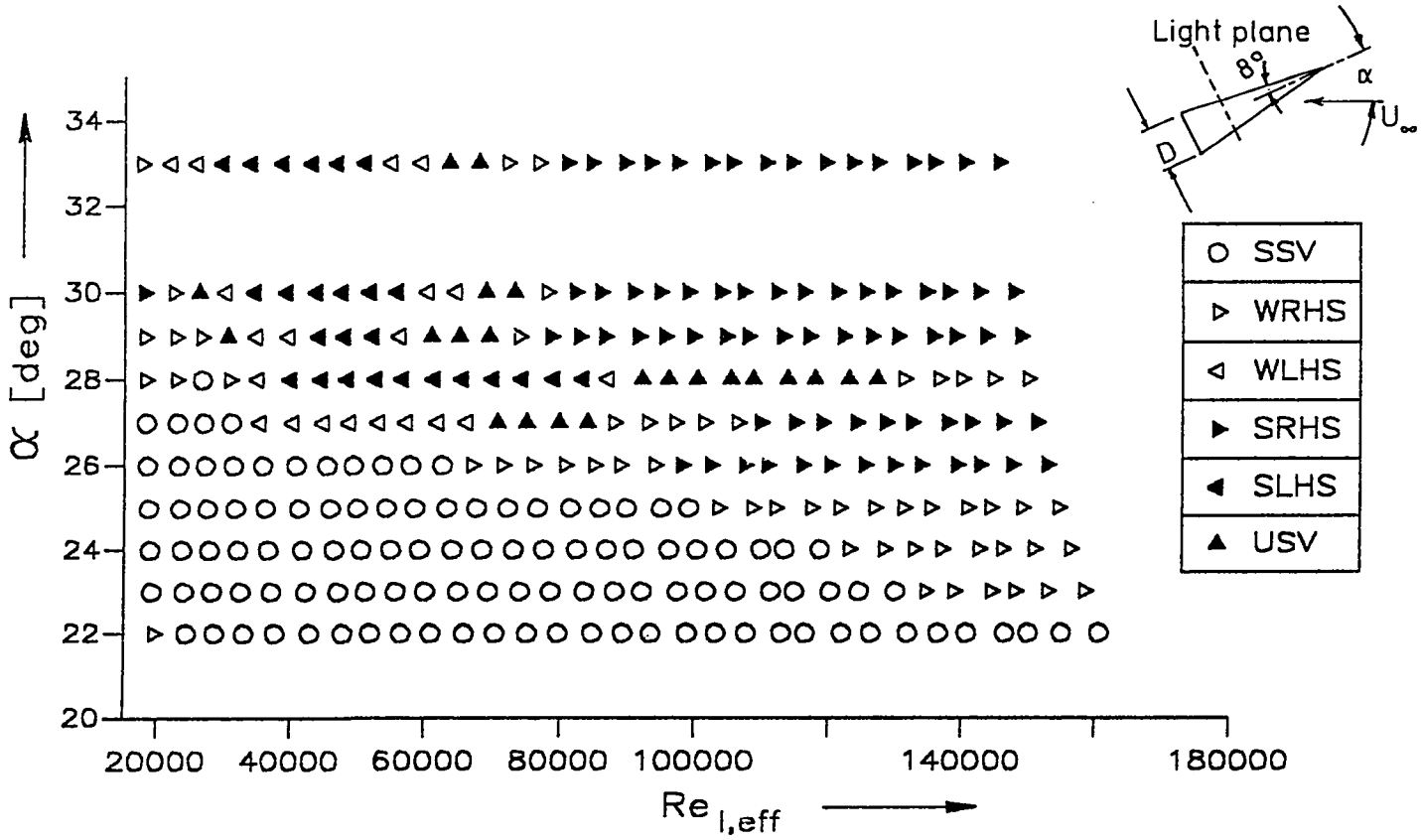

Fig. 4.84 Vortex-flow patterns with variation in angle of attack and effective Reynolds number for circular cone, L = 500 mm, one base-diameter upstream of base (looking from tip to base)

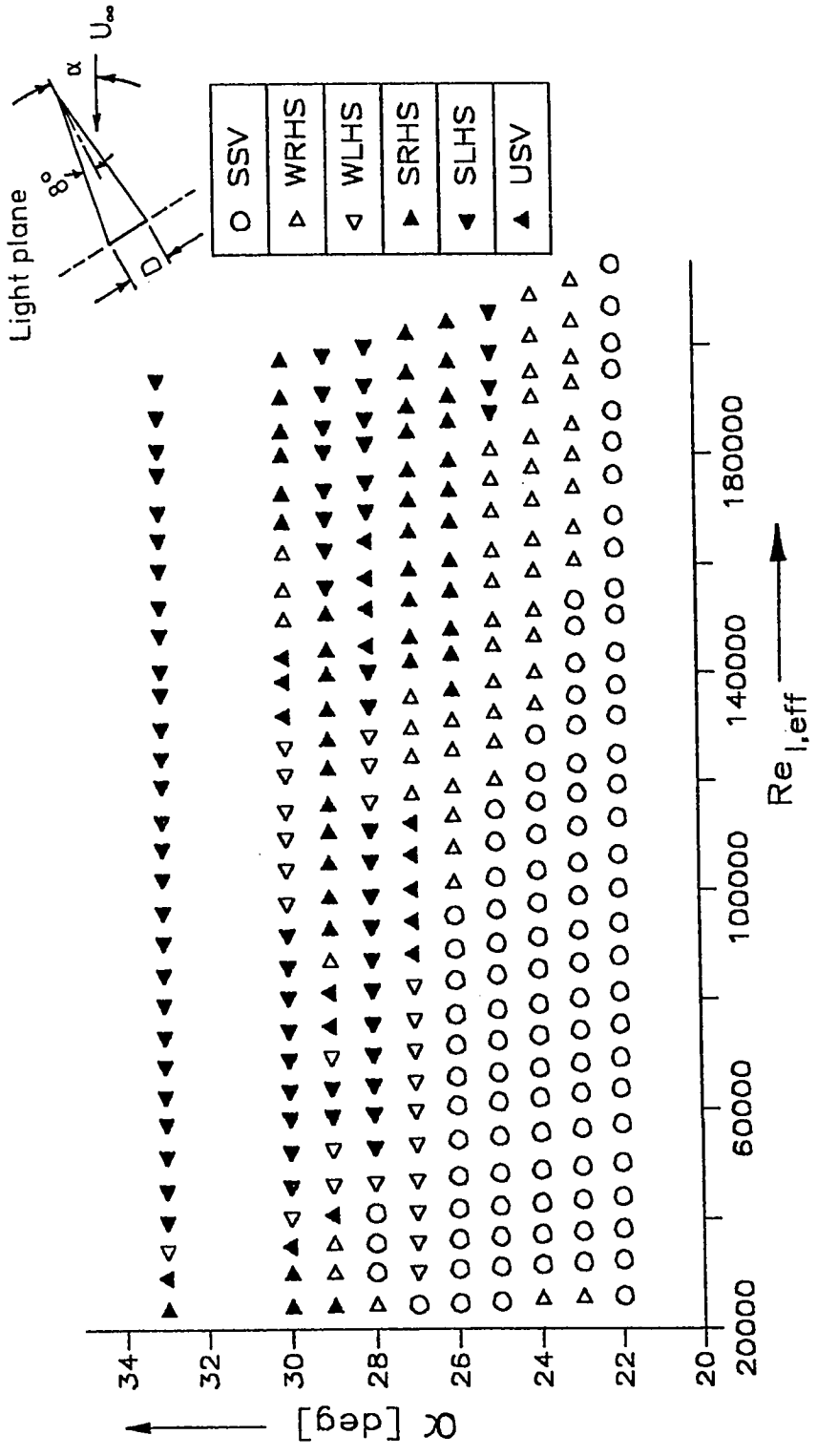

Fig. 4.85 Vortex-flow patterns with variation in angle of attack and effective Reynolds number for circular cone, L = 500 mm, at the base (looking from tip to base)

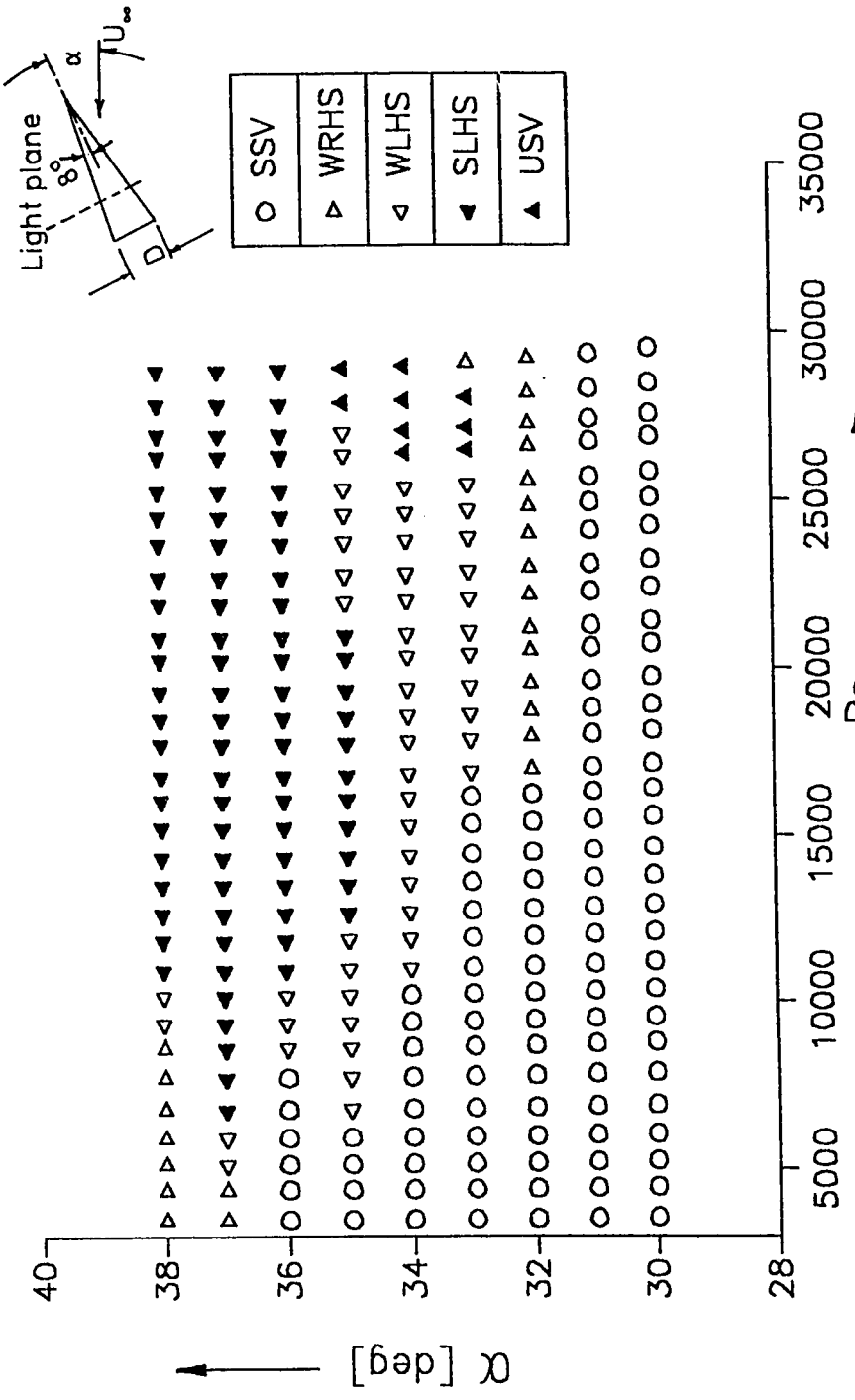

Fig. 4.86 Vortex-flow patterns with variation in angle of attack and effective Reynolds number for circular cone, L = 100 mm, one base-diameter upstream of base (looking from tip to base)

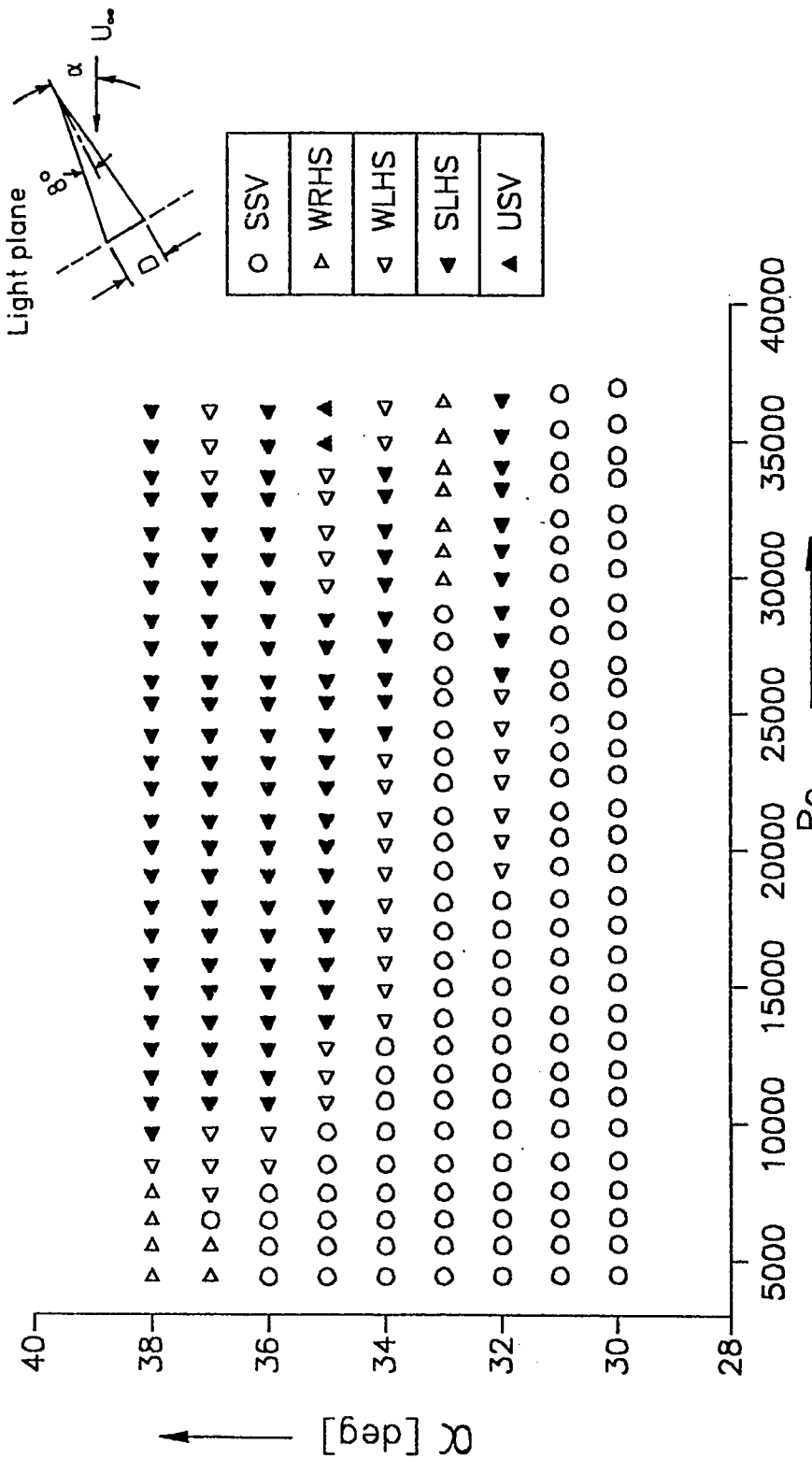

Fig. 4.87 Vortex-flow patterns with variation in angle of attack and effective Reynolds number for circular cone, L = 100 mm, at the base (looking from tip to base)